PB91-208611

UILU-ENG-90-2013

CIVIL ENGINEERING STUDIES
STRUCTURAL RESEARCH SERIES NO. 555

ISSN: 0069-4274

MEASURED INELASTIC RESPONSE OF REINFORCED MASONRY BUILDING STRUCTURES TO EARTHQUAKE MOTIONS

by

Thomas J. Paulson
and
Daniel P. Abrams

A technical report of research supported by the
National Science Foundation
Under Research Grant No. ECE-86-12476

Department of Civil Engineering
University of Illinois at Urbana-Champaign
Urbana, Illinois

October 1990

This report presents the results of a research project which was part of the U.S. Coordinated Program for Masonry Research. The program constitutes the United States part of the U.S.–Japan Coordinated Masonry Research Program conducted under the auspices of the Panel on Wind and Seismic Effects of the U.S.–Japan Natural Resources Development Program (UJNR).

This material is based on work supported by the National Science Foundation under the direction of Program Director Dr. S.C. Liu.

Any opinions, findings and conclusions, or recommendations, expressed in this publication are those of the authors and do not necessarily reflect the views of the National Science Foundation and/or the United States Government.

MEASURED INELASTIC RESPONSE OF REINFORCED MASONRY BUILDING STRUCTURES TO EARTHQUAKE MOTIONS

by

Thomas J. Paulson

and

Daniel P. Abrams

A Report to the National Science Foundation

Research Grant No. ECE-86-12476

Department of Civil Engineering
University of Illinois at Urbana-Champaign
Urbana, Illinois
October, 1990

50272-101

REPORT DOCUMENTATION PAGE	1. REPORT NO. UILU-ENG-90-2013	2.	3. PB91-208611

4. Title and Subtitle
Measured Inelastic Response of Reinforced Masonry Building Structures to Earthquake Motions

5. Report Date
October 1990

6.

7. Author(s)
Thomas J. Paulson and Daniel P. Abrams

8. Performing Organization Rept. No.
SRS No. 555

9. Performing Organization Name and Address
University of Illinois
Department of Civil Engineering
205 North Mathews Avenue
Urbana, IL 61801

10. Project/Task/Work Unit No.

11. Contract(C) or Grant(G) No.
(C)
(G) NSF ECE 86-12476

12. Sponsoring Organization Name and Address
National Science Foundation
Washington, D.C. 20550

13. Type of Report & Period Covered

14.

15. Supplementary Notes

16. Abstract (Limit: 200 words)

Experiments were performed to study the dynamic response of reinforced concrete masonry building structures. Two reduced-scale reinforced masonry perforated shear wall structures were subjected to simulated earthquake motions on a shaking table. A third was tested using conventional static methods to provide insight into differences in behavior of systems that are subjected to artificial static forces and those allowed to develop natural inertial forces.

Experimental data were studied to determine trends in nonlinear dynamic response and to evaluate current practice for seismic design and analysis. Common linear models for assessing lateral drift and distribution of story shear among vertical elements were found to be inadequate for response in the nonlinear range. Analysis of measured response identified simplified procedures for evaluating lateral strength and seismic drift of reinforced masonry structures. It was suggested that sufficient lateral strength could be provided in the piers of a perforated wall structure by placement of minimum amounts of vertical reinforcement and selection of horizontal reinforcement by a capacity design approach. The use of a substitute linear method was suggested for assessing the stiffness (based on lateral drift) of a trial structural configuration. A simple, single-degree-of-freedom nonlinear analysis was suggested for use in evaluating the nonlinear displacement response of a trial configuration.

17. Document Analysis a. Descriptors

Reinforced Masonry, Earthquake, Base Shear, Lateral Drift, Linear, Nonlinear, Stiffness, Strength

b. Identifiers/Open-Ended Terms

c. COSATI Field/Group

18. Availability Statement	19. Security Class (This Report) UNCLASSIFIED	21. No. of Pages 307
	20. Security Class (This Page) UNCLASSIFIED	22. Price

(See ANSI-Z39.18) *See Instructions on Reverse*

OPTIONAL FORM 272 (4-77)
(Formerly NTIS-35)
Department of Commerce

ACKNOWLEDGMENTS

Financial support for this study was provided by the National Science Foundation under grant ECE-86-12476. The project was part of Task 7.1 of the US-Japan Coordinated Program for Masonry Building Research.

Professors D. Foutch, W. Gamble, and M. Sozen are thanked for reviewing the manuscript.

Many others contributed to various phases of this study. The authors are especially grateful to G. Epperson for his assistance in the experimental phase and to A. Tena-Colunga for his contribution to the analytical portion. The authors benefitted from the suggestions and experience of J. Bonacci, Professor S. Wood, and particularly M. Eberhard, who was an invaluable source for advice throughout the study.

Acknowledgment is due to V. Erickson for the construction of the laboratory specimens. T. Balogh is thanked for his efforts in supervising the construction of the test specimens and for designing the static test apparatus. The members of the Machine Shop, under the direction of C. Swan, are also thanked for their timely assistance with the experimental work.

Acknowledgment is also due to H. Dalrymple for his patient assistance in the areas of instrumentation and system control. The efforts of laboratory assistants E. Dornseif, A. Fenrich, K. Kurtz, L. Lawyer and J. Mack are also gratefully acknowledged. J. Gueguen is thanked for proofreading the manuscript.

TABLE OF CONTENTS

Chapter Page

Chapter Page

LIST OF TABLES

LIST OF FIGURES

Figure Page

Figure Page

Figure Page

CHAPTER 1

INTRODUCTION

Masonry is one of the oldest and most traditional of all construction materials currently in use. Masonry buildings have been constructed in many parts of the world to satisfy the demands of economy, esthetics and function. As a result of their performance in recent earthquakes, however, the perceived hallmark of masonry buildings is not their adaptability or ease of construction. Rather, it is the vulnerability to strong ground motions that is now most commonly associated with masonry buildings.

To put this into perspective, it is important to recognize that almost the entire sum of experience with masonry buildings and destructive earthquakes has been with structures which were unreinforced and built with little or no consideration of the potential effects of strong shaking. Although proven in only a few cases, it is reasonable to believe that masonry systems can be engineered and reinforced to ensure survival and serviceability in seismic regions. To make the leap from this belief to the realization of actual buildings which perform well in earthquakes requires the development of design guidelines which reflect a knowledge of how these structures can be expected to respond to strong ground motions.

An essential component of this required knowledge is an understanding of how reinforced masonry buildings behave in the range of response in which lateral displacements are no longer linearly related to lateral forces. Concerns related to energy dissipation, inelastic deformation capacity and "ductility" or "toughness" become paramount when structures are driven to respond in the nonlinear range.

This study is directed towards improving the understanding of how engineered, reinforced masonry buildings respond to earthquakes of varying intensity, with particular emphasis on the nonlinear range of response. It is intended that the knowledge and insights gained from the study will be used to direct the development of computational models and design methodologies for masonry structures. Two dynamic tests and one quasi-static test of one-quarter scale reinforced masonry building systems provide response data for evaluating perceptions of behavior and analytical methods for estimating response.

1.1 Background and Uniqueness of Study

This study was not the first to use shaking table tests to evaluate masonry structures. Although the method has been infrequently used for this type of structure, shaking table studies of reduced-scale masonry building systems have been conducted in Yugoslavia [36], China [38,39,41,42], Japan [37], Italy [7], Mexico [6], and the United States [17]. These vary widely with respect to materials, structural configuration and reinforcement (if any). With the exception of an investigation of single-story houses performed in the U.S. [17], none of the systems investigated could be considered to be representative of the materials and detailing practice characteristic of those used in this country. Even the single-story house tests represented a proof test of a specific configuration and not a general examination of structural response.

The present investigation can be viewed as one of the first to examine the nonlinear response of multistory masonry systems with an eye towards improving seismic design procedures. It is additionally distinct from previous studies in that it was not a completely independent investigation, but rather a component of a coordinated program (TCCMaR [28]) dedicated to developing design guidelines and analytical methods for masonry structures. This study profited from the results of research conducted by other TCCMaR researchers. In particular, the results of studies of scale-model masonry assemblages [18], confirmed the viability of modeling masonry at a reduced scale and guided the selection of materials for this study.

1.2 Objectives and Scope

While the overall goal of this investigation is to better the conceptual understanding of how masonry buildings respond to strong shaking, the research task also has other more specific objectives:

- to provide dynamic test data for the calibration of numerical response models.
- to evaluate commonly accepted practices for seismic design and response analysis.

- to suggest simplifications in design or analysis methods.
- to demonstrate the nonlinear response characteristics of reinforced masonry structures.
- to infer behavior of large-scale test structures.

The accomplishment of these objectives relies on observations and measured response of reinforced masonry building systems. Two reduced-scale structures are subjected to a similar sequence of simulated earthquake motions on a shaking table. Another replicate structure is tested using quasi-static methods typical for laboratory testing of large-scale structures.

The salient features of the experimental program are given in Chapter 2, with additional details supplied in Appendices A, B and C. In Chapter 3, characteristics of the base motions used in the earthquake simulations are presented. Observed response of the dynamically tested structures is presented in Chapter 4. Appendix D contains records of damage patterns, and response waveforms for all dynamic tests are found in Appendix E.

In Chapter 5, selected aspects of the observed response of the dynamic tests are presented and discussed. Calculated estimates of selected response parameters are compared with measured data in Chapter 6. The first part of the chapter considers the estimation of base shear strength of the structures and the second part deals with estimates of lateral drift. The results of Chapter 6 are used in Chapter 7 to comment on the design of reinforced masonry structures.

Chapter 8 presents a comparison of identical structural systems subjected to either dynamic motions at the base or static lateral forces at each floor level. Chapter 9 provides a summary of the study as well as a statement of the principal conclusions.

CHAPTER 2

EXPERIMENTAL PROGRAM

The experimental phase of this study entailed the design, construction and testing of three reduced-scale reinforced masonry building systems. This chapter discusses the features of the experimental program as well as the considerations attendant to the modeling and testing of one-quarter scale masonry structures. Further details of specimen properties and test setups are provided in Appendices A through C.

2.1 Overview of Test Program

The overall objective of the experimental work was to study the dynamic response characteristics of reinforced masonry building structures. A shaking table was used to produce dynamic effects in laboratory test specimens by subjecting them to motions at the base typical of those experienced by actual buildings during an earthquake. Two structures were tested with base motions which were varied in intensity to produce successively increasing levels of damage.

Since the payload limit of the shaking table precluded the use of full-scale structures, it was necessary to construct building systems at a reduced scale. Three-story test structures were constructed at one-quarter scale with different configurations as shown in Fig. 2.1 and 2.2. Each specimen consisted of two perforated flanged walls coupled by floor slabs and was designed to resist lateral forces in the direction of the longitudinal axis of the walls. Perforated, flanged shear walls were used in the study for a number of reasons. The flanges allowed the flexural strength of the pier elements to be varied and also provided stability in the direction transverse to the plane of the walls. The use of perforations of different sizes made it possible to vary the shear strength of the piers as well as their relative flexural and shear strengths. Walls of the first design (RM1, Fig. 2.3) were perforated with a symmetrical pattern of window openings, whereas walls of the second design (RM3, Fig. 2.4) had an asymmetrical pattern of window and door openings. Of primary interest was the distribution of shear to the individual piers and the nature of the resulting inelastic

response mechanisms when the specimens of different strength and stiffness were subjected to similar base excitations.

There may be a tendency to think of the test structures as true building systems and refer to them as such, because their configuration is similar to actual construction. It is thus important to note that the specimens were not intended to be models of full-scale structures, but rather as instruments for improving the understanding of how reinforced masonry systems respond to imposed lateral forces. As such, the models were founded on concepts of structural behavior rather than prototype structures in the field. They were merely structural systems with known material and geometrical properties that were subjected to known excitations.

While the structures had no physical prototype, it was essential that they be constructed of materials comparable to those used in actual construction so that they would behave in a manner characteristic of full-scale reinforced masonry. Consequently, the test structures were constructed with reduced-scale concrete masonry units which were similar to typical eight-inch blocks. Horizontal and vertical reinforcement consisted of steel wire with a diameter approximately one-quarter of that of a No. 4 reinforcing bar (0.121 in). As shown in Fig. 2.5, masonry units were fully grouted.

Both structural designs were subjected to a series of simulated earthquake motions which were derived from the north-south component of the motion measured at El Centro, California in 1940. Only one horizontal component of the ground motion was reproduced by the earthquake simulator (Fig 2.2). The duration of the displacement record was compressed and its amplitude was scaled for successive test runs so that the structures would respond within desired ranges of behavior.

Response of the structures to the base motions was monitored by transducers which recorded absolute accelerations and displacements relative to the base throughout each test run. Measurements included lateral deflections and accelerations of each wall as well as flexural and shear deformations of the piers in the lower stories. Electrical signals from the transducers were digitized and recorded on a computer. Changes in natural frequency and apparent viscous damping of the structures were monitored by performing low

amplitude free vibration tests before and after each test run. Progression of damage was recorded by photographs and sketches of crack patterns after each test run.

In addition to the shaking table tests of RM1 and RM3, a replica of structure RM1 (specimen RM2) was constructed and tested dynamically on base isolation devices and then quasi-statically using hydraulic actuators to impart lateral forces at each floor level. Objectives and descriptions of these experiments, as well as comparisons with the dynamic tests, can be found in Chapter 8 and reference 29.

2.2 Design Considerations

Since each structure represented a test of a physical concept, it was designed to respond in a specific behavioral mode. Flexural behavior was selected as the intended mode of response for both structures for a number of reasons. First, the choice was consistent with the experimental objective of demonstrating that reinforced masonry can behave in a ductile manner within the nonlinear range of response. Second, it is consistent with the current seismic design philosophy, which places a strong emphasis on the obviation of shear failures. Finally, lessons assimilated from the model tests are more easily and confidently extrapolated to full-scale structures when flexural action predominates than when the response is dominated by shear-related behavior.

Horizontal and vertical reinforcement was selected for each structural configuration with the intention that response of the structure would be governed by the flexural strength, stiffness and deformation capacities of the vertical piers (coupled with the flanges). Horizontal spandrel beams were stronger relative to the piers than in a typical full-scale structure because of the oversized slab thickness (discussed in section 2.4) and thus were not expected to deform significantly. The design strategy was to select amounts and arrangements of reinforcement so that the ultimate limit state of the specimens would be governed by yielding of vertical reinforcement followed by crushing of the masonry at the ends of the piers. Shear failure was to be precluded by the placement of sufficient amounts of horizontal reinforcement in the piers. To avoid bond failure, lap splices were omitted

by anchoring the vertical reinforcement to the foundation grillage and extending it continuously to the top of the structure.

2.3 Specimen Description

Structures RM1 and RM3 differed primarily in the layout of window and door openings, width of the flanges and distribution of horizontal reinforcement. No. 11-gage wire, with a diameter of 0.121 inches, was used for both horizontal and vertical reinforcement (Fig. 2.5). Vertical reinforcement, located at the center of the cells, was spaced at 4 inches. Horizontal reinforcement was embedded at mid-depth of a course of blocks and was spaced at different intervals for the two structures. In all cases, percentages of reinforcement were in excess of the minimums prescribed by the 1988 Uniform Building Code [21] for buildings located in seismic zones 3 or 4 (ρ_h and $\rho_v > 0.0007 \times A_{gross}$; $\rho_h + \rho_v > 0.002 \times A_{gross}$).

2.3.1 Design Type RM1

The first structural design (RM1, Fig. 2.3) was based on the assumption that the stocky piers and wide flanges would cause the flexural action of the pair of walls to resemble that of a simple cantilever. It was expected that nonlinear deformations of the structure would result from yielding of the vertical flange reinforcement at the base. To ensure this type of behavior, the amount of vertical reinforcement was limited so that it would yield before the shear capacity of the first-story piers was reached. To this end, flexural reinforcement was restricted to 0.15% of the gross cross-sectional area (No. 11-ga. wire at 4 in. spacing). This percentage is typical for full-scale buildings when minimum code requirements dictate the amount of reinforcement.

Based on results of an earlier study of a statically loaded, full-scale masonry structure of the same configuration as RM1 [2], it was anticipated that the center pier between window openings would attract the majority of the story shear and was thus considered to be the critical element for shear concerns. Horizontal reinforcement, spaced at 6 inches, comprised 0.10% of the vertical cross-sectional area. The total base shear force necessary

to initiate diagonal cracking in this pier was estimated to be 10 kips using a linear elastic finite element model of the structure (plane stress elements). This force was obtained by matching the principal stress from the finite element analysis with the diagonal tension strength (158 psi) of a panel with the same dimensions as the center pier which was tested in diagonal compression (Section B.7.2). The 10 kip cracking force was compared to the base shear corresponding to the estimated static yield strength of the structure (9.5 kips). This estimate was based on an idealization of the structure bending as a cantilever under an inverted triangular distribution of lateral force. Since the estimated diagonal cracking force for the center pier (ignoring any contribution from the exterior piers) was lower than the base shear corresponding to the flexural mechanism, flexural behavior was expected to govern the response of the system.

2.3.2 Design Type RM3

The second structure (RM3, Fig. 2.4) was designed with thinner flanges and more slender piers so that the system response would be more dependent on the manner in which story shear was distributed to the individual piers. Dimensions of the piers were selected so that the shear area of the three piers was the same, while the flexural stiffness varied. The two exterior piers had the same cross-section, but one was six courses tall while the other was the full story height of fourteen courses. The center pier was also six courses tall, but had no flange. Horizontal reinforcement was selected for each pier using a capacity-design type of approach to ensure that the shear strength of the pier exceeded the shear corresponding to the formation of plastic hinges at the top and bottom of the pier. Nominal percentages of horizontal reinforcement were 0.30% for the two short piers and 0.15% for the tall pier.

It was thus expected that deformations of the structure would be primarily the result of flexural and shear deformations of the base-story piers and that the peak strength of the structure would depend on the flexural capacity of these piers and the proportion of lateral force which each pier resisted.

2.4 Properties of Reduced-Scale Masonry

Although it is convenient to refer to the models as "one-quarter scale" masonry structures, direct scaling of material properties was not an intent of the study and no attempt was made to satisfy all the laws of dynamic similitude. The focus of the study was on the response of the structures in the nonlinear range. For this range, in which acceleration is not expected to be proportional to displacement, the laws of similitude are difficult to satisfy.

It was, however, necessary to identify the mechanical properties of the materials so that the structures could be designed and the response measurements could be interpreted. Since the primary concern was that the hysteretic properties of the reduced-scale masonry resemble those of full-scale construction, preliminary studies were performed to examine only those properties which were expected to significantly affect the dynamic response of the model structures. These properties included the stress-strain characteristics of the reinforcement, compressive strength and stiffness of the model masonry, bond characteristics of the reinforcement and grout, and shear strength of the masonry piers.

2.4.1 Reinforcement

The stress-strain characteristics of the reinforcement were important since the response of both test structures was expected to be the result of yielding of the reinforcement in tension. While it was not necessary that the yield stress of the reinforcing wire be directly related to that of a typical full-scale reinforcing bar, it was desirable that the shape of the stress-strain curve for the model and full-scale reinforcement be similar. No. 11-gage brite basic annealed wire was used for all reinforcement in the test specimens. Direct tension tests on wire coupons indicated a mean yield stress of 47 ksi and an ultimate tensile strength of 61 ksi. These tests are described in more detail in Section B.5. A representative stress-strain relationship (Fig. B.5) shows a nearly bilinear curve.

2.4.2 Masonry

Since the peak strength of the specimens was expected to be limited by the crushing of the masonry in the plastic hinge regions, it was also important that the properties of the model masonry in compression were similar to those of full-scale construction. Reduced-scale concrete masonry units were furnished by a block manufacturer in accordance with a specified mix design : two parts (by volume) Type I-A Portland cement and one part masonry sand (sieved through a No. 16 sieve). The blocks were cast in molds fabricated by the same company that manufactures molds for full-scale block. The model blocks had the same relative geometry as a typical eight-inch block including the taper of the face shells. Mortar was Type S and was the same as used in full-scale construction except that only aggregate passing a No. 16 sieve was added. Grout was identical to that used for full-scale construction. Details of the mix designs and mechanical properties of the blocks, mortar and grout are presented in Appendix B.

Sample three-unit prisms were made during the construction of each test structure. Compression tests, performed at the time of each earthquake simulation, indicated average compressive strengths equal to 1215 psi (coefficient of variation equal to 25%) for RM1 prisms, 1318 psi (c.o.v. = 28%) for RM2 prisms, and 1228 psi (c.o.v. = 21%) for RM3 prisms. Sample stress-strain curves are given Figures B.2 - B.4.

2.4.3 Bond Characteristics

In order to determine the splice length required to fully develop the tensile strength of the reinforcing wire, a series of tension tests were performed on No. 10-gage wires lapped within prisms of varying height (Fig. B.6). As discussed in section B.7.1, test data suggested that the lapped wires pulled apart at an equivalent bond stress of 106 psi. Given this stress and the measured properties of the No. 11-gage wire, 14 inches of lap would be required to develop the yield strength of the No. 11 wire. This would have required a splice length of half of the story height, which was felt to be impractical. Consequently, no lap splices were used in the test structures. Although this was not representative of actual construc-

tion, it was considered acceptable since system response and not detailed behavior was of concern.

2.4.4 Shear Strength of Piers

As discussed in section 2.3.1, it was desirable to obtain an estimate of the shear capacity of a reduced-scale masonry pier so that the specimens could be designed to prevent shear forces on the pier from reaching this magnitude. As mentioned previously, the shear force to initiate cracking in the center pier of RM1 was estimated to be 10 kips. In order to determine the peak strength of this pier after cracking, three square reinforced masonry panels having the same size and arrangement of reinforcement as the center pier were subjected to compressive forces along a diagonal axis (Fig. B.8). These diagonal compression tests, described in Section B.7.2, suggested an average shear strength of 240 psi (based on calculation methods of ASTM E519-81 [4]). A procedure presented by Yokel and Fattal [40] predicted the ultimate shear strength of the panel to be 15 kips. Although the state of strain in this type of specimen is complex, and may not be representative of that for a pier in a perforated shear wall, it was simple at one-quarter scale and was one of the only methods available for obtaining at least a rough design estimate of the shear capacity. After cracking of each panel, the shear was resisted by the reinforcement while the cracks grew to widths of over 2 mm with little loss of strength. This suggested that the horizontal reinforcement was sufficiently anchored in the piers to allow for ductile response in the event that diagonal cracking did occur during the earthquake simulation. Thus redistribution of story shear to exterior piers was plausible.

2.5 Specimen Construction

All structures were constructed in the laboratory by the same professional mason (Fig. 2.6). Blocks were laid on a reinforced concrete grillage (Fig. 2.6) which anchored the vertical reinforcement, and served as a stiff foundation. After laying four or five courses of block, all cells were cleared of mortar droppings and filled with grout. High-lift grouting,

common in full-scale construction, was not possible because of the impracticality of using clean-out holes, and/or sponges at one-quarter scale. Floor slabs were cast in place so that the slab weight would be distributed uniformly along the length of the wall. Slab concrete was allowed to fill the top half of the cells of the top course of blocks so that the slab-wall connection would be strong in shear. The thickness of the slabs was oversized so that they would be capable of supporting the steel plates which were secured to each slab for added mass.

After construction, structures were lifted from their bases using an overhead crane, transported to the testing apparatus, and instrumented with displacement and acceleration measuring devices. Further details of the construction, erection and instrumentation of the test specimens are given in Appendix A.

2.6 Simulated Earthquake Motions and Masses

The goal of the experiments was to excite the test specimens similarly to the shaking of actual structures in real earthquakes. To achieve this goal the chosen base motion had to be such that the natural periods of the reduced-scale structures were in the same range of the response spectra as the period of an actual structure would be for a spectrum based on an actual ground motion. It was also necessary that base motions be capable of expending the ultimate strength of the specimens. Characteristics of the structures and the recorded ground motions were evaluated in light of these objectives.

2.6.1 Mass of Structure

Additional masses were placed so that inertial forces would be capable of expending the strength of the test specimens. Steel plates ("story masses") were added at each floor level to obtain the necessary inertial forces at accelerations which were within the operating range of the simulator. These weights were secured to the top and bottom of each floor slab in such a way that they did not add to the flexural stiffness of a floor slab (Section A.2).

The added weights comprised 57% of the total weight per story (2950 lbs) for RM1 and 59% of the total story weight (2850 lbs) for RM3. The added weights increased the vertical compressive stress in the walls, which was desirable since gravity stresses for reduced-scale structures tend to be lower than those encountered in typical full-scale structures. This is because gravity loads in a reduced-scale structure are less than those for a full-scale structure by the scale factor cubed, while the cross-sectional area differs by only the scale factor squared. Specimen RM1 had a nominal gravity stress at the midheight of the base story equal to 38 psi. The weight of the walls constituted 16% of the total weight of the structure, which was a lower percentage than for a typical building.

2.6.2 Input Motions

The selection of input motion was rather arbitrary because the intent of the study was to examine response for any base motion which could be measured. The input motion used for the earthquake simulations was based on the California Institute of Technology record of the north-south accelerations measured at El Centro in 1940 (maximum acceleration of 0.35g) [11]. The El Centro record was chosen since the characteristics of its response spectra appeared to be suitable for studying the change in response with changes in specimen stiffness. The El Centro record was also desirable because of its stationary character, sequence of amplitudes, and the universal nature of its use. The acceleration record was integrated twice to obtain a record of ground displacements. Since structural configuration was selected as the primary experimental variable, only one ground motion was used.

a) Time Scale

Since the natural frequencies of the test specimens were greater than the fundamental frequency of a typical low-rise building, the unmodified El Centro record would have excited them in a manner dissimilar to the way in which a real building would be excited during an actual seismic event. Consequently, the time step between recorded data points was shortened in order to shift the response spectra towards the high end of the frequency

range (Fig. 2.7). Laws of dynamic similitude are sometimes used as guidelines in selecting this time-scale factor, however these laws are appropriate only for systems confined to the linear range of response. It was only important that the expected frequency range of the test structures lie within a similar range of the response spectra as would those of an actual structure with the spectra based on the real time scale (Fig. 2.7). The time duration of the input motion was thus compressed by a factor of 2.5, which was approximately the ratio of the natural periods of a hypothetical full-scale three-story reinforced masonry shear wall structure and that for the reduced-scale specimens.

b) Amplitude

The experimental plan was to scale the amplitude of the base motion for successive test runs of a given structure so that response of a progressively softening structure could be studied. A progression of increasing base motion intensities was established to result in response: a) prior to cracking, b) after cracking and before yield of reinforcement, c) at yield of reinforcement, and d) at the ultimate limit state (Table 2.1).

In order to achieve damage level d), it was necessary to use a different input record for the last run of each test specimen. The same El Centro motion was used except that a high-pass digital filter was employed to remove the extreme low frequency components (less than 0.8 Hz in real time) from the record.

The cracking point and the point of first yield were used to define the limits of ranges "a" through "d" listed above. For structure RM1, the cracking and yield moments were calculated from preliminary material properties, average dimensions and the assumption that the entire structure would act as a single cantilever. A modulus of rupture of 30 psi was used in the calculation of the cracking moment. At a section through the base of the first-story windows the cracking moment was calculated to be 265 k-in, and the moment to cause yield of the vertical reinforcement in the flanges was estimated to be 590 k-in.

Conventional modal analysis (considering only the first mode) was used to determine the spectral accelerations necessary to achieve the estimated cracking and yield breakpoints (Table 2.1). The initial period of RM1 was estimated from a free vibration test to be

approximately 17 Hz. The cracked period was estimated to be 10 Hz based on the ratio of cracked-section properties to gross-section properties of the members.

Before placing any specimens on the earthquake simulator, the simulator was "calibrated" with a concrete block of the same weight as the test specimen to determine the settings of the controller required to produce different amplitudes of base acceleration. A family of linear acceleration response spectra for different base motion intensities was obtained from this calibration. These spectra were entered at the estimated natural periods to determine which spectral curve (i.e. base motion intensity or controller "SPAN") would produce the target spectral acceleration for RM1.

Cracking and yield strengths for structure RM3 were determined from conventional methods for assigning story shear to the individual piers. A base shear was "applied" to the structure and was distributed to each base-story pier in accordance with its relative rigidity. The base shears corresponding to flexural cracking and to yielding of the vertical reinforcement of the piers were determined. These base shears were related to spectral acceleration through modal analysis. Target spectral accelerations for RM3 are shown in Table 2.1.

It was observed from the earthquake simulations of structure RM1 that the relationship between the simulator controller setting (SPAN) and the measured spectral acceleration (top-level acceleration divided by the modal participation factor) was essentially a straight line. Therefore, the SPAN setting to produce the RM3 target spectral accelerations was inferred from the observed SPAN-to-spectral acceleration ratio for the RM1 test runs.

2.7 Anticipated Response

As a rough guide, the response of structure RM1 to different intensities of the El Centro ground motion was estimated from a nonlinear dynamic analysis. The NERDS program [3], which treats the structure as a SDOF system with a constant deflected shape, was used for this purpose. RM1 was "subjected" to the first six seconds of the El Centro ground motion compressed by a factor of 2.5. The base shear strength of the structure (9.5k) was determined from the calculated yield moment (590 k-in) and an assumed inverted trian-

gular force distribution along the height of the structure. The lateral deflection at this strength was estimated from a linear analysis of the structure (using the ETABS program [26]) to be 0.12% of the structure height.

Response maxima calculated by the NERDS model for different amplitudes of base acceleration are presented in Table 2.2. Estimates of lateral drift (maximum top-level deflection divided by the structure height of 93 inches) range from 0.15% for a 0.4g earthquake to 0.43% for a 1.5g base motion.

2.8 Instrumentation and Data Reduction

Response of the test structures was monitored with a combination of acceleration and displacement transducers (and load cells for the static test). Locations of these instruments is presented in Figures C.4 through C.6. Accelerometers measured absolute accelerations in both the longitudinal and transverse directions. LVDT's measured lateral displacements relative to a reference column or recorded relative displacement between two locations on the structures.

Lateral displacements in the east direction were defined to be positive. Accelerations were negative for positive displacements so that inertial forces would be consistent in sense to displacements according to D'Alembert's principle.

Data acquisition and processing is described in Section C.3. Signal conditioners and amplifiers used to process analog output signals from the accelerometers were different from those used to process signals from the LVDT's. Therefore, when plotting displacements versus acceleration-related quantities (base shear, base moment), consideration was given to possible errors in synchronization between acceleration and displacement signals. Accelerometer output signals were delayed by a low-pass filter, while LVDT signals had no such delay. To correct for this, a "delay" of 3.6 msec was removed from the base moment or base shear records when these records were plotted against lateral displacements. This delay value was based on average time delays observed in the accelerometer filters [10]. Adjustment of the records was accomplished by linear interpolation between data points.

The time delay between sampling of channels on the A/D board was found to be insignificant (3.8 μsec interval between adjacent channels) [13] and was therefore disregarded.

CHAPTER 3

BASE MOTIONS

This chapter presents measured characteristics of the base motions used for earthquake simulations of structures RM1 and RM3. Histories of base acceleration and displacement are presented first, followed by Fourier amplitude spectra and linear response spectra of the measured base accelerations for each test run.

3.1 Overview

RM1 was subjected to four simulations of varying intensity of the north-south component of the 1940 El Centro ground motion. As discussed in Section 2.6.2.b, intensities were selected so that the structure would respond within certain ranges of behavior whose limits were defined by the cracking point and the point of first yield (initiation of yielding in flange reinforcement at the base) of the structure (Table 3.1). Spectral accelerations required to produce cracking and yield were estimated using modal analysis and the calculated estimates of cracking and yield strengths for the structures.

Base motion intensities for RM3 were selected with the objective that each earthquake simulation excite the structure into a range of behavior similar to that experienced by RM1 during the corresponding test run. As indicated in Table 3.2, the experimental program for RM3 included two more earthquake simulations than were performed for RM1. Run 4 of the RM3 test sequence was a low-intensity simulation with a peak base acceleration identical to that observed for Run 1 (0.28g). Since this run produced no damage or detectable changes in the structure, the measured response for this run is not reported. Run 6 was added to the program since Run 5 excited the structure into the post-yield range, but did not exhaust its strength. For purposes of comparison, then, RM3 Runs 1 through 3 can be considered to correspond to RM1 test runs of the same number. Results of RM3 Run 6 should be compared to results of RM1 Run 4.

Displacement of the simulator platform was measured by an LVDT internal to the hydraulic actuator. Accelerations at the base of the structure were measured by an

accelerometer mounted on each side of the base girder. Measured peak base accelerations are given for both structures in Table 3.3.

3.2 Accelerations and Displacements

Histories of base acceleration for all runs for structure RM1 are presented in Fig. 3.1. The acceleration histories for Runs 1, 2 and 3 are quite similar to the acceleration record reported by the California Institute of Technology for the same ground motion. The history for Run 4 shows some slight differences due to the removal of the extreme low frequency components from the El Centro record. These differences are more pronounced in the base displacement history, as shown in Fig. 3.2.

Histories of base accelerations and displacements for RM3 (Figs. 3.3 and 3.4) were similar to those recorded during corresponding RM1 simulations. Maximum base accelerations (Table 3.3) were comparable for the two structures in Runs 1, 2 and 3. In the last test run the RM3 (Run 6) base motion contained a peak acceleration which was 26% greater than the peak in the RM1 (Run 4) motion. A comparison of the base acceleration waveforms for these two runs (Figs. 3.1 and 3.3) shows that with the exception of the largest peak, the acceleration amplitude for RM3 Run 6 was less than that of RM1 Run 4.

3.3 Fourier Amplitude Spectra

Fourier Amplitude Spectra of the base accelerations for RM1 are given in Fig. 3.5. The spectra have been normalized to unity so that the frequency content is presented independent of the amplitude of acceleration. The spectra are nearly identical for frequencies below 8 Hz, except for the frequencies removed from Run 4. In Run 1 and 2 the spectra indicate a greater contribution (as compared to Runs 3 and 4) of frequencies above 8 Hz. In both of these cases the accentuated frequency components above 8 Hz are near the characteristic frequency (as determined from a Fourier spectrum of the top-level accelera-

tion) of the structure for that run, thus suggesting some interplay between the structure and the simulator.

Fourier amplitude spectra of the RM3 base accelerations, shown in Fig. 3.6, demonstrate reasonable correlation with the spectra for corresponding RM1 runs. Magnification of certain frequency components as a result of structure-simulator interaction was noted only in RM3 Run 1, again near the characteristic frequency of the structure during that run.

3.4 Linear Response Spectra

Figure 3.7 presents linear acceleration and displacement response spectra at typical percentages of damping for the recorded base motions of RM1 Runs 1 through 4. Normalized response spectra for all runs at 5% damping are shown in Fig. 3.8. The spectra were normalized by scaling the base acceleration records to a peak acceleration of 1.0g. The differences in frequency content above 8 Hz noted in the previous section are also evident in Fig. 3.8, as the linear acceleration response is noticeably different in the 8-16 Hz range (Period range of 0.0625 - 0.125 seconds). The linear displacement response was relatively insensitive to these differences.

These differences are consistent with the structure-simulator interaction effects reported by others [8,30] for shaking table studies of heavy structures. Such effects are usually manifested as a distortion (attenuation of table response) of the dynamic response of the system in a frequency band centered near the natural frequency of the test structure. The distortion generally becomes less pronounced as the structural damping increases. Both of these characteristics are evident in the measured base accelerations of Runs 1 through 3.

Linear acceleration and displacement response spectra for the recorded base motions for RM3 are given in Fig. 3.9. Response spectra for all runs (at 5% damping) calculated from recorded base motions normalized to a peak base acceleration of 1.0g are given in Fig. 3.10. The normalized spectra show trends similar to those observed for RM1. Spectral

acceleration curves for Runs 2 and 3 bear a close resemblance, while response is generally lower for other runs due to the effects of structure-simulator interaction (Run 1) or high-pass filtering of the base motion record (Runs 5 and 6).

Spectral curves for the unmodified base acceleration records of corresponding RM1 and RM3 simulations are compared in Fig. 3.11. Correlation between the RM1 and RM3 curves is satisfactory, considering that the simulator controller settings were adjusted for RM3 test runs so that the base acceleration amplitudes of Runs 1, 2, 3, and 6 would be 70%, 88%, 89%, and 80%, respectively, of the amplitude of the corresponding RM1 test runs (Table 3.3).

A comparison of the overall intensity of each base motion can be made by examining the Housner response spectrum intensities given in Table 3.3. The Housner spectrum intensity is defined as the integral of the velocity response spectrum taken over the range of periods between 0.1 and 2.5 seconds [19]. To account for the time compression factor of 2.5, a period range of 0.04 to 1.0 seconds was used in the calculation of the spectrum-intensity values in Table 3.3. Intensities for only one damping ratio (5%) are reported since the ratio between spectrum intensities for corresponding RM1 and RM3 test runs was found to be insensitive to the damping ratio. Intensity of motion for RM3 simulations was consistently lower than in the corresponding RM1 simulations. For Runs 1, 2, and 3, the ratio of spectrum intensities is close to the ratio of base acceleration amplitudes given in Table 3.3.

CHAPTER 4

OBSERVED RESPONSE OF STRUCTURES RM1 AND RM3

Results of earthquake simulations and free vibration tests of structures RM1 and RM3 are presented in this chapter. Structure RM1, which had the symmetrical pattern of window openings, can be viewed as a control specimen, since tests of structures RM2 (discussed in a subsequent chapter) and RM3 were configured to facilitate comparison of observed response with that of RM1. As discussed in Chapter 2, RM3 was constructed to resemble structure RM1 in all aspects except for the pattern of wall openings, the width of the flanges, and the layout of horizontal reinforcement.

Attributes of the measured base motions were discussed in Chapter 3. Specimen response to these motions, including response histories and progression of structural damage, is described in Section 4.2. Effective frequencies and damping ratios are presented in Section 4.3. Specimen behavior is summarized in Section 4.4.

4.1 Conventions

4.1.1 Sign Conventions

Lateral motion of the test structures was monitored by LVDT's and accelerometers at the midheight of each floor slab. LVDT's measured displacements relative to a reference column and accelerometers recorded absolute accelerations. Positive directions of lateral accelerations, displacements and forces obtained from these measurements follow the conventions outlined in Section 2.8.

4.1.2 Nomenclature

All terms used in the description of specimen response are as defined in the text or follow common usage. At times, terms strictly proper only to linearly-behaving systems (such as "first mode" and "effective frequency") are generalized to apply to nonlinear behavior.

4.2 Specimen Response

4.2.1 Response Maxima

A summary of measured response maxima for each run of RM1 and RM3 is given in Table 4.1. Maxima of base acceleration, a_g, and top-level acceleration, a_3, were obtained from accelerometer measurements. Apparent spectral accelerations, Sa, were deduced from top-level acceleration maxima by assuming first-mode response with a participation factor of 1.3. This participation factor corresponds to a deflected shape which increases linearly from the bottom of the structure to the top and the deflection at the top normalized to a value of 1.0. Amplification of base acceleration is presented as the ratio of the apparent spectral acceleration to the peak base acceleration. Peak deflections measured at the top of the structures were divided by the total structure height (93 inches) to give the percentage of lateral drift. Base shear (V_b) maxima were obtained by summing the measured acceleration at each level multiplied by the tributary story weight. Base shears have been normalized by the total weight above the foundation (8940 lbs for RM1; 8750 lbs for RM3). Maximum base moments, M_b, were determined by summing the product of inertial force at each level and the height of the level above the foundation. Base moments were normalized by the calculated estimate of the moment corresponding to first yield, M_y, which was discussed in Chapter 2 (590 k-in for RM1; 425 k-in for RM3).

4.2.2 Observed Response

Histories of measured displacements and accelerations are presented for each test run for structure RM1 in Fig. 4.1. Base shear and base moment histories are also presented. Scales of the vertical axes of corresponding plots are the same for all runs except Run 4 where the amplitude of motion was significantly larger than in the previous three test runs.

Figure 4.2 shows response histories for each test run of structure RM3. Vertical axes are the same for all runs except for Run 6.

a) Lateral Displacements

Histories of top-level displacement (Figs. 4.1 and 4.2) indicate a somewhat typical response to the El Centro ground motion. The most prominent sequence of large-amplitude response occurred in the first 2 1/2 to 3 seconds of shaking. Other series of large-amplitude cycles appeared near the 4 to 5 second and 10 to 11 second marks of the event. A comparison of waveforms for successive test runs of a structure indicates a pronounced decrease in the frequency of the structure with an increase in the magnitude of lateral drift. This is more clearly shown in Figs. 4.3 and 4.4 where displacement waveforms for the first and last test runs of each structure are compared (at different scales).

Figs. 4.3 and 4.4 also show the relationship between displacements at the second and third levels. The close similarity in the shape of the waveforms indicates that the structures displaced primarily in the first mode of vibration throughout all test runs. This observation is corroborated by deflected shapes viewed at instants of maximum displacement, as discussed in section 4.2.2.e. Since the deflected shape was essentially invariant for all amplitudes of motion, the lateral deflection waveform at any level contains all the necessary information about sequencing and frequency content of the displacement of the structure. Thus, top-level deflections will subsequently be used to describe the displacement characteristics of the structures.

A comparison of base moment and top-level deflection histories (plotted in Figs. 4.3 and 4.4 at different scales to facilitate comparison) indicates a close correlation in sequencing and frequency content. This suggests that lateral deflections were primarily the result of flexural deformations.

b) Lateral Accelerations

Inspection of the histories of lateral acceleration at the top level (Figs. 4.1 and 4.2) indicates a lack of high frequency components, especially in the early test runs. This observation is corroborated by plots of Fourier amplitude spectra of average top-level accelerations in Figs. 4.5 and 4.6. These spectra, which give an indication of the relative

energy content of the response at different frequencies, reveal that response of the structure was dominated by frequencies near the first-mode frequency. Only in the last test run for each structure did the acceleration waveform appear to suggest the presence of higher frequencies, however the Fourier spectra for these runs show that the acceleration response contained a relatively small amount of energy at frequencies above the fundamental frequency.

c) Comparison of Response Histories for RM1 and RM3

A comparison of Fig. 4.1a and 4.2a shows that while the base acceleration amplitude was lower throughout the first simulation of RM3 than it was for RM1, RM3 displayed a greater sensitivity to the ground motion than did RM1. This is demonstrated by the response during the 4-5 sec., 6-6.5 sec., and 10-11 sec. intervals of the simulation. While RM1 acceleration and displacement response subsided when a sequence of base acceleration pulses ended, RM3 cycled for a length of time approximately twice as long as the duration of the base acceleration pulse. This was most noticeable near the 10 sec. mark in the record where RM3 cycled for almost 1 1/2 seconds after response of RM1 had ceased. Amplitude of top-level displacement response was greater for RM3, while top-level acceleration amplitudes were nearly identical for the two structures during the first run.

In Run 2 (Fig. 4.1b and 4.2b), the tendency for RM3 to cycle longer than RM1 was observed only in one portion of the record (4-5 sec.). In the first five seconds of Run 2, top-level displacements of RM3 were approximately twice those of RM1; in the remainder of the test, displacements were of similar magnitude. Top-level accelerations were nearly the same for the first two seconds of this run. After the initial two seconds, RM3 accelerations were noticeably smaller than those of RM1. Top-level acceleration pulses observed between 5 and 9.5 seconds in the RM1 record were essentially absent from the RM3 record.

In Run 3 (Fig. 4.1c and 4.2c), the duration of the response cycles was similar for both structures. Peaks of large-amplitude, top-level displacement cycles were generally 2 1/2 times greater for RM3 than for RM1. RM3 displacement response was noticeably more demanding than RM1 response in the 1-3 sec. and 10-11 sec. intervals. The amplitude of

top-level acceleration response was greater for RM1 than for RM3 during most of Run 3. This was especially evident between the 4 and 5 sec. marks of the test, although the base acceleration amplitude was also noticeably larger for RM1 during this segment of the test.

A comparison of the response of the two structures in the final test run (RM1 Run 4 - Fig. 4.1d; RM3 Run 6 - Fig. 4.2e) reveals perceptible differences. The large base acceleration pulse at the beginning of the test (1.0 sec.) caused RM3 to undergo five cycles of large-amplitude displacement, while a similar pulse effected only moderate displacements in RM1. Large displacements of RM1 occurred only after the next large acceleration peak at 1.9 sec. in the record. Top-level accelerations of RM3 were in the range of one-third to one-half of the RM1 accelerations throughout the run. These differences appear to be consistent with the different strengths of the structures and levels of damage observed before the last test run. For instance, it was likely that the first large base-acceleration pulse in the last run was required to bring about yield in the base story of RM1. Base-story piers of RM3, on the other hand, were observed to have yielded before the last test run; thus the initial large pulse caused a series of large displacement cycles in that structure. Locations at which the two displacement waveforms cross the time axis ("zero crossings") suggest that RM1 cycled with a higher frequency than RM3 during the first five seconds, after which the zero crossings of the two structures occurred at the same locations.

d) Moment-Deflection Hysteresis

Overall hysteretic behavior of the structures is illustrated by plots of base moment (adjusted for accelerometer delays as described in Chapter 2) and top-level deflection in Figs. 4.7 and 4.8. Scales of the plots and the selected time intervals for the last run for each structure differ from those used for the other runs. Base moment was selected since flexural action appeared to dominate the response of the structure. Top-level deflection was used since deflections measured at the top were more reliable than those measured at the lower two levels. Also, since the deflected shape was essentially invariant throughout the testing, deflection at any level would convey the same information contained with the hysteresis plots.

Hysteresis plots for RM1 (Fig. 4.7) show the response of the structure to be essentially linear throughout Runs 1, 2 and much of Run 3. Some yielding is noted in Run 3. All plots indicate reductions in stiffness from the previous run. Severe stiffness reductions are observed in Run 4, and can be attributed to the combined effects of cracking, yielding of reinforcement and sliding along bed joints during that run. Significant dissipation of hysteretic energy is evident during at least three cycles of response in Run 4. Hysteretic response of the softened structure (after the first few seconds of Run 4) indicates a "pinching" phenomenon where the stiffness is temporarily reduced between the unloading and reloading stages and then is restored upon reloading. This effect is most likely the result of sliding along the bed joints which was observed during this run.

Hysteresis plots for RM3 (Fig. 4.8) indicate that except for differences in apparent stiffness, the primary and hysteretic response was quite similar to that of RM1 for the first three test runs. Response was essentially linear during Runs 1 and 2, and yielding was evident in Run 3. Yielding continued in Run 5 and inelastic response was observed in the first two seconds of that run. Large reductions in stiffness and strength occurred during the first two seconds of Run 6. Peak strength and displacement for this run were both achieved in the first large-amplitude response cycle. After this cycle, the structure's ability to resist lateral force and to dissipate energy was substantially reduced.

Selected cycles of hysteretic response for RM1 and RM3 are superimposed in Fig. 4.9 to illustrate changes in the properties of the systems. A typical cycle of response for different ranges of behavior is shown (a-cracking; b-pre-yield or yield; c and d-post-yield). The vertical segment of loop "c" for structure RM3 corresponds to a portion of the test during which top-level displacements exceeded the limits of the LVDT's. The average stiffness (slope of a line joining the displacement peaks) inferred from cycle "d" was approximately 1/20th of the initial stiffness for RM1 and 1/15th of the initial stiffness for RM3.

Inspection of the hysteresis loops for RM1 and RM3 reveals dissimilarities in the post-yield response of the two structures. Fig. 4.10, which shows base acceleration and top-level displacement histories for the last simulation of each structure, indicates that

while the two structures were subjected to similar base accelerations the displacement response for the first 4 1/2 seconds of the test was noticeably disparate. As discussed in the previous section, the difference in response appears to be the result of the manner in which each structure responded to the largest base acceleration pulse (at the 1.0 sec. mark of the test). At that time in Run 4, vertical reinforcement in the base story of RM1 had just begun to yield, thus the energy of the large pulse was spent in yielding this reinforcement and large amplitude displacement cycles did not occur until the next large acceleration pulse (at 1.9 sec. in the record). RM3, on the other hand, was observed to have gone through a few cycles of post-yield response in Run 5. As a result, when it encountered the acceleration pulse at 1.0 sec. in Run 6 (which was 26% larger in amplitude than the same pulse in RM1 Run 4), the structure immediately responded with a series of large-displacement cycles and rapid loss of strength.

e) Lateral Force Distributions

Inspection of the hysteresis plots in Figs. 4.7 and 4.8 reveals that while the hysteretic loops exhibit the general trends that might be expected from a reinforced masonry structure, some are irregularities noted in the shape of the loops during the last test run. In particular, at peaks of large-amplitude cycles in RM1 Run 4 and RM3 Run 6, sharp increases or decreases in base moment are observed for moderate or small changes in lateral deflection. This phenomenon might be explained by variations in the distribution of lateral inertial forces along the height of the structure at successive instants in time. Force distributions at successive instants near the two peaks of one large-amplitude cycle in each test run for structure RM1 are shown in Fig. 4.11 and indicate that even though the distribution remained basically linear throughout the first two test runs, significant variations in the lateral force profile occurred in the later runs. The same trends were observed for structure RM3.

The effect of the irregular force distribution on the hysteretic response of the structures can be seen in Figs. 4.12 and 4.13, where a sample sequence for one large-amplitude cycle of the last test run (RM1 Run 4 and RM3 Run 6) for each structure is shown. The sequence

of force profiles shown in these figures indicates a "whiplash" type of effect which was characteristic of most large-amplitude cycles in the last two test runs of both structures. In the first part of the loading slope, lateral forces are concentrated in the lower stories. The resultant of the lateral forces moves upward as the loading slope is traversed until the peak base moment is passed, at which point the plurality of force is shifted rapidly to the third story. The unloading slope is characterized by a linear (inverted triangle) distribution.

Irregularities in the hysteresis curve at peak response can be discussed using Fig. 4.14, which focuses on four points near peak response of the same response cycle for RM1 which was shown in Fig. 4.12. In a given half-cycle, rapid decreases (points 13-14) and increases (points 14-15) in base moment between points of maximum response were observed, resulting in an incurvation between base moment maxima. This behavior is contrasted with an ideal linear elastic-perfectly plastic behavior which is closely approximated by the dashed lines connecting base moment maxima. The "non-ideal" observed behavior can be understood with the help of the profiles shown in Fig. 4.14. While the deflected shape remains somewhat constant from point 12 to point 15 (the deflected shape at point 15 is misleadingly pinched at the second level since the displacements at that level exceeded the limits of the LVDT), the force profile undergoes the aforementioned whiplash. Top-level deflection increases from point 13 to point 15 while top-level force remains essentially constant. While the top-level force is not changing, however, the whiplash effect causes sharp reductions in the forces at the lower two levels (as noted in the force profile for point 14), resulting in a lower base moment. As the force profile is restored to the linear shape seen for point 15, the base moment increases accordingly.

Changes in the shear and moment profiles with the variations in the force distributions are also shown in Fig. 4.14. In addition, the resultant of lateral forces is superimposed on the force profiles and is seen to vary in height above the base. At times the location of this resultant can be quite different from that prescribed by the 1988 UBC for the design of this structure (0.76 x height of the structure as shown by the dashed line). This is more clearly shown in Fig. 4.15, where the height of the resultant (or the moment-to-shear ratio at the base divided by the structure height) is plotted at instants during the last test runs when the

base shear was larger than 2.0 kips. It is interesting to note, however, that the height of the observed resultant vacillated about the UBC height and was quite close to the UBC resultant at instants of maximum base moment response (points 13 and 15 in Fig. 4.14).

f) Transverse Accelerations

Transverse accelerations were recorded at the top of the structure (Figs. C.4 and C.6). A comparison of waveforms and Fourier amplitude spectra for top-level transverse accelerations and lateral accelerations measured at the west end of the structure is presented for the third and last test runs for RM1 and RM3 in Figs. 4.16 and 4.17. The amplitude of transverse acceleration was always significantly less than that of lateral acceleration except at 1.0 sec. of RM3 Run 6, when the transverse acceleration reached 48% of the lateral acceleration. Fourier spectra show that the transverse accelerations contained higher frequency components than did the lateral accelerations. The spectra also suggest that torsional response of the structure was small when compared to lateral response.

4.2.3 Observed Damage

Each test structure was visually inspected (as described in section C.3.2) before the first earthquake simulation and following each simulation. Cracking patterns are documented in Appendix D. Final crack patterns for one side of each structure are shown in Figs. 4.18, 4.19 (RM1) and 4.20, 4.21 (RM3).

For structure RM1, some hairline cracking was observed in the mortar joints before the first simulation. These cracks were most likely the result of shrinkage, although some may have occurred during movement of the specimen from the construction area to the simulator platform. No additional cracks were noted after the first test run. After Run 2, horizontal (flexural) cracking was observed at the top of the base-story piers. It was suspected that segregation of grout at a cold joint (interface between successive grout pours) caused flexural cracking to initiate at the top rather than the bottom of the piers. After Run 3, this crack had propagated around most of the first story and flexural cracks had appeared at the bottom of these piers.

The crack pattern of the south base-story wall after RM1 Run 4 (Figs. 4.18 and 4.19) reveals significant diagonal tension cracking, especially in the exterior piers. The orientation of the diagonal cracks corresponded to a situation when shear was combined with axial compression on the pier. It is believed that flexural cracking along a joint at the top of the base-story piers permitted sliding along this joint. As a consequence, the center pier was incapable of resisting much of the story shear and nearly all of the shear was resisted by the one exterior pier which was in axial compression.

In structure RM3, only a few hairline cracks were present before the first simulation. Although the structure was expected to remain in the precracked range in Run 1, slight flexural cracking was observed at the top and bottom of the north side center pier during this run. Most of the additional cracking in Run 2 occurred in the flanged west piers. Flexural cracks appeared at the top and bottom of these piers and in the flanges. In addition, slight diagonal cracking was seen in the north side west pier, suggesting that this pier was attracting a large part of the story shear. These cracks extended in both diagonal directions during Run 3, indicating that the west pier was resisting a significant share of the story shear for both directions of lateral loading. Also in Run 3, flexural hinges were detected at the top and bottom of the two short piers. Flexural cracking was observed in the slender exterior pier both at the bottom of the pier and at the third horizontal joint below the top of the pier. Segregation of grout at this level was again proposed as the reason why cracking occurred at this joint and not at the top of the pier. Run 5 produced no further cracking in the structure. Hinging of the two short piers was prevalent during this run. In the final test run, further hinging of the piers resulted in crushing of the masonry in localized areas at the top and bottom of these piers. The flexural hinges and crushed masonry are clearly seen in the west base-story pier (south wall) shown in Fig. 4.21. The final crack pattern of the south base-story wall (Figs. 4.20 and 4.21) shows that the slender exterior pier sustained diagonal cracking during the last simulation. It was expected that as the capacity of the two short piers was depleted, the tall pier was called upon to resist most of the story shear. Once the slender piers cracked in diagonal tension, the base shear capacity of the structure was exhausted.

Cracking was observed in the upper two stories of RM1 and RM3, however the damage in those stories consisted chiefly of flexural cracking of the piers and was relatively minor even after the last test run.

4.3 Characteristic Frequencies

Estimates of characteristic frequency and effective percentage of critical damping were obtained from free vibration tests before and after simulations, and from top-level acceleration response during the simulations.

4.3.1 Free Vibration Tests

Each earthquake simulation was preceded by a small-amplitude free vibration test (as described in section C.1.3) to evaluate the natural frequency and damping of the structure. Top-level acceleration response during free vibration is presented for RM1 in Fig. 4.22 and for RM3 in Fig. 4.23. First-mode natural frequencies were obtained from Fourier amplitude spectra of this response (shown in Figs. 4.22 and 4.23) and are reported in Table 4.2. The first-mode frequency of RM1 shifted from its initial value of 15.5 Hz to 4.0 Hz (74% reduction) after the last earthquake simulation. The 13.2 Hz initial frequency of RM3 decreased to 5.0 Hz after the last test run (62% reduction).

Top-level acceleration waveforms were filtered to exclude high frequencies, and a logarithmic decrement procedure was applied to the filtered waveforms (Figs. 4.22 and 4.23) to obtain effective damping factors. These factors are reported in Table 4.2 and range from 2% before the first simulation for both structures to 16% (RM1) or 13% (RM3) after the last simulation.

4.3.2 Effective Frequency

Since Fourier amplitude spectra of top-level accelerations measured during the earthquake simulations showed that response was generally confined to a narrow frequency band (Figs. 4.5 and 4.6), the frequency corresponding to the peak amplitude in the Fourier spectrum was chosen as an "effective" frequency for each test run. Effective frequencies are listed in Table 4.2 and were lower (by 10-20% for RM1, 7-42% for RM3) than the frequencies measured during the subsequent free-vibration test.

4.4 Summary of Observed Response

Measured response of structures RM1 and RM3 indicated that they displaced primarily in the first mode and that lateral deflections were the result of flexural deformations. Fourier amplitude spectra of top-level accelerations were dominated by frequencies near the frequency of each structure's first mode. Some differences in the response histories of the two structures were observed, most notably in the final test run when they exhibited a dissimilar response to a large base acceleration pulse.

Relationships between base moment and top-level deflection response characterized the primary and hysteretic response of the structures. Response of the softened structures was marked by a pinching behavior and incurvation at peak amplitudes. Both phenomena inhibit the capacity of the structure to dissipate energy. Lateral force profiles were seen to vary considerably for the softened structures and affect the shape of the hysteresis curve, although the force profile at peak response might be characterized by an inverted triangle.

Damage of the structures was concentrated in the first story. Flexural cracking along the bed joints at the top and bottom of the first story piers of RM1 led to a sliding mechanism in the final test run. This prevented some piers from resisting lateral shear while another pier was required to resist more shear than it was capable of withstanding. Diagonal tension cracking of the exterior piers of RM1 was the most likely limit state for RM1. Damage of RM3 was concentrated in the short, flanged exterior piers during the first few tests. Cracking along bed joints at the top and bottom of these piers was the predominant form

of damage. Flexural hinging at the top and bottom of the short piers was prevalent during the third and fifth runs and led to crushing of the masonry during the final test.

The final free-vibration frequency was 26% of that measured during the initial free-vibration test for RM1 and 38% of the initial free-vibration frequency for RM3. Effective damping factors were seen to increase with the decrease in frequency.

CHAPTER 5

DISCUSSION OF OBSERVED RESPONSE

Measured response of structures RM1 and RM3 during dynamic testing was presented and discussed in Chapter 4. Further aspects of response for these two structures are examined in this chapter, particularly for response in the inelastic range. The chapter focuses on characteristics which will be most useful in evaluating design methods and in suggesting simplified methods for design and response estimation.

5.1 Apparent Frequency and Stiffness

Histories of measured response (Figs. 4.1 and 4.2), indicated that at all levels of damage the vibration of the structure was dominated by a single frequency. This perception was supported by Fourier spectra of measured top-level accelerations (Figs. 4.5 and 4.6) which exhibited a narrow frequency band, even in the last test run when both structures sustained significant amounts of damage. These observations suggest that response of the structures throughout all levels of damage could be characterized by a single frequency.

Given this inference, apparent first-mode frequencies are plotted versus lateral drift for all test runs in Fig. 5.1 as an indication of the softening of the structures with increasing amplitudes of motion. The apparent frequencies are those measured during each earthquake simulation (from Fourier spectra of top-level accelerations) and during free vibration after each simulation. Free vibration frequencies were consistently higher than frequencies during an earthquake simulation due to the lower amplitude of vibration. The decreasing trend was, however, the same as for the frequencies obtained from the test runs. As indicated in Table 5.1, the final frequency of both structures was reduced to approximately one-fourth of the initial frequency. The reduction in frequency deduced from the apparent stiffness of the structures during the first and last test runs is also given in Table 5.1. The apparent stiffness was determined as the slope of a line joining the displacement peaks of hysteresis loops in Figs. 4.7 and 4.8. The good agreement between observed frequency reductions and those inferred from apparent stiffness implies that a

substitute linear stiffness should be suitable for estimating peak response of a nonlinear system.

To take this notion one step further, the relationship between top-level deflection and top-level acceleration response is shown in Fig. 5.2. For a single-degree-of-freedom (SDOF) linear system subjected to a sinusoidal excitation, the peak acceleration should be related to the peak displacement by the square of the circular frequency (diagonal line in Fig. 5.2). To see how well this simple representation matches the measured response of the test structures (whose response was not linear in the later runs and whose base excitation was not sinusoidal), top-level accelerations are plotted versus top-level displacements at four instants of time in each test run. The four instants correspond to prepeak, peak acceleration, peak displacement, and post-peak ranges of response. Top-level acceleration was divided by the square of the circular frequency obtained from Fourier spectra of the acceleration record. For a given test run the frequency measured during the previous run was used with the prepeak and peak acceleration values, while the frequency measured during the current run was used with peak displacement and post-peak values. Considering all the possible reasons for deviation, the correlation between the two response parameters and the idealized representation was good, even in the last runs. This reinforces the perception that response maxima could be estimated with an approximate linear model.

5.2 Lateral Displacement Response

In Chapter 4, it was noted that the close similarity between displacement histories at the first, second and third levels suggested that both structures displaced in the first mode of vibration throughout all test runs. When deflected shapes at each instant of time were shown in succession on a computer screen, it was evident that the deflected shape was essentially invariant in a linear (inverted triangle) configuration for all runs. One indicator of the deflected shape is the modal participation factor, c_n. For uniform lumped mass at each level, this factor is expressed by:

$$c_n = \frac{\sum \varphi_{in}}{\sum \varphi_{in}^2} \qquad (5.1)$$

where φ_{in} is the shape coordinate at level "i" for mode "n". For a three-story structure with φ normalized to 1.0 at the top, the first-mode participation factor is 1.29 for a triangular displaced shape. Average values are shown in Table 5.2 for the third and last test runs. The variation in the factor during the final test runs is shown in Fig. 5.3. While the factor was essentially invariant during Run 3, it was seen to drop slightly after the first few seconds of the last test run suggesting a greater concentration of damage in the first story. The averages given in Table 5.2, however, imply that an inverted triangle representation was still appropriate.

The observation that displacement response was governed by the fundamental mode, and that the structures deflected with a constant shape implies that the structures behaved as SDOF systems. Consequently, it would be appropriate to represent the displacement response of the structures with a single generalized coordinate for the nonlinear range of response.

This is further illustrated in Figs. 5.4a and 5.4b where the measured top-level displacement of both structures during the third and the last test runs is compared to that of an SDOF linear, damped oscillator. The response of the oscillator was determined using the Newmark Beta method for the recorded base acceleration, frequency, and equivalent viscous damping of the test run. In each case the specified frequency was that determined from the top-level acceleration record of the run. The damping ratio was inferred from the free vibration test after the run. In Fig. 5.4a and 5.4b, both the periodicity and magnitude of the measured displacement response were well reproduced by the oscillator after the first 2-3 seconds of each test. Prior to this time the experimentally observed displacements were always lower than those of the oscillator. This is understandable, since most of the damage in each test run was believed to have occurred in the 1-3 second range. Before this time, the structure was responding with a higher frequency than represented by the oscillator. This is shown more clearly in Fig. 5.4c which focuses on the top-level displace-

ment response of RM1 during the last test run. The top figure compares the measured response with an SDOF oscillator having the frequency and damping inferred from Run 3. The bottom figure makes the same comparison with parameters obtained from Run 4 (the same as in Fig. 5.4a). It can be seen that the oscillator with the "pretest" properties matches the measured response up to shortly after 0.75 second (length "a" in Fig. 5.4c). The other oscillator provides a good match after the two second mark (length "c"). It is interesting to note that this simple comparison brackets the portion of the test during which most of the damage to the structure was likely to have occurred. Since neither oscillator matched the measured response in length "b", it is probable that the changes in dynamic properties during this time are reflective of the damage incurred.

5.3 Lateral Acceleration Distribution Across a Story

When formulating an analytical model of a structure it is common to assume that all mass tributary to a floor level can be "lumped" at that level. In doing this, it is implicitly assumed that all elements whose masses are lumped together have the same acceleration at any given instant. To examine this perception, accelerometers were placed at several locations across a particular story. Accelerations at these locations at the same instant in time were compared to see if there were any variations due to in-plane deformations of the piers or out-of-plane excitations of the flanges. Acceleration distributions are plotted for each of the three stories in Fig. 5.5 for the last two runs of structure RM1. The instant of time represented for each distribution was the time of maximum acceleration at the particular story level. The distribution shown in Fig. 5.5 indicates that accelerations were nearly constant across any particular story and thus the use of a lumped mass model is appropriate.

5.4 Dynamic Amplification

Dynamic amplification of base acceleration has been plotted versus lateral drift maxima for each test run in Fig. 5.6 to examine the effect that softening of the structure had on the amplification of ground motion. Amplification was taken to be the apparent spectral acceleration divided by the maximum base acceleration. For structure RM1, amplification in the first test run was 1.26. It reached a peak value of 1.63 in the second run and dropped to 0.92 in the final test run. The amplification for RM3 was 1.54 in the first run, peaked at 1.60 in the third run and was 0.50 in the last run. Both structures exhibited a similar trend, with amplification initially increasing and then dropping off for the last two tests.

While it is inappropriate to make generalizations about this trend on the basis of two structures and one ground motion, the observed decrease in amplification with damage at least suggests that design should be focused on response past the proportional limit. This is because both structures were more tolerant of the shaking after cracking and yielding had occurred. It was apparent for both structures during the last test runs (RM1 Run 4, RM3 Run 6) that they were able to resist strong shaking through inelastic effects. Because of rapid losses of strength and stiffness, each structure attracted much less load after reaching its peak response in an early cycle. Although the ultimate limit state had been reached through brittle failure in shear, or crushing of masonry in compression, each structure remained intact during the remainder of the base motion.

5.5 Distribution of Story Shear

Traditionally, reinforced masonry perforated shear wall structures have been designed by treating each pier (masonry elements between openings) as an individual element [5,12,14]. The base-story piers are usually considered to be restrained at both ends and act in double-bending. The design base shear is apportioned to the piers in accordance with their relative stiffness. Typically, both flexural and shear deformations are considered in the determination of relative stiffness while the effect of axial loads is neglected. Often

the gross (uncracked) section properties are used in the stiffness calculations. Distribution factors determined for structures RM1 and RM3 using this type of approach (the "pier model") are given in Fig. 5.7. A perusal of these factors reveals that the consideration of cracking and direction of loading can have an impact on the design shear force for a given pier.

An effort was made to evaluate the distribution of story shear using pier distortions measured by LVDT's (Figs. C.4 and C.6) during the tests. The method was based on shear strains inferred from measured diagonal and axial deformations of the piers. The relative amount of shear resisted by a pier at any point in time was determined as:

$$V = G_m \gamma A_v \qquad (5.2)$$

where: G_m = shear modulus
γ = "measured" shear strain
A_v = shear area of pier

The shear strain was determined as:

$$\gamma = \frac{(\delta_{d1} - \delta_{v1} \sin\theta + \delta_{d2} - \delta_{v2} \sin\theta)}{2h \cos\theta} \qquad (5.3)$$

where: δ_{d1} and δ_{d2} are the measured deformations along the two diagonals
δ_{v1} and δ_{v2} are the measured deformations along the two verticals
θ = angle formed by the diagonals and the horizontal
h = pier height

A "distribution factor" was calculated for each pier by dividing this shear by the sum of the calculated shears for all piers at the base story. Sample plots of the shear distribution determined by this method are presented in Fig. 5.8 . One plot is shown for each structure during the test run immediately preceding the yield stage. Distribution factors are plotted for one direction of loading at instants when the base shear (determined from measured accelerations) exceeded 2.0 kips. Fig. 5.8a (RM1 Run 3) presents the loading situation

where pier 1 was in axial compression and pier 3 was in axial tension (due to overturning moments). The plotted points suggest that, on the average, piers 1, 2, and 3 resisted approximately 7%, 28%, and 62% respectively, of the story shear. These values are compared with the "pier model" estimates in the table above the plot. It is evident that the "experimental" values do not agree with the estimates based on either cracked stiffness or uncracked stiffness.

In Fig. 5.8b (RM3 Run 2) distribution factors are plotted for loading which caused axial tension in the pier 1 and axial compression in the slender pier 3. Average factors inferred from the plot are again compared with the pier model estimates in the table above the plot. The experimental values are radically different from the pier model values. Also, the factors imply that the presence of an axial compressive force on a pier significantly increases the amount of shear that the pier attracts and resists, an implication which contradicts the findings of Fig. 5.8a.

It appears that all that can be said of the results of these shear distribution estimates is that they are inconclusive. The method used assumes that all piers have the same constant shear modulus. However, it is possible that cracking in the piers had a significant influence on the shear modulus of each pier, thus rendering the above assumption false and the estimation method invalid.

While a "quantitative" evaluation of the shear distribution may not be possible, a more qualitative look at the measured pier distortions and damage patterns might provide some insight into the shear behavior of the piers. Pier deformations (as measured by LVDT's shown in Fig. C.4) and observed crack patterns (Appendix D) of structure RM1 will be examined below with this intent. The shear behavior of the piers of RM3 (Fig. 5.10) was qualitatively similar to that of RM1 (Fig. 5.9), and therefore will not be discussed.

Insight can be gained by examining the relationship between the base shear and the diagonal distortion of the two exterior piers, as shown in Fig. 5.9. Positive base shear in each figure corresponds to lateral forces applied towards the right, a situation in which overturning moments would produce axial tension forces in pier 1. Fig. 5.9a (Run 3), which is indicative of the distortion of the exterior piers during all pre-yield runs, indicates that

the stiffness of each pier varied according to the orientation of the applied force. For example, instrument #9 recorded large extensions for positive lateral loading since in this case deformations due to axial tension and shear combined. The same was true of instrument #18 on the opposite pier when the loads were reversed. Also, instrument #10 (for positive loading) and instrument #17 (for negative loading) remained in extension despite the fact that shear forces should have resulted in diagonal contraction. These extensions were a result of axial (tension) deformations which exceeded shear distortions. When loads were reversed, small distortions were measured since extensions resulting from shear distortions were offset by contractions as a result of axial compressions. These observations do not contradict the pier model, however it is evident that the effect of axial force on the pier stiffness should be considered in such a model.

In the post-yield case (Run 4 , Fig. 5.9b) the effect of axial forces on the pier deformations was again evident. When the exterior piers were in axial tension (positive loading for instrument #9 and negative loading for instrument #18), elongation of the vertical reinforcement contributed significantly to the diagonal deformations. When the loads were reversed, however, little contraction was recorded. When the exterior piers were subjected to axial compression (negative loading for instrument #10 and positive loading for instrument #17), inelastic elongations were observed, probably due to diagonal tension cracking which was observed in the exterior piers during this run. Final crack patterns (Fig. 4.18) confirm this intuition since the orientation of the diagonal cracks in the exterior piers was as would be expected when shear was acting with axial compression. An explanation for these observations could be that in the post-yield range axial tension in the exterior piers caused bed joint cracks to open, thus reducing shear stiffness. Axial compression, on the other hand, closed these cracks and enhanced both the shear attracting and resisting capacity of the piers.

Thus the pier model appears to be incapable of accurately predicting the apportionment of story shear between the piers during post-yield response. The center pier of RM1, which was predicted by the model to resist the largest percentage of story shear (Fig. 5.7), was actually quite ineffective in this capacity after flexural cracking (as noted in Section 4.2.3).

At any instant the majority of the shear appeared to have been attracted to the pier resisting axial compression.

5.6 Summary

Selected aspects of response for the two dynamically tested specimens were examined in this chapter. Inspection of measured response and Fourier amplitude spectra of top-level accelerations revealed that response of both structures could be characterized by a single frequency, even in the nonlinear range where "modal frequency" is a meaningless concept. This observation, coupled with perceptions drawn from trends in apparent frequency with increasing damage and from a comparison of peak response parameters, suggested that response maxima could be estimated with an approximate linear model.

Lateral displacements were noted to be governed by the fundamental mode shape, thus implying that the response history could be expressed with an SDOF idealization. This perception was confirmed by a comparison of the measured displacement response with that of an SDOF linear, damped oscillator. Lateral accelerations were seen to be constant across each story of a structure. This confirmed the appropriateness of lumped mass models.

Both structures exhibited hysteretic damping sufficient to limit the amplification of base accelerations during strong shaking. This suggested that design could be focused on response past the proportional limit.

Deformations recorded by LVDT's mounted on the piers of the structures were found to be incapable of providing a reliable estimate of the distribution of shear to individual piers. Resistance of shear by the piers was seen to be strongly influenced by reversals of axial force.

CHAPTER 6

STRENGTH AND DRIFT ESTIMATES

In this chapter, measured response during the dynamic tests is compared with the calculated estimates of selected parameters. The chapter attempts to evaluate the observed behavior of the reduced-scale structures in light of accepted principles of mechanics and experience from structural engineering practice for reinforced masonry or reinforced concrete structures. The focus is on those issues which would be important to a designer of reinforced masonry perforated shear wall structures.

In section 6.1, measured base shear maxima are compared with calculated estimates of the lateral load capacity of the structures. Section 6.2 examines the correlation between lateral displacements predicted by the analytical models and experimental values.

6.1 Base Shear Capacity

Of interest to a structural designer is the lateral load capacity of a structure, usually defined in terms of the base shear strength, V_b. The specimens tested in this study are part of a class of perforated shear wall structures in which the piers between the openings are relatively weaker than the horizontal spandrel elements. For this class of structure, it is generally accepted that the lateral strength corresponds to a mechanism in which plastic hinges form at the top and bottom of each base-story pier (Fig. 6.1). In the test structures, the oversized thickness of the floor slabs enhanced the strength of the horizontal elements, thus increasing the probability that this type of "story mechanism" would form. Examination of 8mm film footage of the specimens taken during the final earthquake simulations indicated that hinging at the ends of the base-story piers was prevalent for both structures.

The expression for lateral strength of the base-story mechanism can be obtained by considering equilibrium of the piers or from the principle of virtual work:

$$V_b = \sum V_i = \sum 2\frac{M_i}{h_i} \qquad (6.1)$$

The expression can be applied for either direction of loading and is independent of the distribution of lateral forces on the structure. Given the known pier heights (h_i), the task of calculating the base shear strength becomes one of determining the flexural capacity of the individual piers. These capacities were determined from ultimate strength procedures using the following assumptions:

1) Material properties as measured from component tests:
   Steel reinforcement: f_y = 47ksi ; f_u = 61 ksi
   Masonry: f'_m = 1220 psi ; e_{mu} = .0022 .
2) Linear distribution of strain across the section depth.
3) Rectangular stress block with a masonry stress of 0.85f'_m and a depth of 85% of the distance from the compression edge to the neutral axis.
4) Average effective depth and cross-sectional dimensions of piers (Figs 2.3 and 2.4).

Flexural capacities of the piers are sometimes calculated without considering the effects of axial loads induced by overturning of the structure. For a symmetrical structure such as RM1, the increase in flexural strength of the exterior pier subjected to axial compression from overturning might be expected to be offset by the decrease in strength of the opposite pier in axial tension. Flexural capacities of the piers of both structures are shown in column 1 of Table 6.1 for the assumption of no axial load. The base shear strength (eqn 6.1) corresponding to this situation is given in col. 1 of Table 6.2. The different strengths for the two directions of loading for RM3 reflect the effect of the different pier heights and the fact that the flexural capacity of the flanged sections varies with the direction of loading. The peak base shear measured during the earthquake simulations is listed in the last column of Table 6.2. The base shear was determined by summing the product of the measured acceleration at each floor level and the mass tributary to that level. As indicated, different peak base-shears were measured for different directions of loading. Because the assumed mechanism is not dependent on the lateral force profile, the calculated and measured dynamic base-shear strengths would be expected to be similar. A comparison of the measured and calculated strengths (cols. 1 and 4) indicates that the measured base shear

always exceeded the calculated strength by a significant margin. It is also interesting to note that the symmetrical structure (RM1) recorded different strengths for the different loading directions. This result cannot be explained by the above calculation procedure.

A more accurate estimate of the lateral load capacity of the test structures can be obtained by considering the effect of reversals of axial force on the flexural capacity of the piers. The assumptions and methods used for this are identical to those previously employed, except that an attempt is made to:

1) quantify the level of axial force (due to dead load and overturning moments) on each pier for a given direction of loading, and
2) account for the effect of axial force on the flexural capacity of the section.

Gravity loads, determined from measured weights of the specimen, were assigned to each pier based on its width and a tributary width equal to half the width of the adjacent opening(s). The overturning moment and consequent force on the exterior piers was calculated from the distribution of lateral force at the time of maximum base shear during the test. The center pier was assumed to resist no axial overturning forces. Net axial loads on each pier are listed in Table 6.1. Given these net forces, flexural capacities of each pier section were obtained from moment-axial force interaction diagrams developed from the material properties and ultimate strength assumptions mentioned above. Flexural capacities of each section are listed in Table 6.1 (col. 4) along with the shear force corresponding to this capacity (col. 5). The shear force for the piers in axial tension was taken to be zero. It was assumed that the tensile forces on these piers caused the observed bed-joint cracks to open and thus inhibited their ability to attract shear.

The shear capacity of each pier was calculated considering the contributions of both the masonry and the horizontal reinforcement. The masonry cracking strength was calculated as suggested by Blondet et al. in reference 9 :

$$v_{cr} = \sqrt{v_{cro}^2 + \frac{v_{cro} f_a}{1.5}} \qquad (6.2)$$

$$v_{cro} = [\,3.5 - 1.75\,M/Vd\,]\sqrt{f'_m} \quad \text{for } M/Vd < 1 \qquad (6.3)$$

where : v_{cro} = cracking strength at zero axial load
f_a = axial stress on the pier
M/V = calculated moment-to-shear ratio for the pier
d = depth of pier section

The shear capacity of each pier, determined from equation 6.4 below, is listed in Table 6.1 (col. 6) :

$$V_{tot} = v_{cr} b_w d + \frac{A_v f_y d}{s} \qquad (6.4)$$

where b_w is the pier width and A_v, f_y, and s are the cross-sectional area, yield stress and vertical spacing, respectively, of the horizontal reinforcement.

The shaded boxes in Table 6.1 denote the governing shear value for each pier. It can be seen that the flexural capacity was expected to dictate the limiting shear value for RM3 piers. For structure RM1 the calculated strengths indicate that diagonal tension (shear) is the anticipated limitation for the exterior pier in net axial compression. This is a contrast to the "zero axial load" case, where flexure was expected to govern the capacity of the exterior piers. Final damage patterns for structure RM1 indicated that diagonal tension was the likely limit state for most of the exterior piers.

Base shear capacities obtained by summing the governing shear value from Table 6.1 are shown in col. 2 of Table 6.2. The effect of including axial load in the determination of pier strengths is to raise, in most cases, the calculated lateral load capacity. This is most noticeable in the "load left" case for structure RM3 where the calculated capacity is nearly double that for the zero axial load case. It is evident, however, that the calculated base shear capacities still do not match those measured experimentally nor explain the unequal maxima for the two loading directions of the symmetrical structure.

As a final refinement in the calculation of base shear strength, the capacity of each pier was recalculated using "effective" pier heights shown in Fig. 6.2. These heights were obtained from final damage patterns for each structure (Figs. 4.18 and 4.20). This was based on the observation that flexural hinges did not always form at the level of the top or bottom

of the adjacent opening. The effective pier heights, defined by the observed hinge locations, were sometimes shorter than the design heights, sometimes longer and not necessarily the same for both walls. Base shear strengths, calculated using these revised pier heights and the shear and flexural capacity methods described above, are presented in col. 3 of Table 6.2. The calculated capacities are within 5% of the peak strengths measured during the dynamic tests for all cases except one direction of loading for RM3. For that case, if it is assumed that the exterior piers in axial tension can attract shear, the calculated capacity increases to 12.2k, which approaches the measured value. Considering the uncertainties associated with the assignment of axial load and hinge locations to the piers and the possible variations in material properties, a 5% discrepancy is not unreasonable. The use of the observed pier heights was also able to account for the observed difference in peak base shear for the two loading directions for RM1.

In Table 6.2, estimates of the base shear capacity of the statically-tested replica of RM1 (RM2, described in Chapter 8) are also presented. Capacities were calculated using the methods described above and observed pier heights. For both directions of loading, the calculated capacities were 36% greater than the peak base shear measured during the static test (from load cells). In light of this result, it may be the case that the method used to calculate base shear strength is somewhat artificial. For instance, the calculation method does not consider the sliding which was observed along the bed joints at the top of the center piers during the last dynamic test of RM1. If this sliding preceded the attainment of the peak base shear it is possible that the center pier's ability to attract shear was also inhibited. Were this situation to be considered, the calculated strength of RM1 would be closer to the strength measured for its statically-tested twin (RM2).

6.2 Lateral Displacement

Another issue of importance to a designer is that of the lateral deflection of the structure. Lateral distortion is often used as an indicator of the amount of damage expected in a structure. Since lateral deflections were observed to vary linearly from the base to the

top of the structure throughout testing, the overall drift ratio provides a convenient index of expected damage. Thus "lateral drift," as used in this chapter, refers to the top-level deflection expressed as a percentage of the structure height.

Three analytical models which might be used to estimate deflections in the linear range of response are examined first. While the peak nonlinear deflection is a more important displacement parameter, it may be the case that an estimate of deflection in the linear range is needed to assess a cracking limit state. Methods for evaluating the expected peak nonlinear deflection are also appraised. Equivalent linear methods are investigated since these methods can produce deflection estimates from relatively simple input parameters. A nonlinear model is also examined because this type of model can supply additional information about the entire history of lateral displacements.

6.2.1 Linear Analytical Models

It is of interest to examine the correlation between lateral drifts measured during the earthquake simulations and currently available analytical models. Although analytical models under development [15] are expected to be able to provide good estimates of lateral deflection of perforated shear walls, such models are not yet in use. Consequently, the following three models were chosen to provide drift estimates for comparison with the test data:

1) simple "pier model"
2) frame model
3) linear elastic finite element model.

The first two models were chosen because of their frequent use in preliminary design of perforated shear wall structures. The third model is admittedly less likely to be used in a design environment, but was available from another study [35].

In the pier model the flexibility of the system is defined by flexural and shear distortions of each pier in a story. The rotations at the top and bottom of each pier are restrained and the story stiffness is calculated as the sum of the stiffnesses of each pier in the story:

$$k_{tot} = \sum k_i = \sum \left(\frac{12 E_m I}{h^3} + \frac{GA}{1.2 h} \right) \qquad (6.5)$$

where E_m and G are Young's modulus and the shear modulus of the masonry and I,A and h are the moment of inertia, shear area and height of the pier, respectively.

The frame model was executed using the ETABS program [26] which considers the intersections between the spandrels and the piers to be rigid. The piers were modeled as columns with heights as indicated in Fig. 6.1. The "rigid zones" encompassed the masonry and portion of the floor slab directly above and below each pier. The portions of the spandrels above and below the openings were considered to be the beam elements.

The finite element model was executed using the FINITE program [25]. A rather coarse mesh (Fig. 6.3) was constructed of shell elements. The walls, flanges and slabs were modeled with the same four-noded rectangular shell element which had six degrees of freedom per node. This element combines both flexural and membrane actions.

Each model was used to calculate overall drift of both structures for each test run. Forces were applied in an inverted triangular distribution so that the base shear was equal to the peak base shear measured during the test run. Mechanical properties of the masonry were obtained as mean values from prism tests and are listed in Table 6.3. The shear modulus, G, was taken to be 40% of E_m. The stiffness of each element was "cracked" in accordance with crack patterns observed before each test run. For the pier and frame models this was done directly by using the cracked section properties for all runs after the first one. The finite elements were "cracked" by assigning them an equivalent modulus of elasticity based on the cracked moment of inertia [$E_{cr} = (I_{cr}/I_g)E_m$]. For each run E_{cr} was assigned to the elements observed to be cracked (from documented crack patterns) in the previous test run.

The "stiffness" of each model is reflected by the calculated initial frequency (based on gross-section properties) which is given in Table 6.4. The initial frequency estimated by the analytical models always exceeded the frequency of the structures measured in free vibration before the first test run. It was recognized, however, that the measured initial frequency was lower than the actual uncracked frequency due to cracking in the structures

which resulted from shrinkage and handling. Of the models considered, the finite element model provided the best representation of the initial frequency of both test structures.

Deflection estimates of the linear models are presented and correlated with experimental values in Table 6.4 and Fig. 6.4 (for RM1 only). The "piece-wise linear" appearance of the calculated estimates in Fig. 6.4 is due to the variation of member stiffnesses for the different test runs.

It is not reasonable to expect the three linear models to provide reliable estimates of lateral drift for post-yield response (Run 4 for RM1 and Run 6 for RM3). For these runs, measured drifts exceeded 2.5 times the FEM drifts and 10 times the drifts calculated with the pier model. For smaller amplitude test runs, however, the correlation was also poor. For example, the pier model predicted drifts during Run 1 which were less than 1/7 of those measured. The frame model also underestimated the measured drifts for the early test runs. The FEM model had the best correlation, but measured drifts still exceeded estimates by as much as 75% for the same low-amplitude test runs. Some of the measured drift for RM1 may have been attributable to sliding along the bed joints at the top of the base-story piers which was observed particularly for the later test runs. All the chosen linear models are, then, significantly over-stiff even at low amplitudes of displacement.

6.2.2 Peak Nonlinear Drift (Linear Models)

The linear models discussed in the previous section were not intended to reproduce the peak lateral drift of the test specimens during the final test runs. The peak inelastic drift expected of a structure during strong shaking is, however, of greater importance to a designer. Therefore, two relatively simple procedures for estimating or at least bounding the peak inelastic displacement are investigated.

a) Structure with Substitute Linear Stiffness

In Chapter 5 it was suggested that the nonlinear response of the test structures could be represented by a substitute linear system with appropriate stiffness and damping characteristics. The correlation between measured displacement waveforms and displace-

ments calculated by an SDOF linear, damped oscillator (Fig. 5.4) reinforced this perception. In Table 6.5, measured drift maxima for the third and last test runs are compared with peak drifts calculated by the SDOF model described in Section 5.2. The values of apparent frequency listed in the table are those obtained from lateral accelerations measured during each test run. Percentages of equivalent viscous damping were determined from free vibration tests performed after the run.

The percentages of lateral drift listed in Table 6.5 are the maximum drift values determined by the SDOF model multiplied by a modal participation factor of 1.29 (Section 5.2). In all cases the calculated maximum drift exceeds the value measured during the test. In Run 4 for RM1, the calculated estimate is 54% greater than the measured peak, while in RM3 Run 6 the calculated value exceeds the probable maximum value by approximately 30%. [The "probable maximum value" of 1.6% for RM3 (shown in parentheses in Table 6.5) was estimated from the measured displacements during Run 6. As explained earlier, the top-level drift in that run exceeded the reported maximum (1.3%) which was the limit of the top-level LVDT.]

The substitute linear system used in this comparison thus provided a conservative estimate of the nonlinear drift of the test structures. Although the estimates may appear to be too conservative, it should be noted that the characteristic frequency and damping factor used for each run was representative of the condition of the structures after most of the damage occurred in the run. This is evident from Fig. 5.4 where the displacement response of the SDOF oscillators closely matches the measured response after approximately the three-second mark of the test. Peak displacements always occurred before this time in the test. It is therefore plausible that an SDOF oscillator with a higher frequency and different value of damping than those shown in Table 6.5 could provide a better estimate of the peak drift. It would be inappropriate, however, based on the limited test data, to suggest a better combination of frequency and damping. The intent was simply to show that a substitute linear model gave a potentially useful bound to the peak nonlinear displacement.

For such a model to be a useful design tool, it must be possible to determine the substitute values of frequency and damping from the calculated initial properties of the system. Although specific guidelines cannot be formulated from the test data, characteristics of the observed response of the structures can provide some indications as to how this might be done. For instance, it was observed that nonlinear displacements were accompanied by a decrease in the frequency of the structures. This decrease in frequency (from the first to the last test run) was shown in Chapter 5 to be approximately the same as that inferred from the decrease in apparent stiffness of the structures. In addition, it was observed that nonlinear displacements led to an increase in the ability of the structures to dissipate energy, which was manifested by an increase in the apparent viscous damping.

Observations such as these led to the development of the "substitute structure" method for reinforced concrete systems [16]. In that method the peak nonlinear response of a system is approximated by a linear response analysis of a substitute system. The stiffness and damping of the substitute system are based on the calculated initial stiffness of the system and a selected index of the amount of nonlinear deflection to be permitted in the structure. On the basis of the above discussion it seems reasonable that a similar procedure would be appropriate for reinforced masonry systems.

b) Linear Spectral Analysis

It has been observed that the nonlinear displacement of reduced-scale reinforced concrete structures which have certain strength and stiffness characteristics can be satisfactorily estimated by a linear spectral analysis [34]. This observation is based on a study by Shimazaki and Sozen [31] which demonstrated that the maximum nonlinear displacement of SDOF oscillators with suitable combinations of strength and period was bounded by the displacement estimated from a linear response calculation. Specifically, the linear analysis provided a reasonable estimate of peak displacement provided the system satisfied:

$$TR + SR > 1.0 \qquad (6.6)$$

where:

$$SR = \text{Strength Ratio} = \frac{\textit{Base Shear Strength}}{\textit{Base Shear Calculated by Linear Spectral Analysis}}$$

$$TR = \text{Period Ratio} = \frac{\textit{Calculated Initial Period} \times \sqrt{2}}{\textit{Characteristic Period of Ground Motion}}$$

It should be noted that the study was based on results obtained from a nonlinear analytical model using hysteresis rules developed for reinforced concrete systems. The hysteretic behavior of reinforced masonry systems is similar enough to reinforced concrete systems that an investigation of the above procedure for the reinforced masonry specimens would appear to be warranted.

The determination of peak lateral drift using the above method is summarized for the final test runs in Table 6.6. The characteristic period of the structures, T_o, was suggested by Shimazaki to be the initial period calculated from gross-section properties multiplied by $\sqrt{2}$. This effectively reduces the uncracked stiffness by a factor of 2 to account for anticipated softening of the structure. As noted in the previous section, the initial uncracked period of the structure is an elusive value. Initial period estimates from three analytical models were quite different and all exceeded the initial period measured before testing. However, to preserve the intent of the method (that is, to base T_o on the calculated uncracked period) the initial periods estimated with the finite element model were used. These initial periods, listed in column 1 of Table 6.6, are approximately 20% lower than the measured initial periods, although it is clear that the measured initial values reflect some degree of cracking. The Shimazaki factor of $\sqrt{2}$ was used as a "starting point" for the softening index, although it is possible that a higher value is more appropriate for lightly reinforced masonry wall structures.

The characteristic period of the ground motion, T_g, is defined to be the period at which the energy response ceases to increase with increase in period (Fig. 6.5). For the 1940 El Centro motion the characteristic period is approximately 0.55 seconds. Therefore, the motions used in this study, which were compressed by a factor of 2.5, had a characteristic period of 0.22 seconds.

The base shear strength was taken as the smaller strength of the structure for the two directions of loading. The final result would not have changed if the larger strength had been used. The strengths were normalized by the total specimen weights of 8.94k (RM1) and 8.75k (RM3).

The final parameter required was the base shear as calculated from a linear analysis. According to the Shimazaki procedure, this was the base shear corresponding to the spectral acceleration of a linear oscillator with a period of T_o and a damping factor of 0.02. Consequently, spectral accelerations were estimated from the linear response spectra in Figs. 3.7 and 3.9. for the appropriate test runs. The corresponding first-mode base shear was then determined as:

$$V_b = c\, Sa \sum m_j \varphi_j \qquad (6.7)$$

where: S_a = spectral acceleration
c = first-mode participation factor described in Section 5.2
m_j = mass at floor level j
φ_j = shape coordinate at level j.

A linear deflected shape was assumed for the determination of c and φ_j. Shimazaki determined spectral displacements from an idealized response spectrum defined for two period ranges:

$$S_d = 2\, D_g\, (T/T_g)^2 \qquad \text{for } \frac{T_g}{3} < T < T_g \qquad (6.8a)$$

$$S_d = 2\, D_g\, (T/T_g) \qquad \text{for } T_g < T < 2\,T_g \qquad (6.8b)$$

where: S_d = idealized spectral displacement of an oscillator with period T and 2% damping.
T_g = earthquake characteristic period
D_g = spectral displacement of an oscillator with period T_g and 10% damping.

Deflection at the third level was determined by multiplying S_d by the modal participation factor.

The idealized displacement response spectrum for RM1 Runs 3 and 4 is shown in Fig. 6.6 along with the displacement spectra for the recorded base motions at 2% and 10% damping. The idealized spectrum provides a reasonable fit to the actual spectrum for 2% damping.

As seen in col. 9 of Table 6.6, the sums of the strength and period ratios for the final test runs (RM1 Run 4 and RM3 Run 6) fall below the limit used by Shimazaki and thus the linear analysis described above might be inappropriate. A more recent study by Bonacci [10], however, suggested that for systems in which SR + TR < 0.85, the linear analysis could still be used, but with a modification to the idealized displacement response spectrum. The modification consisted of replacing equation 6.8a with 6.8b. As shown in Fig. 6.6b for RM1 Run 4, this means that the straight-line portion of the idealized spectrum is extended to the origin. Since the combination of strength and period ratios for the last test runs was less than 0.85, then this method (eqn 6.8b) was tried. Results shown in Table 6.6 (rows 1 and 2) for the final runs indicate a good correlation between the drift estimated from the idealized linear spectrum and the experimental value.

Row 3 of Table 6.5 indicates that the drift estimated by the linear method matches the probable maximum drift for RM3 (1.6 %) if the softening index applied to the calculated initial period is changed from $\sqrt{2}$ to $\sqrt{3}$. The intent in showing this, however, is not to manipulate the test data to get an exact correlation with the linear method, but rather to gain insight into the determination of T_o. In particular, it was observed that the peak drift estimated by the linear analysis matched the maximum measured drift when the calculated uncracked period was lengthened by $\sqrt{2}$ for RM1 and $\sqrt{3}$ for RM3. The higher value for RM3 is consistent with the greater degree of softening (as compared to RM1) which was observed in the first two test runs of RM3. In addition, the values of T_o (Table 6.6, column 3) which resulted in the "exact" drift correlation fall between the free vibration periods measured before and after Run 2 for each structure. At this point in the testing the structures were thought to be "partially cracked," a state similar to that intended by

Shimazaki for the use of the method. It appears, therefore, that the linear analysis described in this section is appropriate for estimating the peak nonlinear deflection of a reinforced masonry structure, although further consideration should be given to the softening index applied to the uncracked period.

In rows 4 and 5 of Table 6.6 the Shimazaki method is also evaluated for the third run of each structure using the values of T_o which resulted in the best drift correlation for the last test runs. For these runs the combination of strength and period ratios for both structures exceeds the Shimazaki threshold of 1.0. Since T_o in both cases falls in the range of equation 6.8a, this equation was used to determine the drift values listed in col. 10 of Table 6.6. The estimated drifts bound the measured maxima and are within 30% of them. This correlation is considerably better than the one found with the analytical models discussed in Section 6.2.1.

6.2.3 Peak Nonlinear Drift (Nonlinear Models)

The linear model discussed in the previous section showed promise of providing useful estimates of the peak nonlinear displacement of each structure. An investigation of SDOF nonlinear models is also worthwhile, since these models can provide an idea of the number and sequence of large-displacement cycles in addition to an estimate of the deflection maxima.

The NERDS computer program [3] was used to calculate displacements of the two structures during the final test runs. The program computes the nonlinear dynamic response of an SDOF system to a record of ground accelerations given the following information:

1) relative mass at each floor level
2) story heights
3) assumed deflected shape
4) hysteresis formulation.

The constant average acceleration method [27] is used to integrate the equations of motion. The hysteresis rules are formulated from information provided by the user:

1) initial stiffness defined by the base shear and lateral drift corresponding to the formation of a collapse mechanism
2) slope of the unloading curve
3) force-reversal slope.

The program allows these parameters to be input for each direction of loading so that asymmetrical force-deflection characteristics of the structure can be accounted for. Viscous damping is assumed to be zero for large-amplitude excitations.

The program was supplied with the above parameters based on observed response during the last test run of RM1 and RM3. The "mechanism" strength was taken to be the peak base shear measured for each direction of loading (Table 6.2). The lateral drift corresponding to this strength was approximately 0.2% of the structure height for both structures. The unloading slope was assumed to be the same as the initial loading slope. The reversal slope was assigned a low value (2% of the loading slope for RM1; 15% of the loading slope for RM3) to account for sliding along bed joints which was observed during the final test runs.

Calculated displacements are compared with the experimental values in Fig. 6.7. The periodicity of the calculated response is remarkably similar to that of the measured response for both structures. The correspondence between the amplitudes of the peaks is also impressive, especially for RM1.

The results indicate that an SDOF nonlinear analysis was capable of providing a satisfactory description of the observed displacement response of the two structures. Although the input parameters were based on experimental observations, they could have been predicted before the test. Limit analysis was shown earlier to have given a good estimate of the base shear capacity. A mean drift of 0.2% at yield is considered typical for low-rise reinforced masonry structures. The force-reversal slope, while somewhat subjective, was similar to that used in other models [23] and seems justifiable based on the observed slip characteristics of masonry structures.

6.3 Summary

Base shear and lateral displacement response of the reduced-scale structures were investigated in this chapter. The aim was to study the correlation between response predicted by selected methods and models with that observed experimentally. Response prediction was not intended to be an end in itself, but rather a vehicle for understanding observed behavior and for evaluating current design procedures in subsequent chapters.

The lateral force capacity corresponding to a story-mechanism was estimated using the traditional pier model and by a method which accounted for reversals in axial force. The pier model provided unreliable estimates of the measured dynamic base shear strengths. A method in which pier capacities were calculated considering axial force, loading direction and observed pier heights was found to give reasonable estimates of the measured dynamic base shear strength for most cases. A discrepancy between calculated strength (8.0k) and observed strength (12.8k) for one direction of loading of RM3 remains largely unaccounted for. Base shear capacities calculated by the same method for the static test specimen were 36% greater than the peak base shears measured during the static test.

Three common linear models were found to be inadequate for estimating the measured lateral deflection of the test structures, even at small amplitudes of displacement. The use of a linear system with substitute stiffness and damping values appeared to be promising for the estimation of nonlinear deflection. A linear spectral analysis, developed from observed response of reinforced concrete systems, gave good predictions of the peak nonlinear displacement of the structures. Displacements calculated by an SDOF nonlinear model gave a good representation of the frequency and amplitude of displacements measured during the final test runs.

CHAPTER 7

COMMENTS ON DESIGN OF REINFORCED MASONRY STRUCTURES

In this chapter, the observed response of structures RM1 and RM3 is used in conjunction with the calculated estimates of response parameters from Chapter 6 to comment on design practice for reinforced masonry structures. Concerns related to the proportioning of reinforced masonry systems for adequate strength and stiffness are discussed.

7.1 Application of Strength and Drift Estimates

7.1.1 Pier Design

The discussion of the calculation of base shear strength in Section 6.1 can be coupled with the design considerations presented in Chapter 2 to provide suggestions for determining the lateral strength of reinforced masonry perforated shear wall structures. For this type of structure, strength considerations are centered around the provision of sufficient flexural and shear capacities for the pier elements.

a) Distribution of Story Shear to Piers

As briefly discussed in the previous chapter, the design of perforated wall structures has traditionally centered on the distribution of story shear to the individual piers in that story (the so-called "pier model"). Given a prescribed set of lateral forces, the primary challenge revolved around the assumptions and methods used to apportion the story shear to the piers. Once this was accomplished, pier moments were determined and vertical and horizontal reinforcement selected according to accepted practice.

Frequently the distribution of story shear is based on the relative gross-section stiffness of the piers without considering axial loads or the direction of loading [5,12,14]. This "method" was developed under design specifications [20] which expected all the masonry elements to remain in the linear range of response for all loading conditions. The discussion in section 5.5 suggested that for the structures tested in this study the distribution of

shear was strongly influenced by reversals of axial force. It could, then, be suggested that the pier model be revised to account for cracking, variations in axial force, and for the different stiffnesses of the flanged sections for opposite directions of loading.

An easier design approach may be the procedure used to estimate the base shear strengths of the model structures (Section 6.1). The advantage of this approach is that an explicit determination of pier stiffnesses is unnecessary. The procedure used in Section 6.1, restated as a design process, is as follows:

1) Select vertical reinforcement for the piers. Minimum percentages of reinforcement prescribed by design codes are often appropriate.
2) Estimate net axial load on piers and determine flexural capacity of pier sections for each direction of loading.
3) Determine shear forces associated with flexural capacities in 2).
4) Ensure that the sum of the shear forces of all piers in a story exceeds the story shear dictated by the prescribed lateral forces.
5) Select horizontal reinforcement for piers such that the provided shear capacity exceeds the shear forces determined in 3).

By making an initial selection of the vertical reinforcement in the piers, the pier moments are based on calculated flexural capacities rather than on an estimated percentage of story shear assigned to that pier. An explicit calculation of pier stiffness is thus avoided. The consideration of variations in axial load and loading direction insures that horizontal reinforcement is chosen for the shear corresponding to the maximum flexural strength of the pier.

To illustrate these points the estimated percentage of story shear resisted by each pier of the structures is shown in Fig. 7.1 for two methods. In column 1 of the table, the percentage was determined from relative pier stiffnesses calculated by the traditional pier model (based on gross sections and without considering axial load). In col. 2, percentages are based on the shear corresponding to flexural capacities listed in col. 5 of Table 6.1 (axial load and direction of loading considered). The shaded values in Fig. 7.1 indicate the maximum percentage of story shear which each method would "assign" to the individual

piers and which would be used in the selection of horizontal reinforcement. The difference between the two approaches is evident and indicates that the amount of required shear reinforcement (if any) would always be less when based on the pier model. A comparison of the percentages in Fig. 7.1 with experimental observations reveals that the percentages obtained by considering reversals of force (col. 2 in each table) are truer to the observed behavior of the structures (Section 5.5). The exterior piers were observed to be stiffest when in axial compression due to overturning and to have little stiffness when subjected to net axial tension.

b) Capacity Design

Part of the design process enumerated in section a) is the capacity design approach familiar to designers of reinforced concrete frames. In this approach sufficient shear strength is provided to exceed the shear corresponding to the maximum feasible flexural strength of a section. Horizontal reinforcement for the piers of RM3 was chosen according to this approach and the observed damage of RM3 suggested that flexural hinging, followed by crushing of the masonry, limited the capacity of that specimen. Horizontal reinforcement for RM1 was not assigned according to a capacity design. Horizontal reinforcement was placed to satisfy minimum code provisions and was considered adequate to prevent shear failure based on the "zero axial load" analysis. Strength estimates which considered reversals of axial load, however, suggested that the shear strength of the base-story exterior piers would limit the lateral load carrying capacity of the structure (Table 6.2, col. 6). Final damage patterns for RM1 indicated that severe diagonal tension cracking occurred in some of the exterior piers.

c) Plastic Hinge Locations

It may be recalled from Section 6.1 that estimates of base shear capacity from conventional calculations were in reasonable agreement with measured strengths only when "observed" pier heights were considered in the calculations. It was surmised that hinges formed at locations other than those anticipated because segregation of grout at certain

levels weakened those joints. It is likely, then, that the unexpected hinge locations can be attributed, at least in part, to the difficulty of controlling the construction of the reduced-scale specimens. As a result, it is inappropriate to comment on whether or not this phenomenon would be reproduced in a large-scale structure. Future tests of large-scale perforated wall specimens [24] will help to address this concern.

7.1.2 Lateral Drift Estimates

The procedure outlined above for supplying the structure with adequate strength does not guarantee that the resulting structure will have sufficient stiffness to limit the amount of damage to an acceptable level. Damage control requires reliable methods for estimating peak nonlinear drift so that the estimated drift can be compared to the chosen tolerable level of drift. Based on the evaluation of drift estimation methods in Chapter 6 it appears that, at present, substitute linear methods are the most promising for obtaining a bound to the peak nonlinear drift expected of a structure. Both the substitute structure method and the Shimazaki\Bonacci linear spectral analysis which have been proposed for reinforced concrete systems seem to be suitable for use with reinforced masonry systems (with some modification). The use of a simple SDOF nonlinear model to obtain information about the displacement history of a structure also appears to have merit.

As noted in the development of the linear spectral analysis [10], the best use of the above methods is not strictly as predictors of lateral drift, but as vehicles by which to evaluate competing structural schemes in the initial design phase. Substitute linear models and SDOF nonlinear models afford the simplicity of quickly estimating the maximum amount and number of cycles of nonlinear deformation of a structural system for a given ground motion or an expected range of motions.

It is therefore recommended that a substitute linear model, such as the ones discussed in Chapter 6, be used to check that a trial configuration possesses enough stiffness so that anticipated nonlinear displacements remain below a prescribed limit. This check may be most effective when it precedes the above strength considerations. In this way required

stiffness, based on well-chosen limits of lateral drift, can be used as the criterion for evaluating preliminary configurations.

7.2 Limitations of Methods Considered

Estimates of base shear capacity and lateral drift are useful only to the extent to which the parameters used in the calculation methods can be confidently predicted. Therefore, it is of value to briefly consider some of the difficulties and uncertainties involved in determining these parameters.

7.2.1 Lateral Strength

The calculation of base shear strength was based on accepted principles of mechanics and properties from component tests. While the axial load on the piers was determined from experimentally determined base moments, these loads could be calculated from an assumed lateral force profile and a design base shear. Also, it is assumed that the locations where plastic hinges will form in the piers of an actual structure can be predicted or controlled.

7.2.2 Lateral Drift

For the structures considered, estimates of peak nonlinear drift from the linear spectral analysis depend heavily on the relationship between the characteristic period of the structure and the characteristic period of the ground motion. While the characteristic period of the ground motion (as it is defined in Chapter 6) can be obtained with confidence, the estimate of the initial period of the these structures is still elusive. Typical models considered in Chapter 6 (pier model, frame model, finite element model) all gave initial frequency estimates which were significantly lower than those measured before testing. It is interesting to note that the pier model, which gave the frequency estimate that was furthest from the measured value, is the "shear beam" method which is allowed by the UBC [21] for the determination of initial period.

As noted in Chapter 6, reasonable estimates of strength and initial stiffness for the SDOF nonlinear model could be obtained without the test results. Base shear capacity could be based on limit analysis and drift at yield taken as a typical value for low-rise reinforced masonry structures. The most uncertain input parameter was the slope of the hysteresis curve between the unloading and reloading segments. The values chosen for this parameter were based on experimental observations and more experience is needed before this parameter could be confidently estimated in the initial design phase.

7.3 Design Approach

What tends to get overlooked in the discussion of base shear strength and deflection maxima is the issue of hysteretic behavior. As noted in Chapter 5, the hysteretic response of RM1 and RM3 exhibited some differences. Base shear is plotted versus top-level deflection for the last test run of each structure in Figs. 7.2 and 7.3 for the purpose of making some general observations and to provide some support for the methods described earlier in this chapter. The hysteresis loops are shown for "windows" of time during the first 5.3 seconds of each test.

One notable feature of the hysteretic behavior is the apparent degradation in strength (as measured by the base shear) which occurred in the post-peak strength range of response. This degradation was most pronounced immediately after the attainment of the peak strength (window 1). The characteristics of this were somewhat different for the two structures. Focusing on the "positive" response of RM1 (Fig. 7.2, window 1, upper right quadrant), it can be seen that the reduction in strength began immediately after the peak strength was reached (at 0.2% drift) with the most significant drop beginning at 0.3% drift. It was assumed that diagonal tension cracking in the exterior piers led to the immediate strength reduction. Inspection of windows 2 and 4, however, indicates that not all of the apparent reduction in strength was actually lost. Peak positive base shears in these windows were higher than would have been inferred from the apparent reduction in window 1. Base shears of 81% and 77% of the peak in window 1 were reached in windows 2 and 4.

Response in the positive quadrants for RM3 (Fig. 7.3) revealed some differences from that of RM1. Window 1, for instance, shows that after the initial reduction in stiffness there was a range of nonlinear displacements for which strength degradation did not occur. The stiffness of the structure was observed to change at 0.2% drift, but strength reduction was postponed until 0.7% drift. This is consistent with the observation that a flexural mechanism was more dominant for RM3 than it was for RM1. In contrast to RM1, however, the initial reduction in the strength of RM3 was never recovered. The maximum positive base shear attained after the first large-amplitude cycle was only 47% of the peak strength, although this could be due to the inability of the structure to attract force rather than a loss of strength.

Conclusions from these results are difficult to reach. RM1 showed a more immediate reduction in strength, but appeared to "regain" some of the loss and respond well (at approximately 80% of the peak strength) during a number of post-peak cycles. RM3, on the other hand, was able to sustain a range of nonlinear displacements before strength reduction occurred. The behavior after the first large-amplitude cycle would appear, however, to violate the usual requirement that structures be able to sustain a number of large-displacement cycles without a critical loss of strength.

Strength degradation noted in reinforced masonry shear wall structures has led to the suggestion that lateral drift of these structures be limited to confine them to the range of displacements for which this degradation does not occur [22]. The above discussion neither strengthens nor weakens this proposal. The behavior of RM3 might confirm such a limit, but the response of RM1 might suggest less stringent limits.

These considerations do, however, allow some generalizations about the methods considered in this chapter and the design process as it applies to reinforced masonry structures. For instance, the above discussion seems to highlight the importance of an agreed-upon value or basis for the determination of acceptable lateral drift. If this limit were to be tied to the prevention of strength degradation, the displacement at which strength decay begins would appear to be the most important parameter. Also, a knowledge of the peak strength, to the extent to which it may affect this parameter, would also be

important. Methods for making reliable estimates of base shear capacity and lateral displacement would then be necessary. As discussed earlier in this chapter, adequate methods for obtaining these estimates are not currently available. Current design methods, based on a working-stress approach and the distribution of story shear to piers using unrealistic stiffnesses do not permit a proper assessment of the lateral load capacity of a structure. A method which determines the ultimate capacity of the piers while considering the influence of loading direction and axial load (as in section 6.1) is more suitable for this task. Also, in section 6.2 it was noted that some existing linear models are poor predictors of pre-yield drift and give no useful information about nonlinear displacements. A linear model, such as the one proposed by Shimazaki and extended by Bonacci, would appear to be more appropriate for estimating peak lateral drift. A simple SDOF nonlinear model also seems to be potentially useful for this purpose.

Even if strength degradation were to be allowed and the resulting larger displacements permitted, a lateral drift limit to minimize structural damage and protect people and building contents would still be necessary. In this case the above comments also apply, since a more serious attempt at estimating peak drift than is suggested by current design codes would be desirable.

CHAPTER 8

COMPARISON OF STATIC AND DYNAMIC RESPONSE

This chapter presents correlations between response of the same structural system subjected to either dynamic shaking or static lateral forces. Two reduced-scale test structures were constructed with identical designs and were tested using two different methods. The first structure, RM1, was subjected to simulated earthquake motions on a shaking table. Its response was presented and discussed in Chapter 4. The second structure, RM2, was forced to displace through the same history at static rates using computer controlled servohydraulic actuators.

The correlation presented in this chapter is intended to provide insight into the differences in behavior of the same structural system subjected to either natural inertial loadings as a result of shaking, or to artificial static forces. In this way, an assessment can be made of the most common methods for simulating earthquake effects in the laboratory: static tests of large-scale structures and dynamic tests of reduced-scale structures. For the comparison, the two structures were purposely kept at the same small size. Details of the construction, erection, instrumentation and testing apparatus for the static test of specimen RM2 are provided in Appendices A, B and C.

The study focused on variations in strength, stiffness and energy dissipation for structures subjected to pseudo or real dynamic lateral forces. Because 85% of the mass was concentrated at the floor levels, effects related to differences between distributed and lumped inertial forces were not a primary concern. However, differences in response for systems subjected to either fluctuating or fixed lateral force distributions were of primary interest as were effects related to strain rate.

8.1 Experimental Procedure

The static test specimen (RM2) was constructed with a configuration and reinforcement pattern identical to that of structure RM1 (Figs. 2.2 and 2.3). A loading rig was fabricated so that response of the shaking-table specimen could be imitated in much the same way

that large-scale specimens must be tested : at static rates. The test setup is shown in Fig. 8.1. The model structure was bolted to the test floor, and a 25-kip servohydraulic actuator was attached to each floor slab and reacted against a steel frame.

The static test apparatus and the loading procedure are described in detail in Appendix C (Section C.1.2). The following is a brief summary of the manner in which lateral forces and displacements were applied to the structure. A separate controller was used for each of the three actuators. The top actuator was operated in displacement control in accordance with a history equal to that of measured records from the shaking-table specimen. Actuators at the first and second levels were operated in force control such that an inverted triangular force distribution would result. A computerized loading system was developed for the static tests. A flow chart for the computer program is shown in Fig. 8.2. After displacement command signals were sent to the third-level actuator from an analog function generator, the third-level force was measured and used as the basis for forces to be applied at the lower two levels. Deflections at the top level were measured relative to the strong floor, and compared to target peaks. If a peak was reached, a 5-volt signal was sent from the computer to the function generator which caused it to reverse its ramp function, and then a new target peak was read from the input array. As seen by comparing displacement response for dynamic and static tests (Fig. 8.3) the control system functioned as intended.

With this automated control system, it was possible to vary the lateral force distribution at any instant of time. It was originally thought necessary to sequence the lateral force distribution with the top-level deflection in an identical manner to that measured on the shaking-table. However, this was not done because such precision was believed to be unjustified in terms of the sensitivities observed with the dynamic lateral force distributions, and probable construction differences between the twin specimens. The moment-to-shear ratio at the base for the simpler inverted triangular distribution did agree well with the nominal moment-to-shear ratios observed at large amplitudes during dynamic shaking (Section 4.2.2.e). Furthermore, the simpler distribution was the same as used convention-

ally for engineering calculations which added another aspect to the correlation between static and dynamic specimens.

The loading rate was considered static because a single earthquake run took approximately six to eight hours. A corresponding test run on the shaking-table lasted approximately 20 seconds. In the final static test run, the top level of the structure was displaced at a rate of 0.0012 inches/second. In comparison, the "loading rate" for the final dynamic test, determined as the peak single-amplitude top-level deflection divided by one-quarter of the natural period of vibration, was approximately 14 inches/second.

A computer program was developed to sample and record data from 32 channels. Measurements included lateral forces and displacements at each floor level as well as flexural, shear and sliding deformations of each pier in the first story. The program sampled data at approximately ten-second intervals and provided a continuous screen display of the lateral force profile and base moment vs. top-level deflection hysteresis. Because of the high sampling rate (100,000 samples per second) and the slow loading rate, data could be acquired without pausing.

8.2 Specimen Response

LVDT's mounted at the midheight of each floor slab measured displacements relative to a reference column. Lateral forces at each floor level were recorded from the load cells of the actuators.

8.2.1 Response Maxima

A summary of response maxima for each run of the static test is presented in Table 8.1. Base shear (V_b) maxima were obtained by summing the measured force at each level and were normalized by the weight above the foundation (8940 lbs). Maximum base moments, M_b, were determined by summing the product of the force at each level and the height above the base. Base moments were normalized by the calculated yield moment (590 k-in). Lateral drift was calculated by dividing the maximum top-level deflection relative to the

base by the total height of the structure. The stiffness factor, K_0, was calculated by taking the lowest average slope of the normalized moment-drift hysteresis curve. Numbers in parentheses are percentages of the corresponding values measured during the dynamic test.

8.2.2 Response Histories

Measured response waveforms are presented in Fig. 8.3 for the fourth and most damaging test run. Results of the dynamic test are shown with solid lines, and those of the static test with dashed lines. The scale for the time axis of the static response was selected for sequencing purposes only, and is fictitious.

Plots of base moment versus top-level deflection during selected time intervals for static test runs 2 through 4 are shown in Figs. 8.4 and 8.5 (dashed lines). Response measured during corresponding intervals of the dynamic test is also shown (solid lines). Marked reductions in both strength and stiffness were observed when the specimen was loaded statically rather than dynamically. Significant differences in stiffness were observed for the test runs that resulted in flexural cracking (Runs 1 and 2), and little difference was observed once the structures were cracked (Run 3). The hysteresis curves for Run 3 were essentially the same for each specimen. However, large differences in stiffness characteristics returned during Run 4 when substantial diagonal tension cracking was observed.

8.2.3 Observed Damage

Cracking patterns recorded from visual inspection of the structure before the first static test and after each following test are presented in Appendix D. Figure 8.6 shows the final damage pattern for one wall of the structure. The base story of RM2 had more hairline cracks than RM1 before the start of testing. The level of cracking in the base stories of the two structures was nearly identical, though, after the third test runs. A comparison of crack patterns for the two structures after the last run shows that the damage to the static specimen was more severe than to the dynamic specimen. This is more clearly illustrated in Fig. 8.7 which compares the final damage patterns in the base stories of the two

structures. While the type of cracking was similar, the extent of the damage was much more pronounced for the static specimen.

8.3 Correlations Between Static and Dynamic Response

A comparison of the observed response of the statically and dynamically tested twin specimens revealed noticeable differences. Response maxima (Table 8.1) indicated that while the two structures were driven to the same top-level deflection, strength and stiffness characteristics were not the same. The static specimen achieved a peak base shear and base moment of only 64% and 79%, respectively, of those reached by RM1. The apparent stiffness of the static specimen after peak strength was reached (Run 4) was about half that of the dynamic specimen.

It could be postulated that differences in behavior are attributable to differences in lateral force distributions. However, at peak response, dynamic force distributions were centered below two-thirds of the height. The shear was higher per unit moment for the dynamic specimen, but more deterioration was seen to occur with the static specimen. This suggests that the observed differences in stiffness deterioration would have been more pronounced had the two specimens been loaded with identical force distributions.

It is more likely that the differences in behavior were attributable to differences in the rate of loading. Cracking strength, inferred from the base moment at first cracking, was found to be nearly identical for both test methods. From the test data, however, it is apparent that the rate of strain can have an appreciable effect on crack propagation. While marking cracks during the static test, it was not uncommon to observe cracking over the course of several minutes. Once a crack formed, alternate stress paths developed in the highly indeterminate system of blocks and mortar joints. Unlike a reinforced concrete structure, there was little or no aggregate interlock within the mortar joints to restrain crack propagation. With dynamic testing, peak deflections were attained on the order of a few hundredths of a second (one-quarter of the natural period of vibration). It is obvious that

the dispersion of cracking as seen with static testing could not have occurred in this short time interval.

The force-deflection curve for the static specimen during Run 4 showed that the stiffness reduced gradually as the specimen continued to attract further load. This was a stable tendency for the first two large-amplitude cycles which yielded reinforcement, but diminished after that because the stiffness had declined to the extent that little force was attracted with the prescribed displacement. This behavior is contrasted with the response of the dynamic specimen where yielding of reinforcement was apparent for three large-amplitude cycles.

8.4 Summary and Conclusions

On the basis of the above observations, it appears that static testing in a laboratory provides a more demanding environment than an actual seismic event. Thus, static testing should be a conservative method for estimating resistance of a structure. It was evident that the dynamic specimen was initially both stronger and stiffer than the static one, and that with successive cycles, had suffered less deterioration in strength and stiffness. Observed damage of the dynamic specimen was obviously much less than that observed for the static specimen (Fig. 8.7) despite the fact that the dynamic specimen had resisted larger forces.

If lateral displacements were to be prescribed on-line during testing in accordance with measured stiffness (as termed the pseudodynamic or generated sequential displacement methods), it should be expected that these observed behavioral differences would be accentuated, and that the static test results should be all the more conservative. In this case, the softer, static specimen should have incurred even greater damage because it would have been forced to larger deflections (assuming that spectral displacements would increase with period).

Although it was not observed in this study, it may be the case that the deformation capacity of the dynamic specimen may be less than that of the static one because larger

story shears are needed to reach the larger flexural strengths. In this case, it may not necessarily be correct to view laboratory static test results as absolutely conservative.

CHAPTER 9

SUMMARY AND CONCLUSIONS

This study focused on the nonlinear response of reinforced masonry structures to earthquake motions. In its most elementary sense the study was an effort to improve the understanding of how one class of building structure behaves when subjected to the demands imposed by a strong earthquake. To be of value to those who design and analyze such structures, the investigation had the following objectives:

1) Evaluate common practices used in the design of reinforced masonry building structures
2) Suggest simplifications for these practices
3) Provide dynamic test data for use in analytical investigations.

To be of value to those who research such structures, a portion of the study was devoted to correlation in behavior between structures tested either dynamically or statically.

9.1 Overview of Experiments

The experimental phase of this study consisted of the design, construction and testing of three one-quarter scale structures. All structures were three-story, reinforced concrete masonry systems with pairs of perforated flanged shear walls as the lateral load-resisting elements. Two of these structures were identical (RM1 and RM2) while the third (RM3) had a different structural configuration and reinforcement.

Test structures RM1 and RM2 were reinforced based on minimum requirements of current masonry design codes [21]. Structure RM3 was assigned a larger percentage of horizontal reinforcement so that a capacity design approach could also be investigated. In both structures, the observed strength, the inelastic deformation capacity, and the nature of the response mechanisms which formed under dynamic loading were of interest.

Structures RM1 and RM3 were subjected to earthquake simulations of progressively increasing intensity on a shaking table. One horizontal component (N-S) of the 1940 El Centro ground motion was compressed with respect to time to form the input motion. The

amplitude of the motion was chosen for each test run to produce response within a desired range of behavior.

Structure RM2 was tested by securing it to a strong floor and applying lateral forces at slow rates with hydraulic actuators at each floor level. The top level was displaced with a history measured during dynamic tests of RM1, and lateral forces were controlled to maintain a linear distribution.

Response of the structures was observed by monitoring the base acceleration (dynamic tests), lateral accelerations and displacements, distortions of the piers, and cracking patterns. Low-amplitude free vibration tests were performed before and after each test run to detect changes in natural frequency and apparent viscous damping.

9.2 Summary

9.2.1 Limitations

Before summarizing the results of the investigation, a few limitations of this particular study should be mentioned. Strictly speaking, the observations and conclusions of the study are valid only for the two structures and one base motion considered. Both the observed behavior and the recorded data will, however, be of value in the development of analytical models which can extend these results to a wider range of configurations and base motions. The development of such models is being actively pursued by other researchers [15] and was not attempted by this study to avoid duplication of effort.

Also, although an attempt was made to obtain dependable estimates of strength and stiffness parameters, this study did not address some essential ingredients of the seismic design process. First, the reliability of any estimate of the response of a structure during an earthquake is tempered by the amount of confidence with which the characteristics of the base motion can be predicted. In addition, methods for estimating lateral drift are effective only to the extent that a drift limit can be chosen to restrict the amount of damage to an acceptable level.

9.2.2 Observed Response of Test Structures

a) Response During Dynamic Tests

Structures RM1 and RM3 responded within the ranges of behavior which were anticipated for the selected intensity of the base motion. Linear response spectra for motions which produced similar response (cracking, yielding of reinforcement, ultimate limit state) in the structures were nearly identical. It was observed that an interaction between the structures and the earthquake simulator had modified some characteristics of the El Centro input motion. As a result, analytical investigations of the structures were based on the recorded base accelerations rather than the Cal Tech record.

Both structures were observed to displace primarily in the first mode. Top-level acceleration response was dominated by frequencies near the frequency of the structure's first mode. Lateral-force profiles were observed to fluctuate once the structures had softened. In general, response at peak base moment was characterized by an inverted triangular force distribution. At peak base shear, the resultant of lateral forces was lower than the resultant for an inverted triangular loading pattern. Phenomena which affected energy dissipation capacity were observed in the hysteretic response of the softened structures. Specifically, a pinching behavior and an indentation of the hysteresis curve at peak response occurred to different degrees in the two structures. Both structures exhibited similar decreases in first-mode frequency and increases in apparent damping as the level of damage increased.

In addition to the above similarities, some differences were observed in the response of the two structures. The most notable differences were related to hysteretic behavior and the way in which each structure took on damage in the last test run. The response of RM1 was primarily flexural during the first few seconds of the final run as hinging occurred at bed joints which had cracked in previous runs. The load-carrying capacity of the structure was reached when nearly all of the story shear was attracted to the one exterior pier resisting axial compression due to overturning. This resulted in cracking of the pier in diagonal

tension which lead to a rather immediate reduction in strength, however the structure was capable of dissipating energy during a few large-displacement cycles after this point.

The behavior of RM3 was dominated by flexural hinging of the piers throughout the tests. Crushing of the masonry at the top and bottom of the short piers and diagonal cracking of the slender exterior piers in the last run limited the capacity of the structure. A range of displacement after peak strength was observed with little or no strength degradation. After the first large-amplitude cycle, the structure had softened to the point that it did not attract appreciable force during the remainder of the test. No transverse stability effects were observed despite the extent of hinging at the top and bottom of the piers.

b) Aspects of Observed Response

Inspection of measured response histories, and the narrow band of frequencies noted in Fourier amplitude spectra of measured accelerations, suggested that response of the structures was of a single-frequency nature throughout all levels of damage. Reductions in the stiffness of the structures, inferred from apparent frequencies measured before and after testing, agreed well with reductions as inferred from the slope of moment-displacement relationships. These observations suggested that a system with a substitute linear stiffness could be used to estimate the peak response of a nonlinear system.

The observed constancy of the deflected shape during testing indicated that an SDOF idealization of a structure would be sufficient to represent the measured displacement response history. Top-level deflection histories calculated by an SDOF damped, linear oscillator were found to provide a good match with the measured histories.

Both structures had hysteretic damping sufficient to limit the amplification of base accelerations during strong shaking. Each structure became more tolerant to base excitations after yielding of reinforcement, suggesting that a strength approach to design should be feasible.

The shear resistance characteristics of the individual piers were seen to be strongly affected by reversals in axial force induced by overturning moments. The traditional pier

model, which ignores this phenomenon, could not adequately account for the observed distribution of story shear, and thus the observed shear distortions of the piers.

c) Calculated Base Shear Strength

Base-shear capacity was estimated using two approaches as noted below. In both cases, the peak strength was assumed to correspond to a mechanism in which plastic hinges form at the top and bottom of each base-story pier. Member capacities were calculated from ultimate strength procedures, using material properties determined from component tests.

The first estimate of the base shear strength was made from calculated flexural capacities of the piers ignoring axial loads. Base-shear capacities determined by this method underestimated the measured peak base shears and were 22% to 51% lower than base-shear strengths calculated with axial load considered. At best, the "zero axial load" approach could be considered to be a conservative "first-cut" at the base shear strength.

A more accurate estimate of the observed base shear strength was obtained by considering reversals of axial force and loading direction for the calculation of pier flexural and shear capacities. Calculated strengths were nominally within 14% of the measured strengths, however when exact distances between hinges were used, calculated strengths were within 5% of measured strengths (for all but one loading direction of RM3).

Although it could be argued that the lateral strength predicted by the pier model errs on the conservative side and is therefore acceptable for satisfying a design base shear value, a more accurate strength estimate is always desirable. For instance, two methods considered in Chapter 6 for estimating peak inelastic drift required a reliable estimate of the peak base shear. In addition, a realistic evaluation of base shear strength forms an important component of a designer's experience in evaluating alternative structural configurations or systems. This is especially true given current design methodologies which place the emphasis on a required base shear strength.

d) Estimates of Lateral Drift

Drift estimates from three common linear models (pier model, frame model, finite element model) were compared to measured drift maxima for all test runs of RM1 and RM3. All three models were found to be overly stiff even for test runs in which the amplitude of displacement was relatively small.

A linear spectral analysis (developed by Shimazaki and extended by Bonacci) was used to estimate the peak nonlinear displacement of RM1 and RM3. In this method, the peak displacement is obtained from an idealized linear displacement response spectrum for a damping factor of 2% at a period corresponding to the initial (uncracked) period of the structure "softened" by a specified factor. The procedure was described in detail in Section 6.2.2.b. Whether or not the method is applicable to a given structure and, to a certain extent the shape of the idealized spectrum, depends on the strength and stiffness characteristics of that structure. Top-level deflections calculated by this method correlated well with the peak inelastic displacements measured during the final test run of the two structures.

Peak inelastic displacements were also compared to displacements computed by a linear SDOF oscillator with "substitute" values of frequency and damping. The substitute frequency was that measured during the final test run of the structure, while the substitute damping ratio was obtained from free vibration tests after the last run. The substitute linear system provided a conservative estimate of the measured peak displacements.

Displacement histories for the base motion recorded during the last test runs was calculated by an SDOF nonlinear model. Hysteresis rules were formulated from observed strength and stiffness characteristics of the structures. The slope of the unloading and force-reversal portions of the hysteresis curve were based on experimental observations. The displacements calculated by the SDOF model provided a good representation of the frequency and amplitude of the top-level displacements measured during the final test runs.

The most important conclusion from the above discussion of drift estimates is not that some of the specific tools considered seemed to be "successful". Other methods might be developed which are more appropriate for the present class of structure. What is significant is simply the observation that linear models were appropriate for bounding the peak

displacement and that a SDOF idealization provided information about the number, sequence and amplitude of the nonlinear displacements.

e) Comparison of Testing Methods

A comparison of static and dynamic tests of the same structural configuration provided insights which were of value in assessing how results of different laboratory test methods should be extended to engineering practice. When one structure was tested on the shaking table, a higher initial stiffness was observed than when its twin was subjected to a similar series of static lateral forces. Differences in apparent stiffness for the two structures reduced after initial flexural cracking, however noticeable differences reappeared near the ultimate limit state. The statically-tested structure reached a peak base shear of only 64% of that attained during the dynamic test.

Differences in observed response were attributed to differences in the rate of loading. The slow loading rate in the static test permitted cracks to propagate to a much greater extent than was possible during the dynamic test. Inspection of damage after the completion of testing indicated a much greater degree of deterioration in the static structure than in the dynamic structure.

These results lead to conclusions that static testing is a conservative method for determining the lateral load resistance of a structure. In addition, pseudodynamic test methods would have been expected to accentuate the observed behavioral differences between the structures, making lateral resistance estimates from this method all the more conservative.

9.3 Comments on Experimental Method and Further Studies

9.3.1 Laboratory Testing of Reduced-Scale Structures

While shaking-table studies of reduced-scale structures is not a new phenomenon, it has been infrequently used in investigations of reinforced masonry systems. This study has demonstrated that it is, however, an attractive and economically viable means for studying

the nonlinear response characteristics of building systems. The apparently conservative nature of the results of large-scale static and pseudodynamic tests makes reduced scale dynamic tests all the more appealing.

The results of the present investigation indicated that dynamic testing of one-quarter scale reinforced masonry structures was an effective method for evaluating overall system response. Cracking, yielding and ultimate limit states were achieved through the selection of base motion intensities. In general, observed response could be explained by accepted engineering principles.

9.3.2 Directions for Future Research

On the basis of the observations from this investigation, general directions for further study can be recommended. Additional dynamic tests of reduced-scale reinforced masonry structures would certainly be of value. Experiments using different structural configurations, patterns of reinforcement, and ground motions than those used in this study would provide further insight into the behavior of masonry buildings, especially in the nonlinear range.

Also, a product of the present study has been a set of measured response histories for masonry structures subjected to dynamic excitations. These histories can be of considerable worth as benchmark data for the calibration of analytical models. These computational models could, among other things, be of assistance in directing the future experiments suggested above.

As more dynamic response data for masonry structures becomes available and analytical models of response are improved, further evaluations of the "simplified methods" suggested in this study would be beneficial. In particular, the methods considered for evaluating nonlinear displacement response might be improved to better reflect the observed characteristics of reinforced masonry systems.

Finally, although it would have been inappropriate to use the results of the present investigation to make recommendations for detailing requirements, the provision of sufficient ductility or toughness is of great concern if masonry structures are to be allowed to

achieve the levels of lateral drift reached in this study. Therefore, investigations aimed at developing detailing methods which will ensure adequate performance for the maximum anticipated level of lateral drift would be worthwhile.

9.4 Concluding Remarks

Because the study was based on a limited number of tests, the most significant conclusions are those of a general nature, rather than specific recommendations. The principal conclusions of the investigation were:

- Modeling at one-quarter scale was a suitable method for investigating dynamic response of an overall structural system.
- Measured deflected shapes were essentially invariant for all amplitudes of motion. Therefore, a single generalized coordinate should be sufficient to represent histories of dynamic response in both the linear and nonlinear ranges.
- Despite nonlinear behavior, each test structure responded with a dominant frequency which could be calculated using an average stiffness of a hysteresis cycle. This suggests that a linear method of analysis might be appropriate for estimating response maxima of nonlinear masonry systems.
- The inelastic deformation capacity of one structure was limited because of sliding along a flexural crack. As a result, the distribution of story shear was not in accordance with that predicted by conventional stiffness models.
- A capacity design approach worked well for one structure which developed plastic hinges at the top and bottom of each base-story pier. Significant inelastic rotations were observed with no loss of stability.
- Deterioration of strength and stiffness can be much more pronounced when test rates are slow.

In addition to these general conclusions, some suggestions were made previously for evaluating lateral strength and deflection and for the use of these parameters in the design process. A procedure was proposed in Section 7.1.1 for providing sufficient strength in the piers of a structure. It involved the placement of minimum amounts of vertical reinforcement in the piers and the selection of horizontal reinforcement by a capacity design method. Pier flexural capacities were based on ultimate strength methods and a consideration of reversals of axial forces.

Also, it was suggested (Section 7.1.2) that substitute linear methods, such as the substitute structure method or the Shimazaki\Bonacci approach with suitable modifications for reinforced masonry, be used to assess the stiffness (based on lateral drift) of a trial structural configuration. It was further suggested that this "drift check" could precede the evaluation of lateral strength in the design process.

The above brief recommendations are intended to help produce safe and serviceable reinforced masonry structures when these structures are expected to experience strong shaking. They attempt to focus the design process on realistic estimates of lateral strength and stiffness. The suggestions for lateral strength determination depart from traditional practice for reinforced masonry structures in that they eliminate the need for an explicit evaluation of pier stiffness. In addition, strength calculations are based on ultimate strength principles and a capacity design approach. The role of lateral drift is raised to one in which an estimate of its probable maximum value is relied upon to ensure that a structural system is stiff enough to avoid unacceptable amounts of damage. These recommendations could result in a straightforward design process in which a reinforced masonry structure is supplied with minimum strength, provided that lateral drift is confined to an acceptable range.

TABLES

Table 2.1 Experimental Program and Target Spectral Accelerations

Test Run	Intended Range	Estimated Spectral Acceleration for Intended Range	
		RM1	RM3
First	pre-cracking	----	----
----	cracking	0.5g	0.4g
Second	post-cracking ; pre-yield	----	----
Third	yield	1.1g	1.0g
Fourth	post-yield ; ultimate limit state	----	----

Table 2.2 Estimated Response of Structure RM1

Peak Base Acceleration (g)	Maximum Top-Level Acceleration (g)	Maximum Top-Level Drift (%)
0.4	1.7	0.15
0.5	1.6	0.16
0.66	1.6	0.19
1.0	1.8	0.33
1.5	2.1	0.43

Table 3.1 Earthquake Simulation Schedule (RM1)

Run	Base Motion	Intended Range	Estimated Spectral Accel. for Intended Range	"Measured" Spectral Accel. during Test[a]
1	El Centro (N-S)	pre-cracking	---	0.4g
---	---	cracking	0.5g	---
2	EC	post-cracking ; pre-yield	---	0.8g
3	EC	yield	1.1g	1.1g
4	Filtered EC	post-yield ; ult. limit state	---	1.8g

[a] Peak third story acceleration measured during test divided by assumed first-mode participation factor of 1.29 (appropriate for linear deflected shape).

Table 3.2 Earthquake Simulation Schedule (RM3)

Run	Base Motion	Intended Range	Estimated Spectral Accel. for Intended Range	"Measured" Spectral Accel. during Test[a]
1	El Centro (N-S)	pre-cracking	---	0.4g
---	---	cracking	0.4g	---
2	EC	first yield	0.7g	0.8g
3	EC	full yield	1.0g	1.1g
5	Filtered EC	post-yield	---	1.0g
6	Filtered EC	post-yield ; ult. limit state	---	1.3g

[a] Peak third story acceleration measured during test divided by first-mode participation factor of 1.29.

Table 3.3 Base Motion Characteristics (RM1 and RM3)

Run		$\frac{RM3_{amp}}{RM1_{amp}}$[a]	Max. Base Acceleration (g)			Spectrum Intensity[b] (5% Damping)		
RM1	RM3		RM1	RM3	RM3/RM1	RM1	RM3	RM3/RM1
1	1	0.70	0.34	0.28	0.82	3.52	2.60	0.74
2	2	0.88	0.49	0.50	1.02	6.71	6.19	0.92
3	3	0.89	0.70	0.67	0.96	9.70	9.21	0.95
---	5	---	---	0.84	---	---	7.61	---
4	6	0.80	1.99	2.50	1.26	16.64	15.41	0.93

[a] Ratio of intended amplitude of base accelerations - based on simulator controller settings

[b] Area below velocity response spectrum between periods of 0.04 and 1.0 seconds

Table 4.1 RM1 and RM3 Measured Response Maxima

Run		a_g (g)		a_3 (g)		Sa (g)		Sa/a_g		Top Drift (%)		V_b/W		M_b/M_y	
RM1	RM3	RM1	RM3	RM1	RM3	RM1	RM3	RM1	RM3	RM1	RM3	RM1	RM3	RM1	RM3
1	1	0.34	0.28	0.56	0.56	0.43	0.43	1.26	1.54	0.03	0.04	0.41	0.38	0.41	0.55
2	2	0.49	0.50	1.03	0.98	0.80	0.76	1.63	1.52	0.09	0.17	0.72	0.73	0.73	1.01
3	3	0.70	0.67	1.39	1.38	1.08	1.07	1.54	1.60	0.19	0.41	0.97	0.91	0.93	1.32
---	5	---	0.84	---	1.24	---	0.96	---	1.14	---	0.49	---	0.98	---	1.29
4	6	1.99	2.50	2.36	1.63	1.83	1.26	0.92	0.50	1.06	1.32	1.65	1.46	1.45	1.57

Table 4.2 Characteristic Frequency and Damping (RM1 and RM3)

Run	Free Vibration				Earthquake Simulation	
	Frequency (Hz)		Damping (%)		Frequency (Hz)	
	RM1	RM3	RM1	RM3	RM1	RM3
Before Run 1	15.5	13.2	2	2		
During Run 1					13.1	10.9
After Run 1	14.7	11.7	2	3		
During Run 2					9.5	6.6
After Run 2	12.3	8.9	5	5		
During Run 3					7.9	5.4
After Run 3	9.4	6.7	6	6		
During Run 4					3.6	---
After Run 4	4.0	---	16	---		
During Run 5					---	4.9
After Run 5	---	6.2	---	6		
During Run 6					---	2.9
After Run 6	---	5.0	---	13		

Table 5.1 Changes in Apparent Frequency

Structure	Free Vibration			Earthquake Simulation			Hysteresis cycle[1]
	Before First Run (f_i)	After Last Run (f_f)	$\frac{f_f}{f_i}$	During First Run (f_i)	During Last Run (f_f)	$\frac{f_f}{f_i}$	$\frac{f_f}{f_i}=\frac{\sqrt{k_f}}{\sqrt{k_i}}$
RM1	15.5	4.0	0.26	13.1	3.6	0.27	0.24
RM3	13.2	5.0	0.38	10.9	2.9	0.27	0.26

(1) Inferred from apparent stiffness of hysteresis cycle

Table 5.2 First-Mode Participation Factors

Structure	Run	Average Modal Participation Factor
RM1	3	1.30
	4	1.21
RM3	3	1.26
	6	1.21

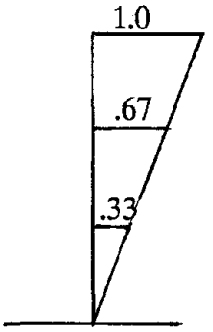

MPF = 1.29

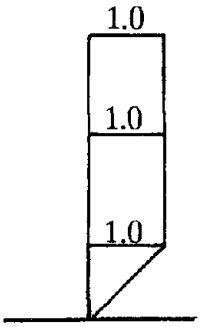

MPF = 1.00

Table 6.1 Calculated Strengths of Base-Story Piers [a]

Structure / Loading Direction / Pier	Pier Height, h_i (in)	Zero Axial Load [1] Flexural Capacity, M_i (k-in)	Zero Axial Load [2] Shear corresponding to flex. cap., V_i (k)	Axial Load Considered [3] Axial Load [c] (k)	Axial Load Considered [4] Flexural Capacity, M_i (k-in)	Axial Load Considered [5] Shear corresponding to flex. cap., V_i (k)	Axial Load Considered [6] Shear Capacity (k)
RM1 : Load Right [b]							
Exterior Pier {1}	16	20.3	2.54	-3.1	6.0	----	----
Center Pier {2}	16	16.1	2.01	2.0	28.9	3.61	4.63
Exterior Pier {3}	16	7.5	0.94	6.5	28.3	3.54	2.66
RM3 : Load Left							
Short Exterior Pier {1}	12	7.5	1.25	5.6	25.7	4.30	4.61
Center Pier {2}	12	7.3	1.22	1.8	14.5	2.42	4.27
Slender Exterior Pier {3}	28	16.1	1.15	-1.9	8.7	----	----
RM3 : Load Right							
Short Exterior Pier {1}	12	16.1	2.68	-1.3	11.3	----	----
Center Pier {2}	12	7.3	1.22	1.8	14.5	2.42	4.27
Slender Exterior Pier {3}	28	7.5	0.54	5.0	24.0	1.71	3.60

[a] Capacities given are for an individual pier with average dimensions

[b] See Table 6.2 for definition of loading direction

[c] Negative number denotes net axial tension

Table 6.2 Calculated and Measured Base Shear Capacity

Structure	Load Direction	Calculated Base Shear Strength (k)			Measured Peak Base Shear (k) [4]
		Design Pier Heights		"Observed" Pier Heights	
		Zero Axial Load [1]	Axial Load Considered [2]	Axial Load Considered [3]	
Dynamic Tests					
RM1	Left	11.0	12.5	13.6	12.9
	Right	11.0	12.5	14.1	14.6
RM3	Left	7.2	13.4	11.7	11.2
	Right	8.9	8.3	8.0	12.8
Static Test					
RM2	Left	11.0	12.5	12.8	9.4
	Right	11.0	12.5	12.7	9.3

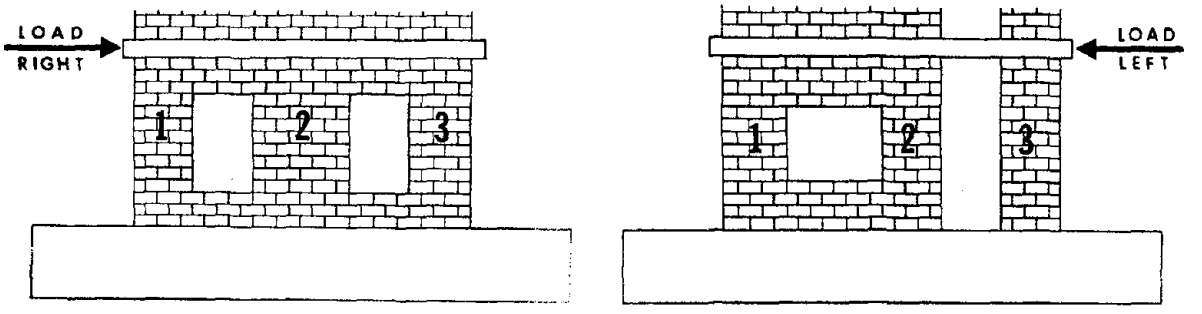

Table 6.3 Material Properties for Deflection Calculations

Structure	Mean Compressive Strength of Prisms f'm (psi)	Initial Tangent Modulus Em (psi)	Shear Modulus G (psi)
RM1	1215	720,000	288,000
RM3	1228	910,000	364,000

Table 6.4 Calculated and Measured Lateral Drift Maxima
(Top-Level Deflection as Percentage of Height)

	Run	V_b/W	Lateral Drift (%)			
			Measured (f_i = 15.5 Hz)[a]	Pier Model (f_i = 38 Hz)[b]	Frame Model (f_i = 24 Hz)[b]	FEM Model (f_i = 19.5 Hz)[b]
RM1	1	.41	.027	.0041	.012	.017
	2	.72	.088	.042	.055	.078
	3	.97	.19	.056	.074	.15
	4	1.65	1.06	.095	.124	.42
	Run	V_b/W	Lateral Drift (%)			
			Measured (f_i = 13.2 Hz)[a]	Pier Model (f_i = 36 Hz)[b]	Frame Model (f_i = 24 Hz)[b]	FEM Model (f_i = 15.5 Hz)[b]
RM3	1	.38	.044	.0061	.0090	.026
	2	.72	.17	.045	.046	.097
	3	.92	.41	.057	.059	.19
	5	.99	.49	.061	.063	.22
	6	1.47	1.32	.091	.094	.48

[a] Initial frequency measured in free vibration before first earthquake simulation

[b] Initial frequency based on gross-section properties

Table 6.5 Calculated and Measured Lateral Drift Maxima
(Top-Level Deflection as Percentage of Height)

Structure	Run	Frequency (Hz)	Damping (%)	Maximum Lateral Drift (%)	
				Calculated	Measured
RM1	3	7.9	6	0.28	0.19
	4	3.6	16	1.7	1.1
RM3	3	5.4	6	0.80	0.41
	6	2.9	13	2.1	1.3[a] (1.6)[b]

[a] Measured maximum drift (based on limit of LVDT)

[b] Probable maximum drift

Table 6.6 Calculated and Measured Lateral Drift Maxima

Structure	Run	Period Ratio					Strength Ratio			SR + TR	Lateral Drift (%)	
		[1] T_i (sec)	[2] Softening Index	[3] T_o (sec)	[4] T_g (sec)	[5] TR	[6] V_b/W^a	[7] V_b/W^b	[8] SR	[9]	[10] Linear Analysis	[11] Measured
Last Test Run												
[1] RM1	4	0.051	$\sqrt{2}$	0.073	0.22	0.33	1.52	3.87	0.39	0.72	1.1	1.1
[2] RM3	6	0.065	$\sqrt{2}$	0.091	0.22	0.41	1.39	3.87	0.26	0.67	1.3	1.3(1.6)[c]
[3]			$\sqrt{3}$	0.111		0.50				0.76	1.6	
Third Test Run												
[4] RM1	3	0.051	$\sqrt{2}$	0.073	0.22	0.33	1.52	1.55	0.98	1.3	0.24	0.19
[5] RM3	3	0.065	$\sqrt{3}$	0.111	0.22	0.50	1.39	1.55	0.89	1.4	0.53	0.41

[a] Lateral Strength Coefficient

[b] Base Shear Coefficient from Linear Spectral Analysis

[c] Probable maximum drift

Table 8.1 Measured Maxima of Static Specimen [1]

Run	V_b/W	M_b/M_y	d_3/H (%)	K_o
1	0.20 (50)	0.22 (54)	0.03 (100)	684 (54)
2	0.52 (72)	0.56 (77)	0.10 (113)	625 (73)
3	0.78 (80)	0.85 (91)	0.20 (106)	403 (94)
4	1.06 (64)	1.15 (79)	0.99 (93)	67 (55)

[1] Numbers in parenthesis are percentages of dynamic measurements

FIGURES

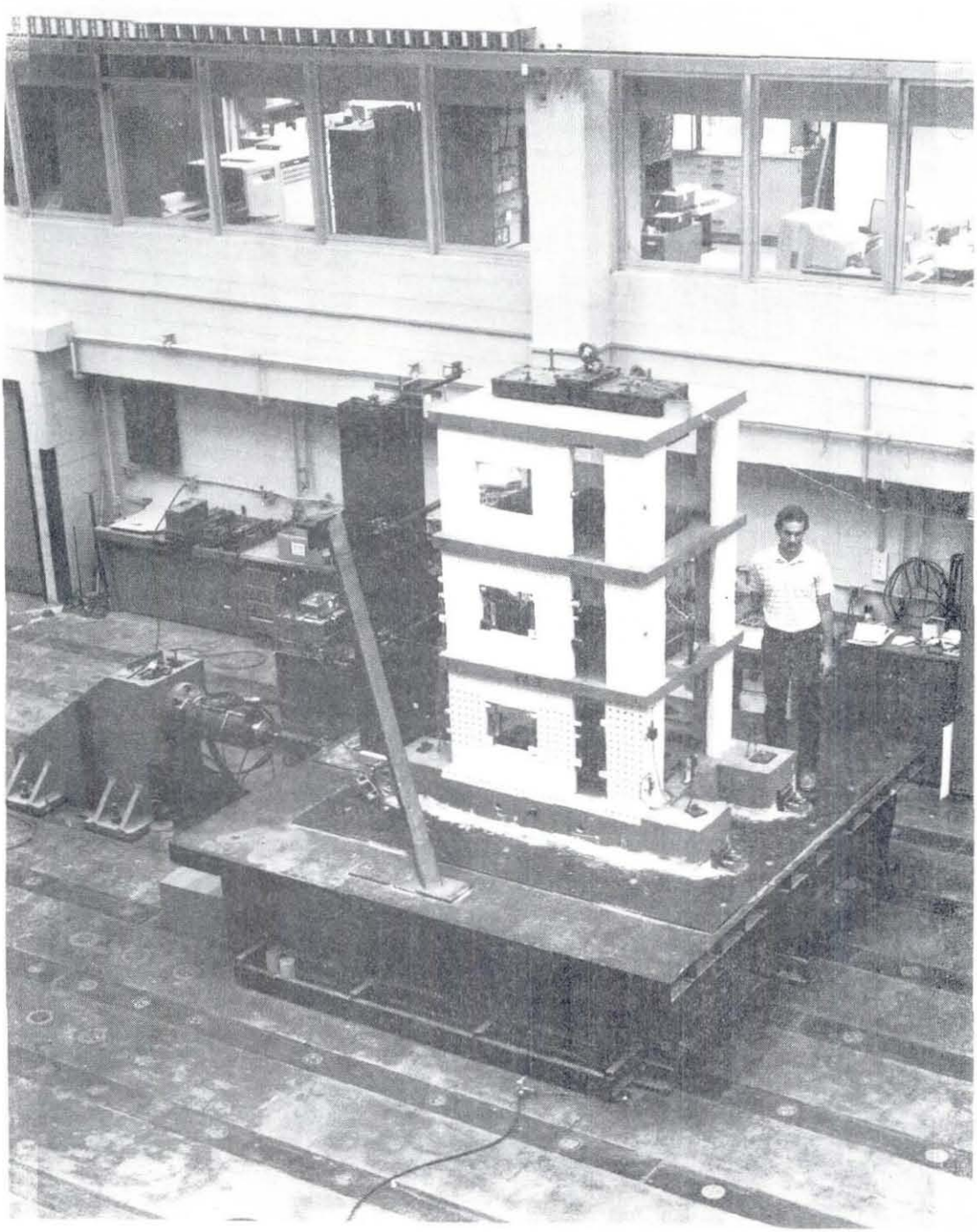

Figure 2.1 Structure RM3 on Shaking Table

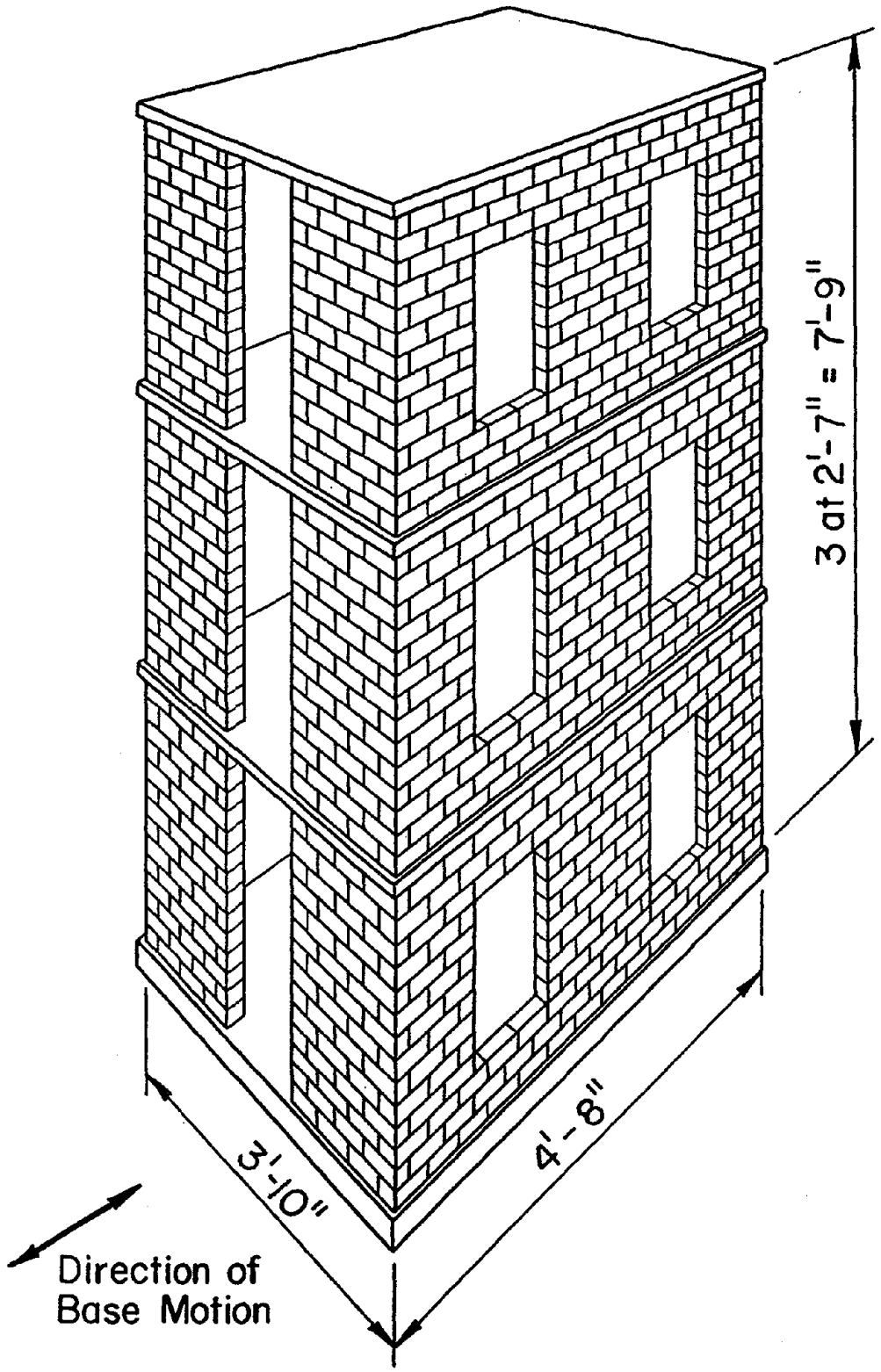

Figure 2.2 Structural Configuration of RM1 and Direction of Lateral Force

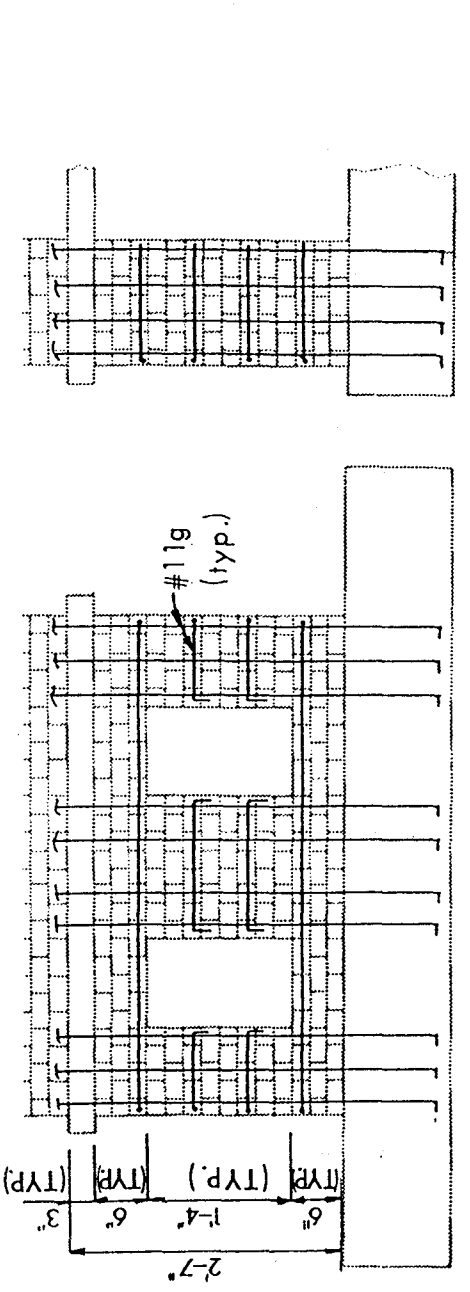

b) Elevation

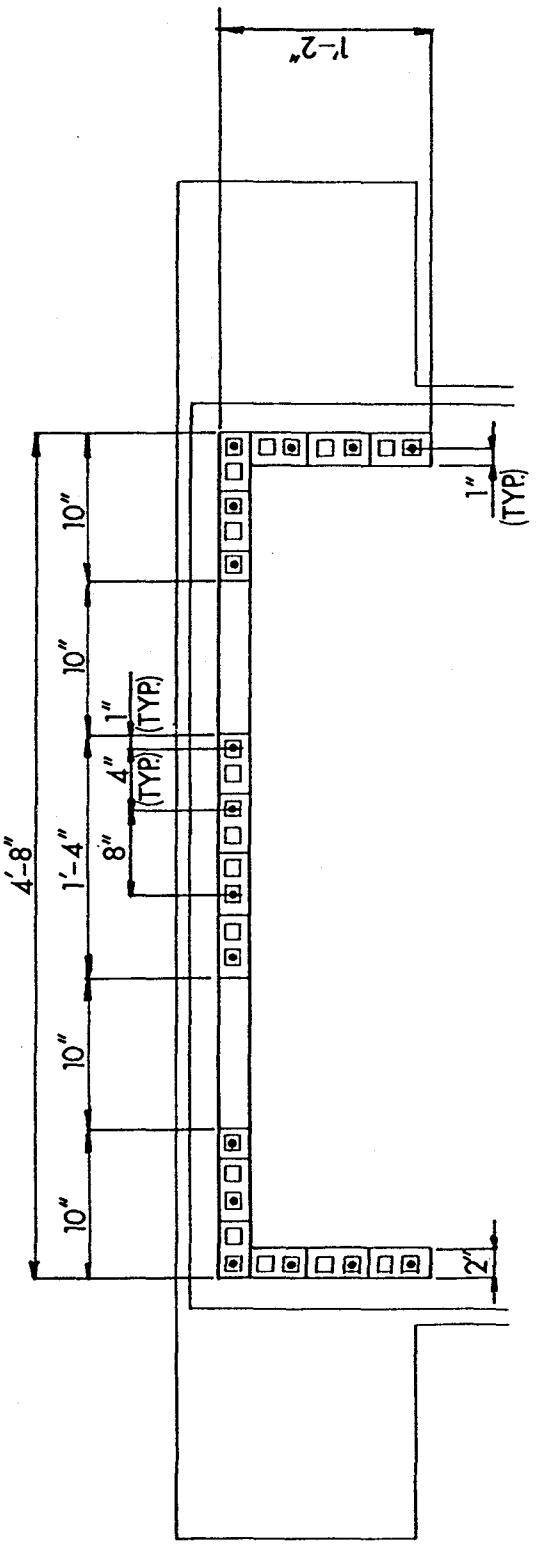

a) Plan

Figure 2.3 Configuration and Layout of Reinforcement for Structure RM1

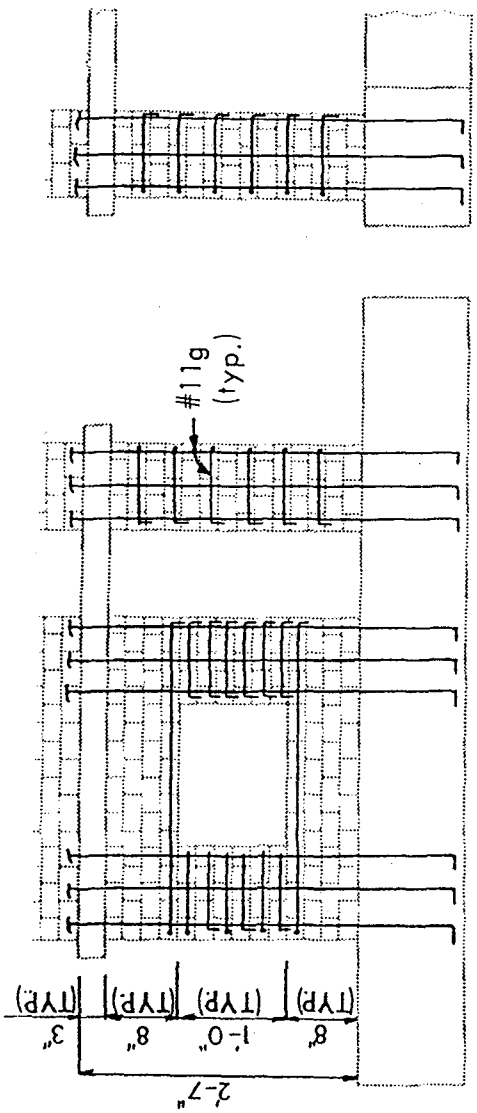

b) Elevation

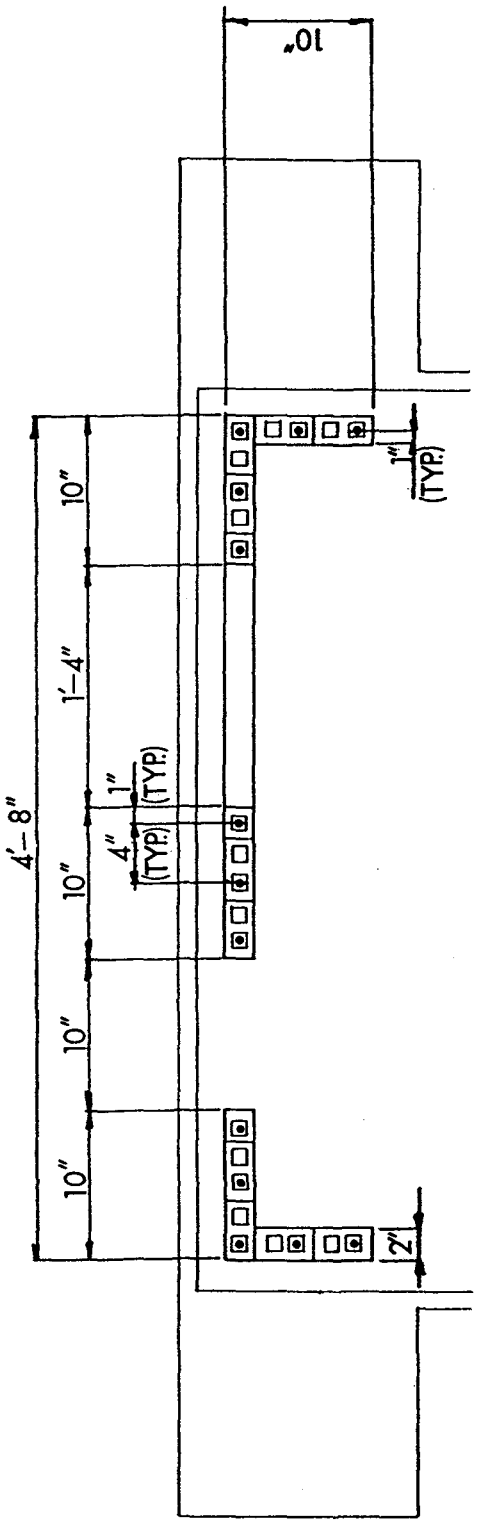

a) Plan

Figure 2.4 Configuration and Layout of Reinforcement for Structure RM3

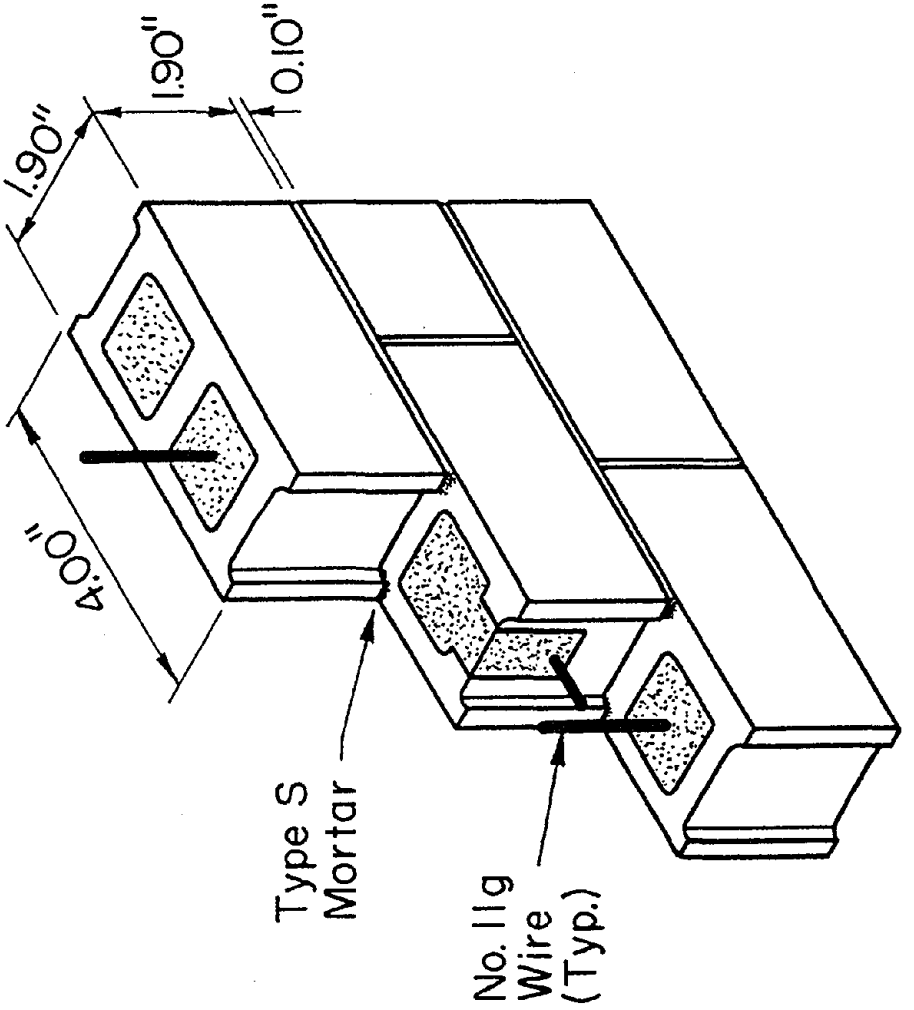

Figure 2.5 Typical Construction

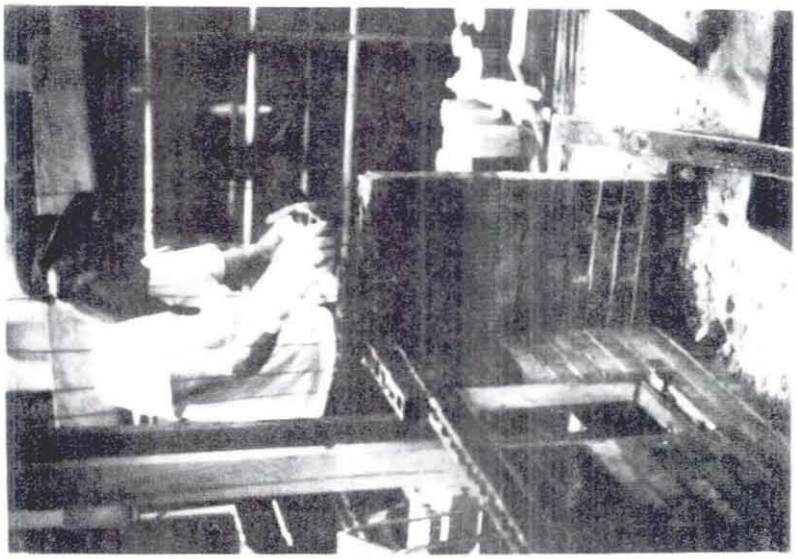

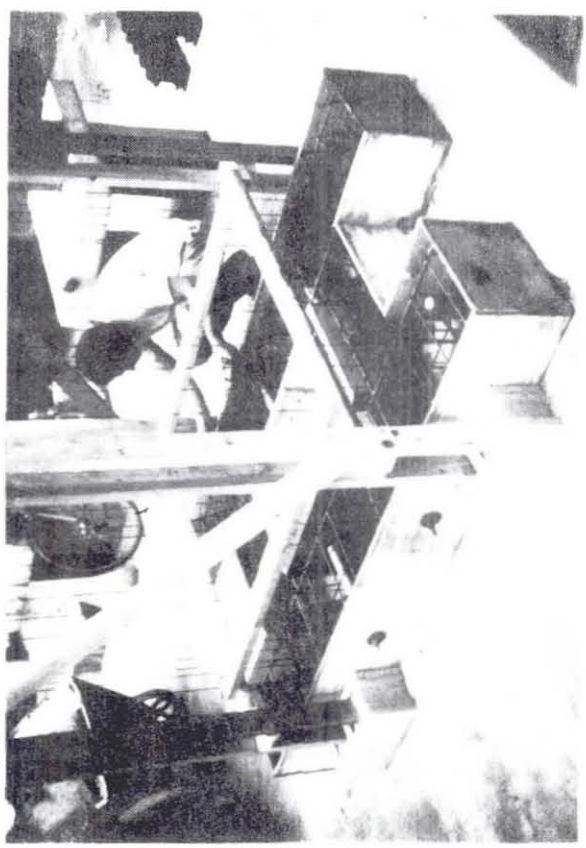

Figure 2.6 Construction of Structure RM1

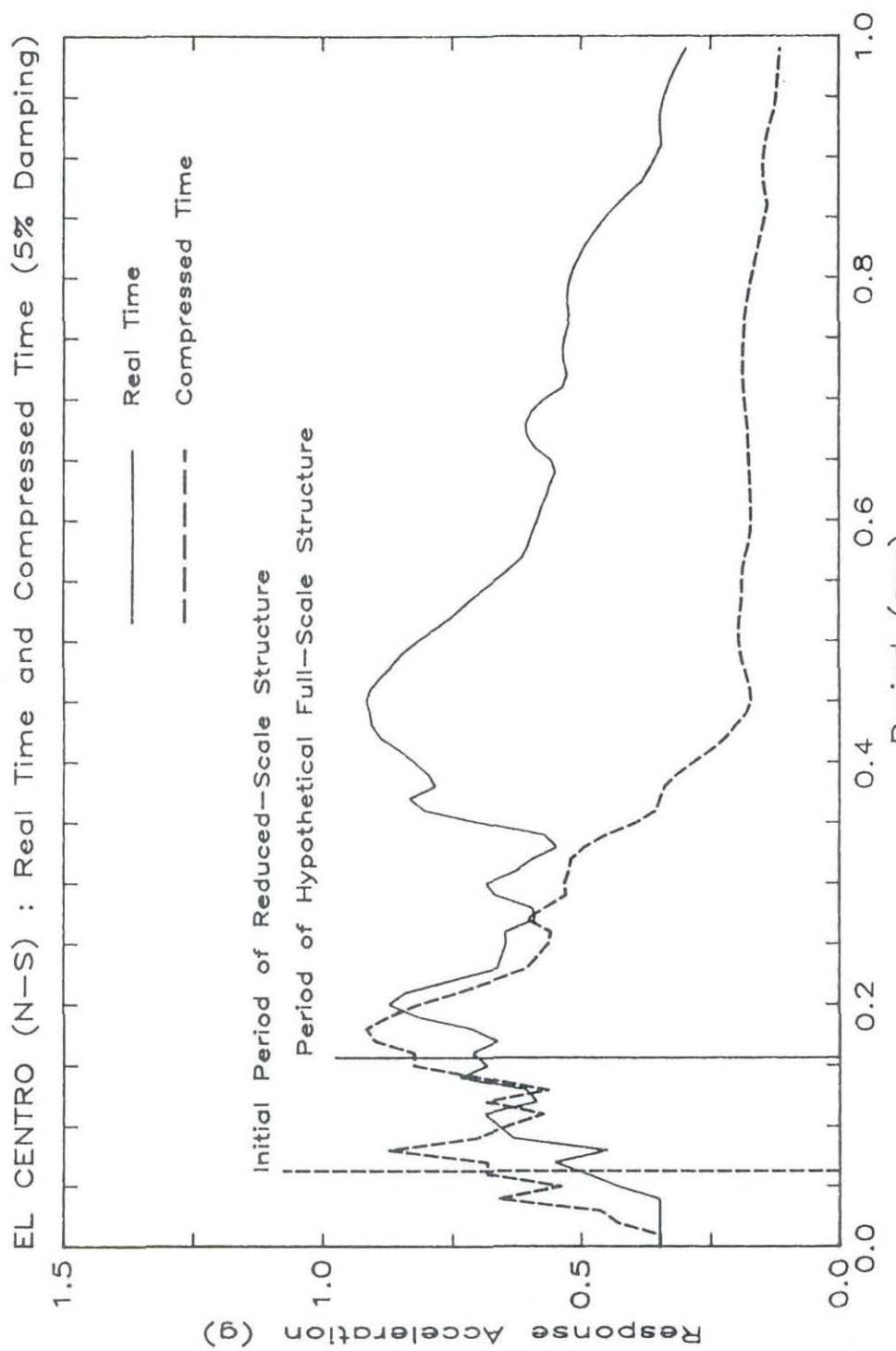

Figure 2.7 Linear Acceleration Response Spectra for El Centro (N-S) Base Motion

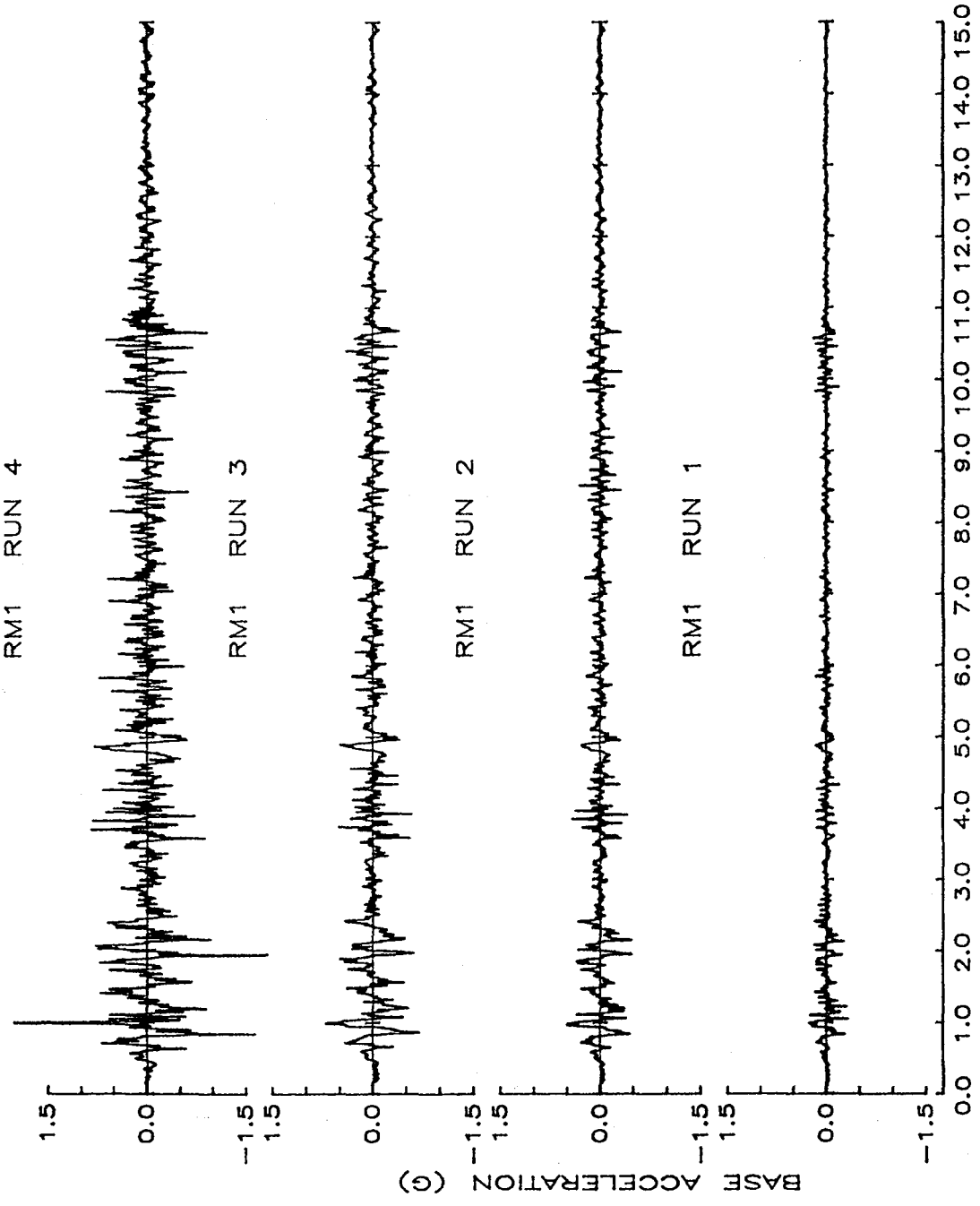

Figure 3.1 Base Acceleration History (RM1)

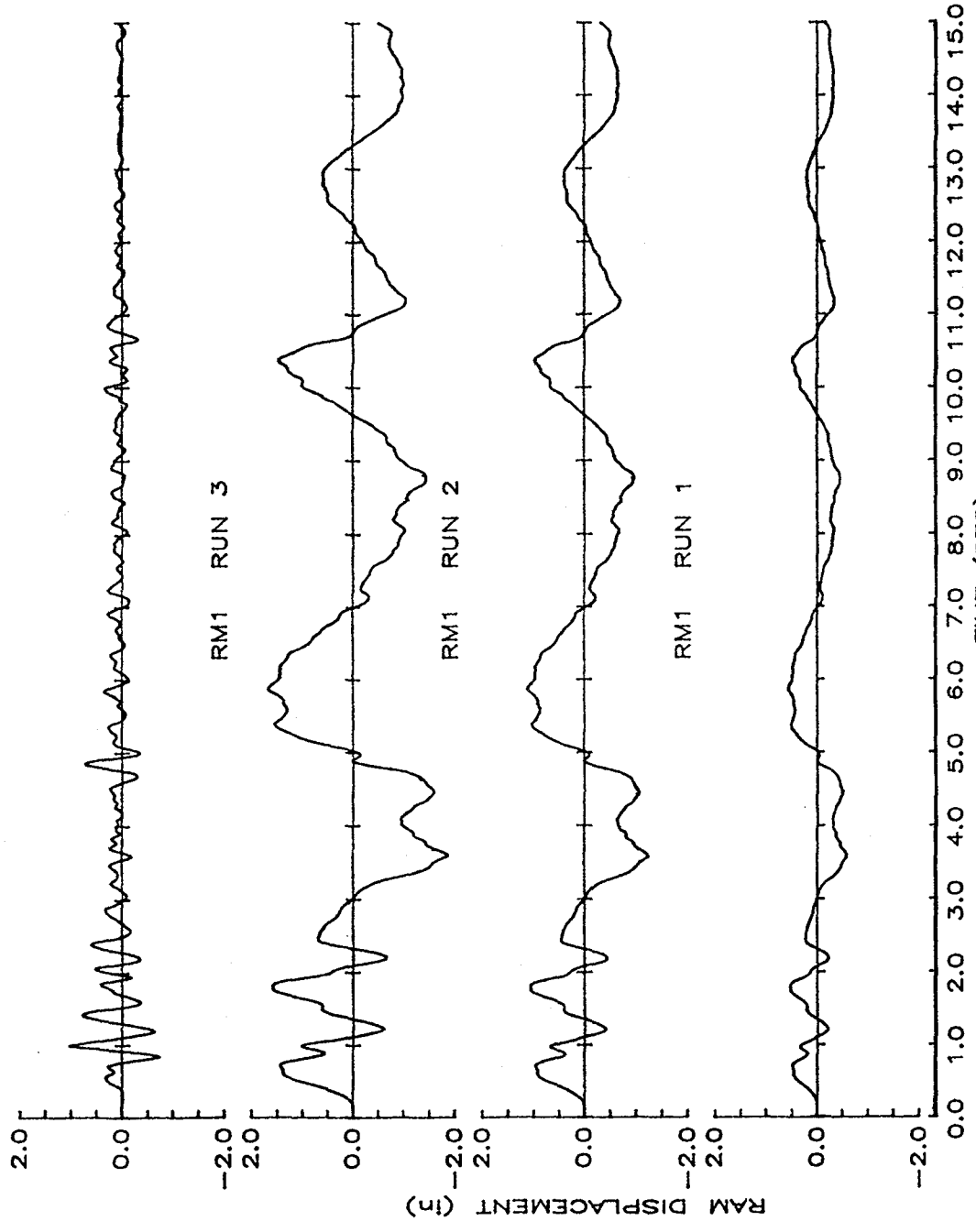

Figure 3.2 Base Displacement History (RM1)

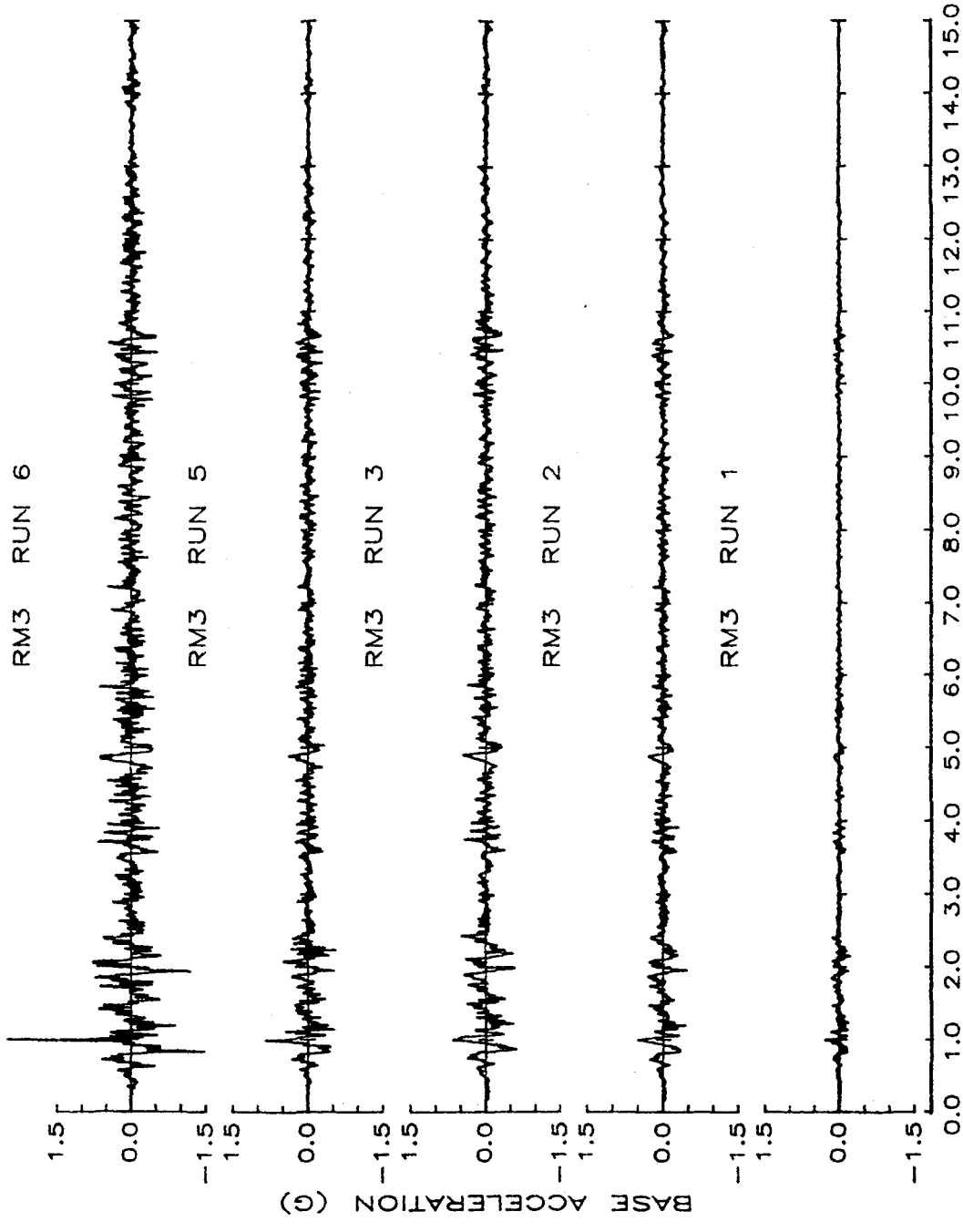

Figure 3.3 Base Acceleration History (RM3)

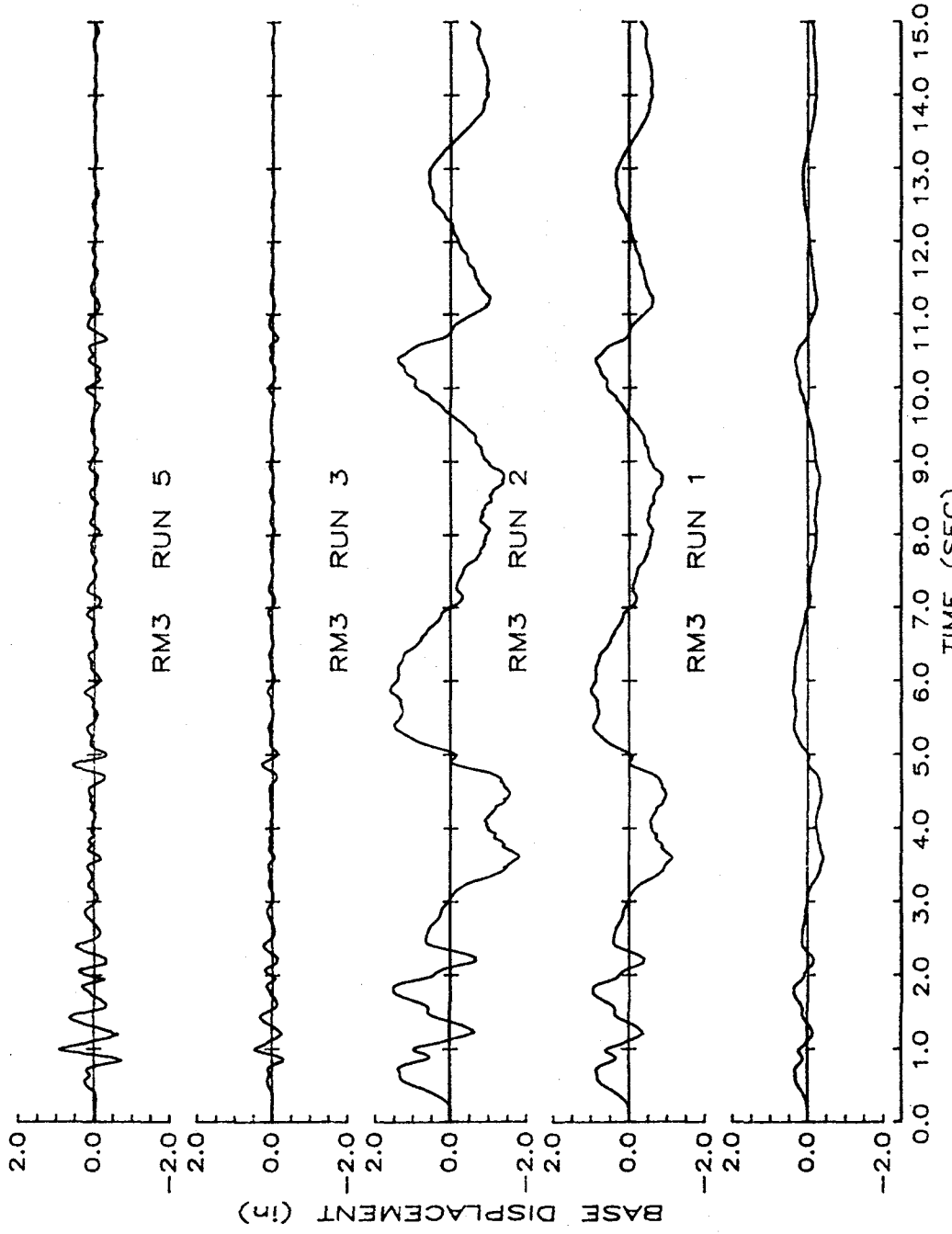

Figure 3.4 Base Displacement History (RM3)

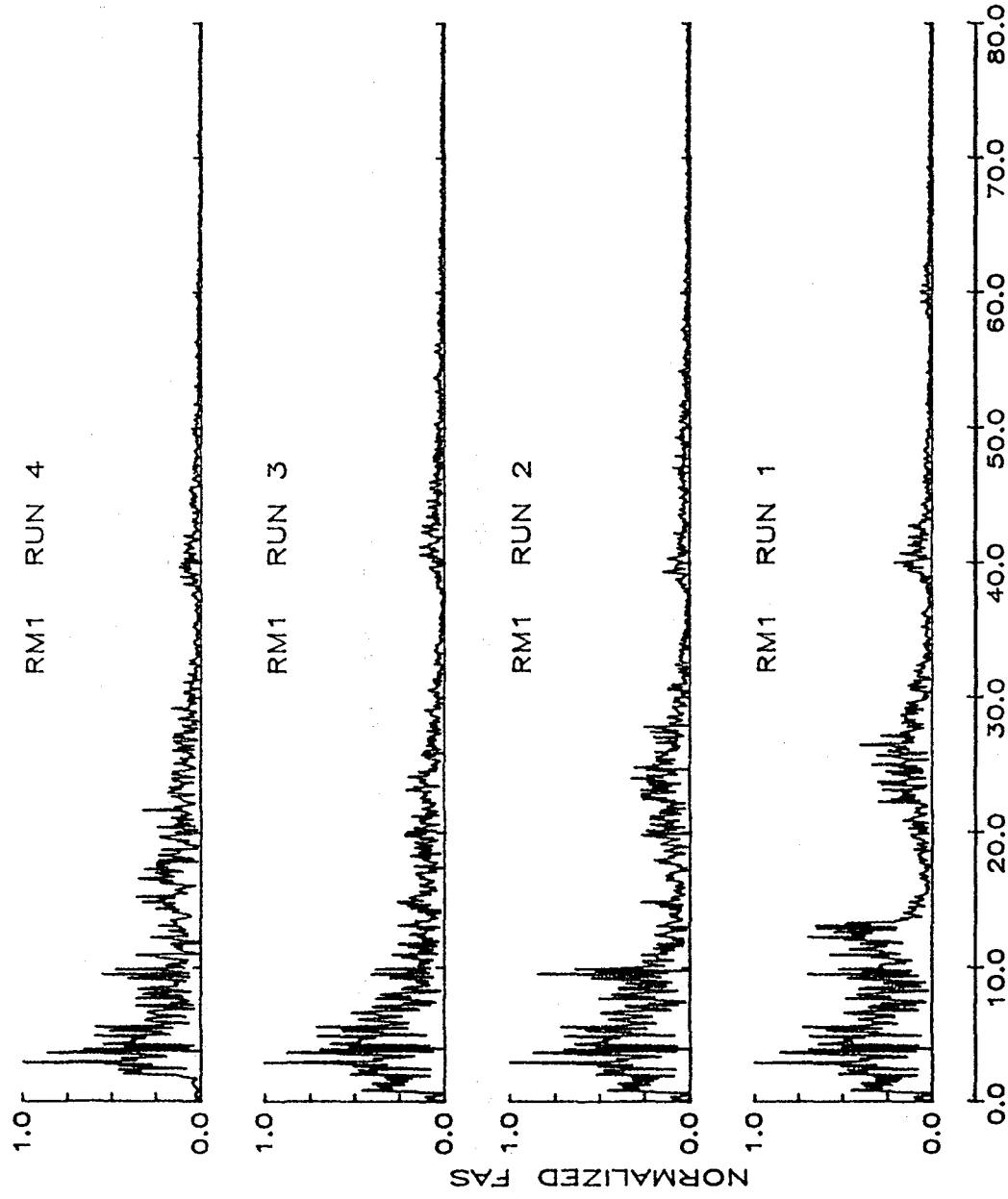

Figure 3.5 Fourier Amplitude Spectra : Base Accelerations (RM1)

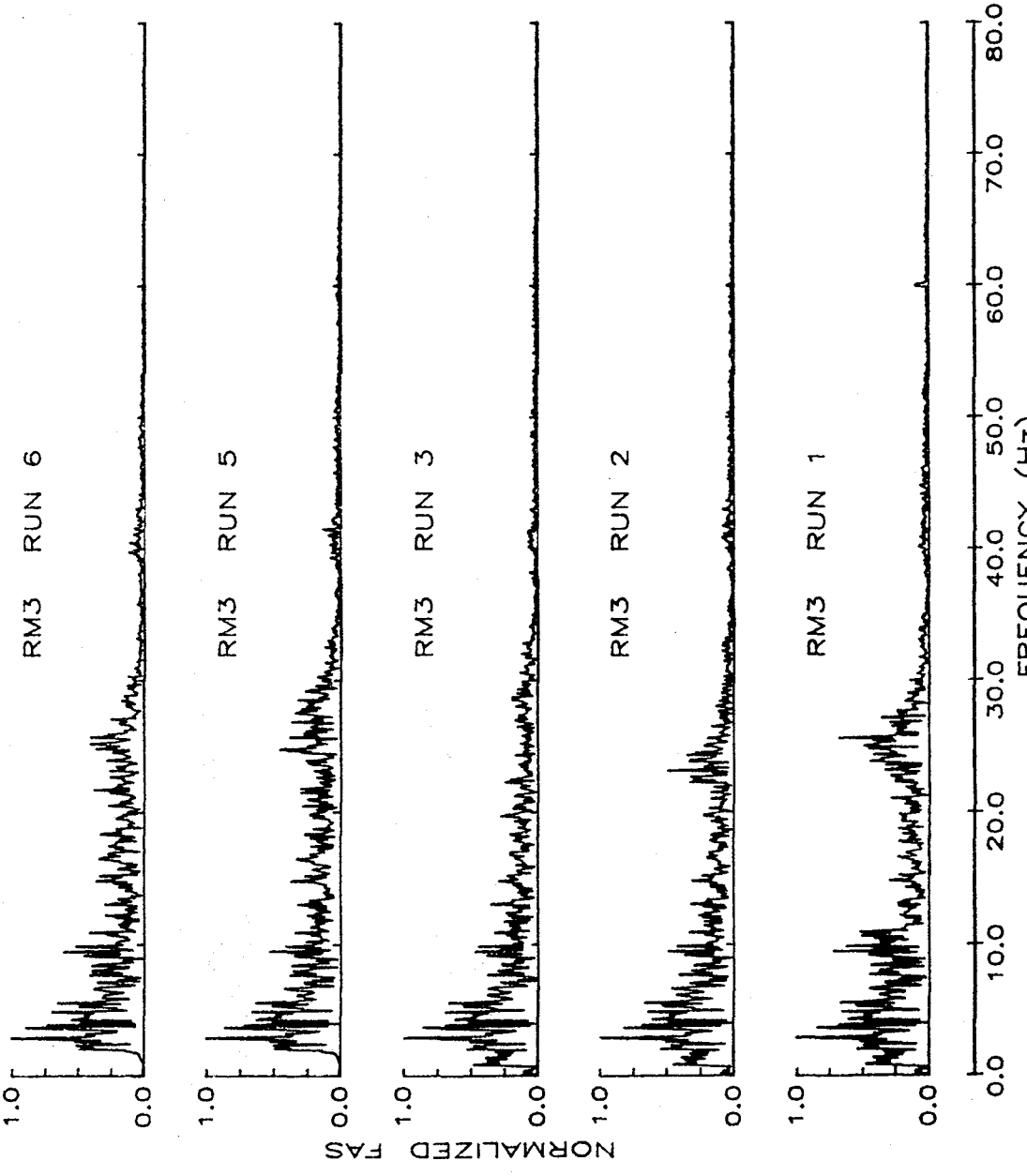

Figure 3.6 Fourier Amplitude Spectra : Base Accelerations (RM3)

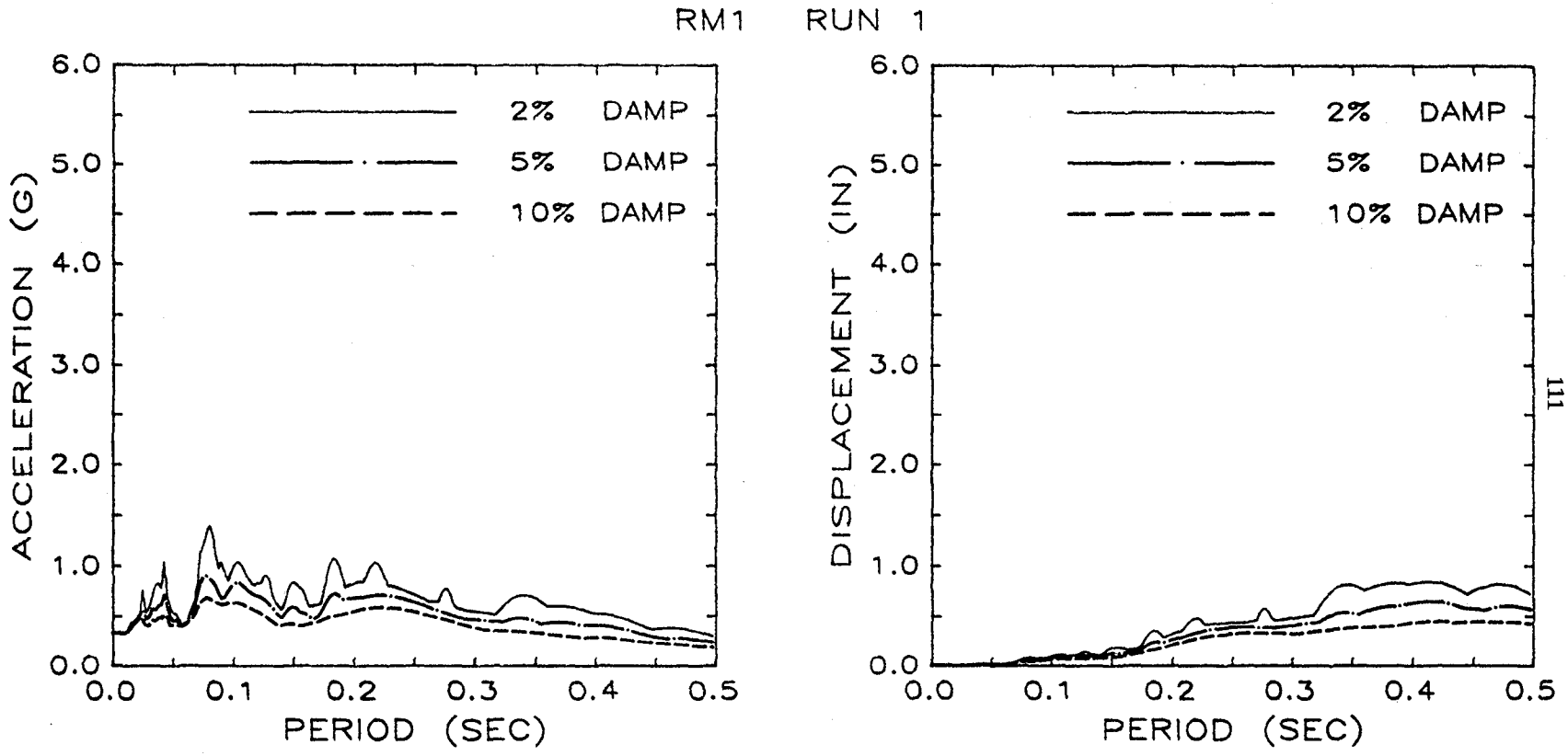

a) Run 1

Figure 3.7 Linear Acceleration and Displacement Response Spectra (RM1)

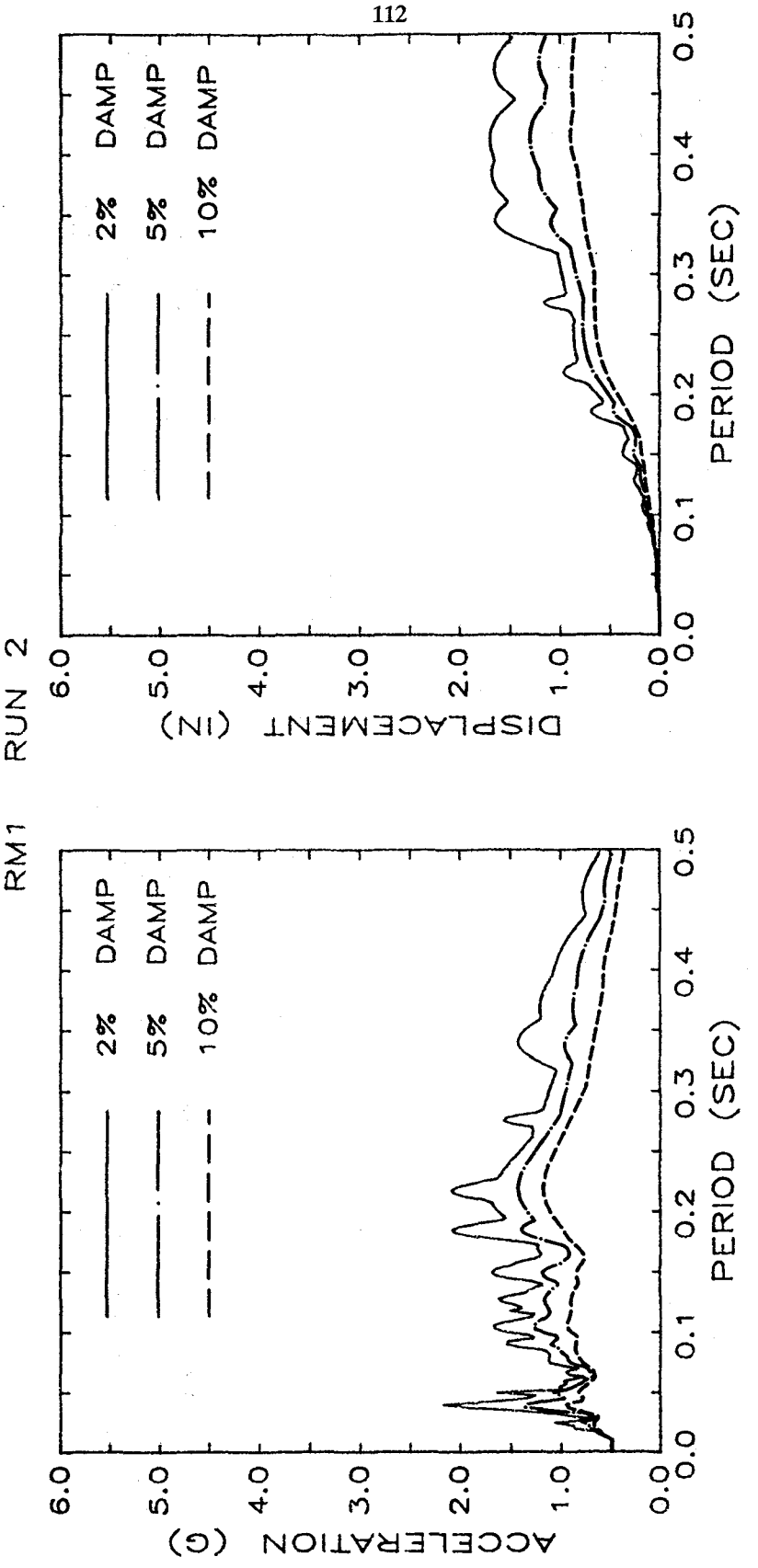

b) Run 2

Figure 3.7 Linear Acceleration and Displacement Response Spectra (RM1)

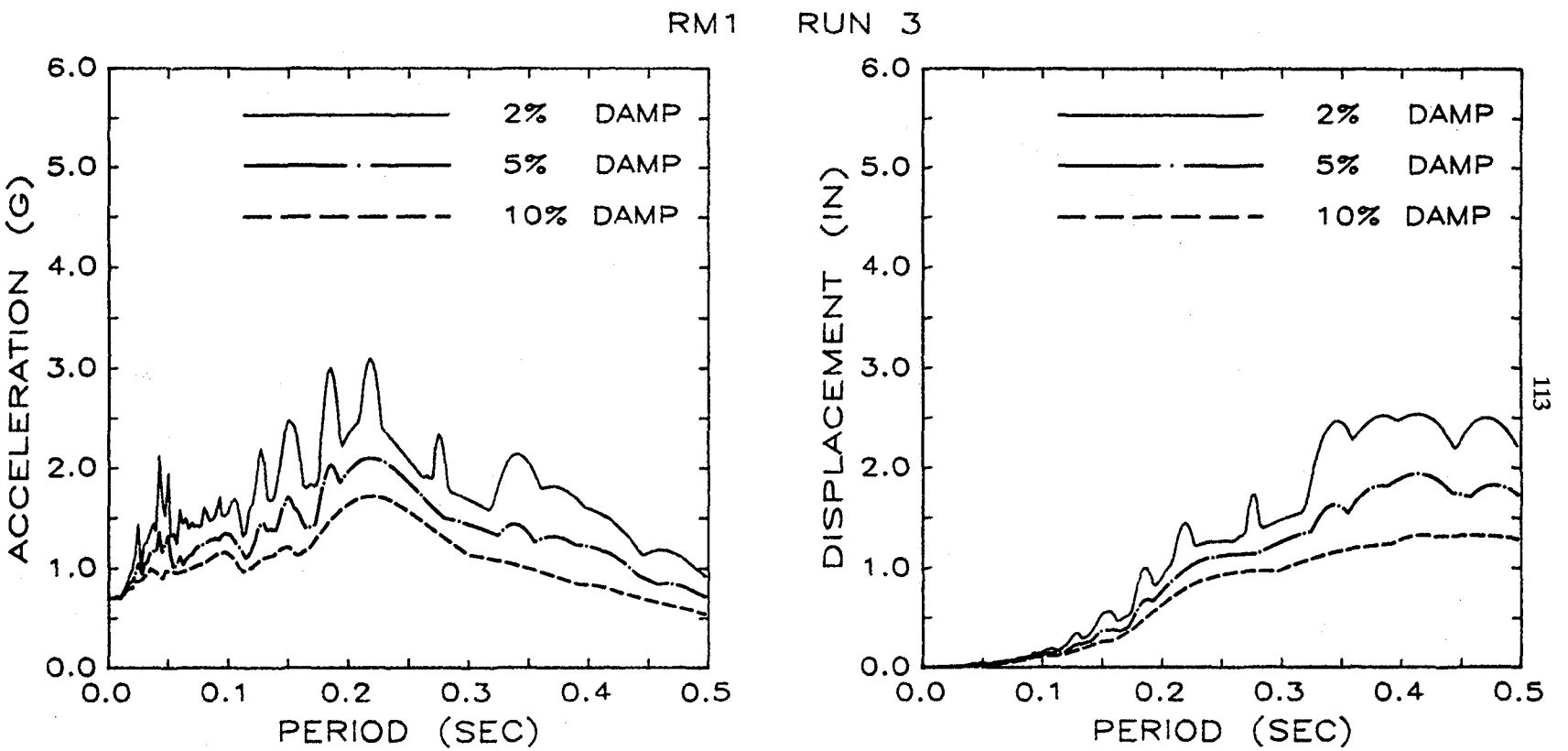

c) Run 3

Figure 3.7 Linear Acceleration and Displacement Response Spectra (RM1)

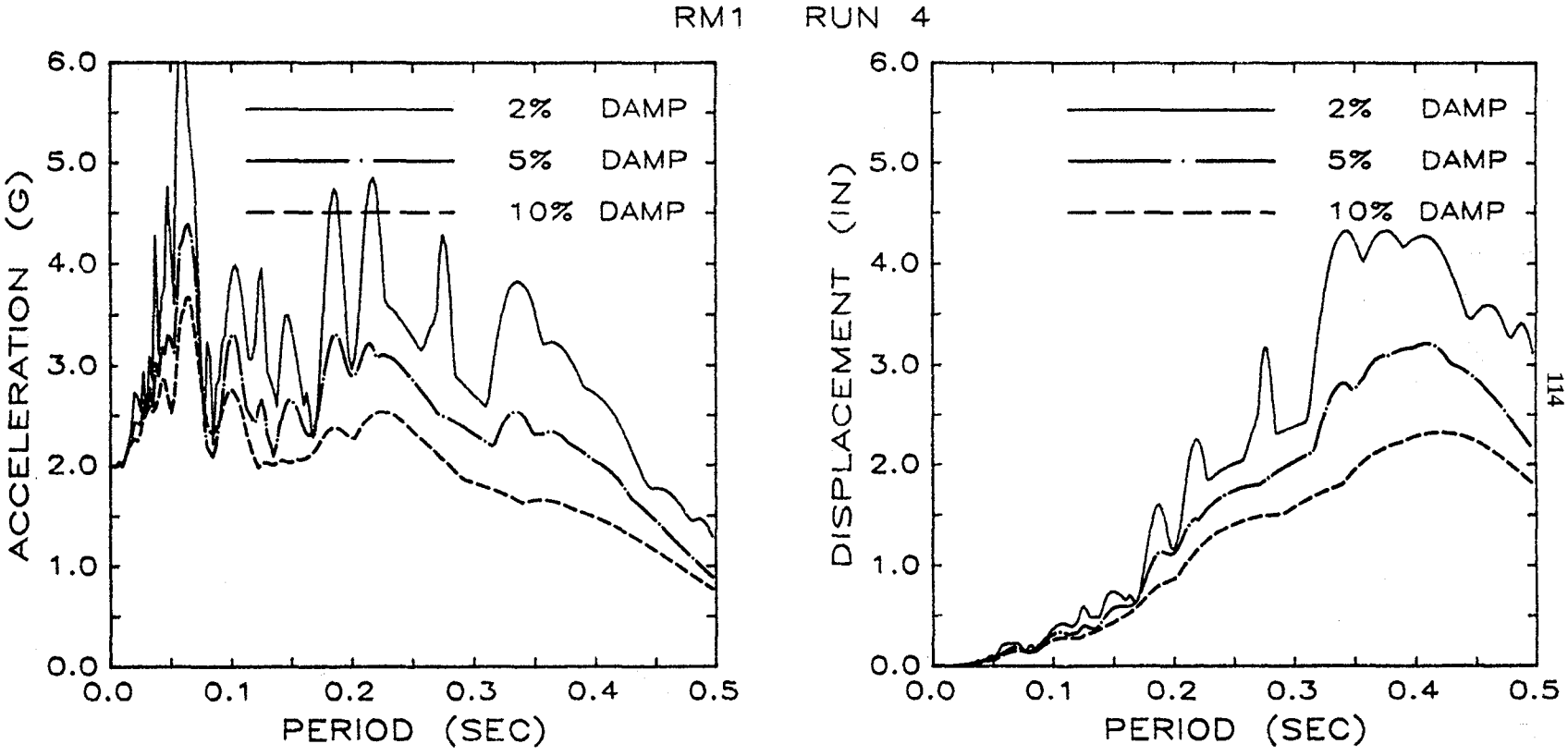

d) Run 4

Figure 3.7 Linear Acceleration and Displacement Response Spectra (RM1)

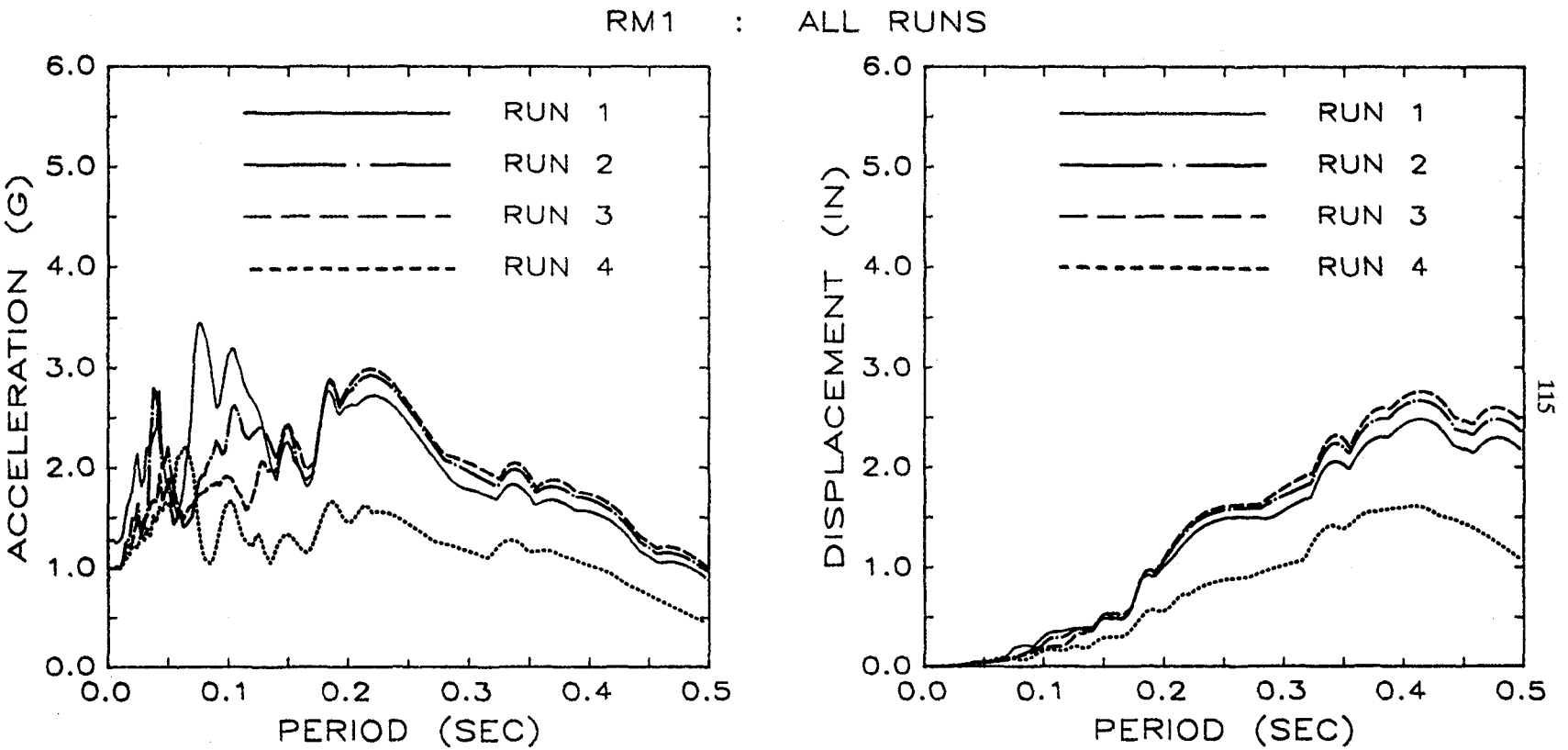

Figure 3.8 Normalized Linear Response Spectra (RM1 Runs 1-4)

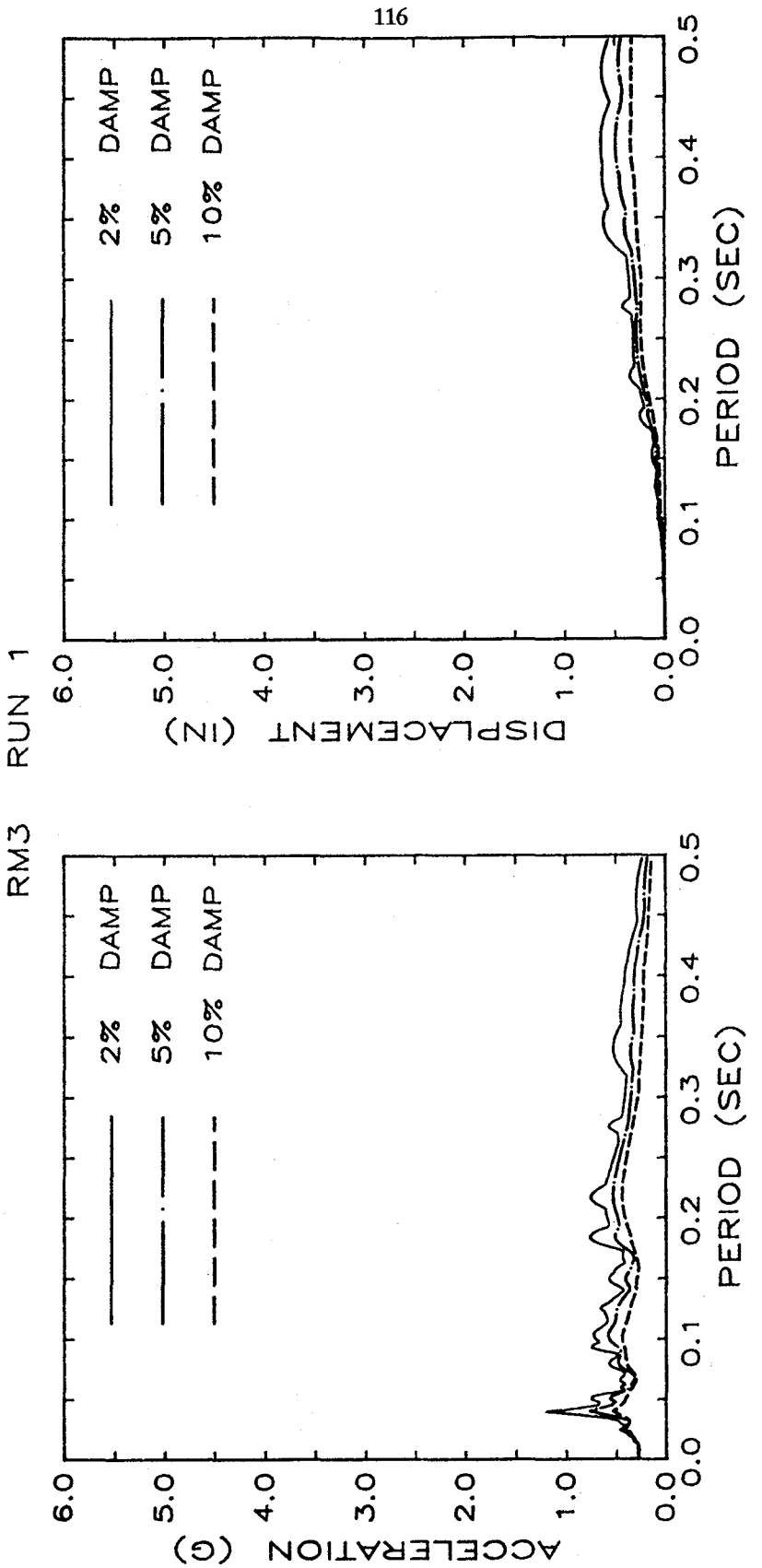

a) Run 1

Figure 3.9 Linear Acceleration and Displacement Response Spectra (RM3)

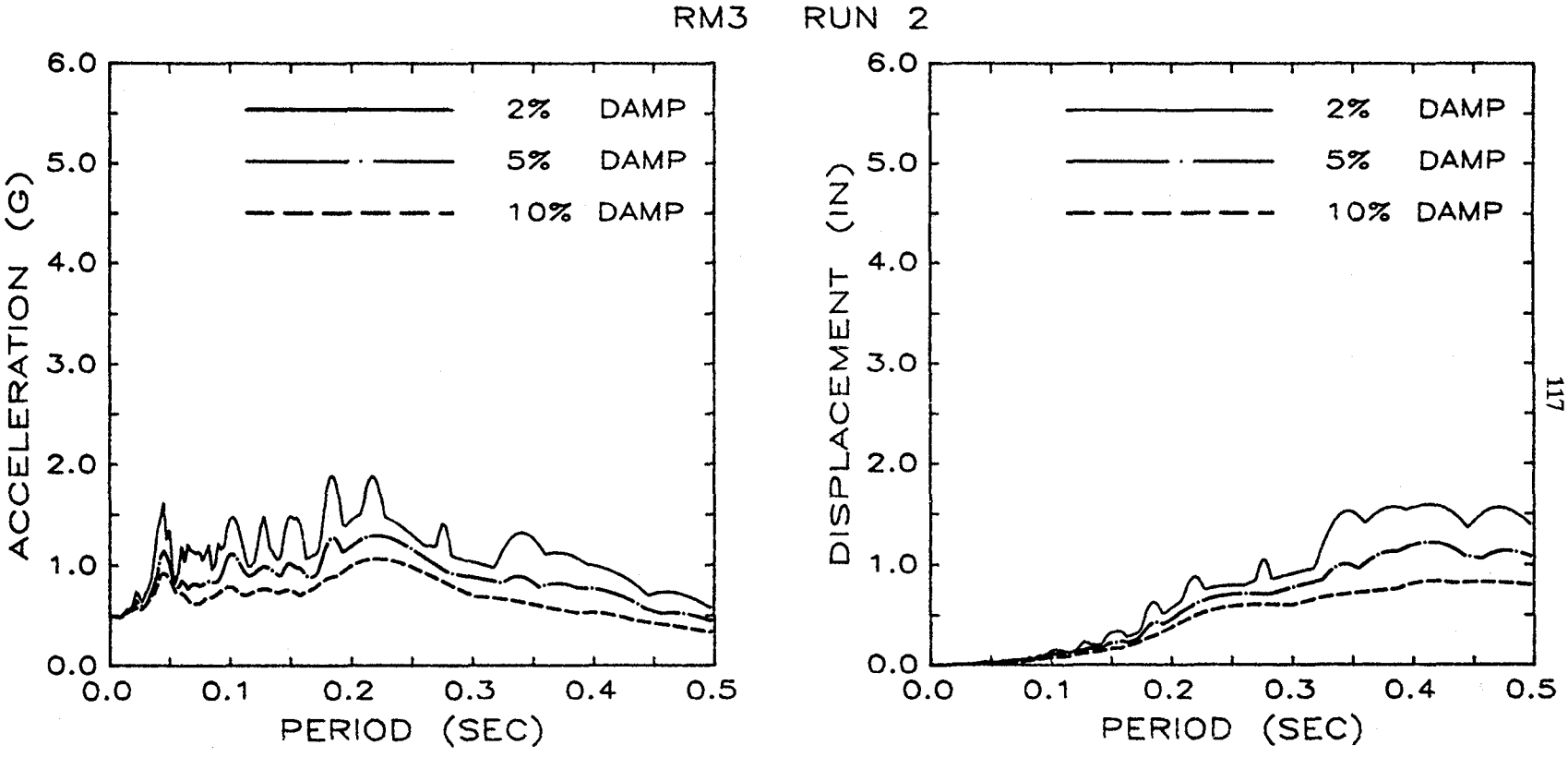

b) Run 2

Figure 3.9 Linear Acceleration and Displacement Response Spectra (RM3)

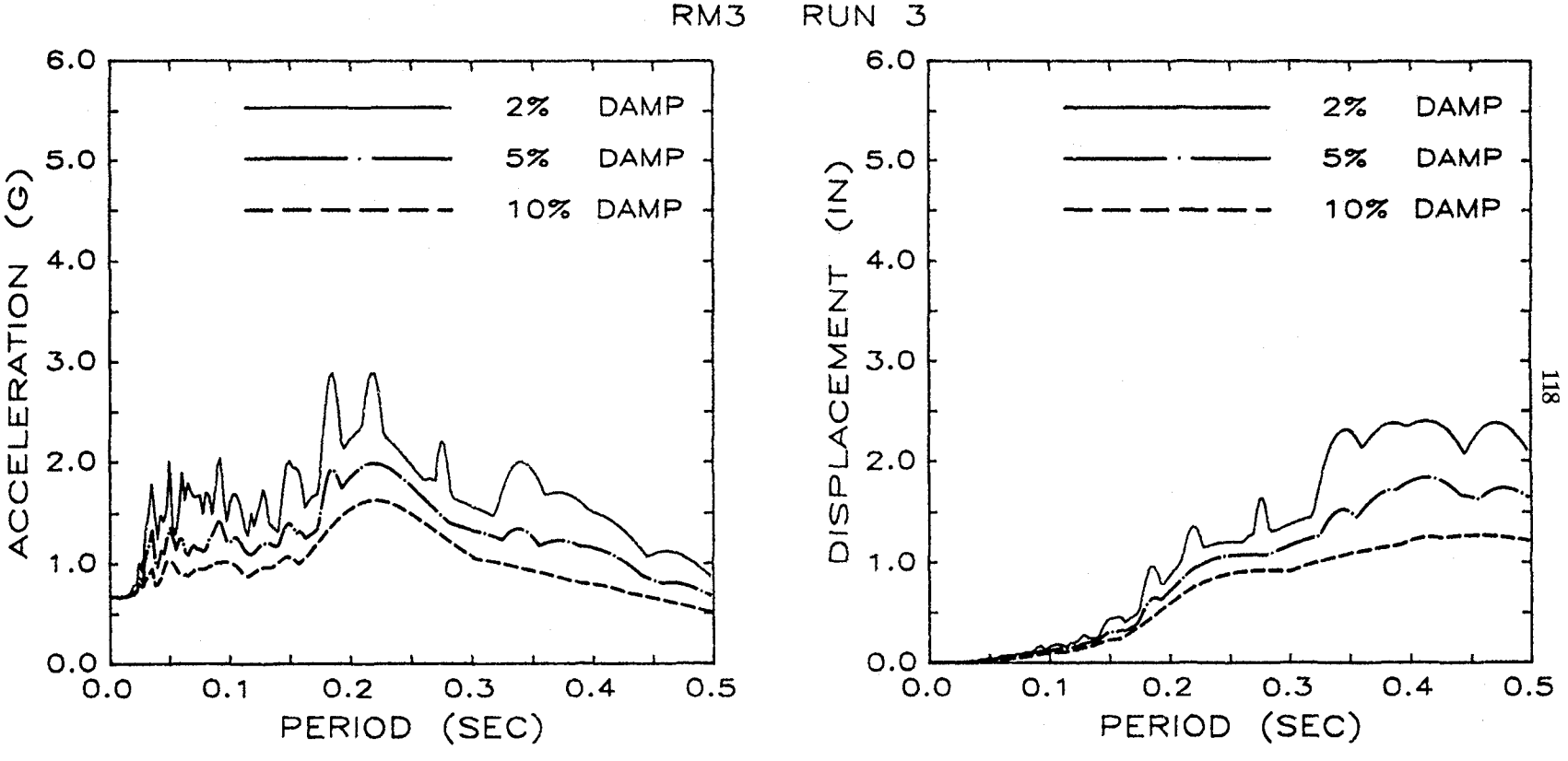

c) Run 3

Figure 3.9 Linear Acceleration and Displacement Response Spectra (RM3)

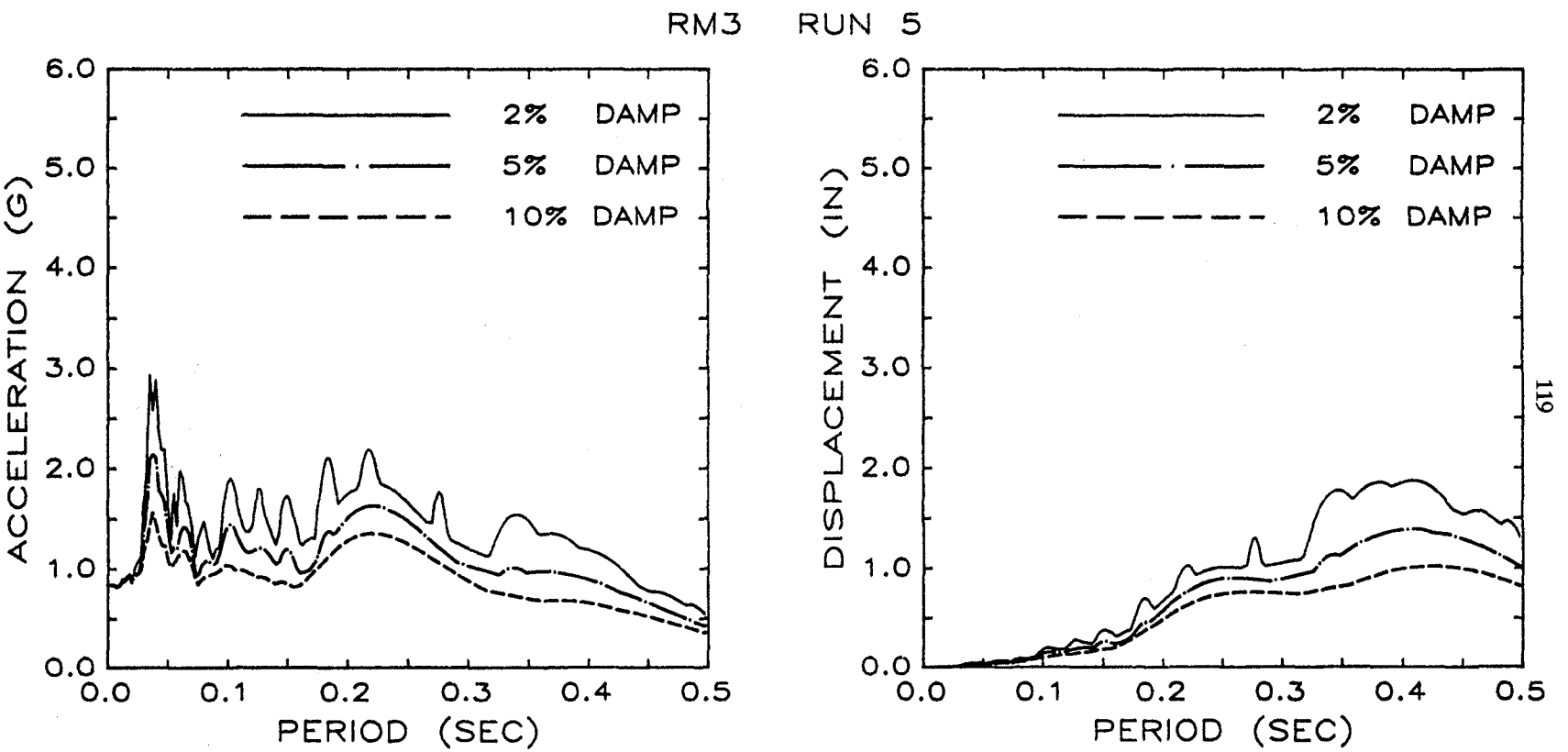

d) Run 5

Figure 3.9 Linear Acceleration and Displacement Response Spectra (RM3)

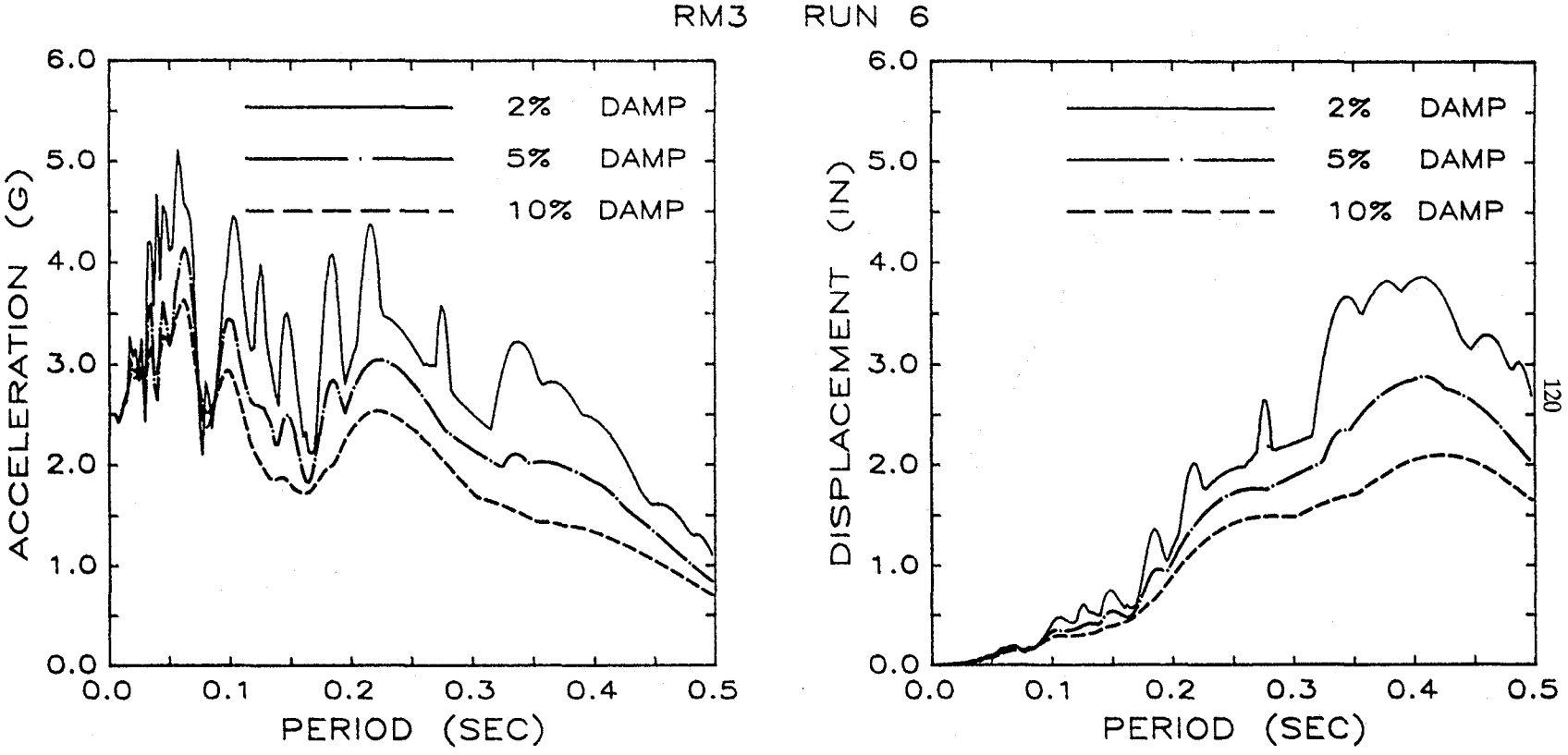

e) Run 6

Figure 3.9 Linear Acceleration and Displacement Response Spectra (RM3)

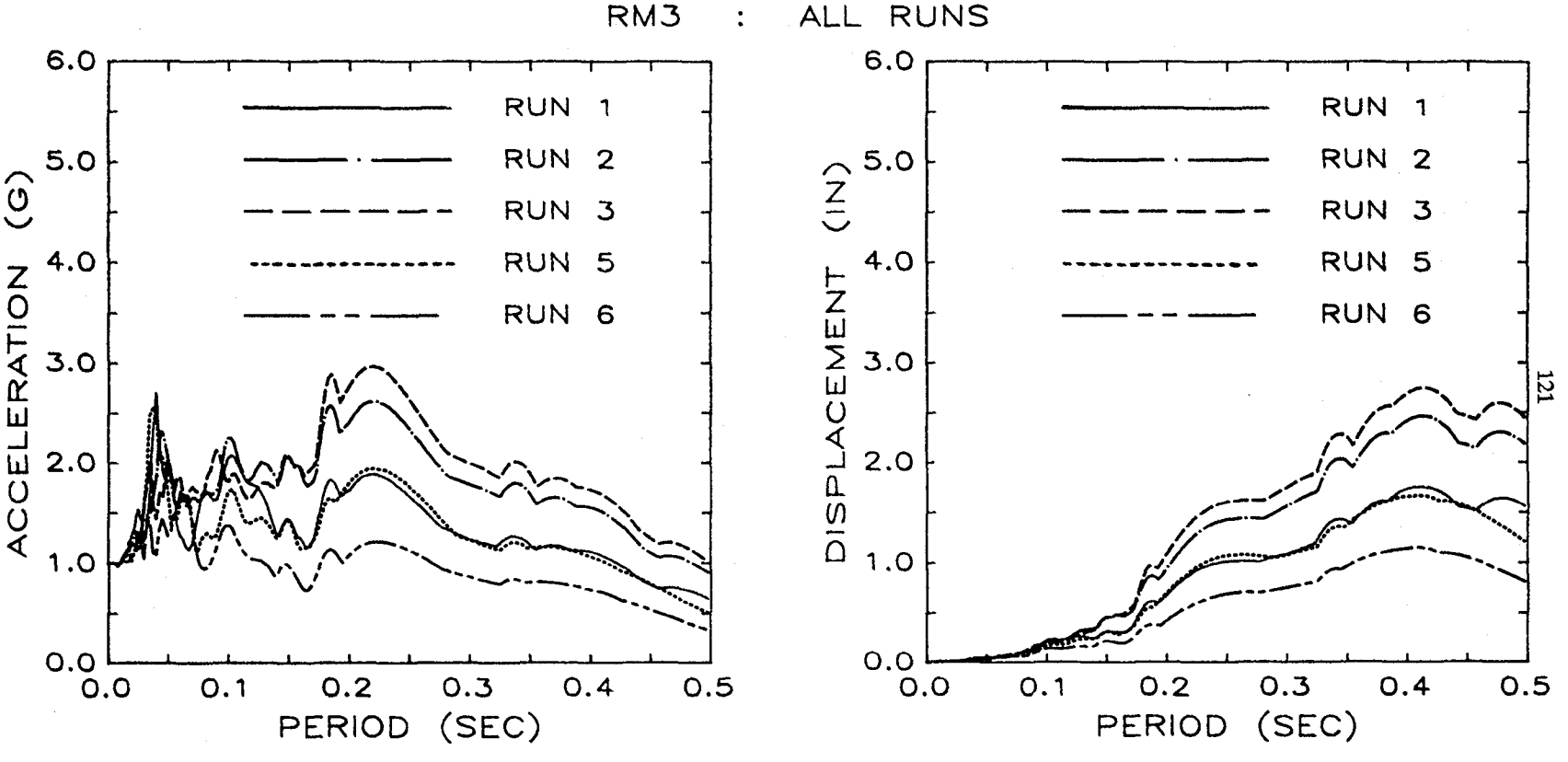

Figure 3.10 Normalized Linear Response Spectra (RM3 Runs 1-6)

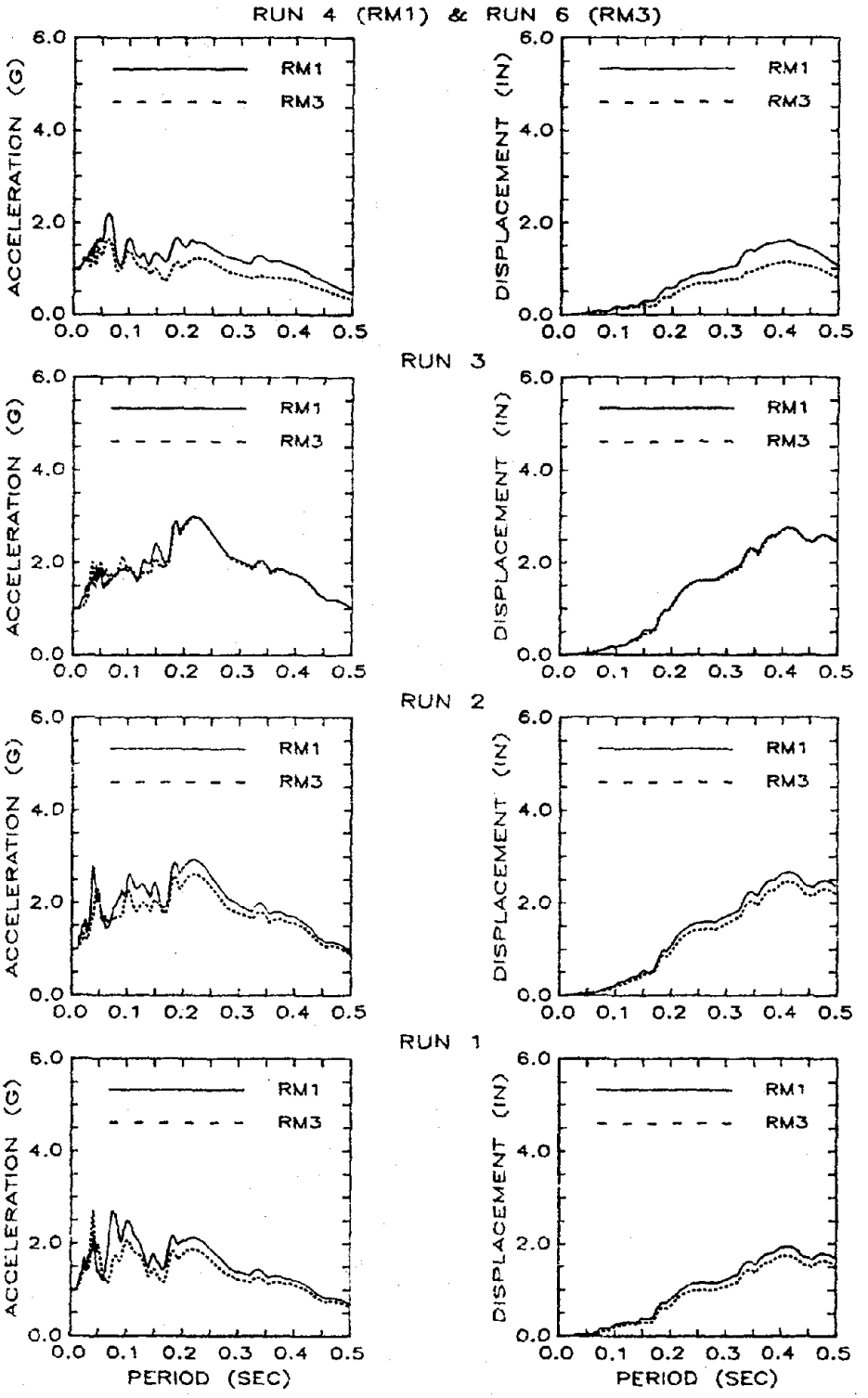

Figure 3.11 Linear Accel. and Displ. Response Spectra (RM1 & RM3 : All Runs)

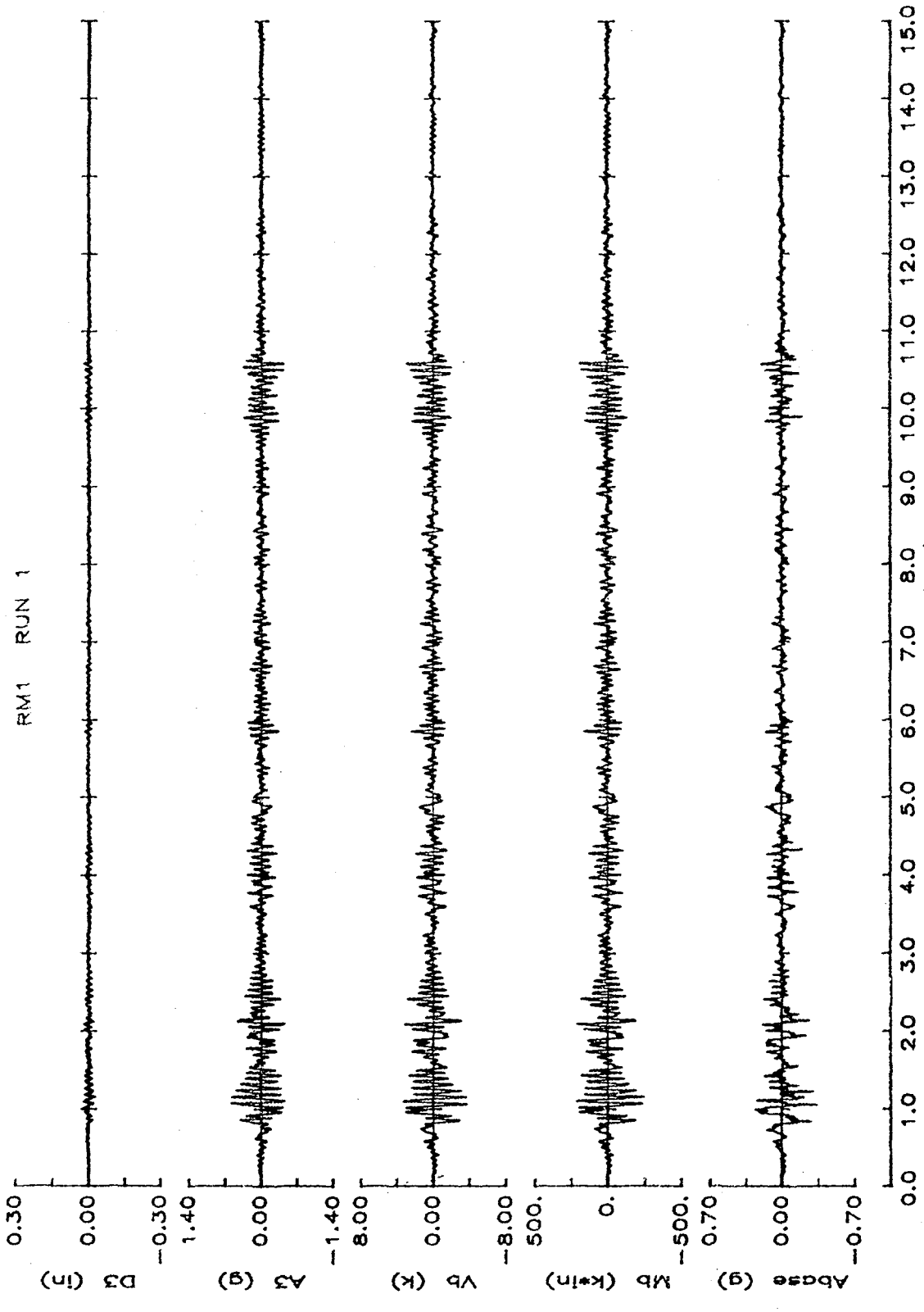

Figure 4.1 Response of Structure RM1 a)Run 1

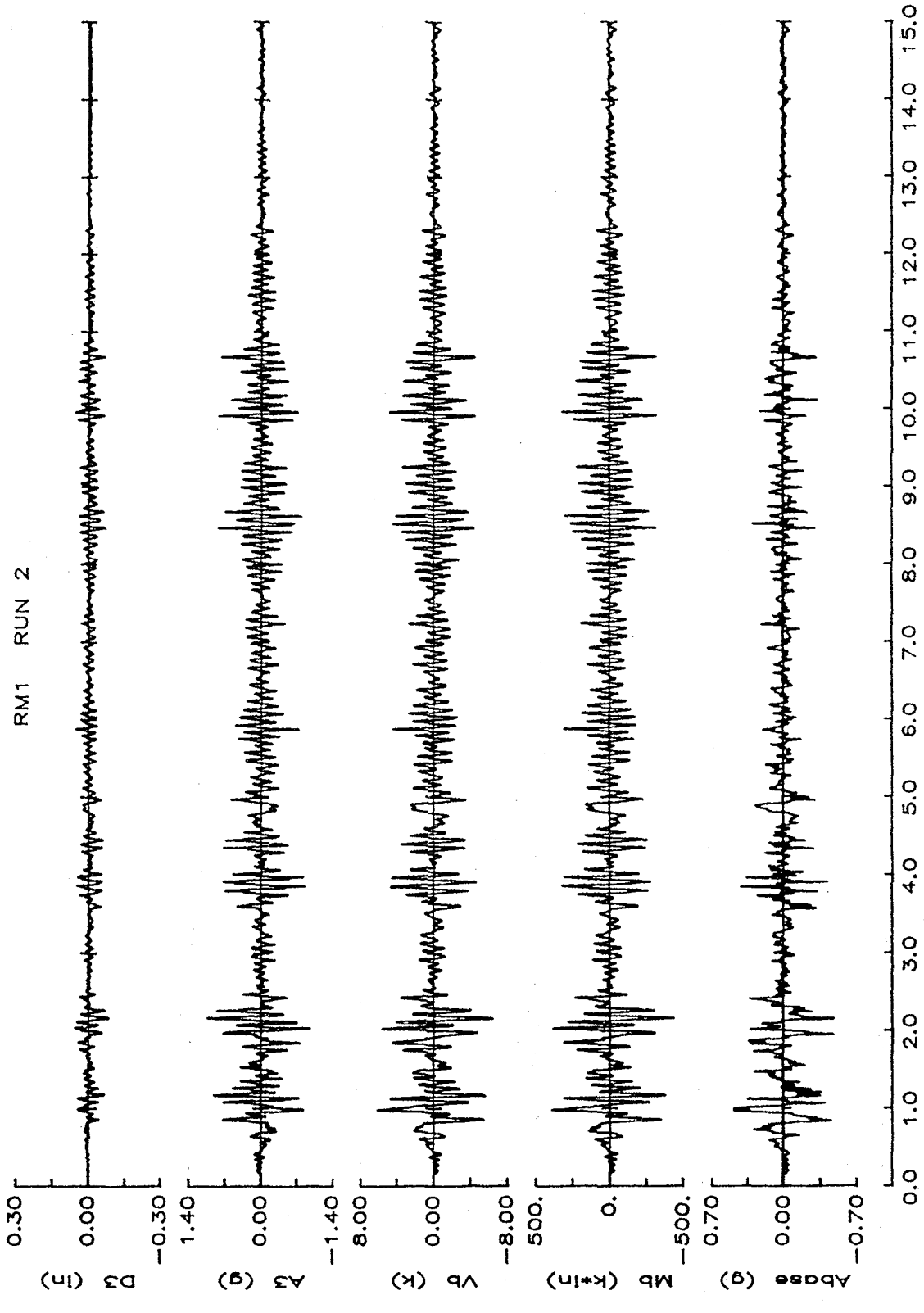

Figure 4.1 (cont) Response of Structure RM1 b) Run 2

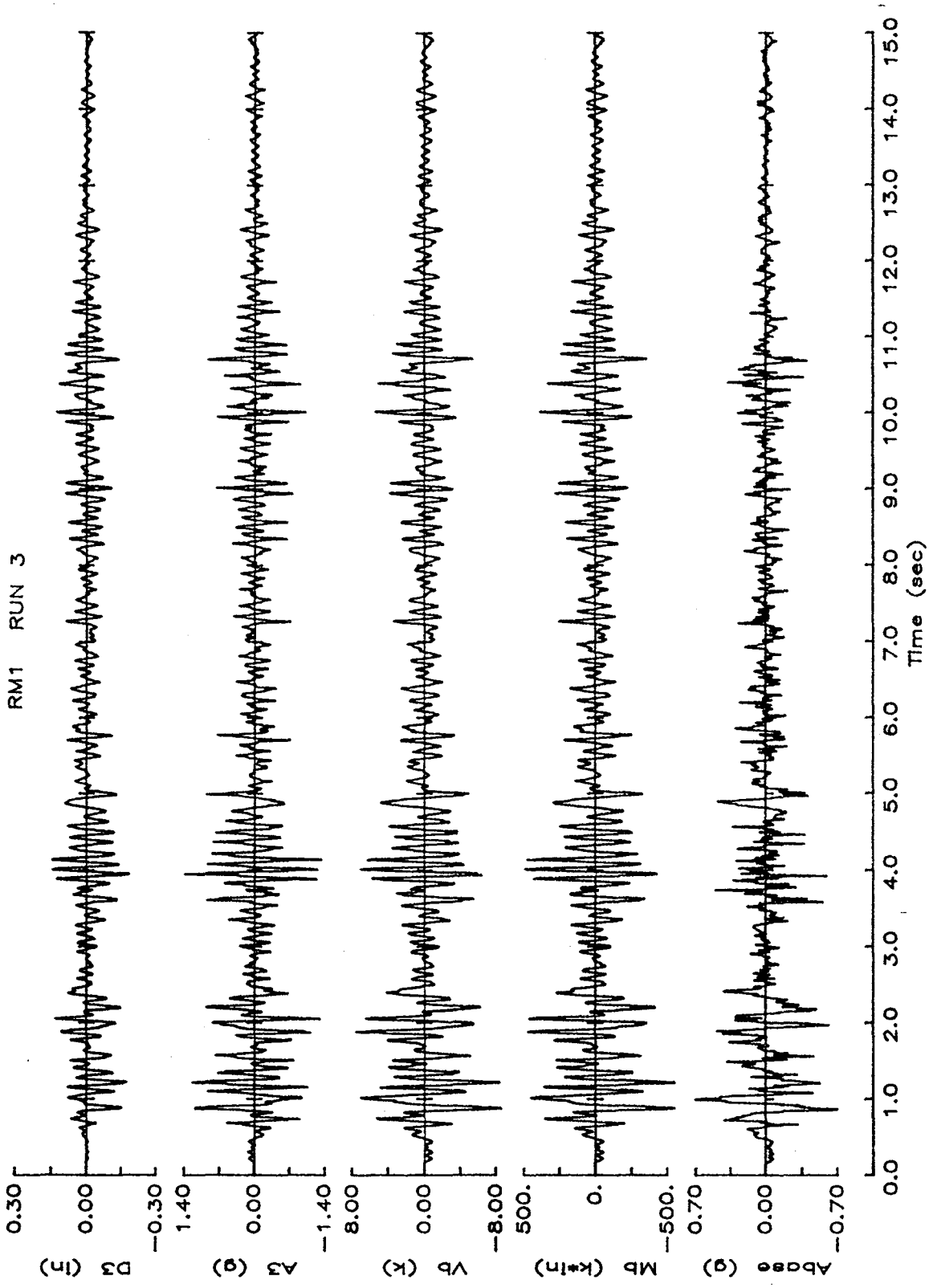

Figure 4.1 (cont) Response of Structure RM1 c) Run 3

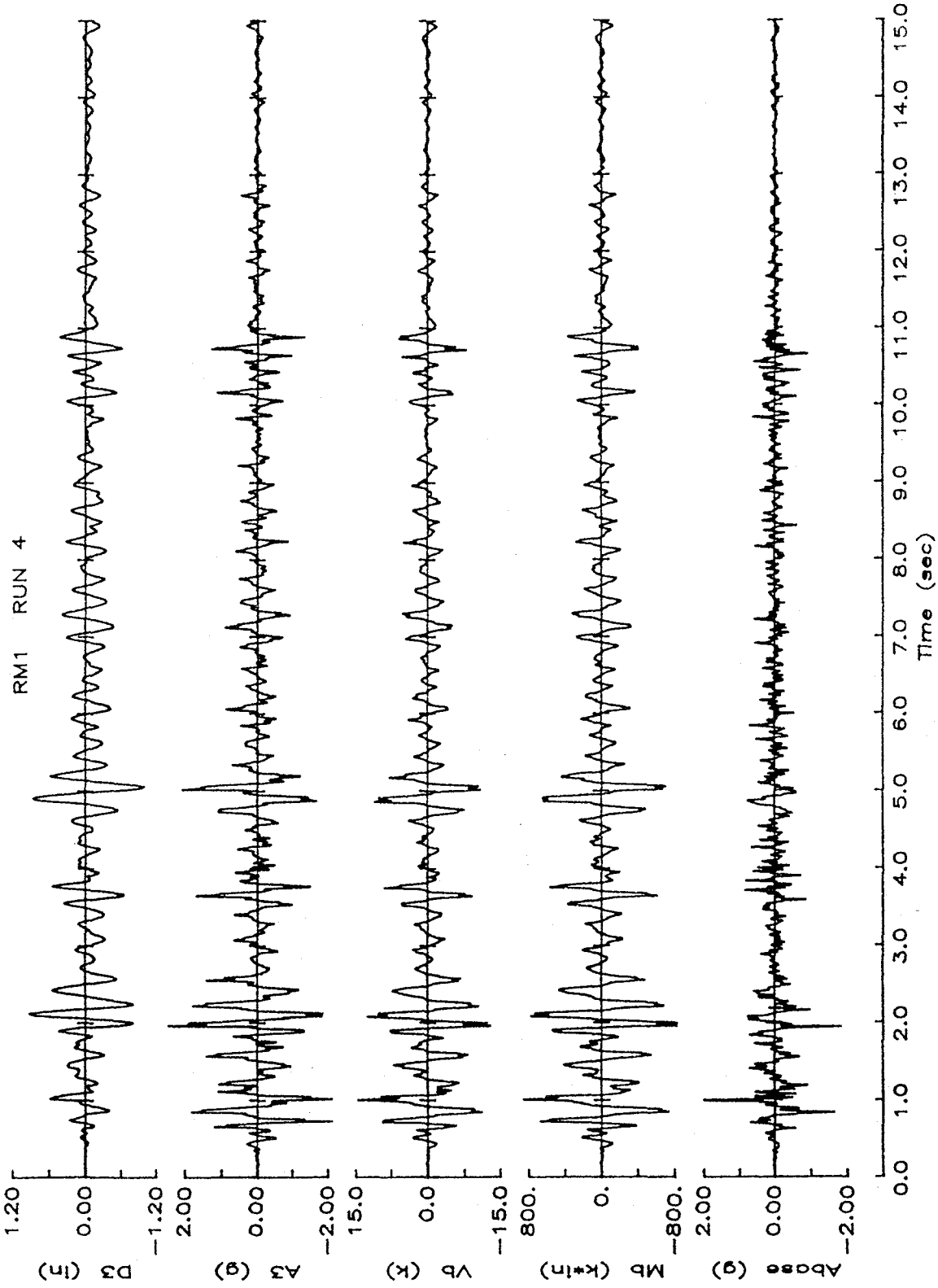

Figure 4.1 (cont) Response of Structure RM1 d) Run 4

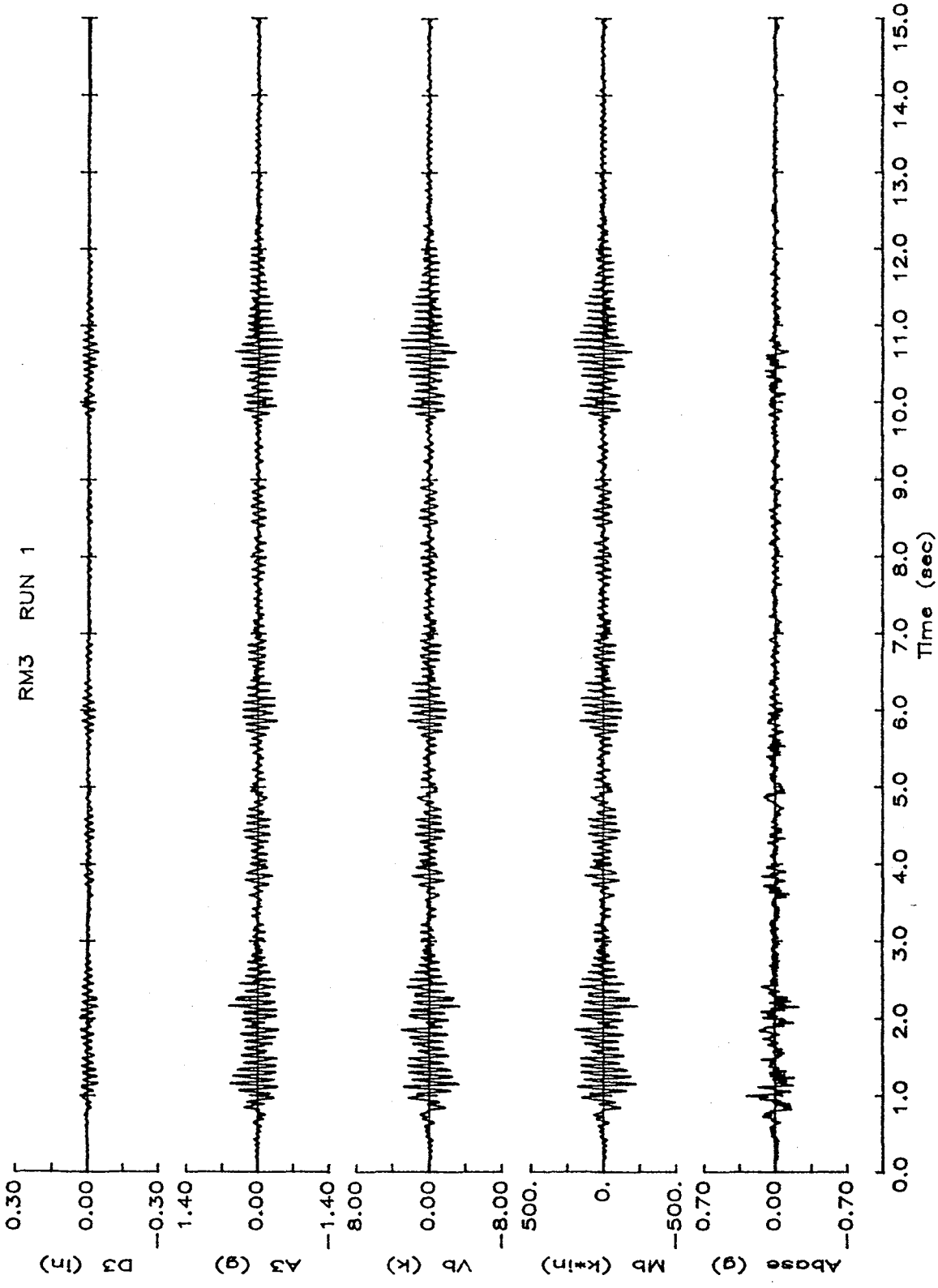

Figure 4.2 Response of Structure RM3 a) Run 1

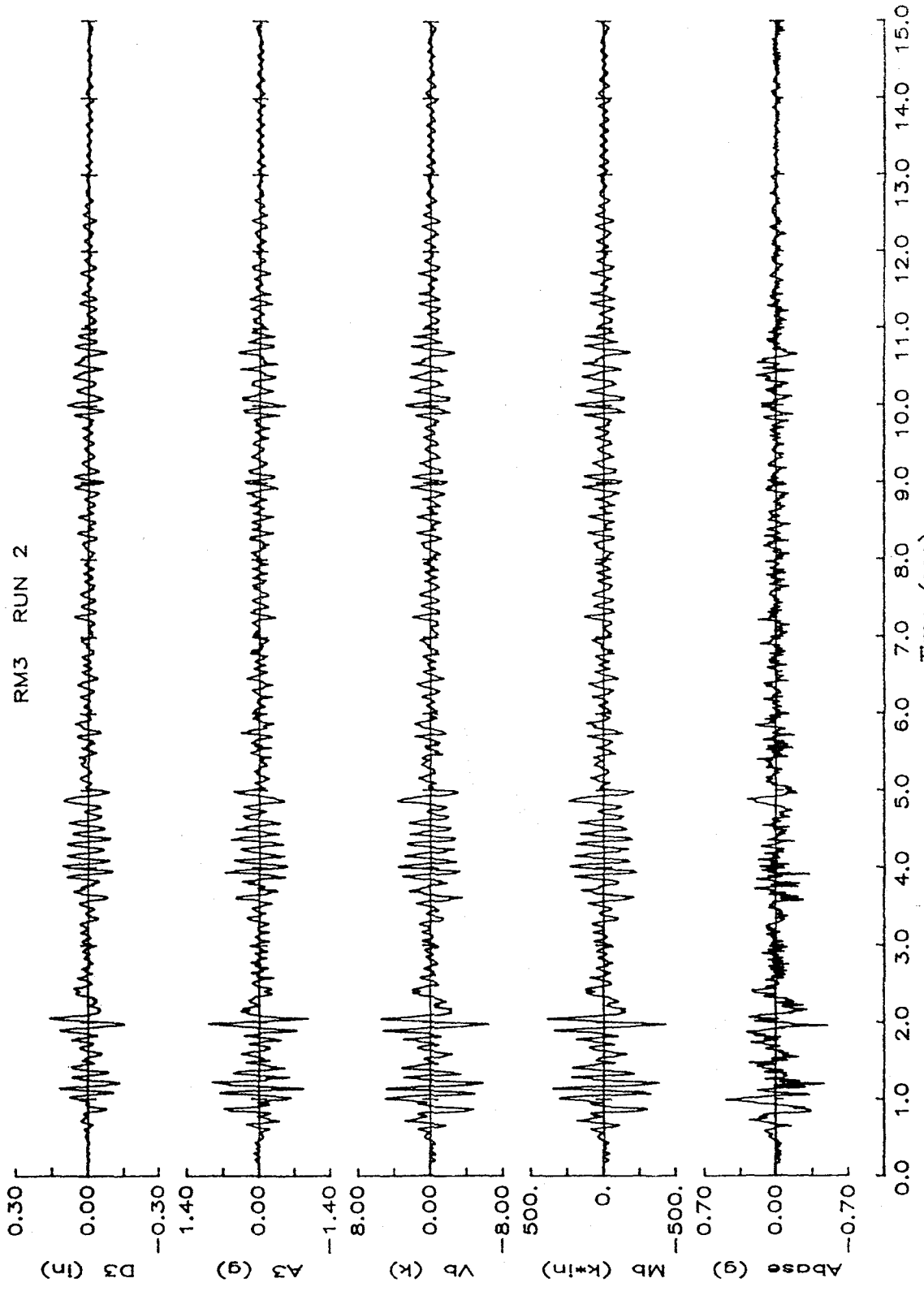

Figure 4.2 (cont) Response of Structure RM3 b) Run 2

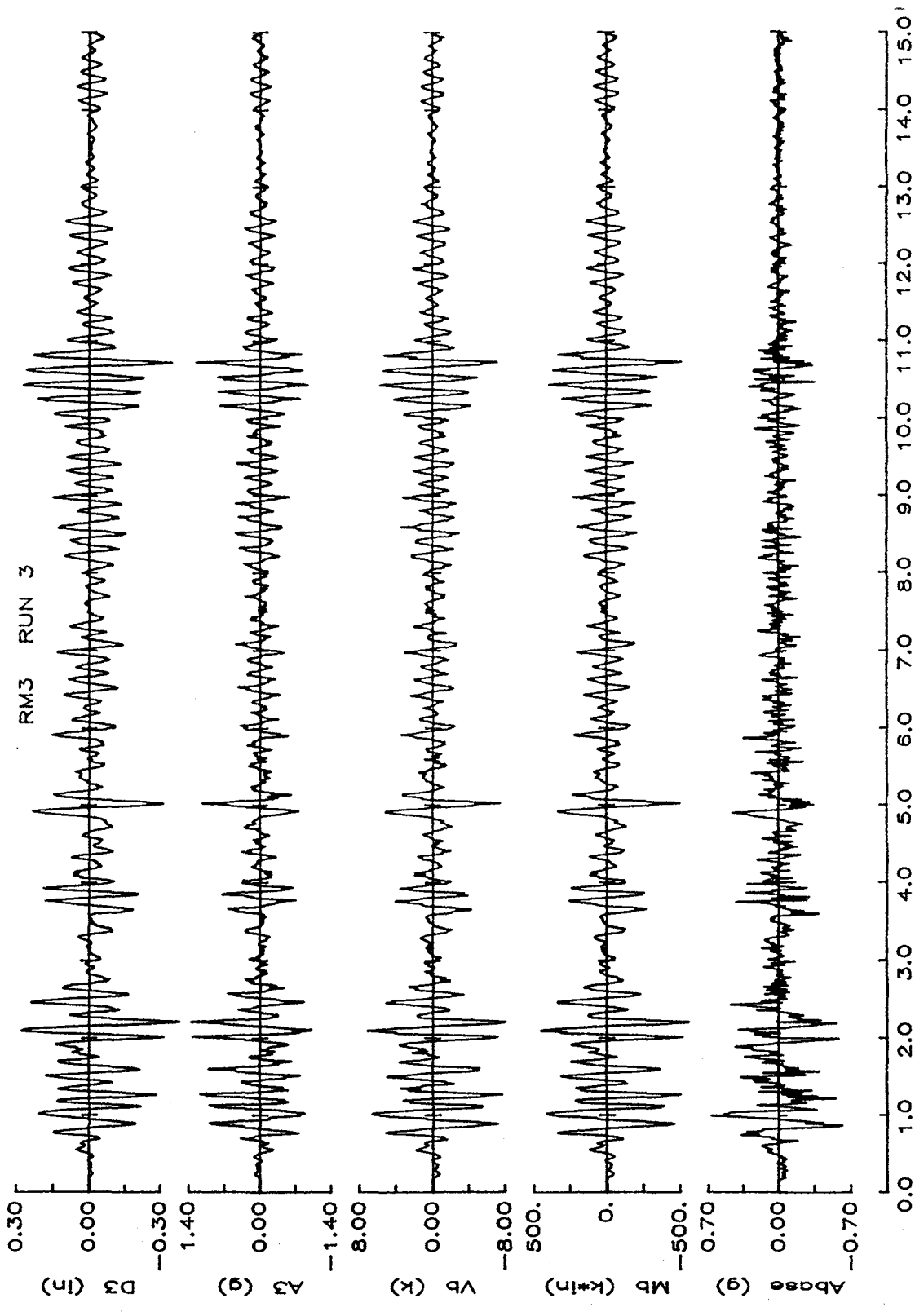

Figure 4.2 (cont) Response of Structure RM3 c) Run 3

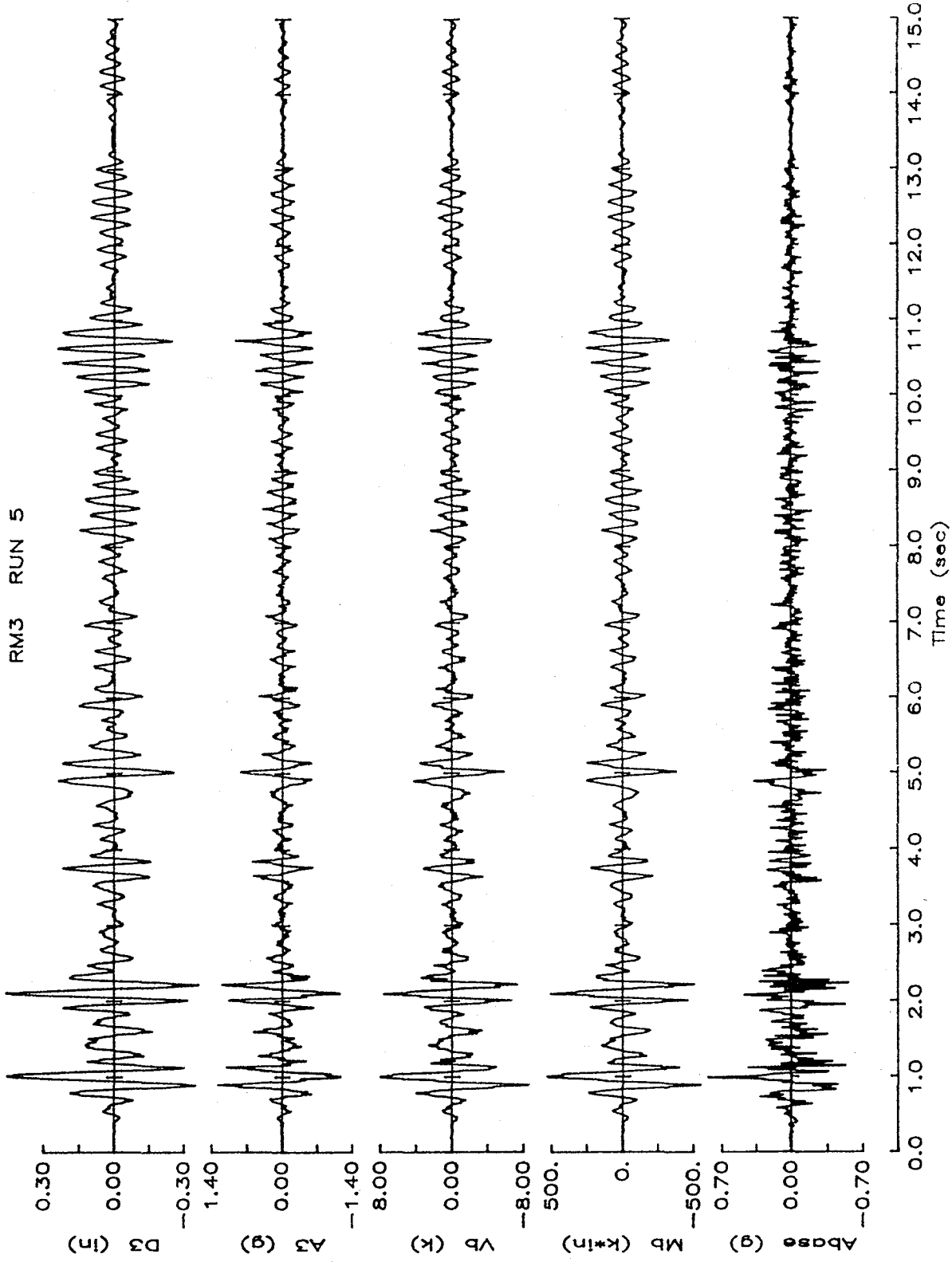

Figure 4.2 (cont) Response of Structure RM3 d) Run 5

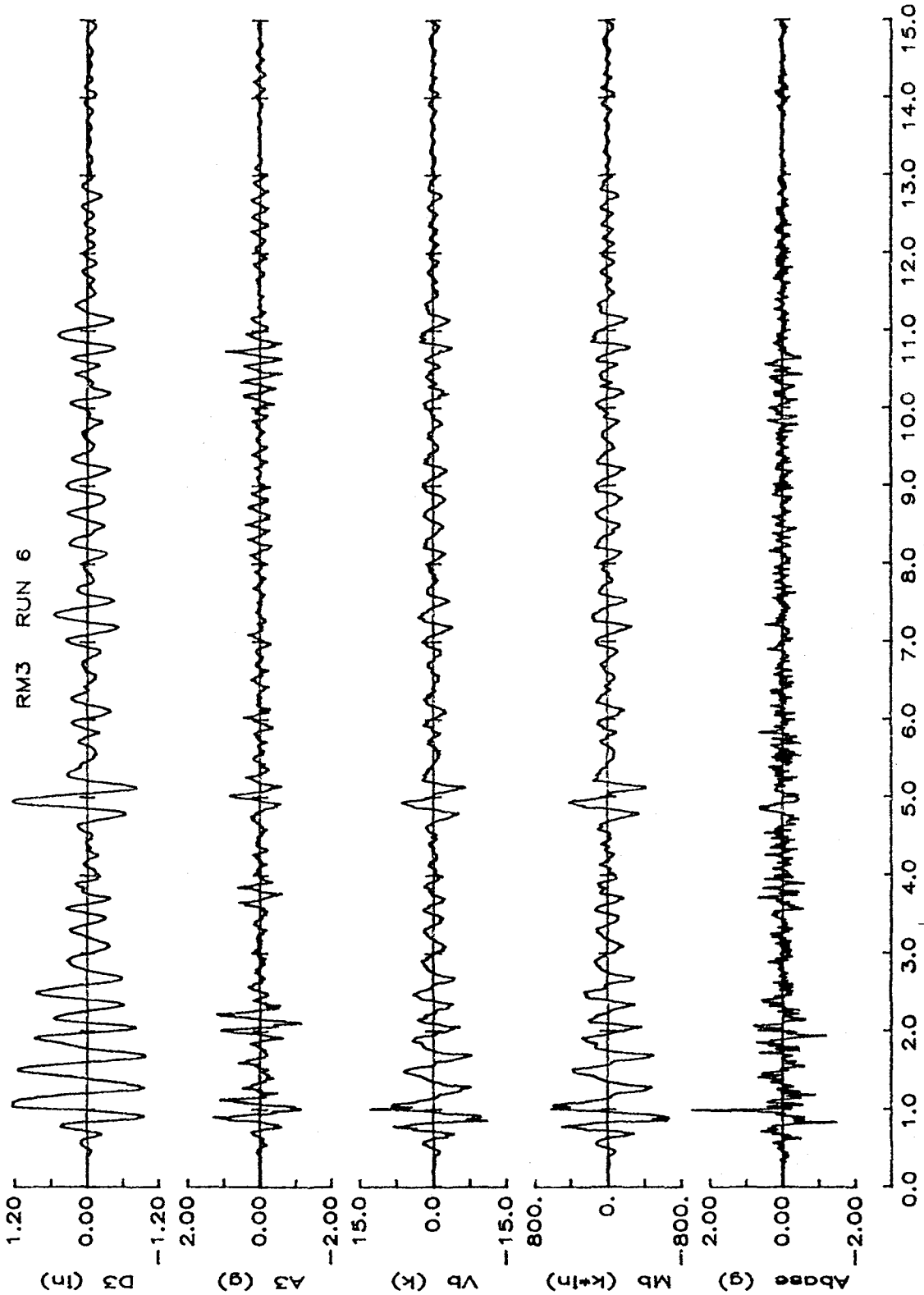

Figure 4.2 (cont) Response of Structure RM3 e) Run 6

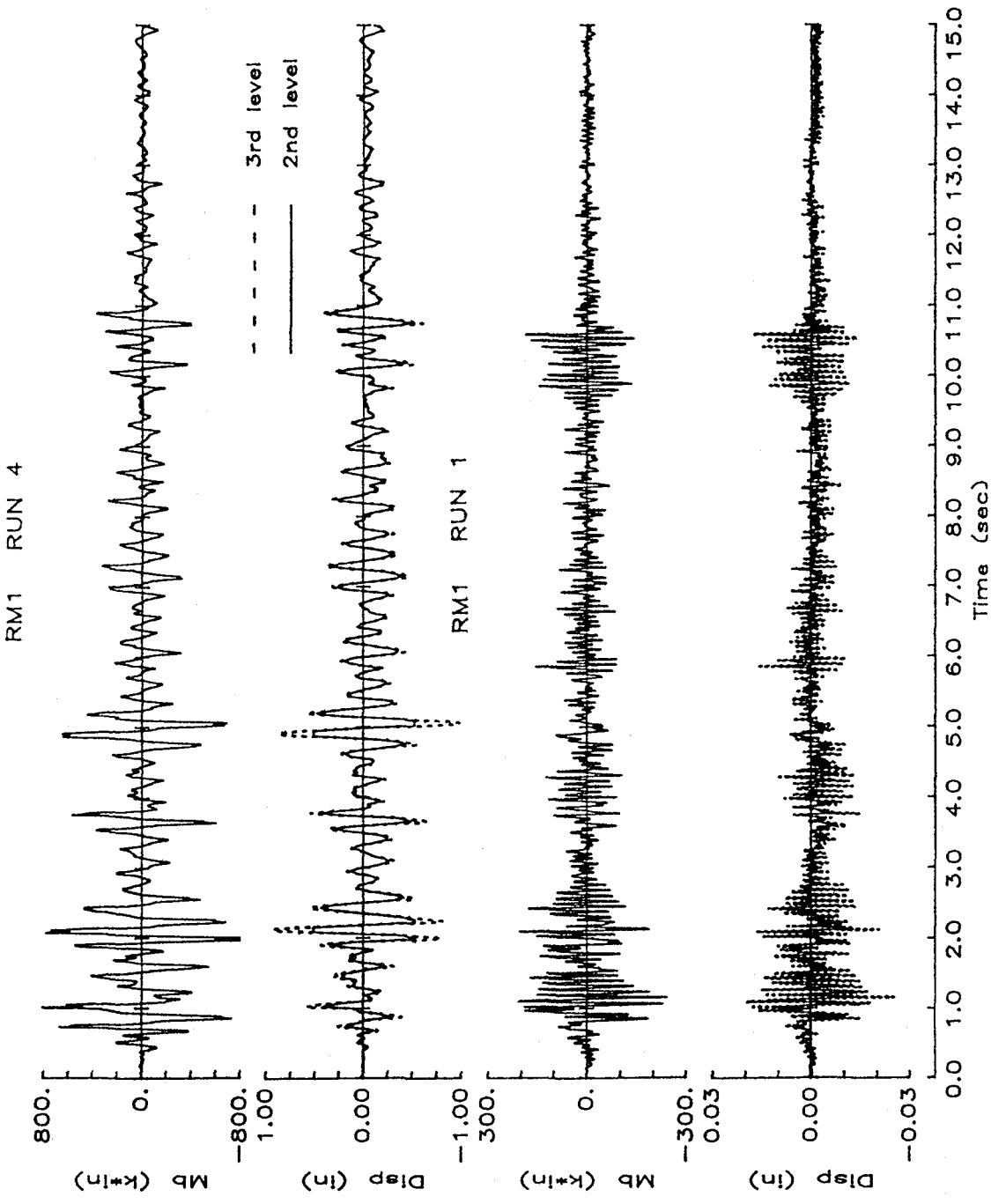

Figure 4.3 Measured Deflections and Base Moments (RM1 Runs 1 & 4)

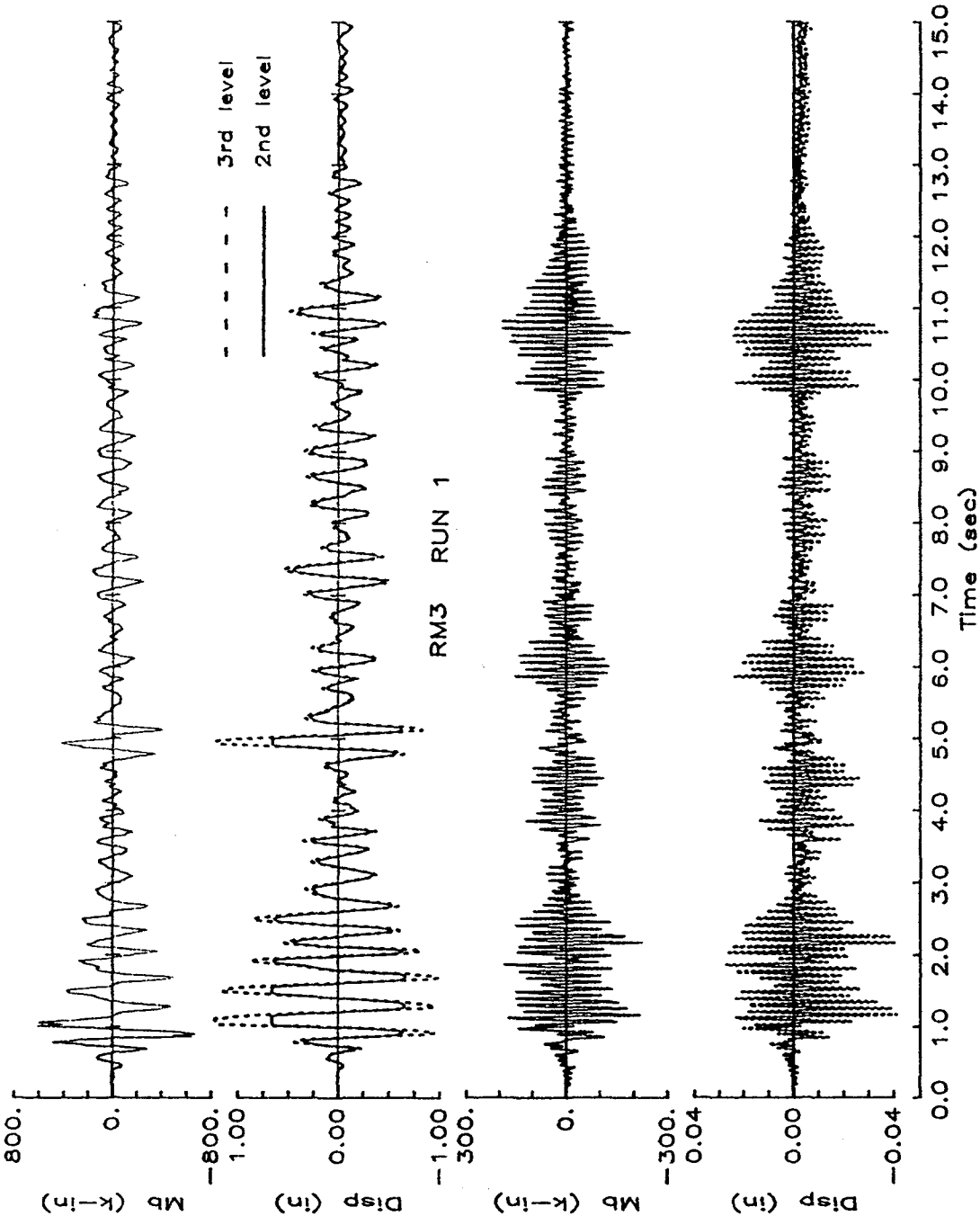

Figure 4.4 Measured Deflections and Base Moments (RM3 Runs 1 & 6)

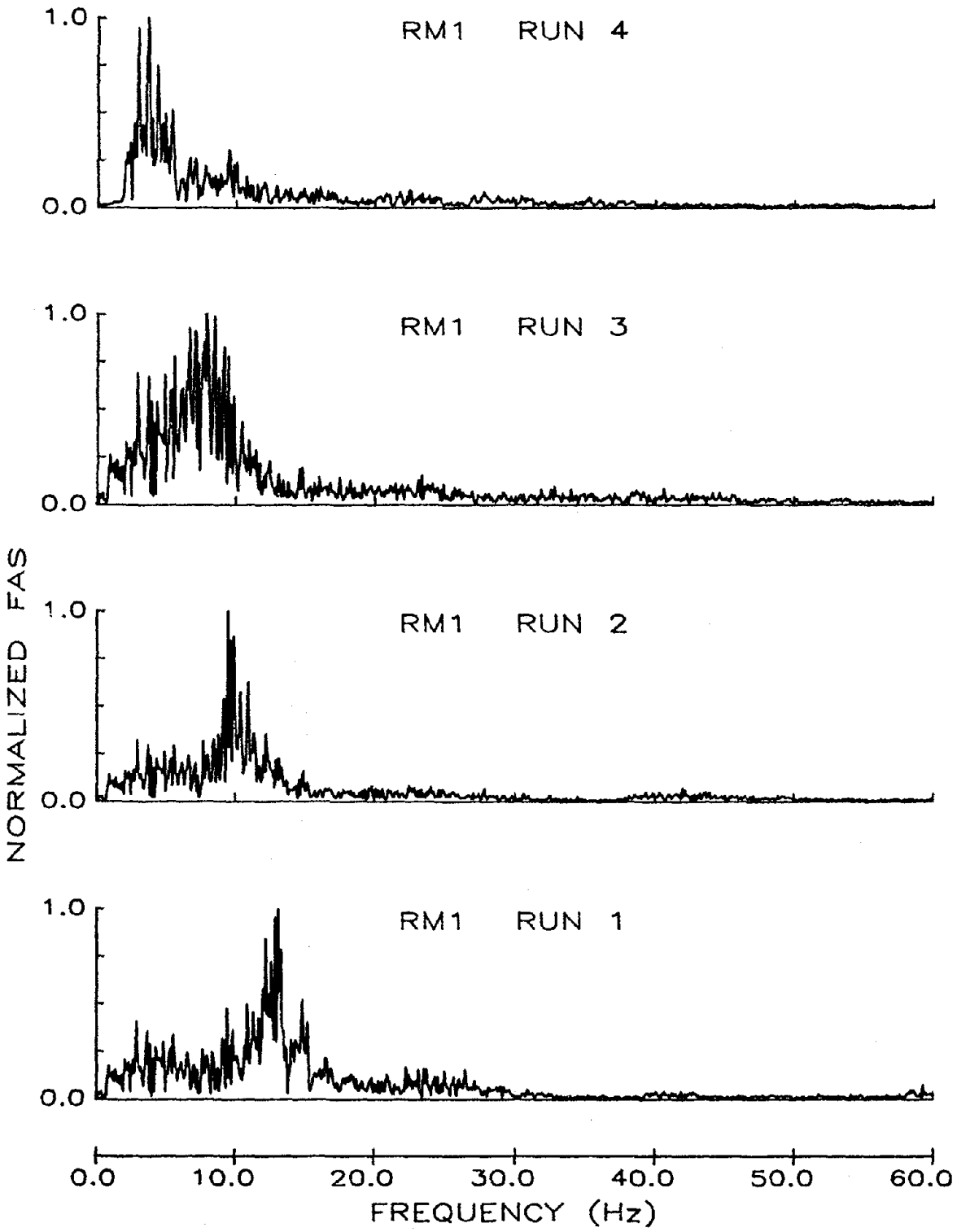

Figure 4.5 Fourier Amplitude Spectra : Top-Level Accelerations (RM1)

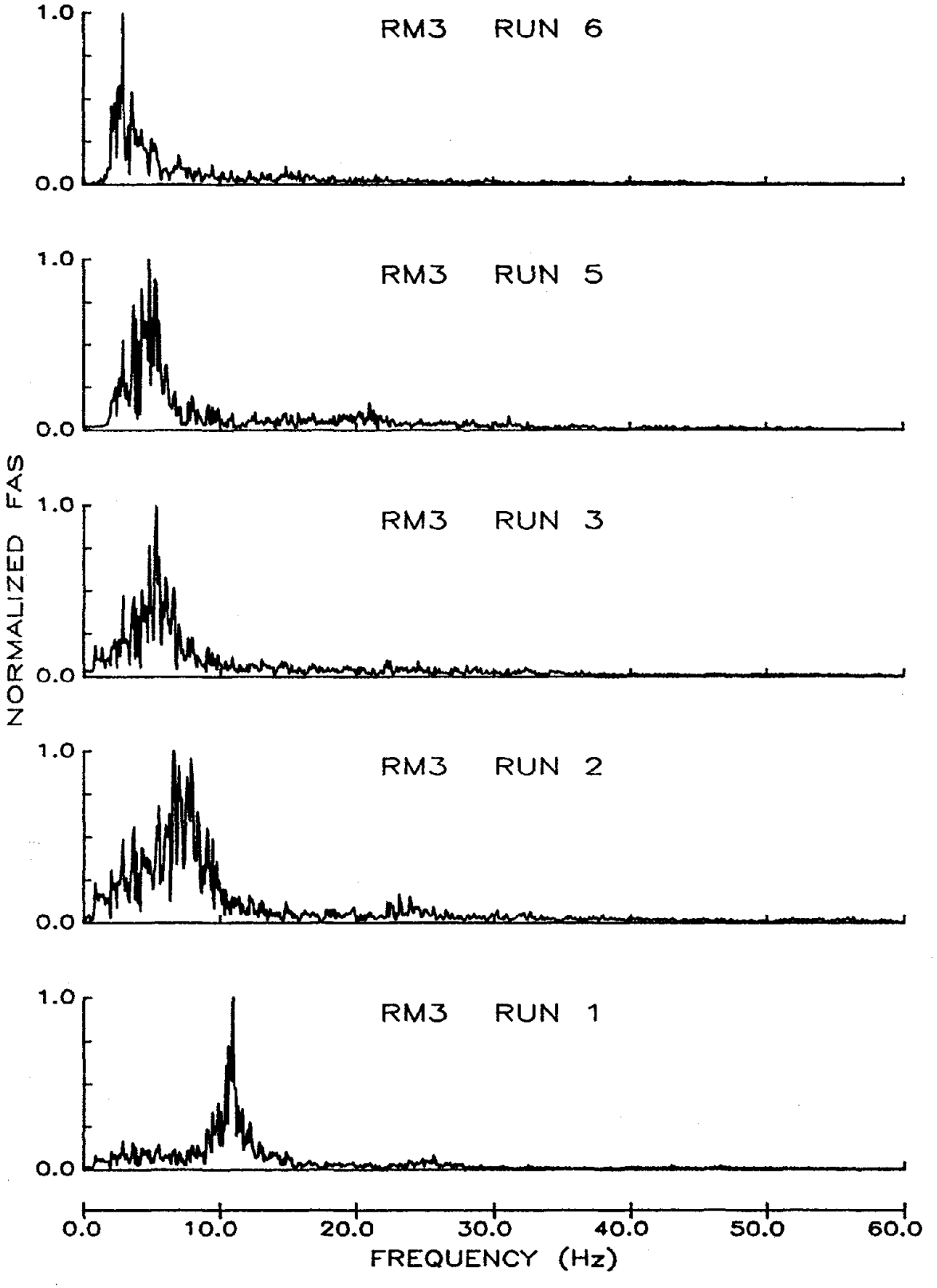

Figure 4.6 Fourier Amplitude Spectra : Top-Level Accelerations (RM3)

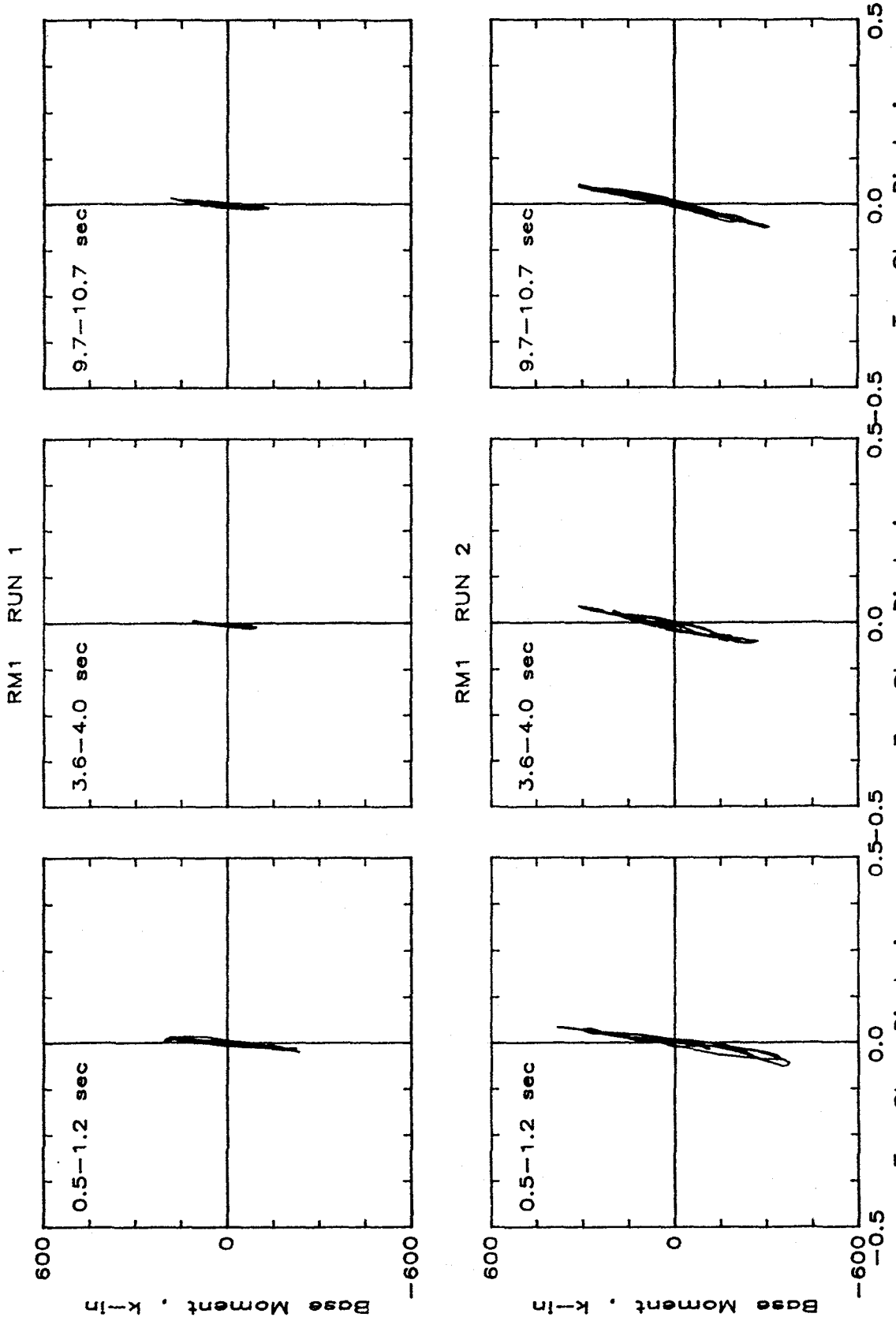

Figure 4.7 Base Moment vs. Top-Level Deflection for Structure RM1

a)Runs 1 & 2

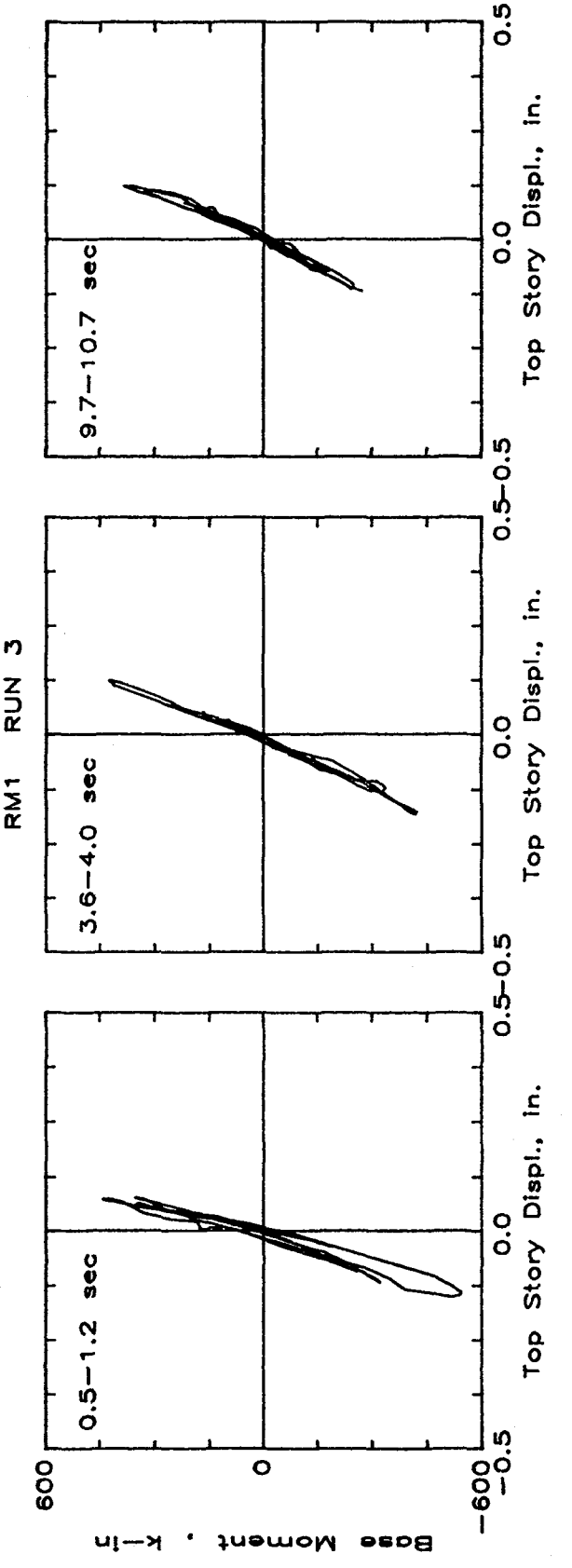

Figure 4.7 (cont) Base Moment vs. Top-Level Deflection for Structure RM1 b) Run 3

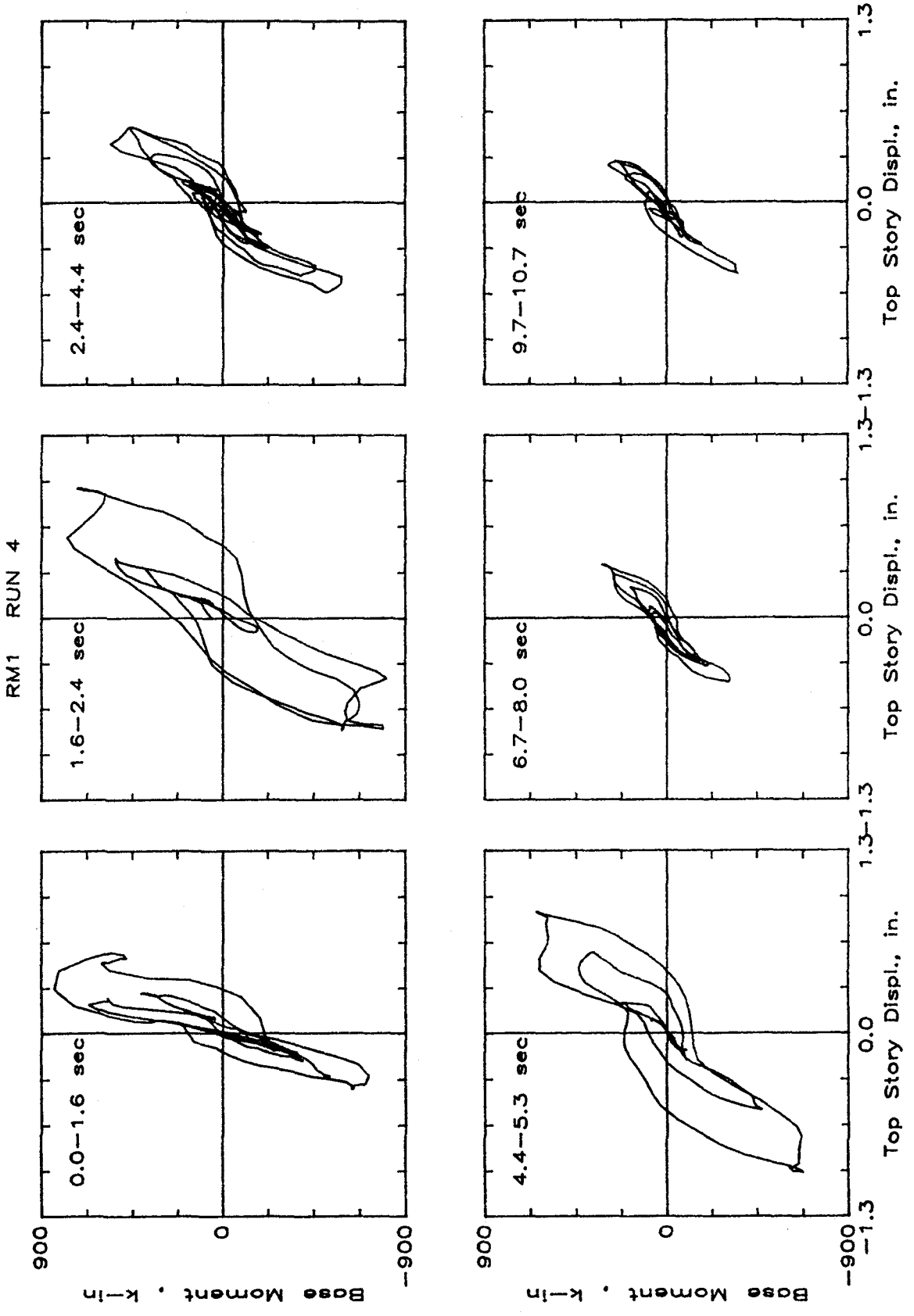

Figure 4.7 (cont) Base Moment vs. Top-Level Deflection for Structure RM1 c) Run 4

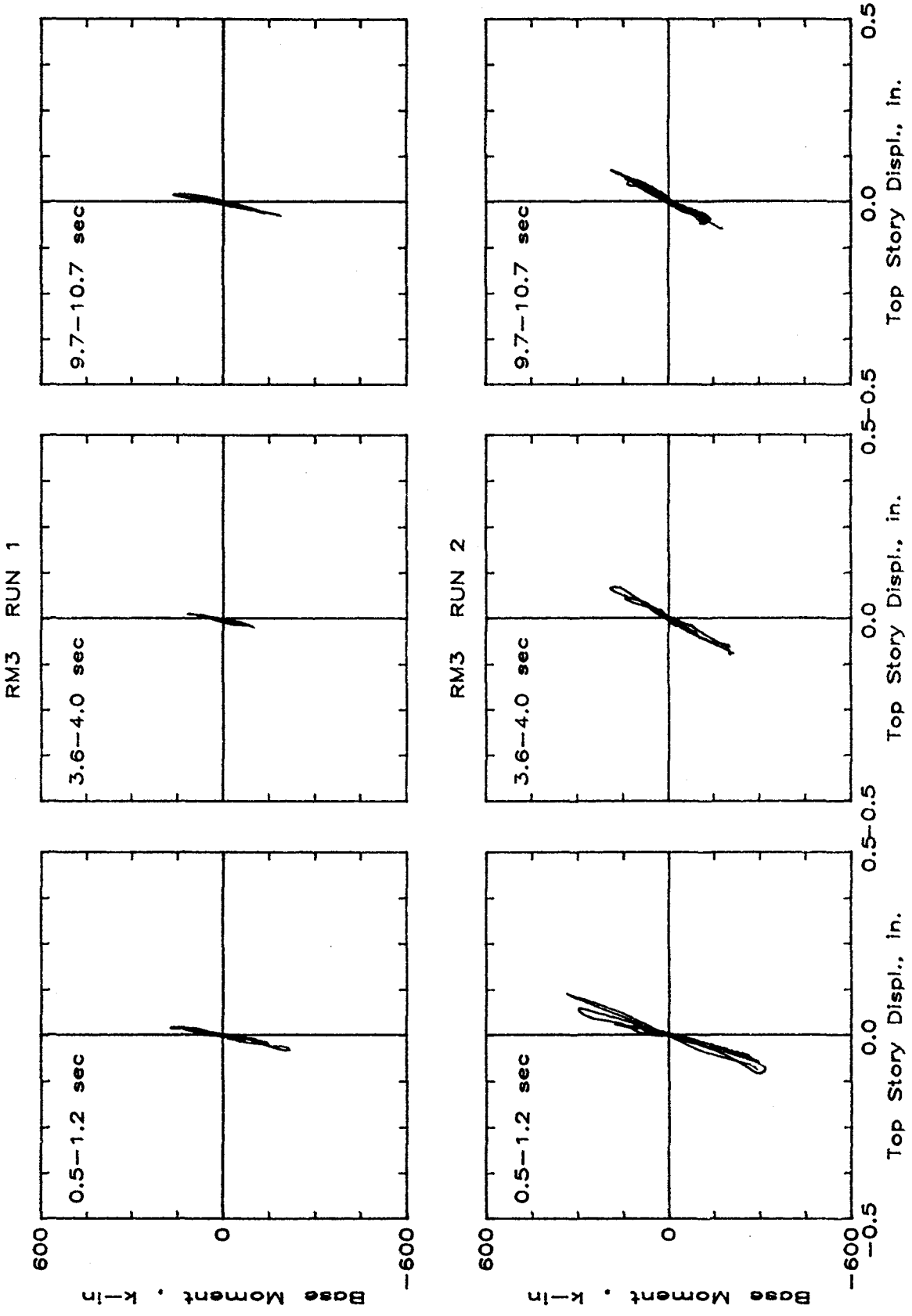

Figure 4.8 Base Moment vs. Top-Level Deflection for Structure RM3

a) Runs 1 & 2

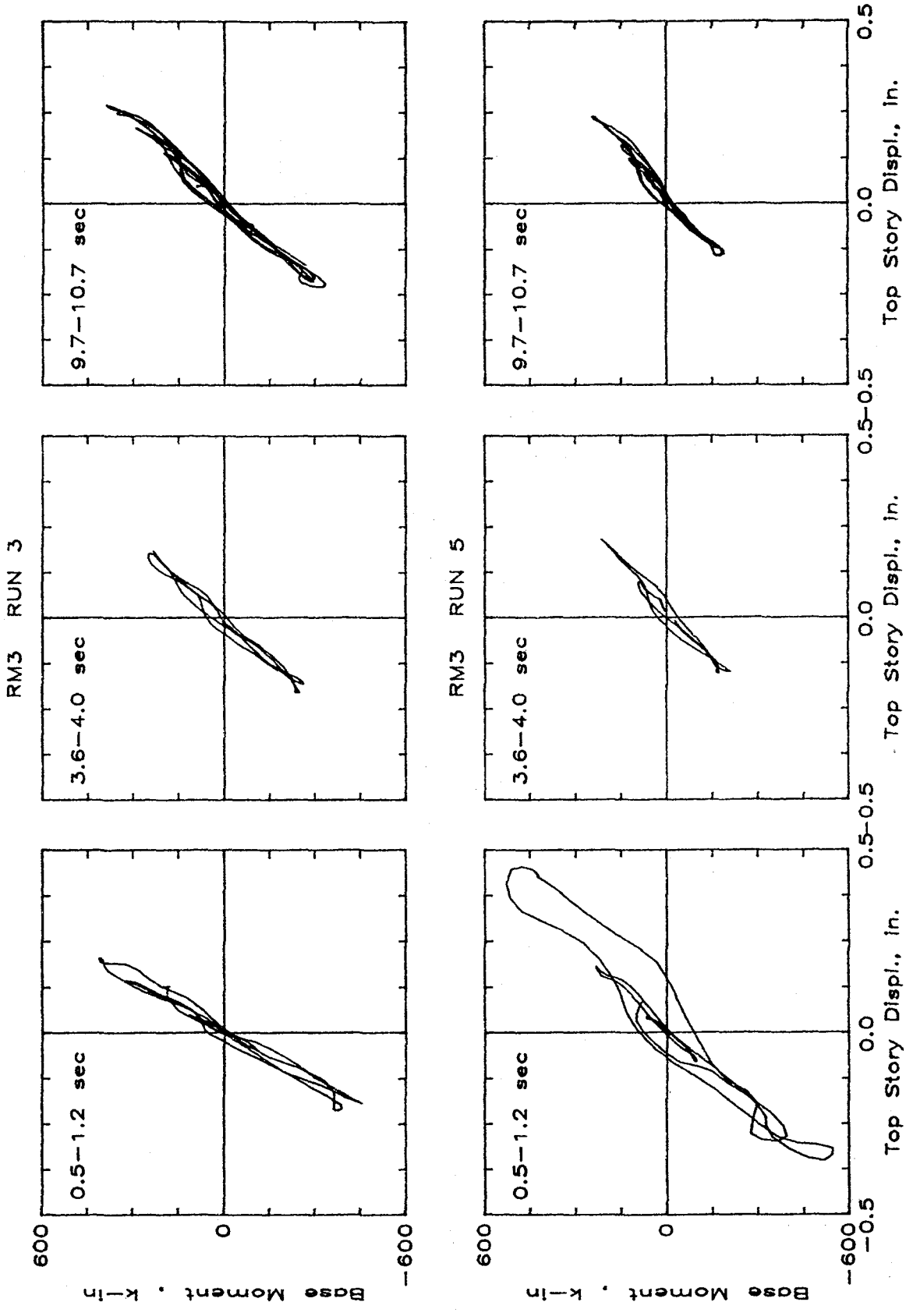

Figure 4.8 (cont) Base Moment vs. Top-Level Deflection for Structure RM3 b) Runs 3 & 5

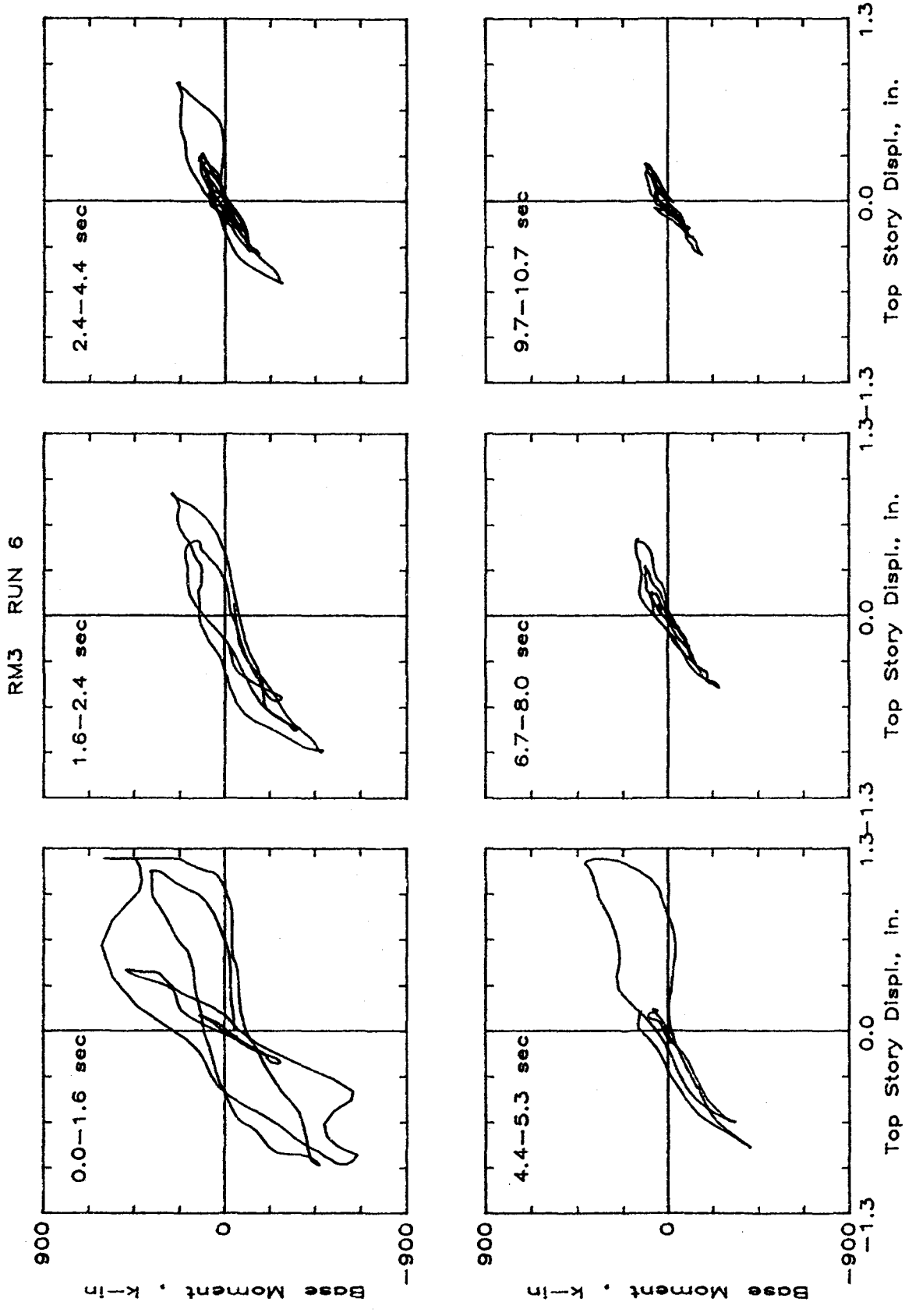

Figure 4.8 (cont) Base Moment vs. Top-Level Deflection for Structure RM3 c) Run 6

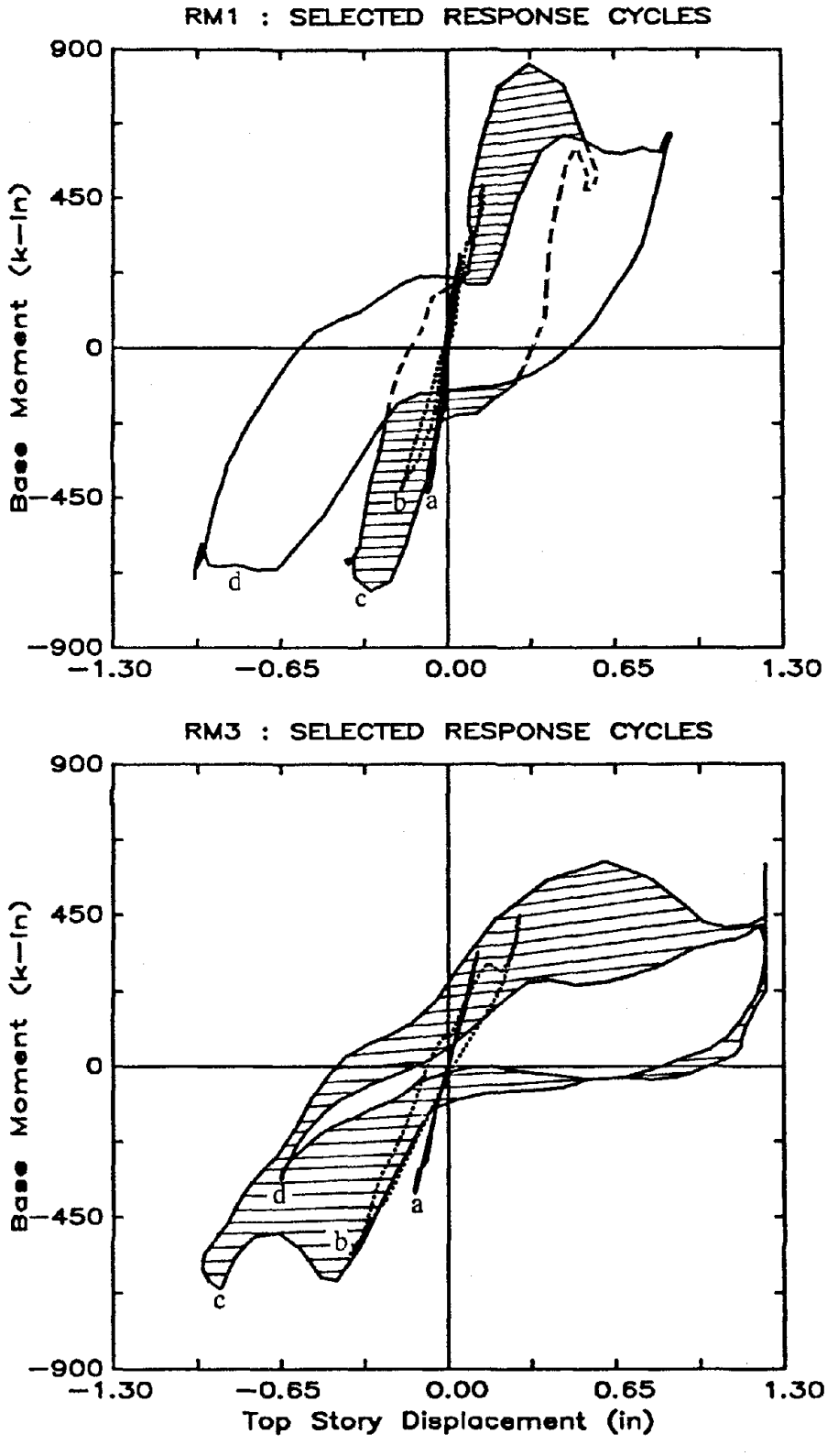

Figure 4.9 Base Moment vs. Top-Level Deflection (All Runs)

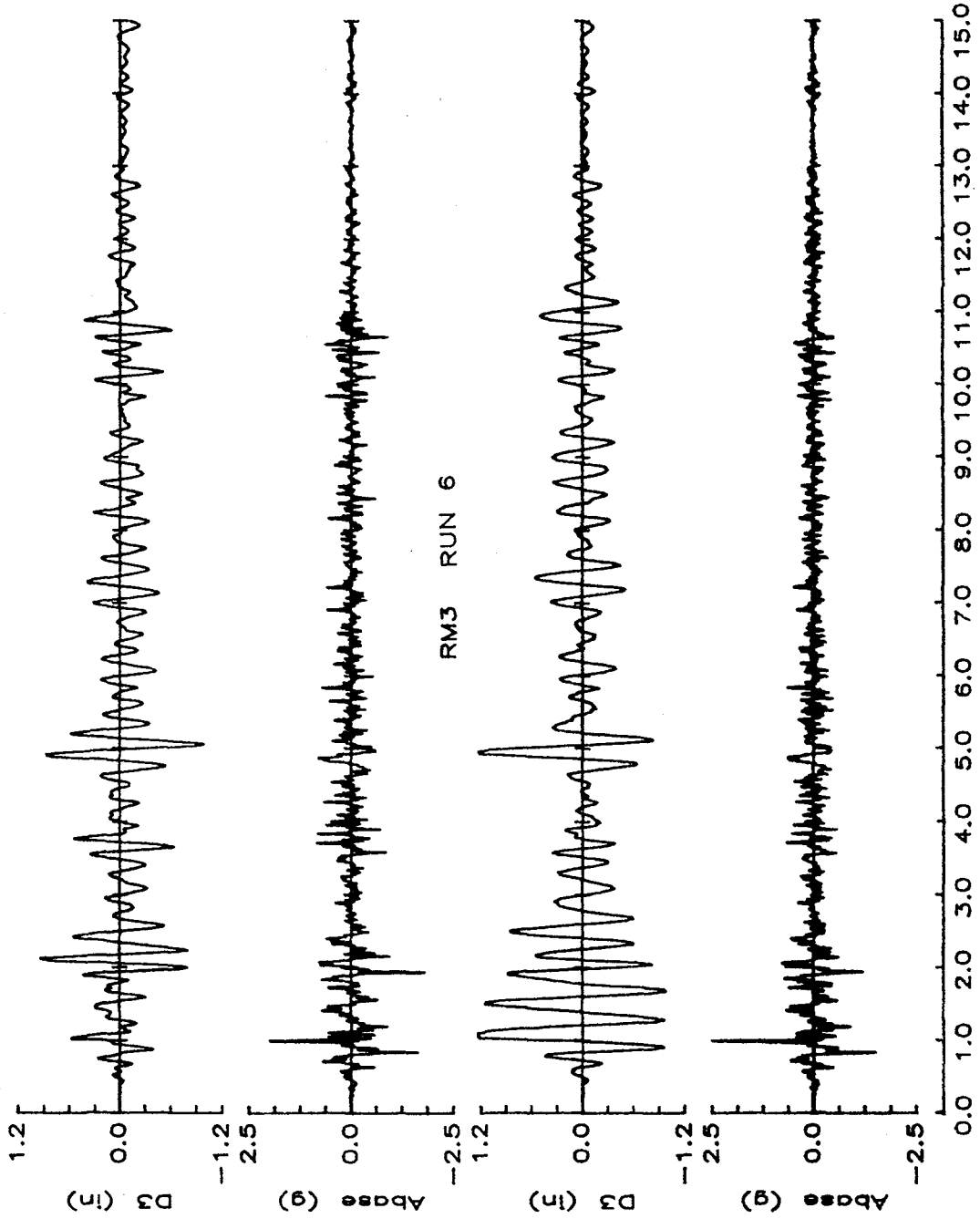

Figure 4.10 Base Accelerations and Top-Level Deflections (RM1 & RM3 : Last Run)

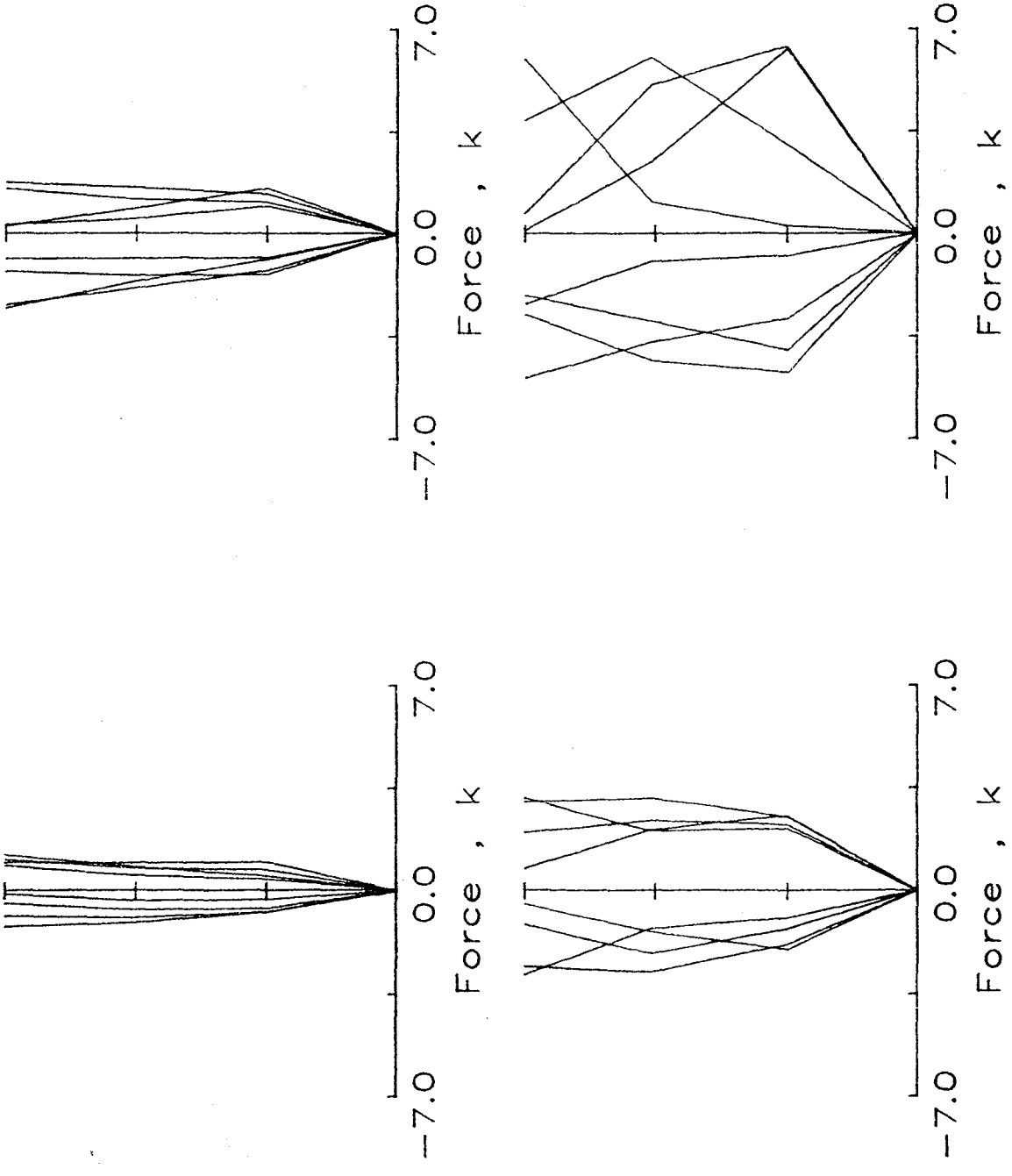

Figure 4.11 Lateral Force Distribution at Selected Time Instants (RM1 : All Runs)

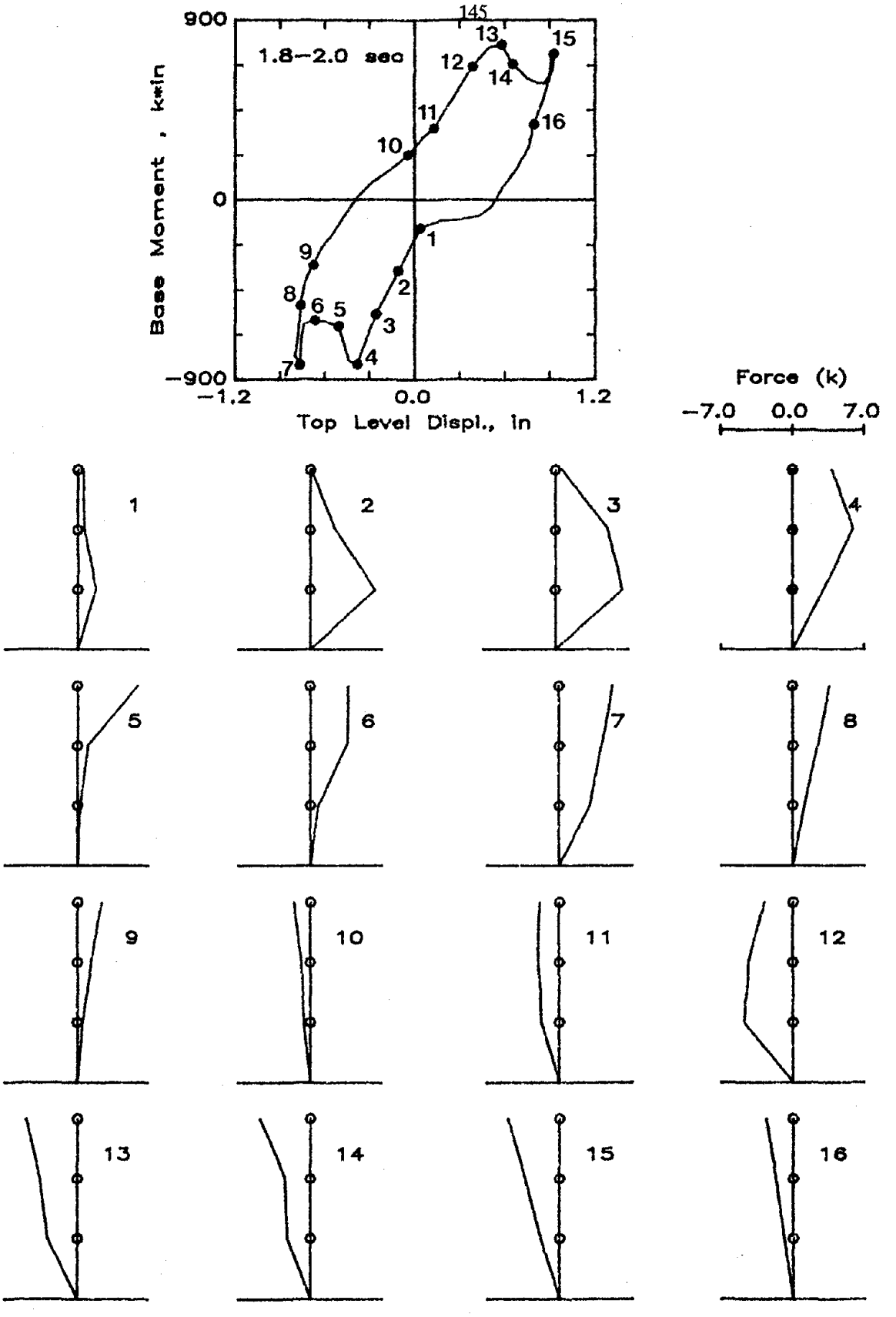

Figure 4.12 Lateral Force Distributions for One Cycle of Response (RM1 Run 4)

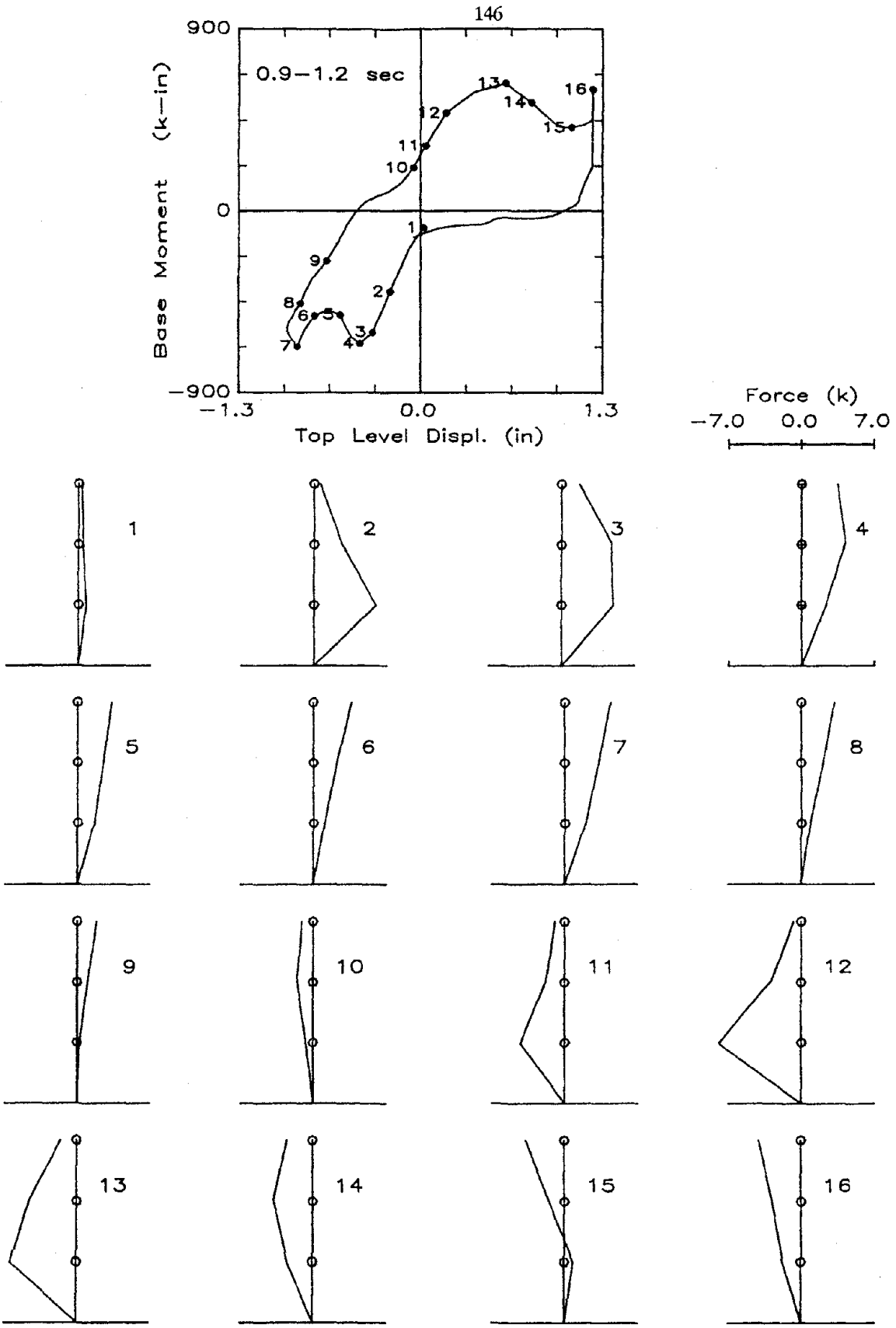

Figure 4.13 Lateral Force Distributions for One Cycle of Response (RM3 Run 6)

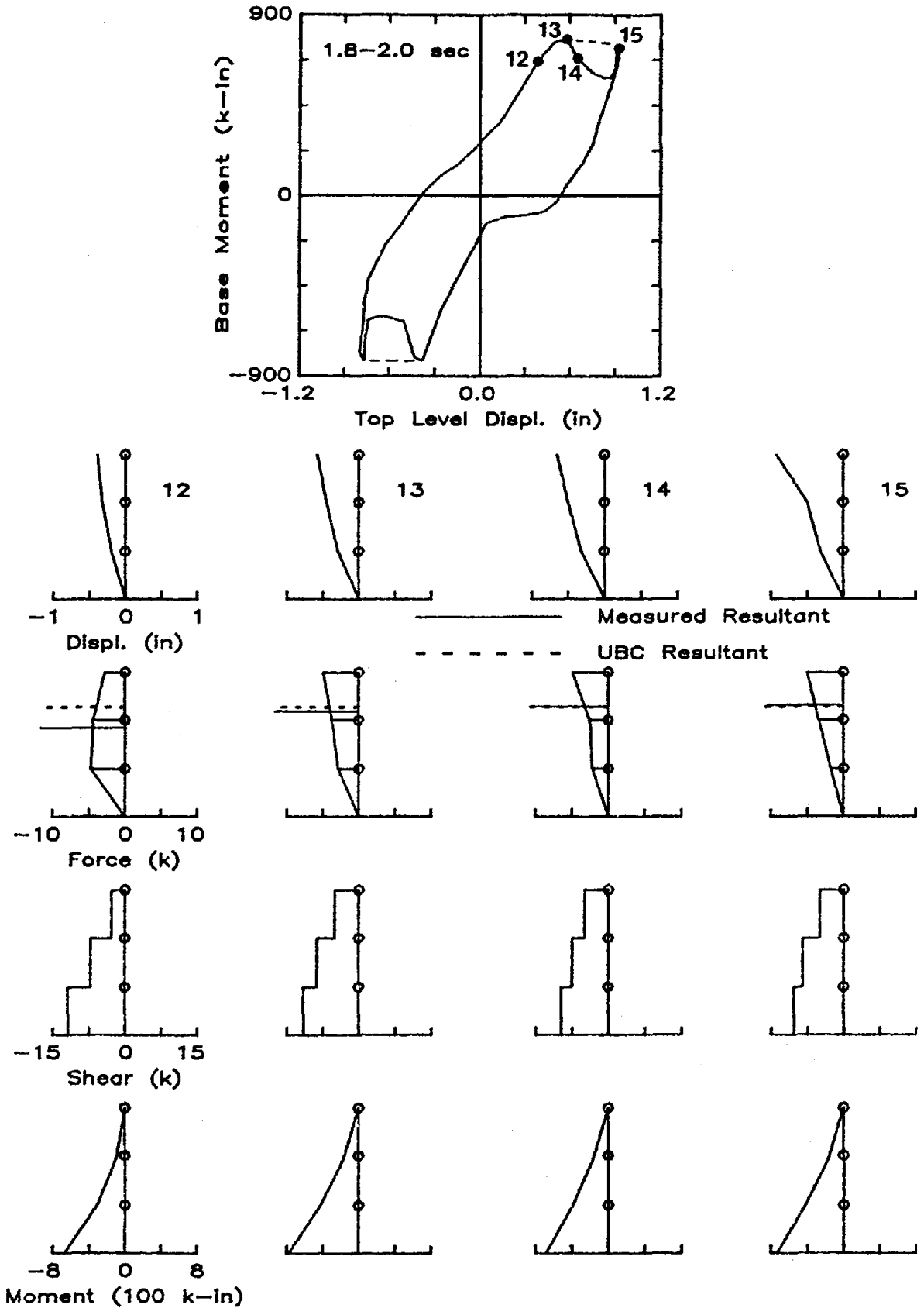

Figure 4.14 Profiles for One Half-Cycle of Response (RM1 Run 4)

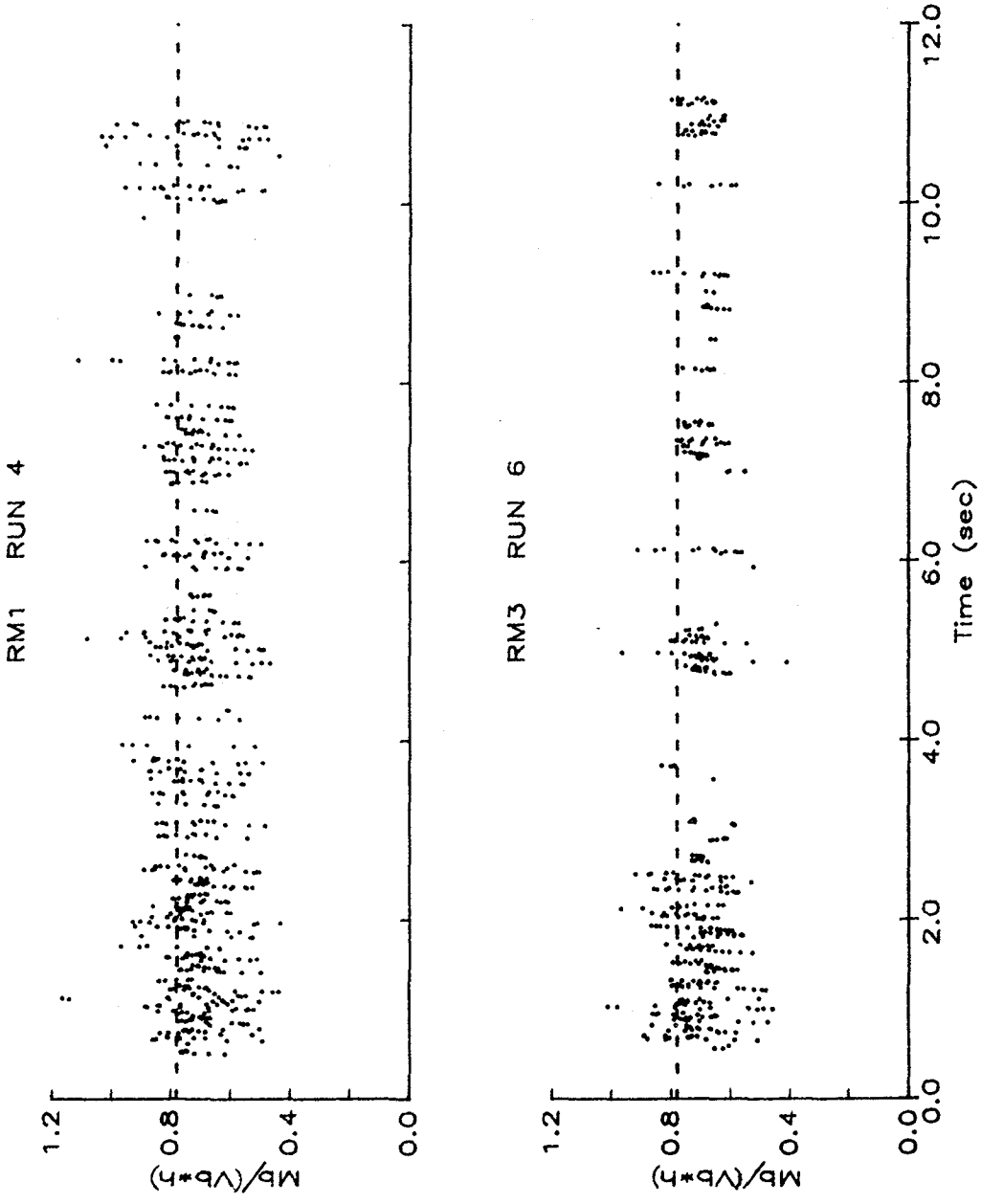

Figure 4.15 Moment-to-Shear Ratio at Base of Structure (Normalized by Structure Height)

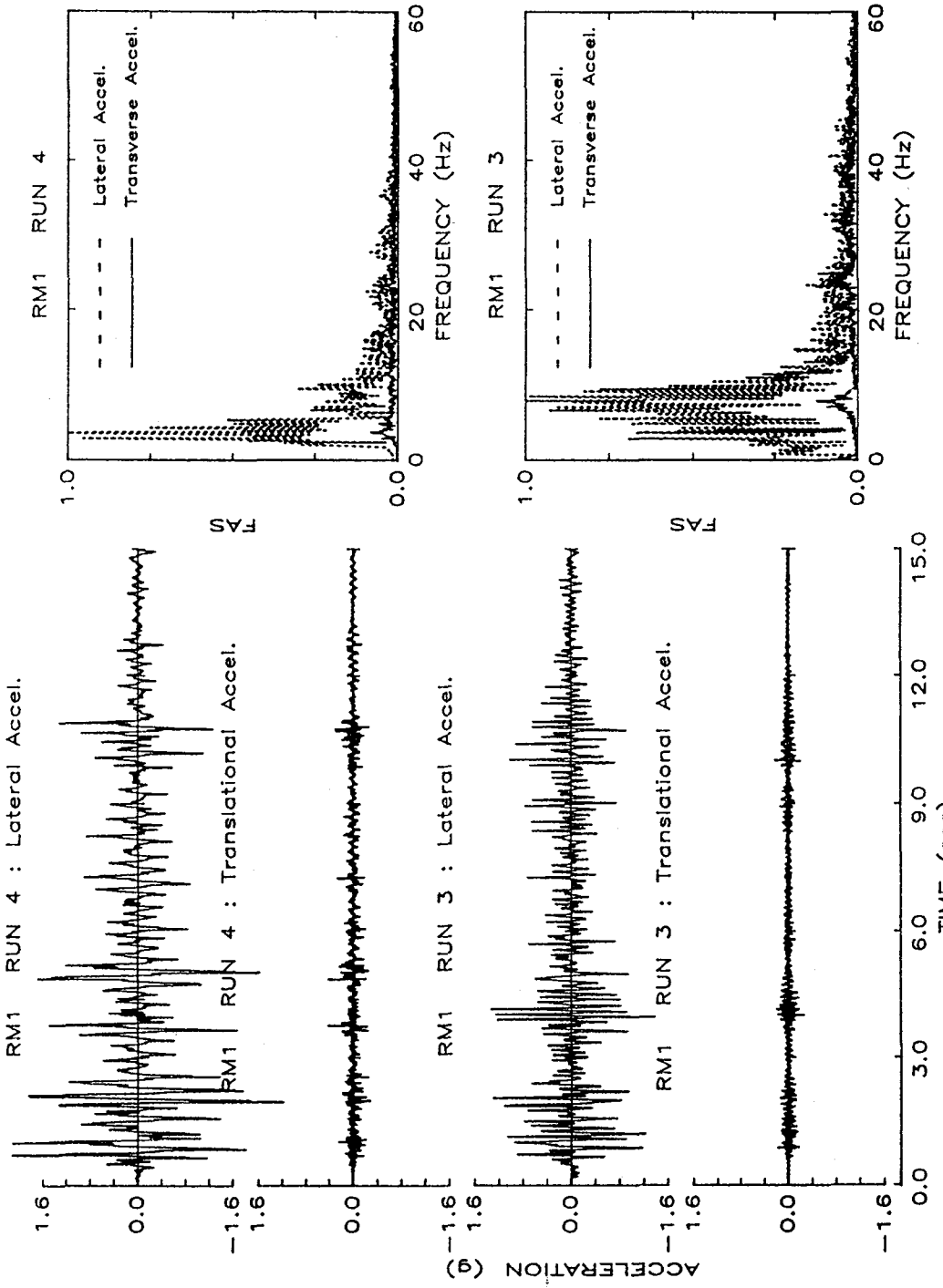

Figure 4.16 Response Histories and FAS for Top-Level Accelerations of RM1

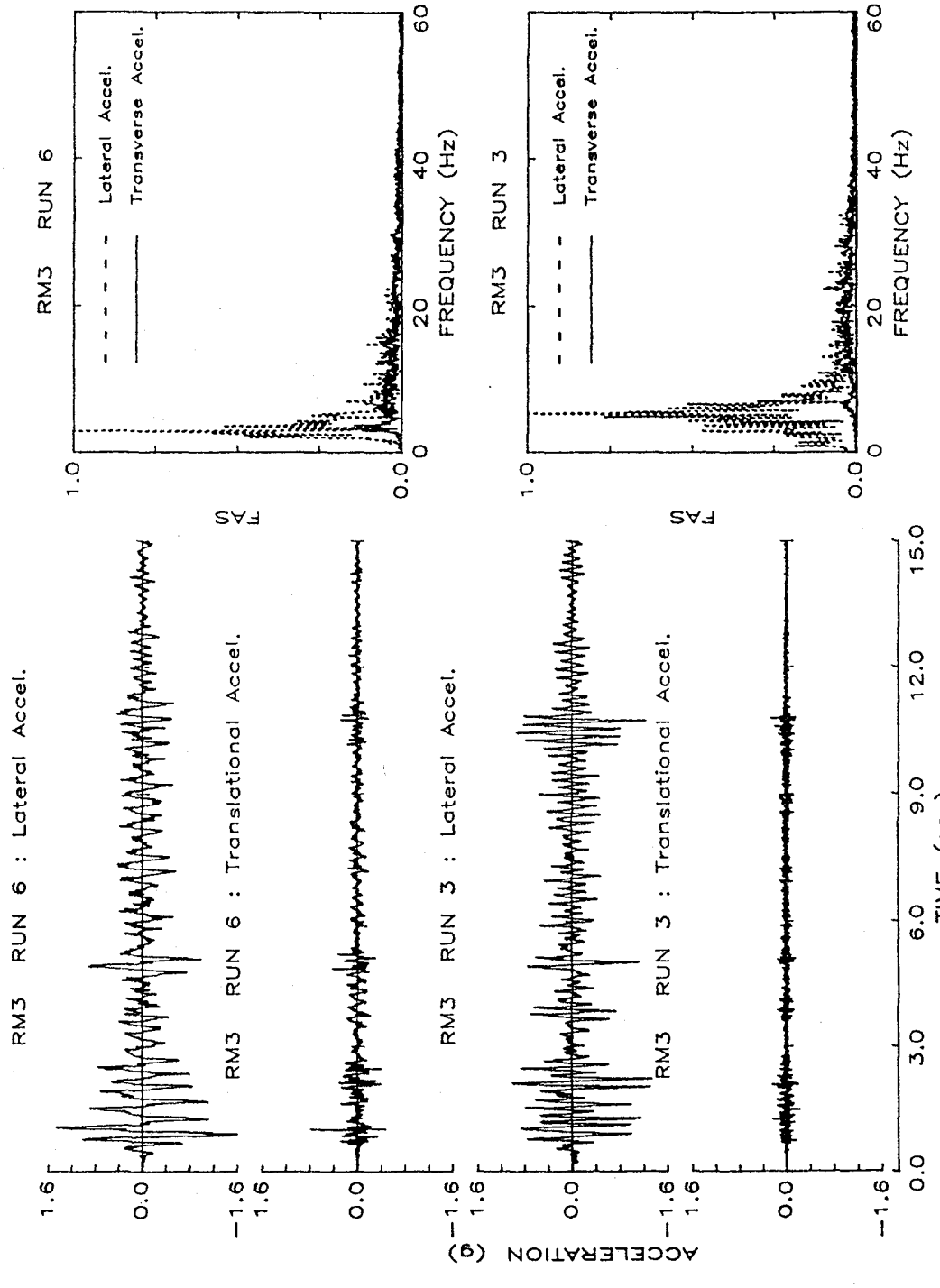

Figure 4.17 Response Histories and FAS for Top-Level Accelerations of RM3

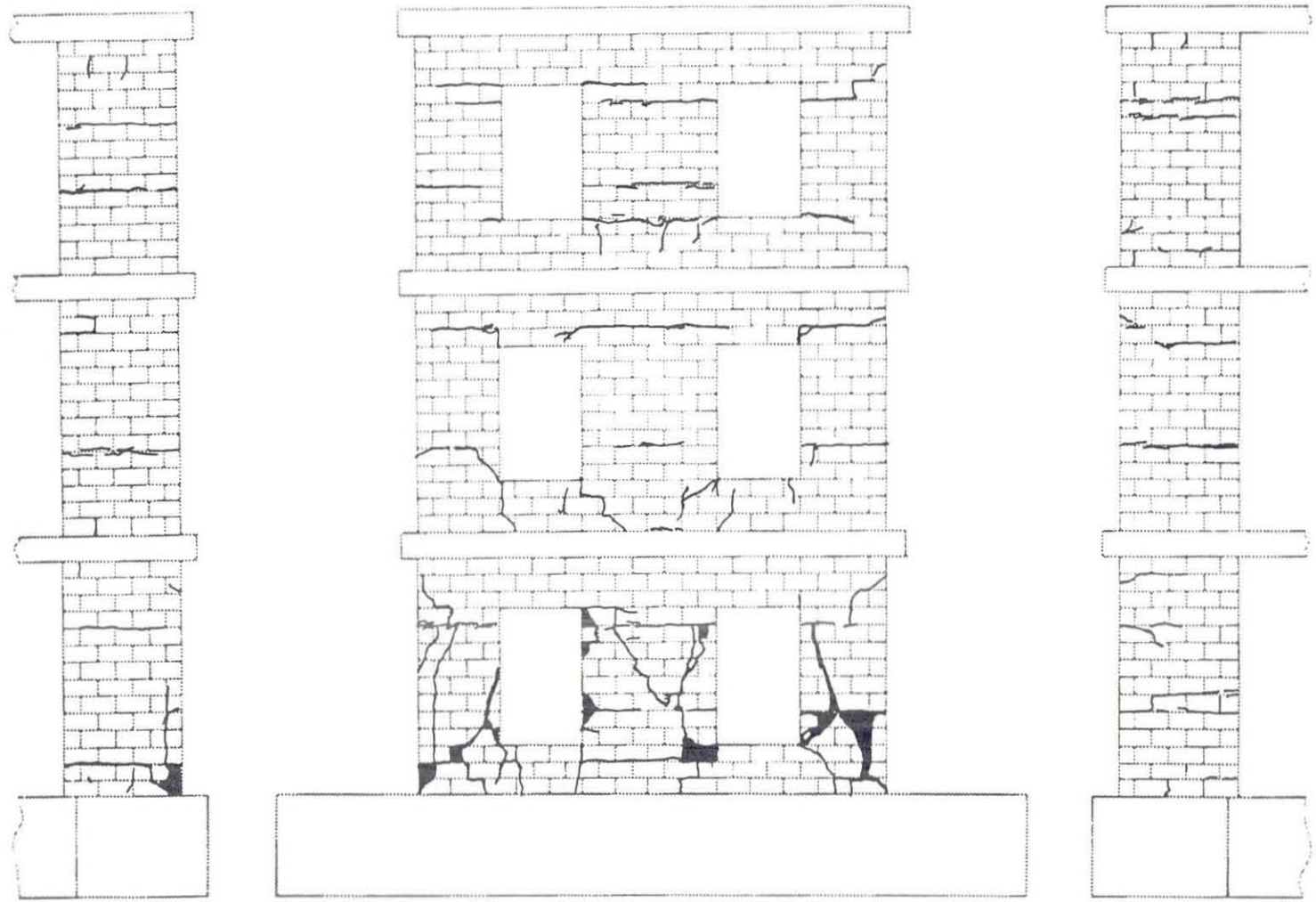

Figure 4.18 RM1 Final Crack Pattern

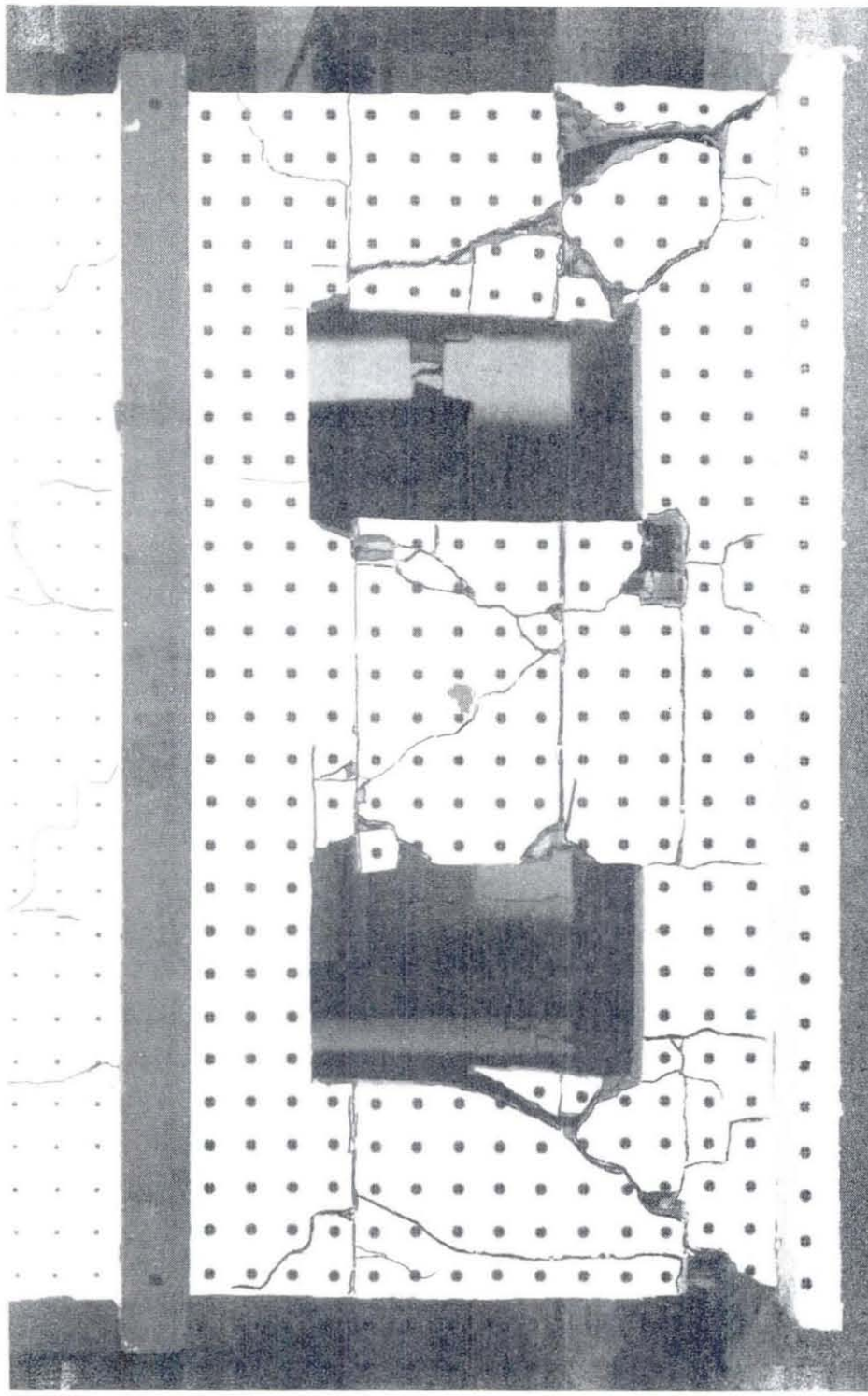

Figure 4.19 Final Cracks : Base-Story of RM1

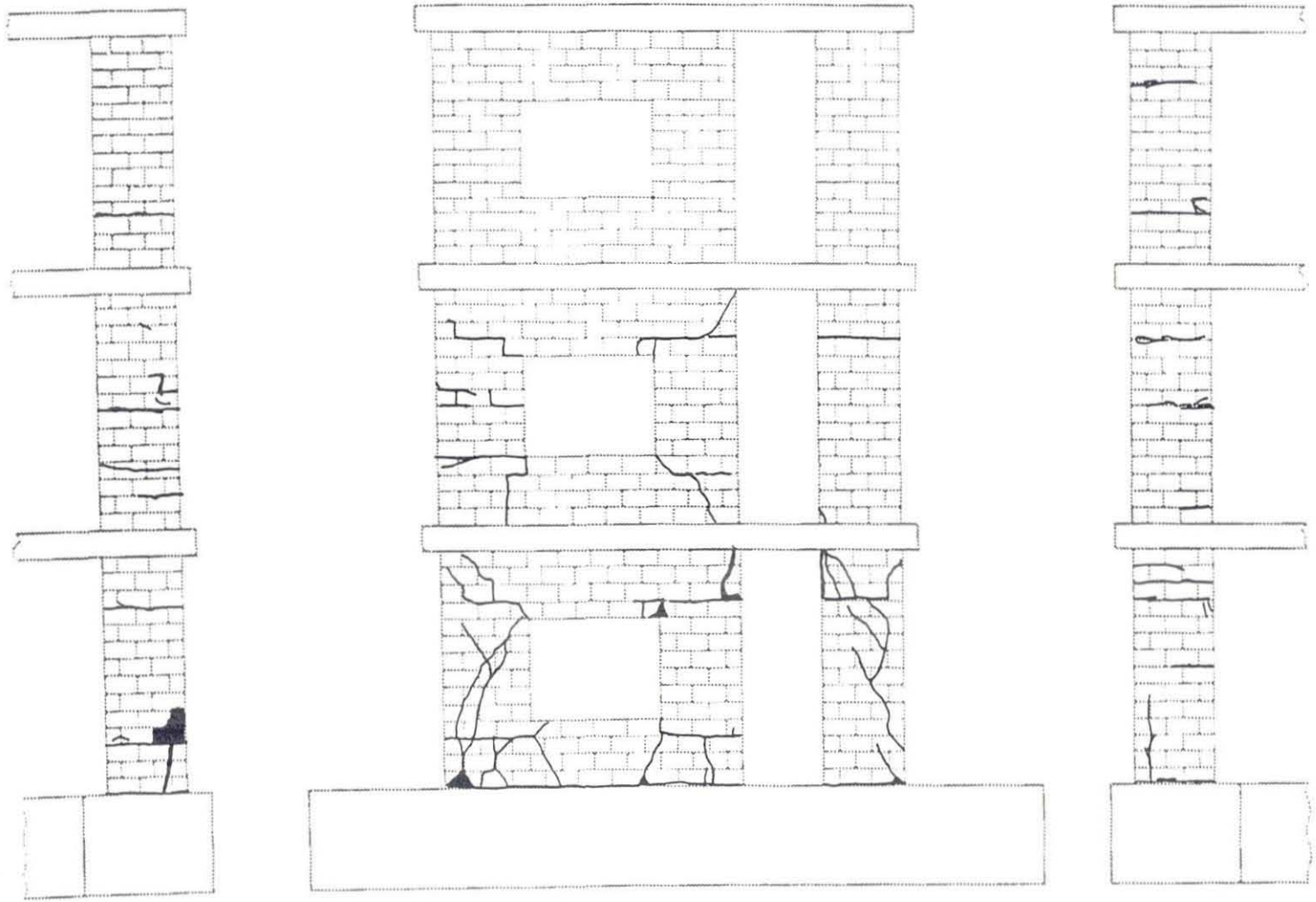

Figure 4.20 RM3 Final Crack Pattern

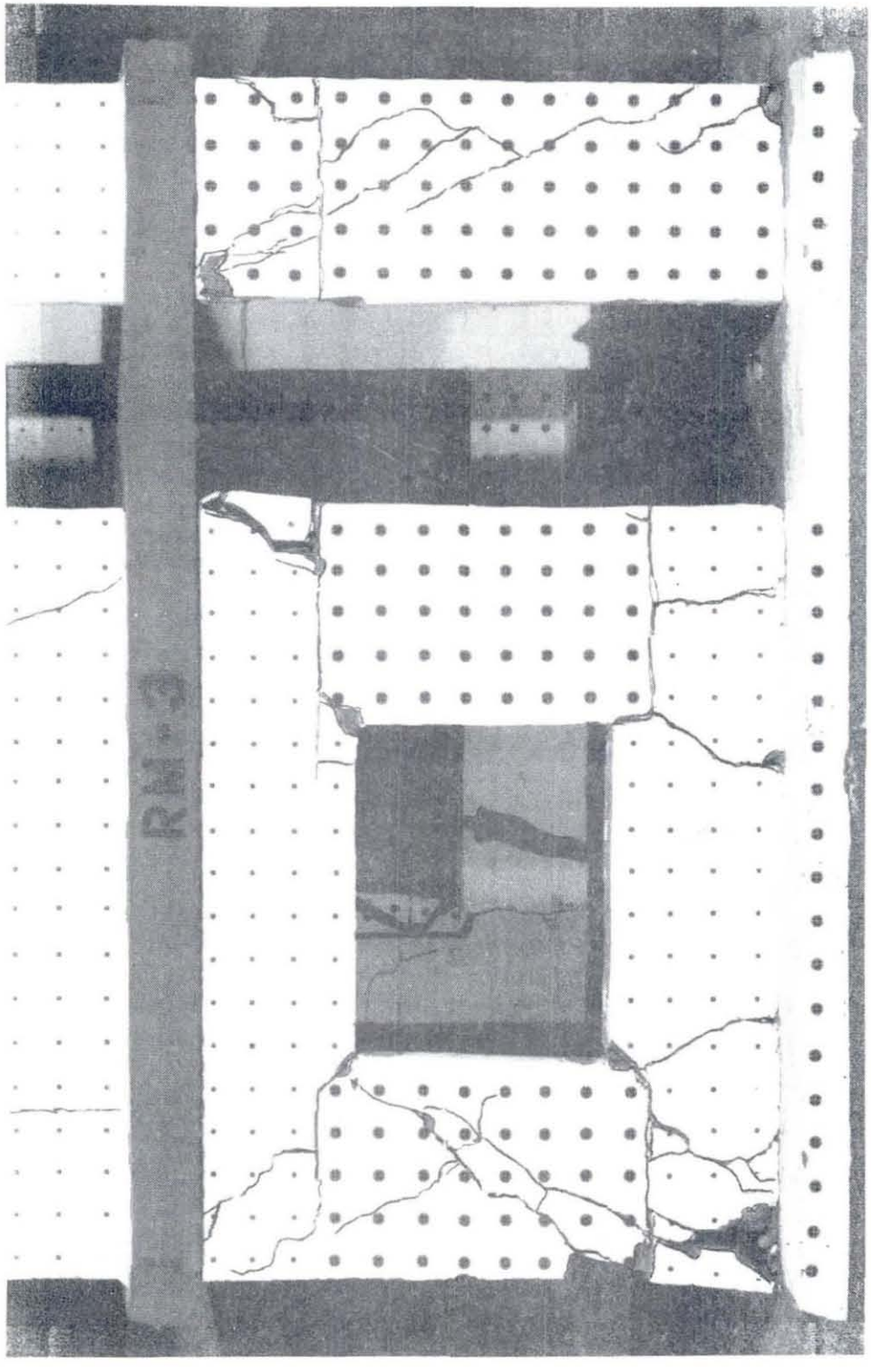

Figure 4.21 Final Cracks : Base-Story of RM3

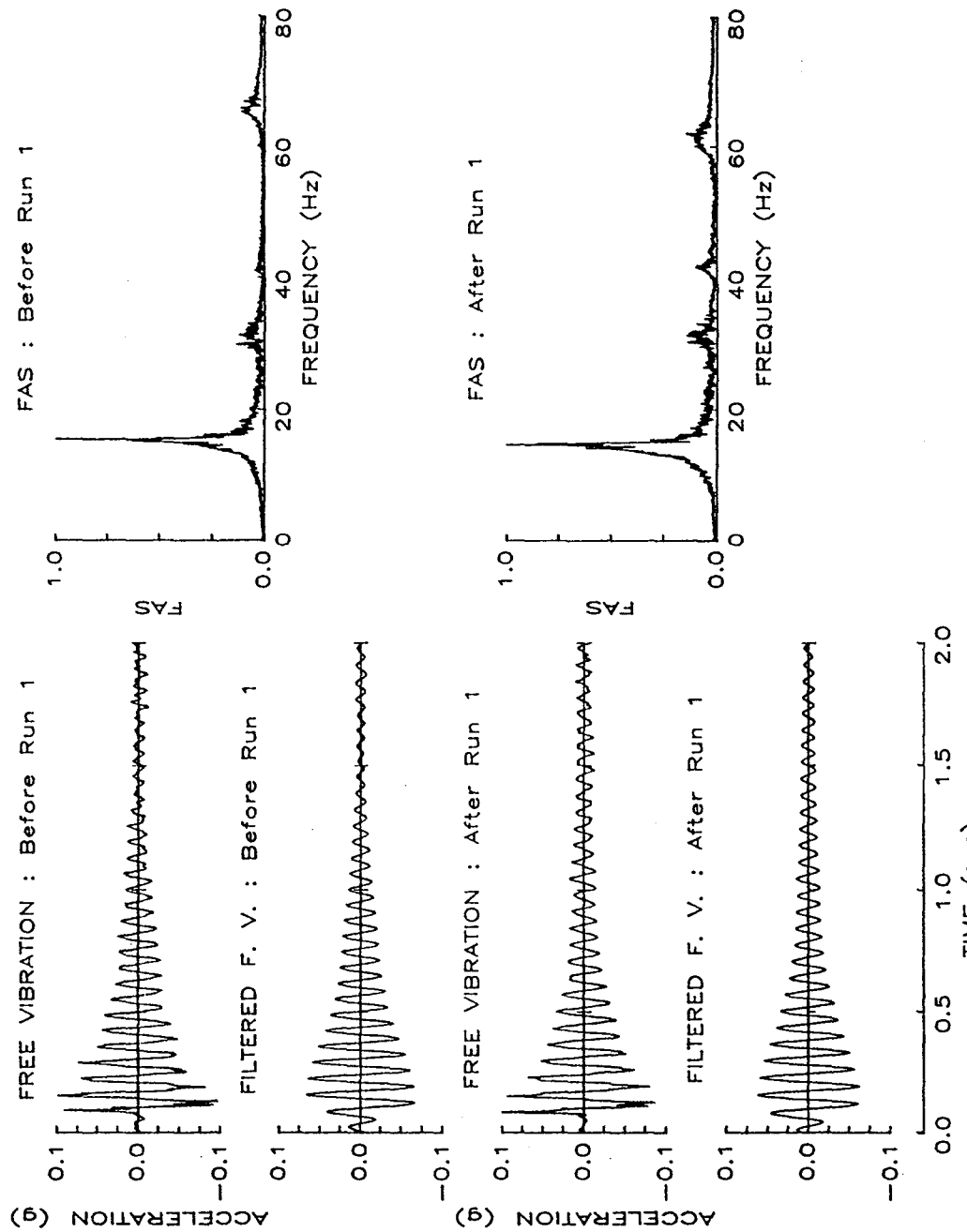

a) Before and After Run 1

Figure 4.22 Free Vibration : Top-Level Acceleration Response of RM1

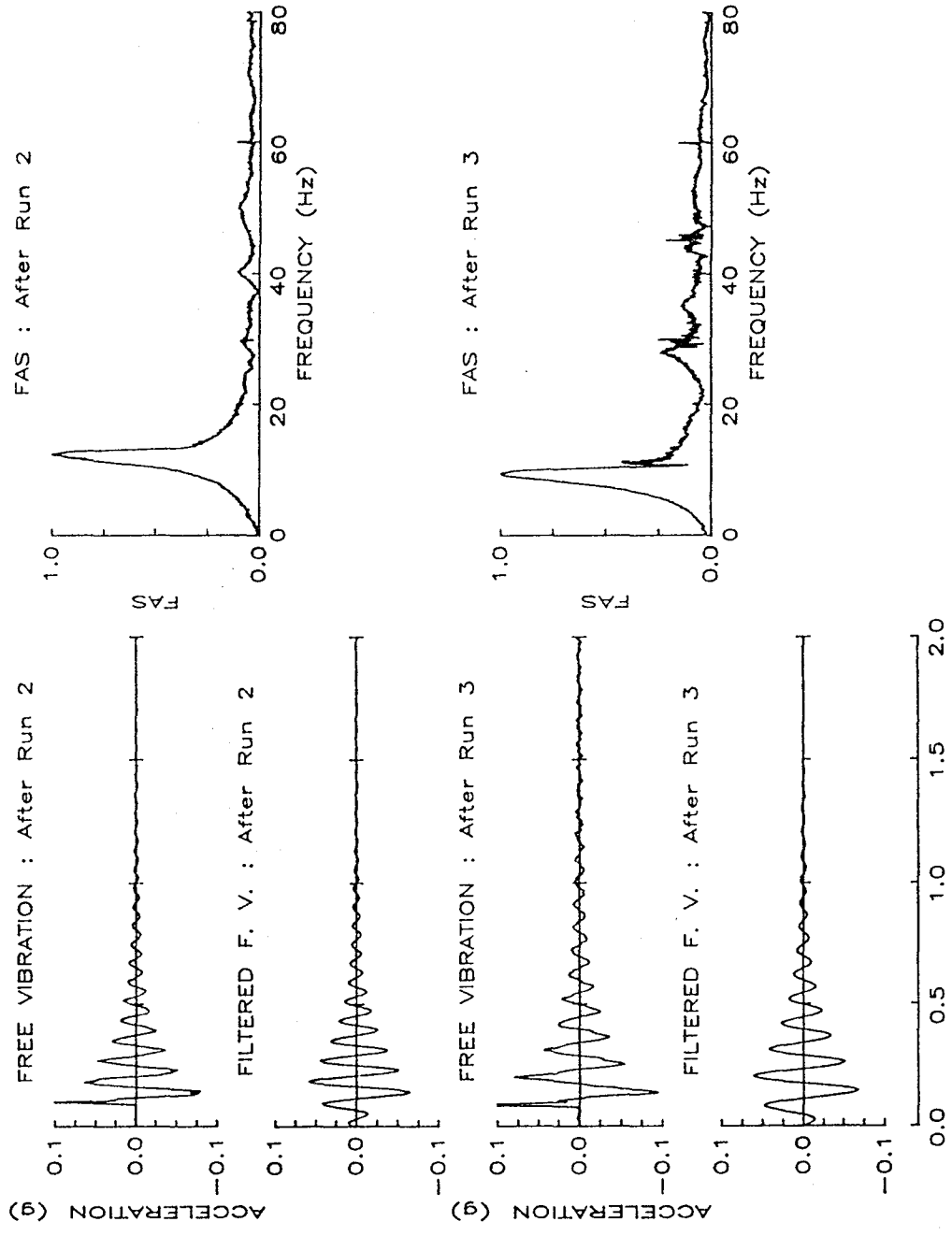

b) After Runs 2 & 3

Figure 4.22 (cont) Free Vibration : Top-Level Acceleration Response of RM1

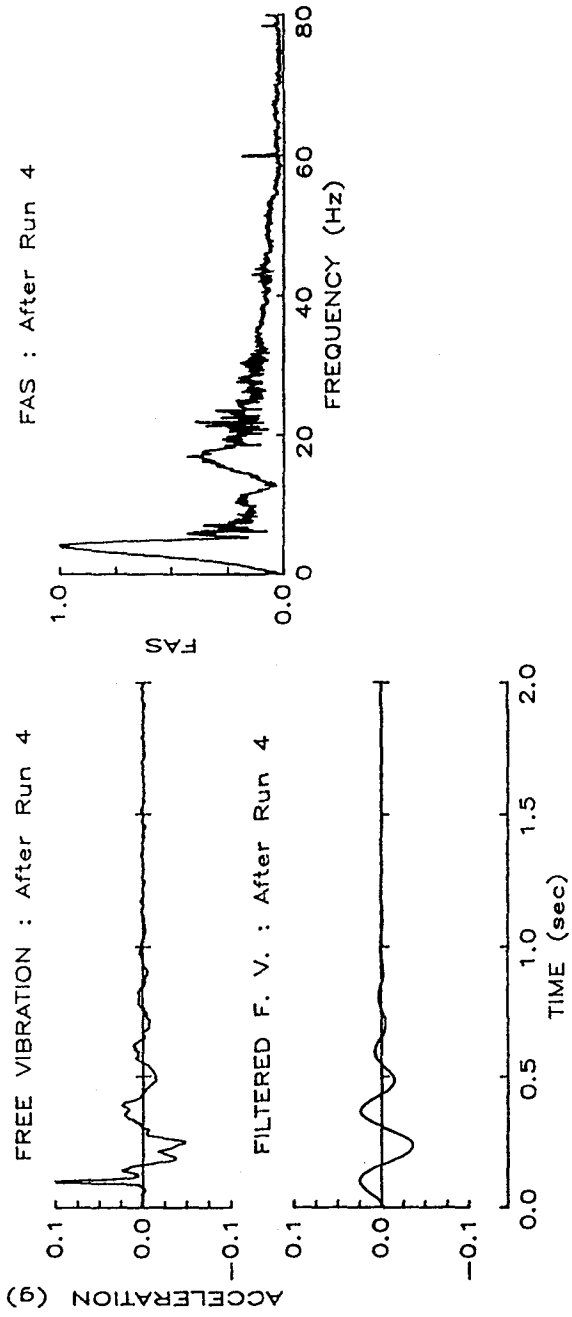

c) After Run 4

Figure 4.22 (cont) Free Vibration : Top-Level Acceleration Response of RM1

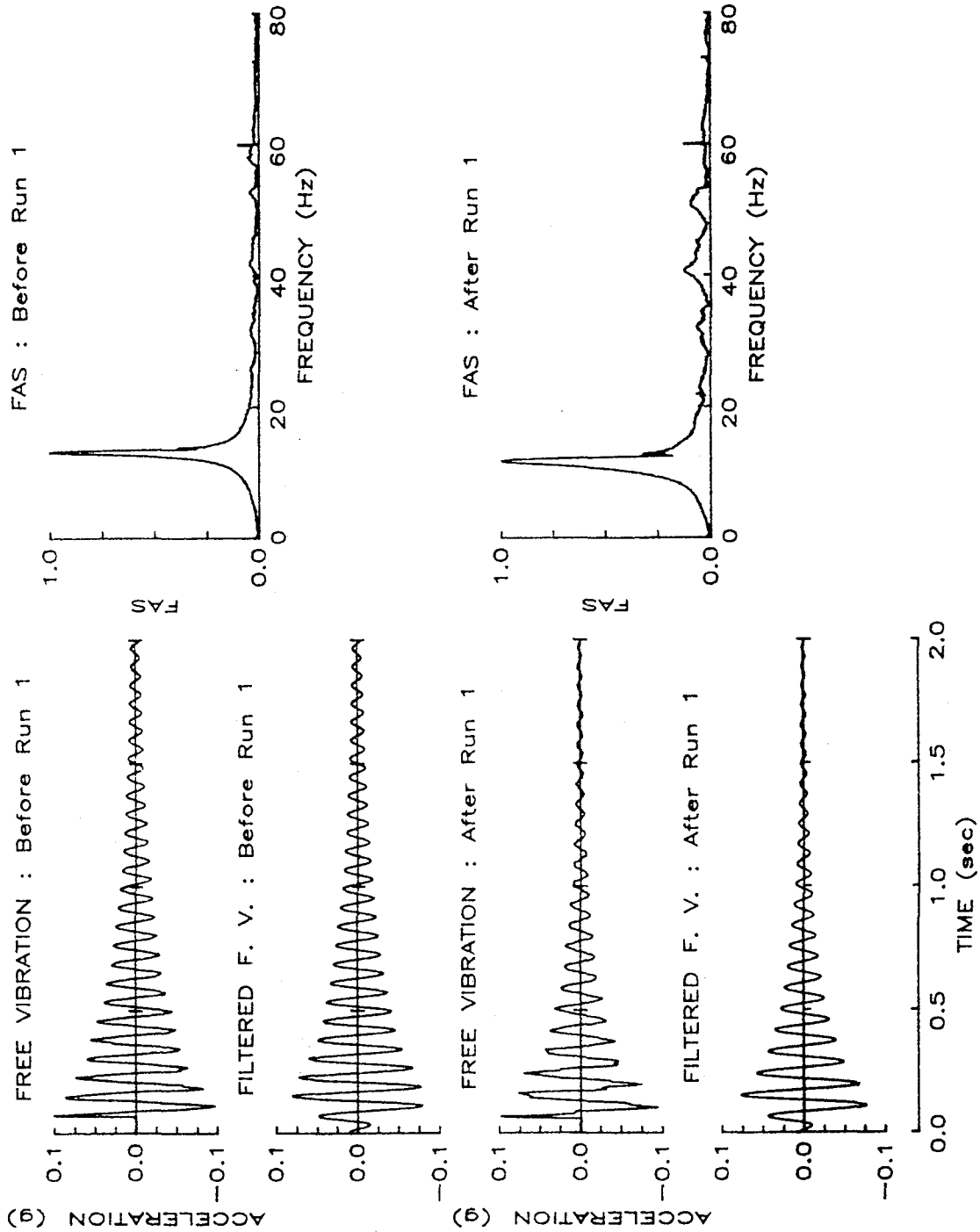

a) Before and After Run 1

Figure 4.23 Free Vibration : Top-Level Acceleration Response of RM3

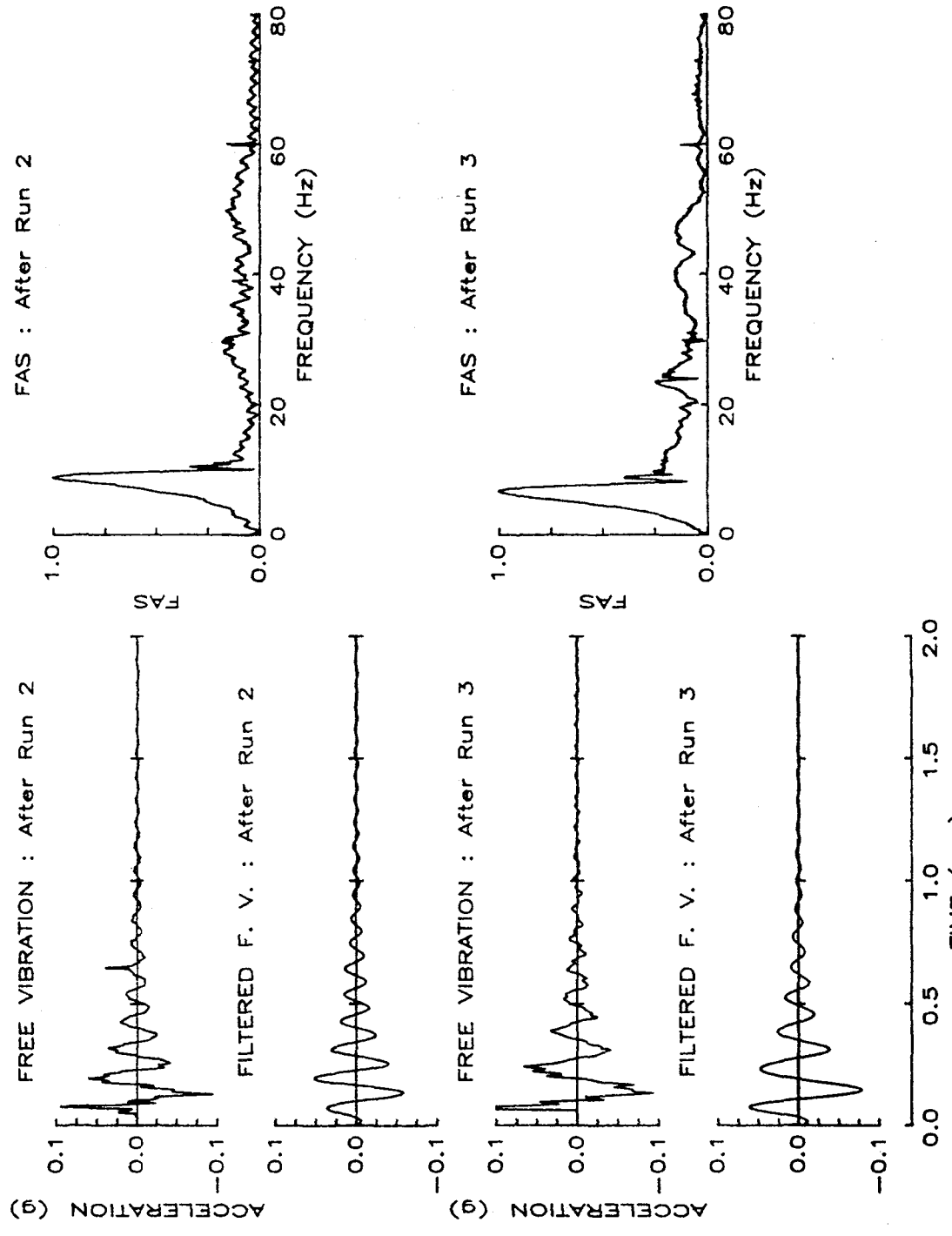

b) After Runs 2 & 3

Figure 4.23 (cont) Free Vibration : Top-Level Acceleration Response of RM3

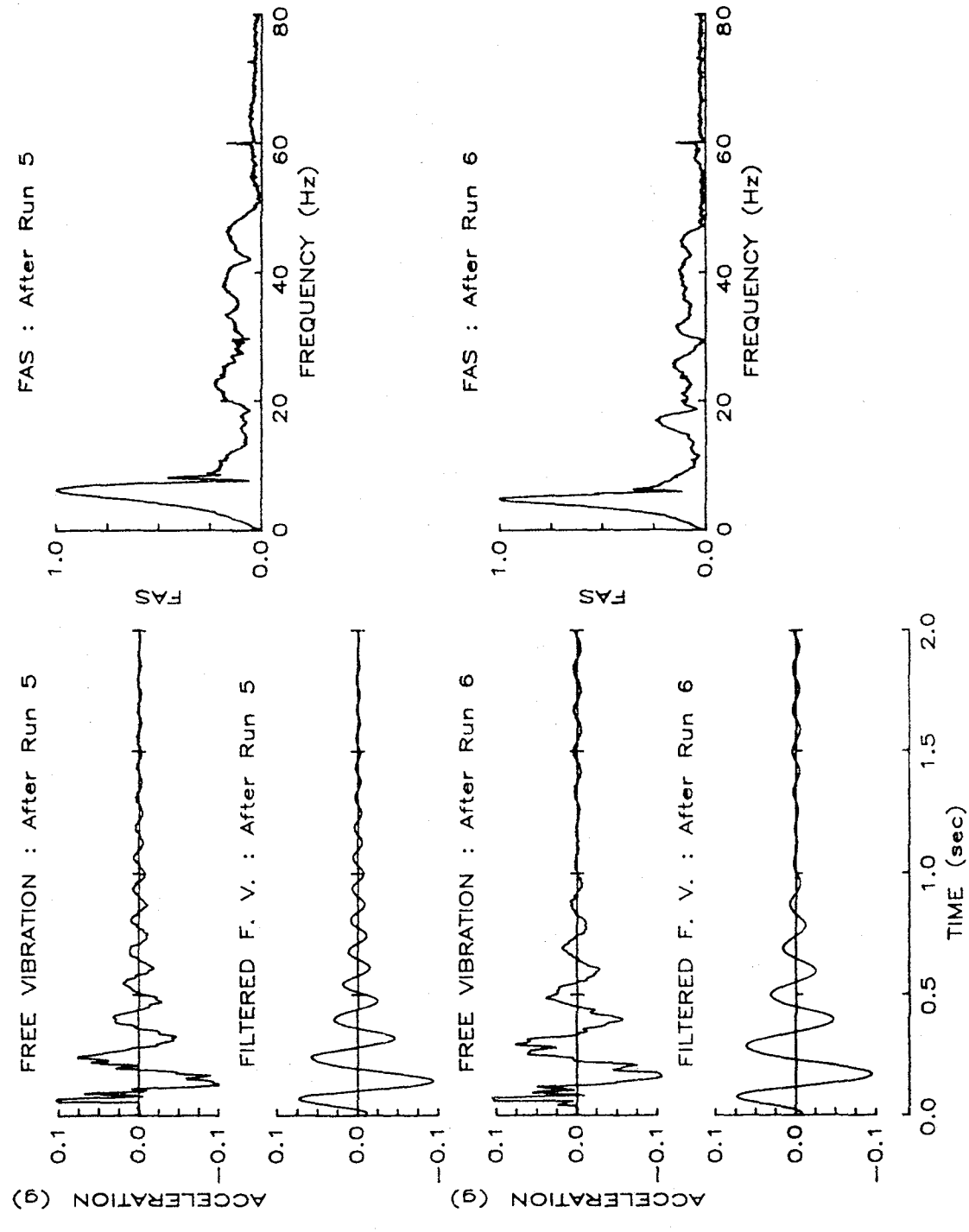

c) After Runs 5 & 6

Figure 4.23 (cont) Free Vibration : Top-Level Acceleration Response of RM3

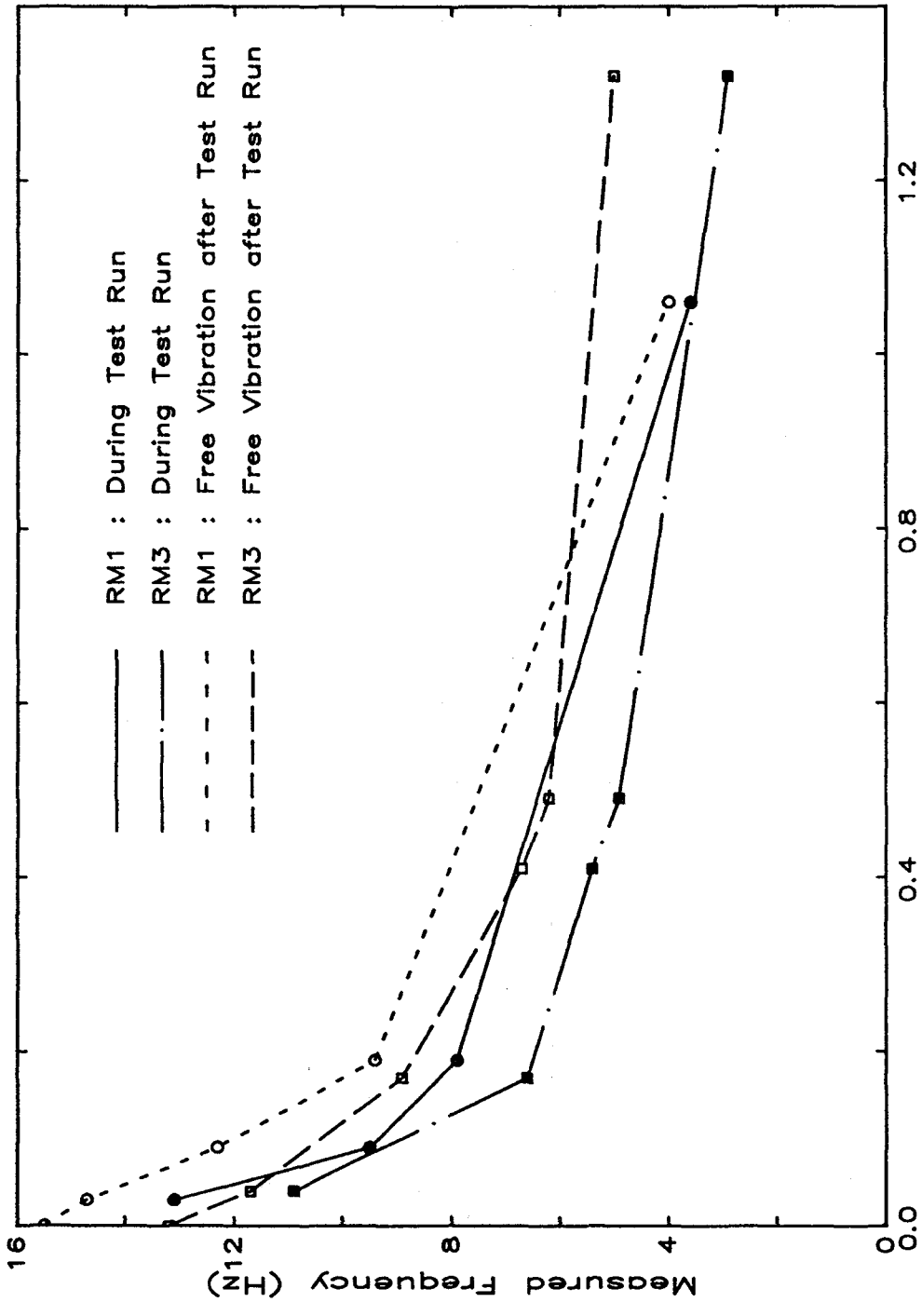

Figure 5.1 Change in Frequency with Test Run

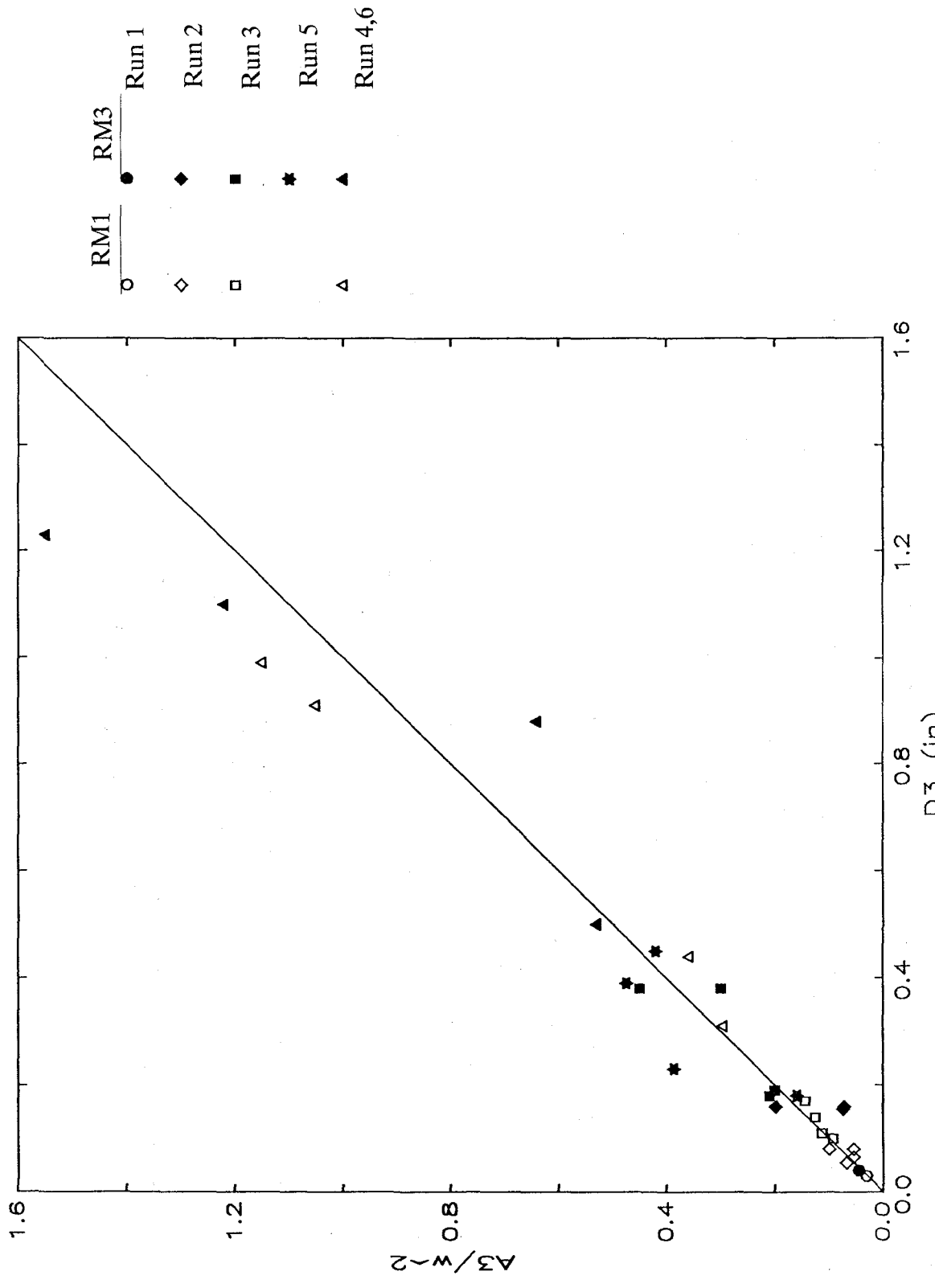

Figure 5.2 Response Maxima and Linear Approximation

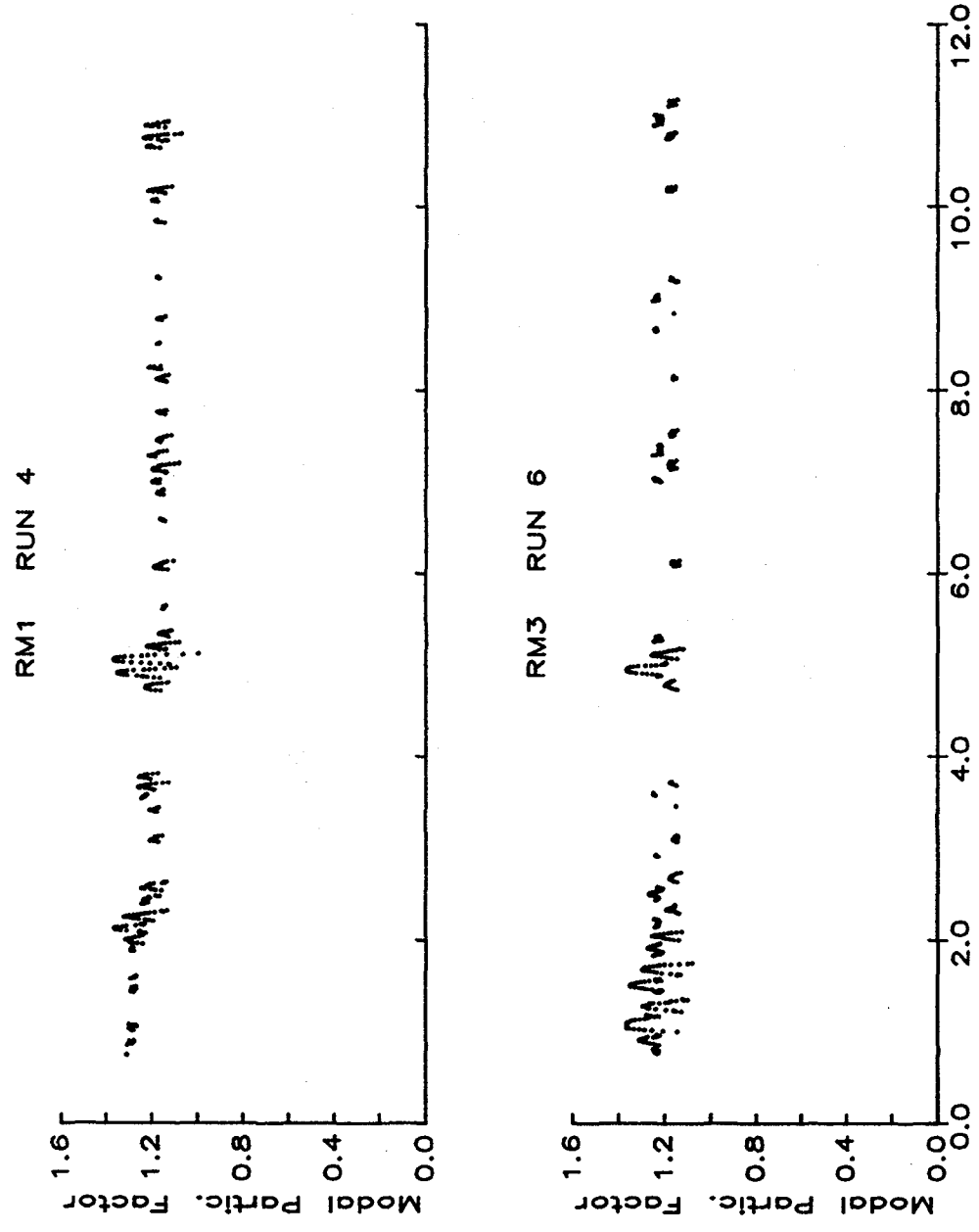

Figure 5.3 First-Mode Participation Factors from Deflected Shapes

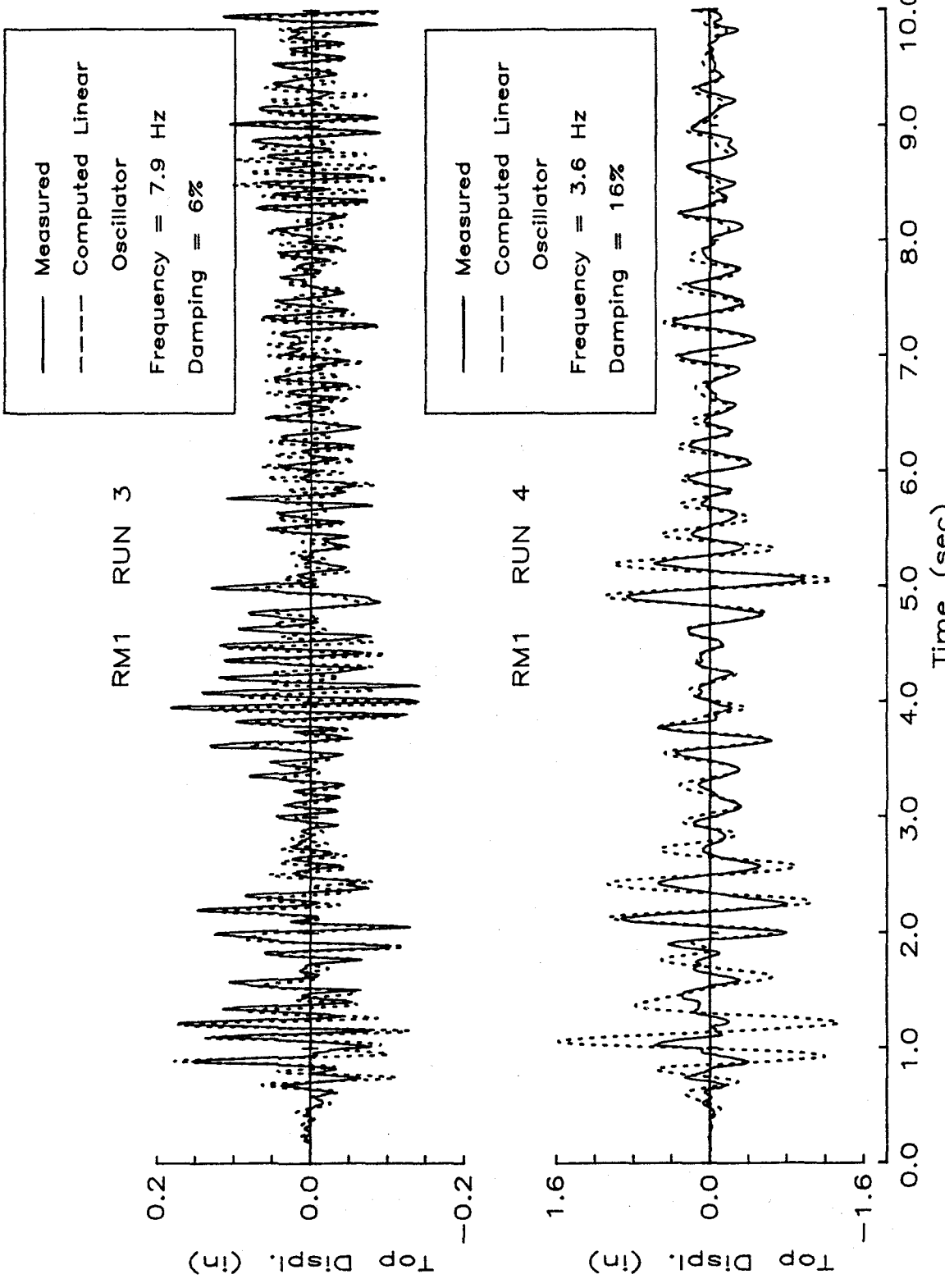

Figure 5.4 Calculated and Measured Top-Level Displacement
a) RM1 Runs 3 and 4

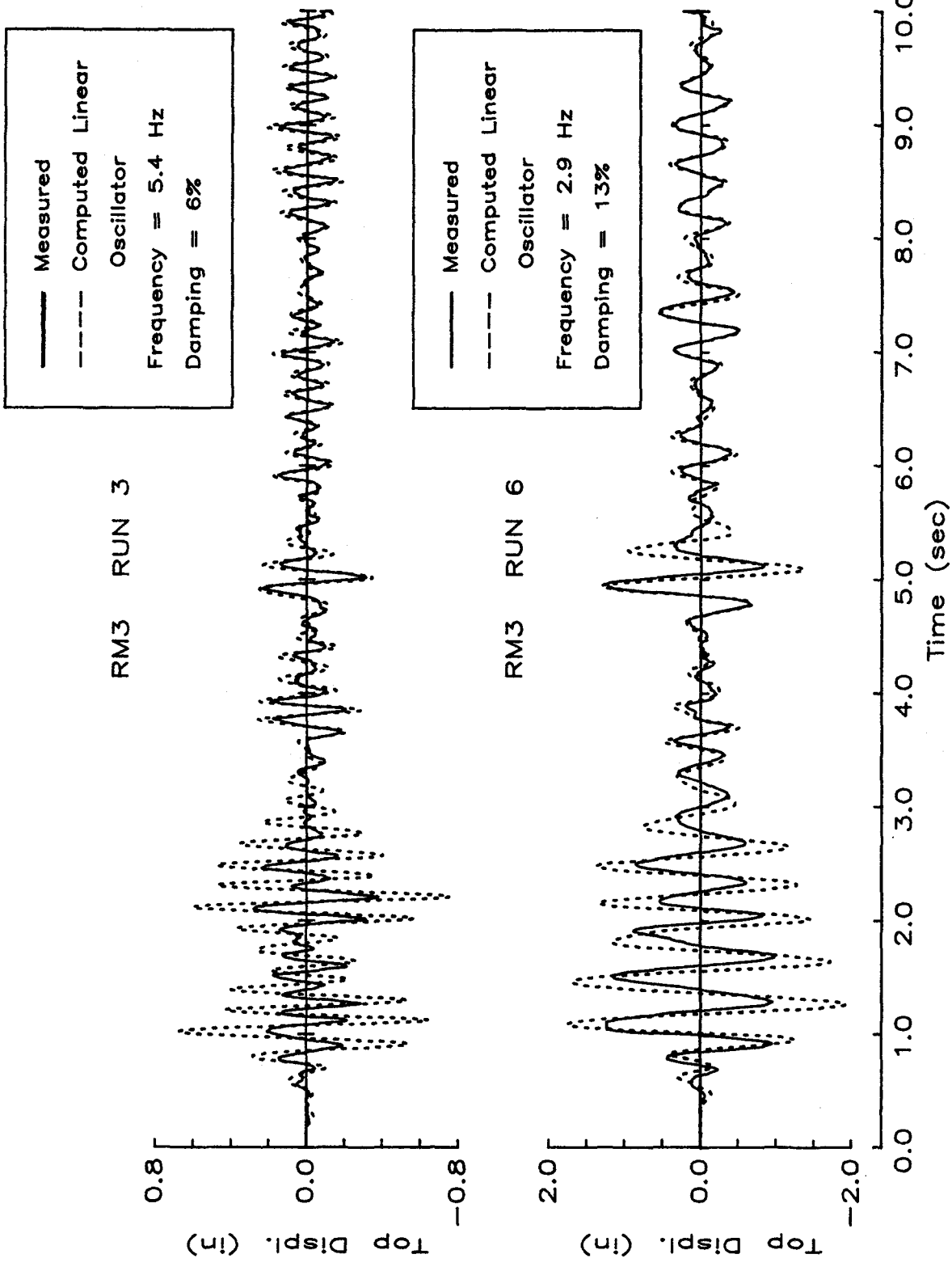

b) RM3 Runs 3 and 6

Figure 5.4 Calculated and Measured Top-Level Displacement

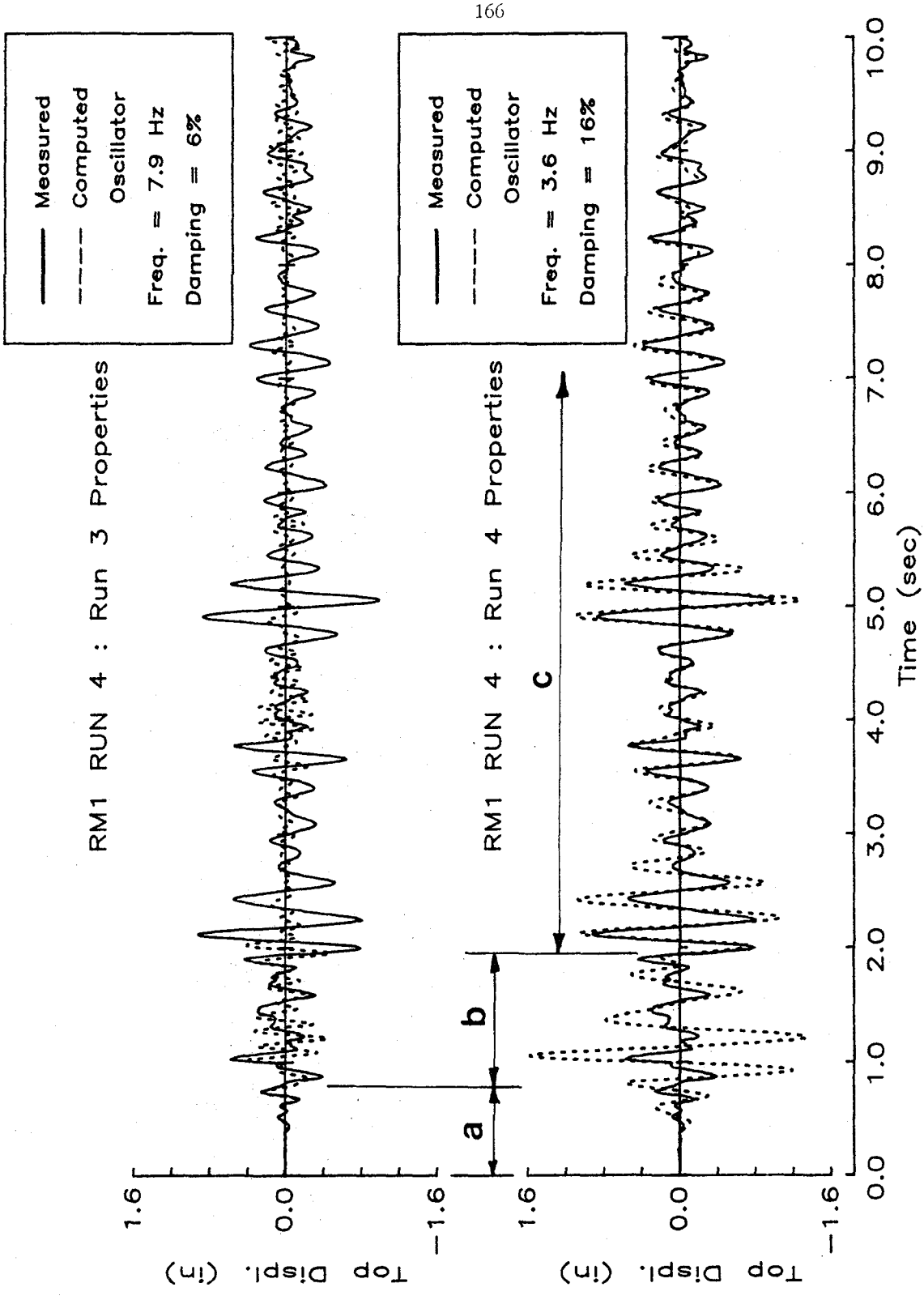

c) RM1 Run 4

Figure 5.4 Calculated and Measured Top-Level Displacement

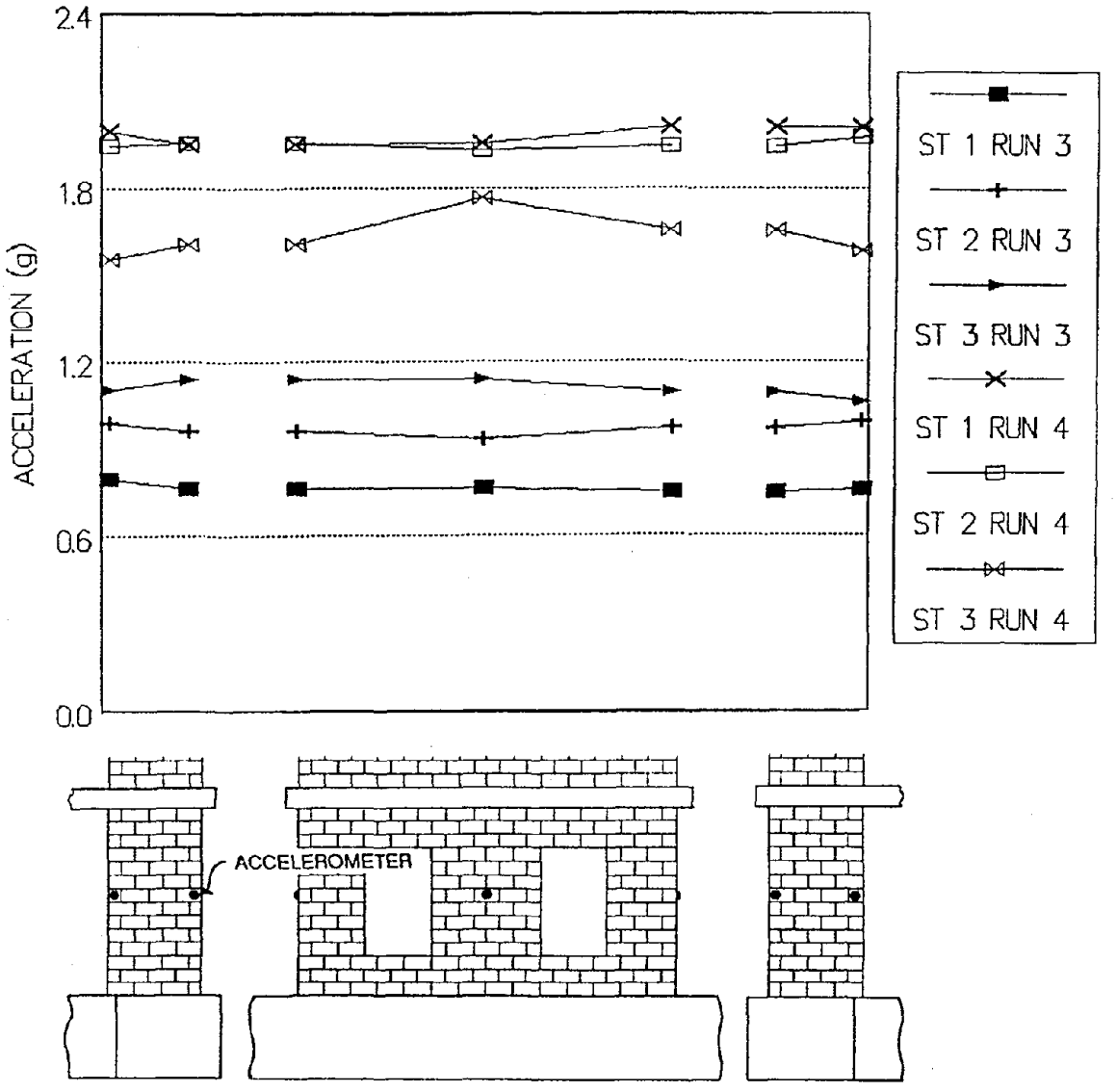

Figure 5.5 Distribution of Acceleration Across Story (RM1)

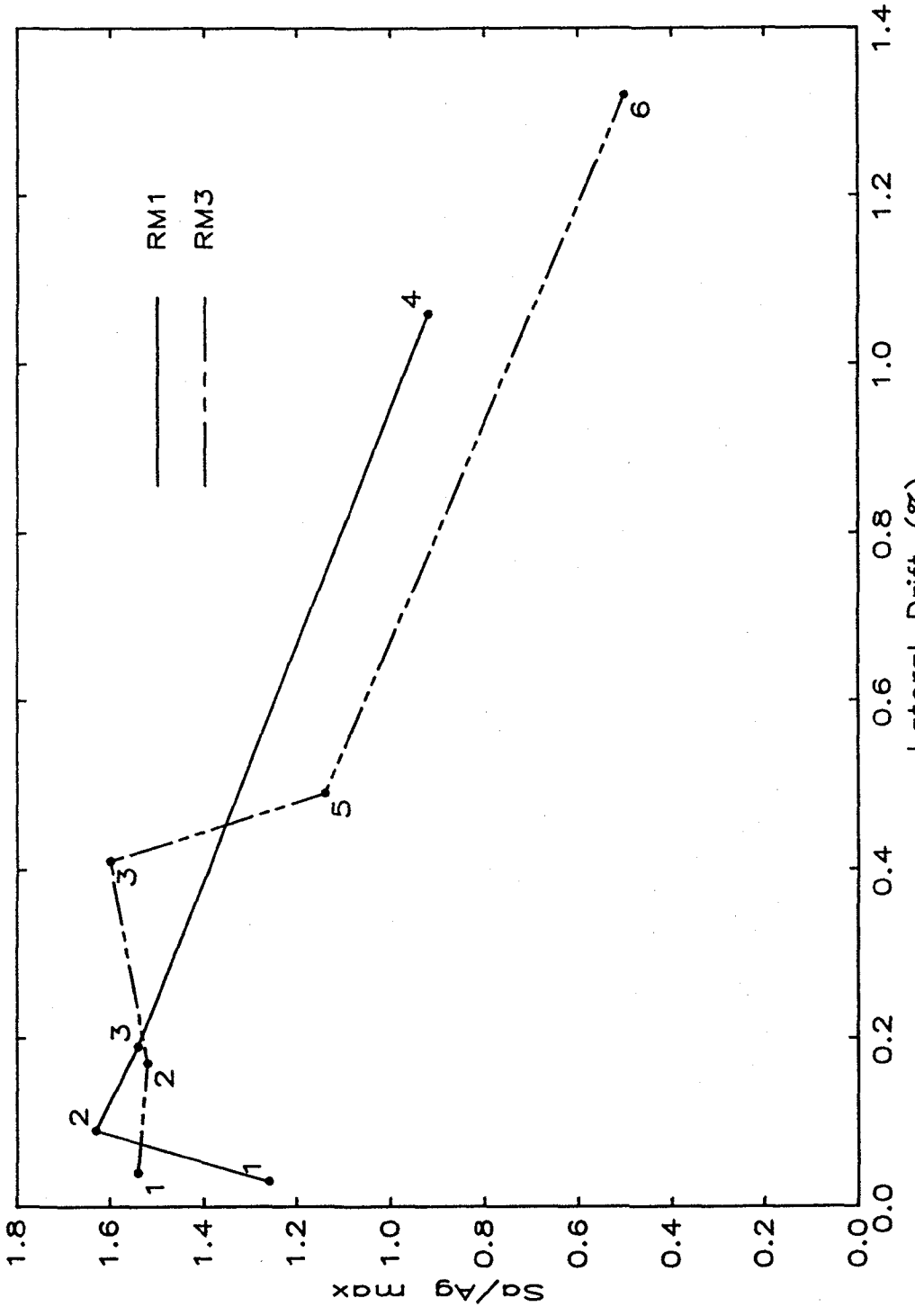

Figure 5.6 Amplification of Base Acceleration with Lateral Drift

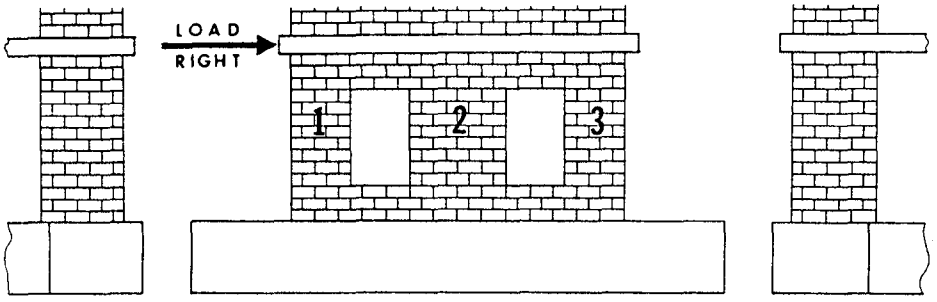

a) Structure RM1

Load Direction	Pier	Distribution Factor	
		Uncracked	Cracked
Right	1	.27	.34
	2	.46	.47
	3	.27	.19
Left	1	.27	.19
	2	.46	.47
	3	.27	.34

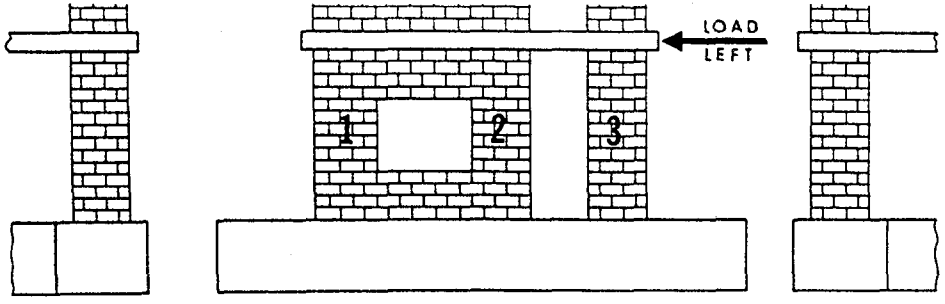

b) Structure RM3

Load Direction	Pier	Distribution Factor	
		Uncracked	Cracked
Right	1	.47	.62
	2	.41	.34
	3	.11	.04
Left	1	.47	.48
	2	.41	.42
	3	.11	.10

Figure 5.7 Shear Distribution Predicted by Pier Model

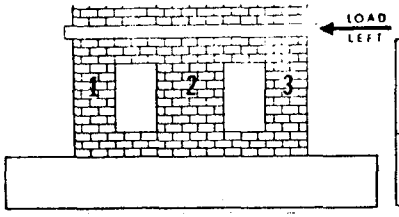

Load Direction	Pier	Distribution Factor		
		Pier Model		Test
		Uncracked	Cracked	(LVDT's)
Left	1	.27	.19	.07
	2	.46	.47	.28
	3	.27	.34	.62

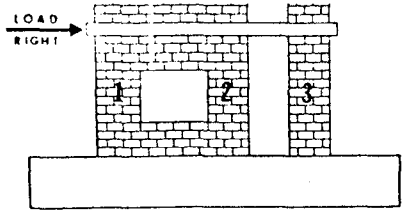

Load Direction	Pier	Distribution Factor		
		Pier Model		Test
		Uncracked	Cracked	(LVDT's)
Right	1	.47	.62	.15
	2	.41	.34	.08
	3	.11	.04	.70

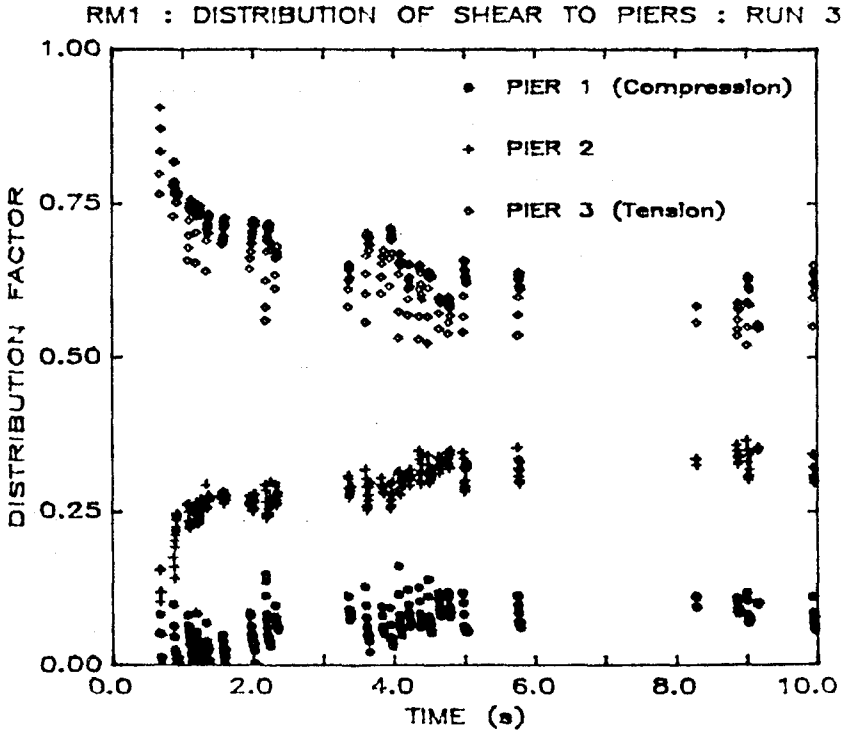

a) RM1 Run 3

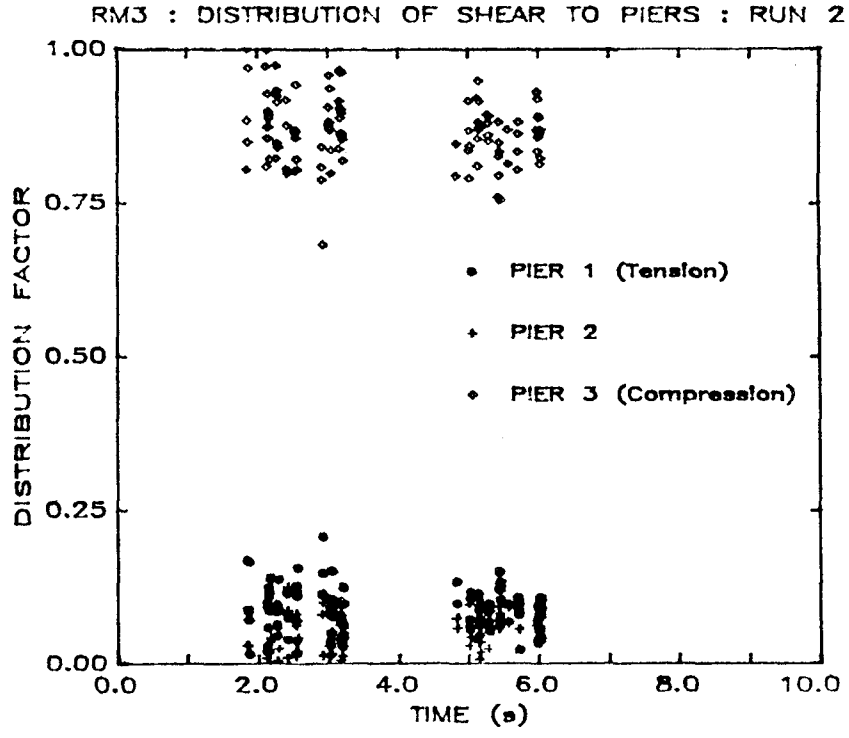

b) RM3 Run 2

Figure 5.8 Distribution of Story Shear to Individual Piers

a) Run 3

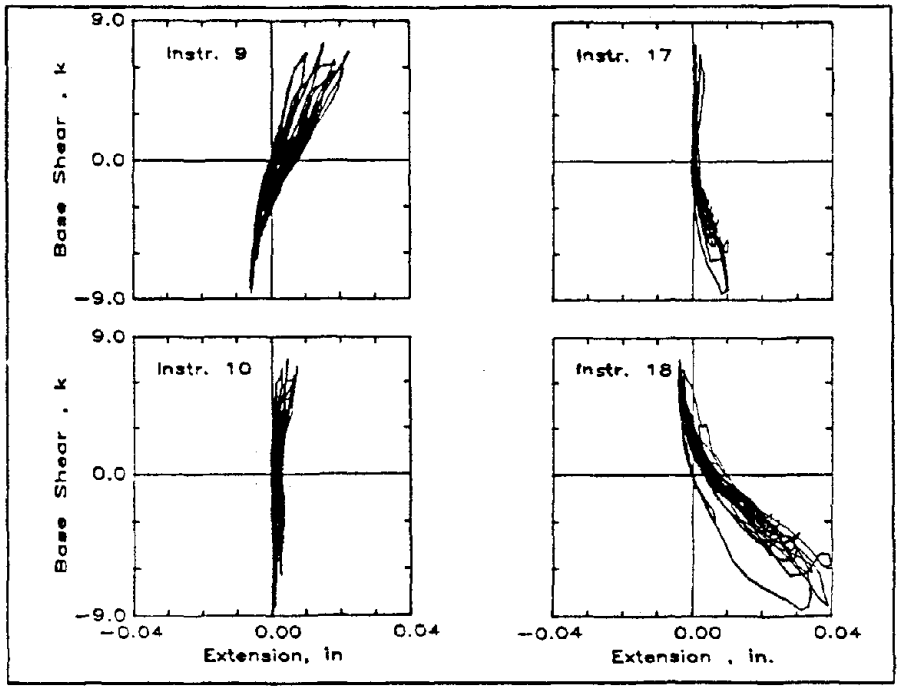

b) Run 4

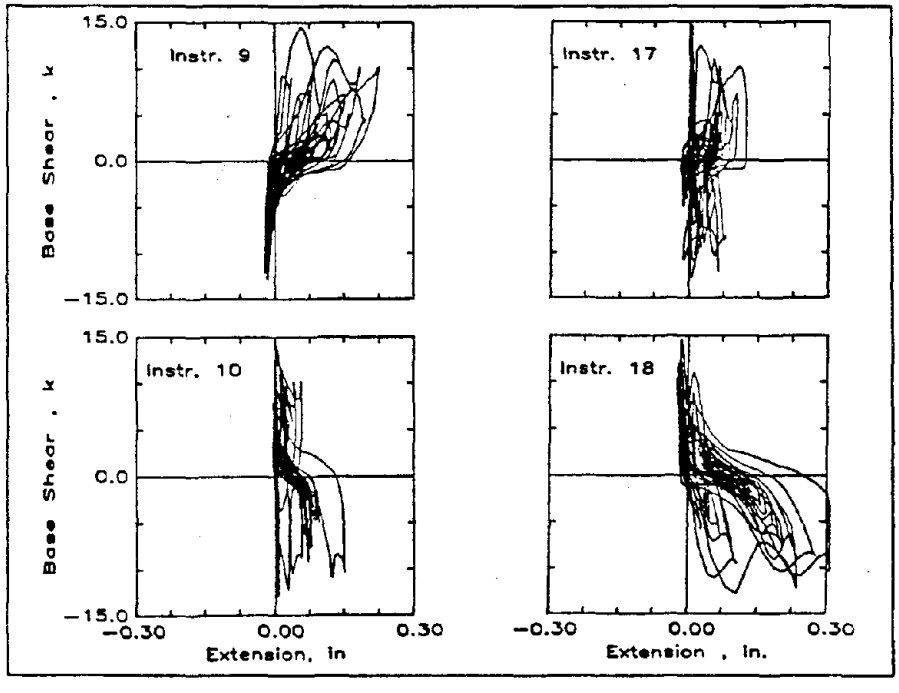

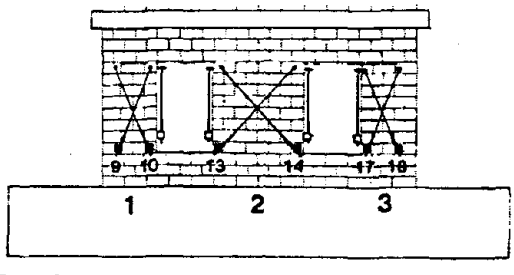

Figure 5.9 Base Shear vs. Diagonal Distortion (RM1)

a) Run 3

b) Run 6

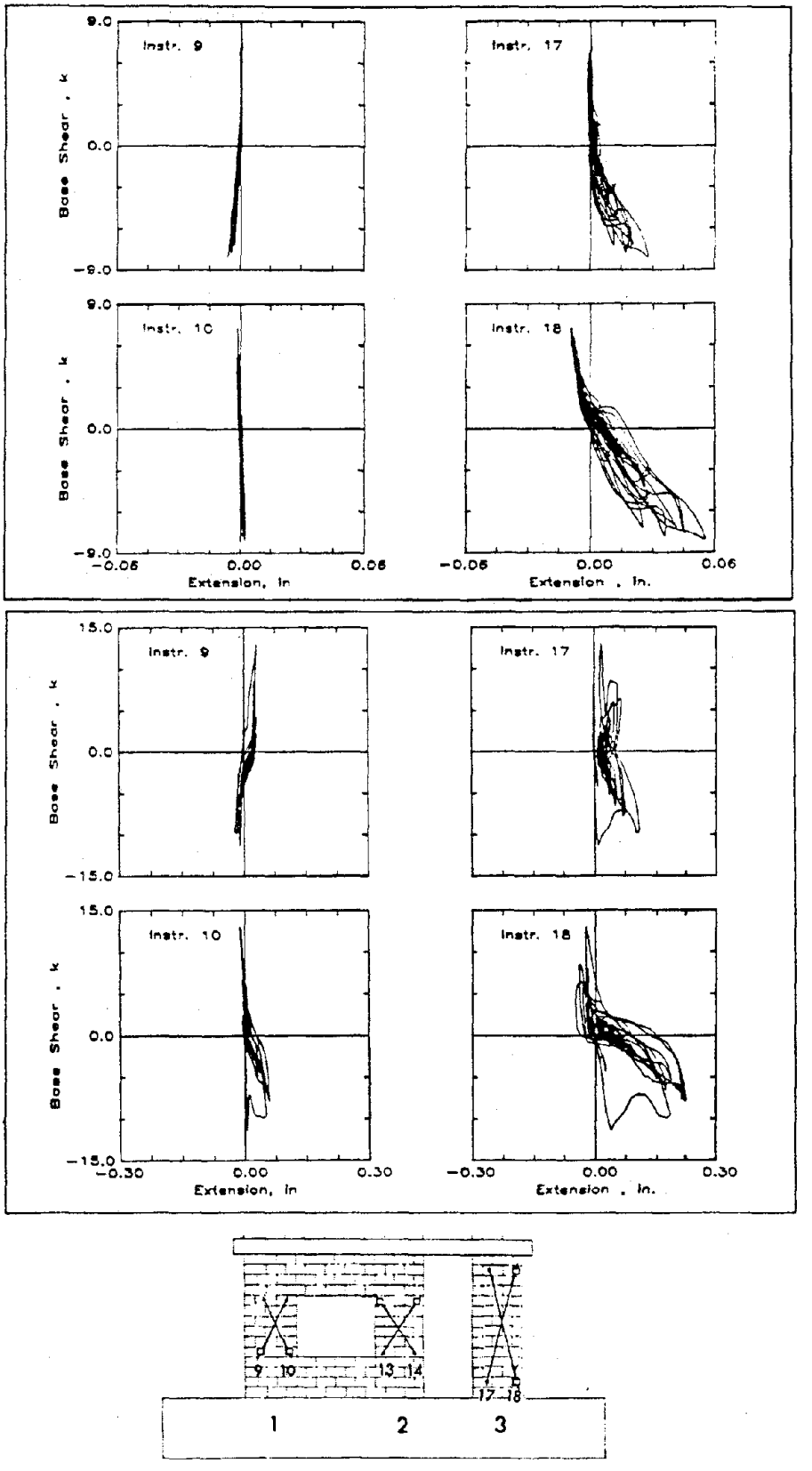

Figure 5.10 Base Shear vs. Diagonal Distortion (RM3)

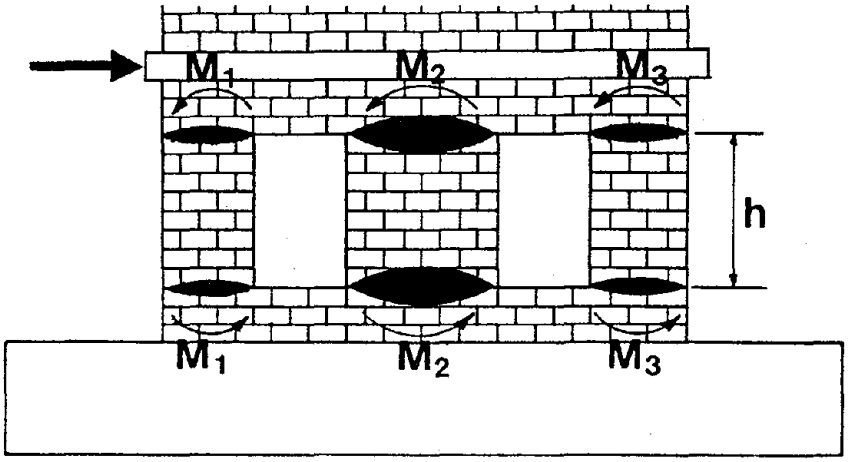

a) Structure RM1

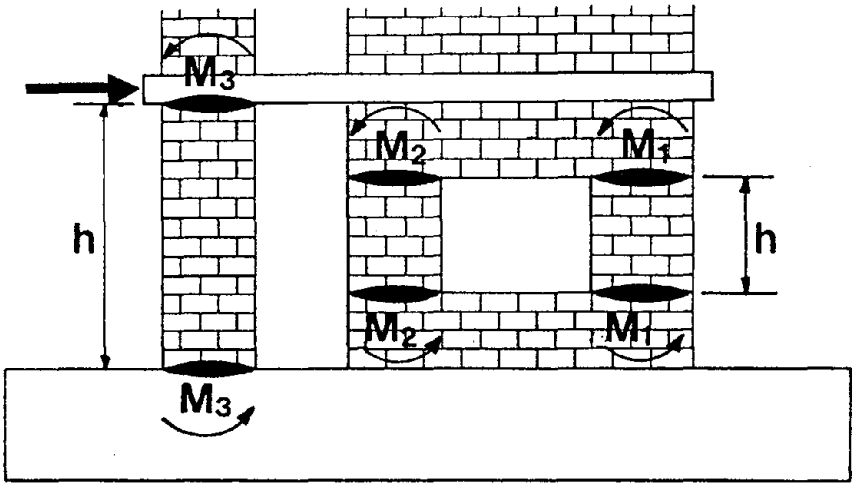

b) Structure RM3

Figure 6.1 Assumed Collapse Mechanism

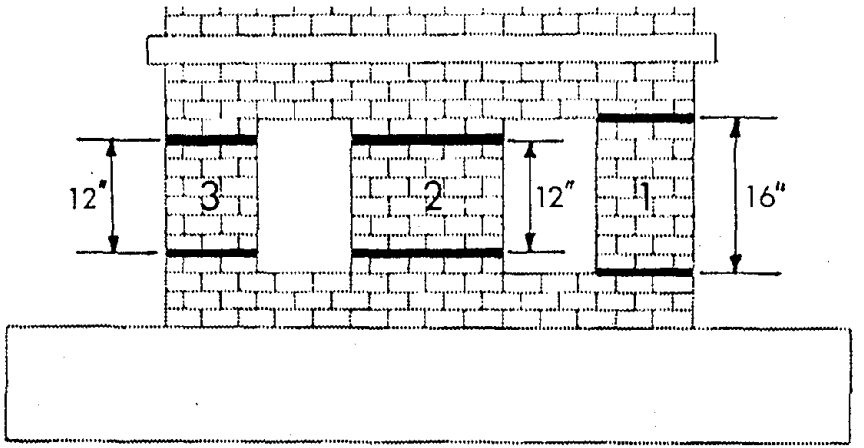

NORTH WALL

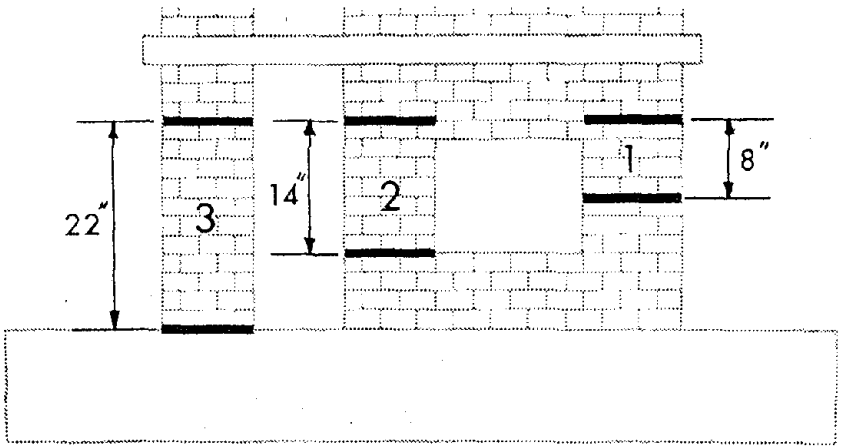

NORTH WALL

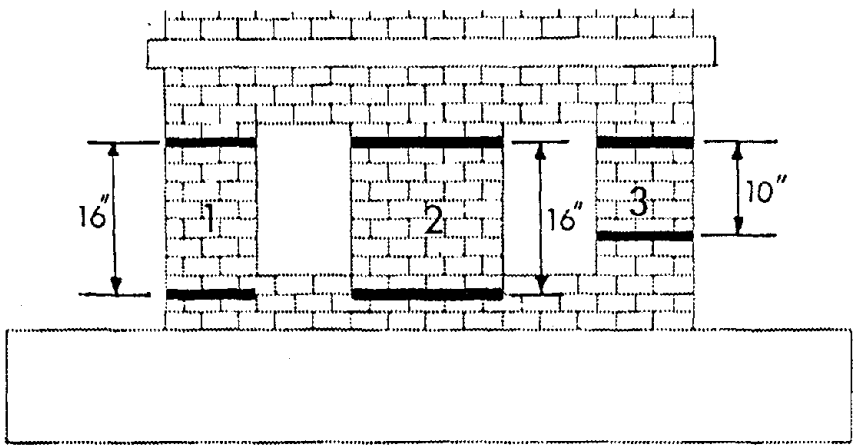

SOUTH WALL

a) Structure RM1

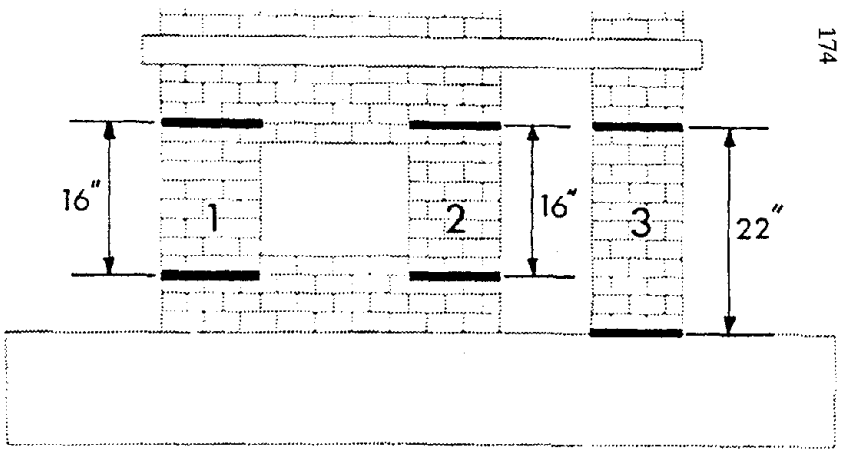

SOUTH WALL

b) Structure RM3

Figure 6.2 Observed Pier Heights

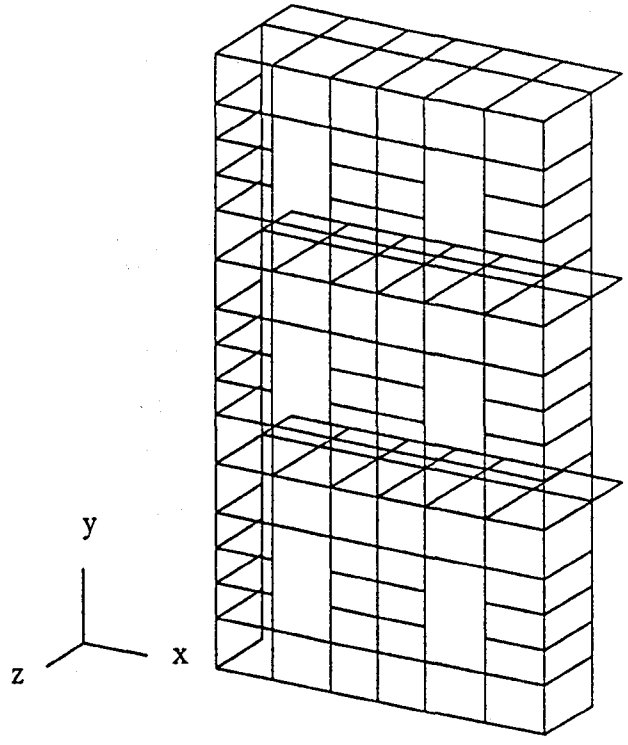

a) Structure RM1

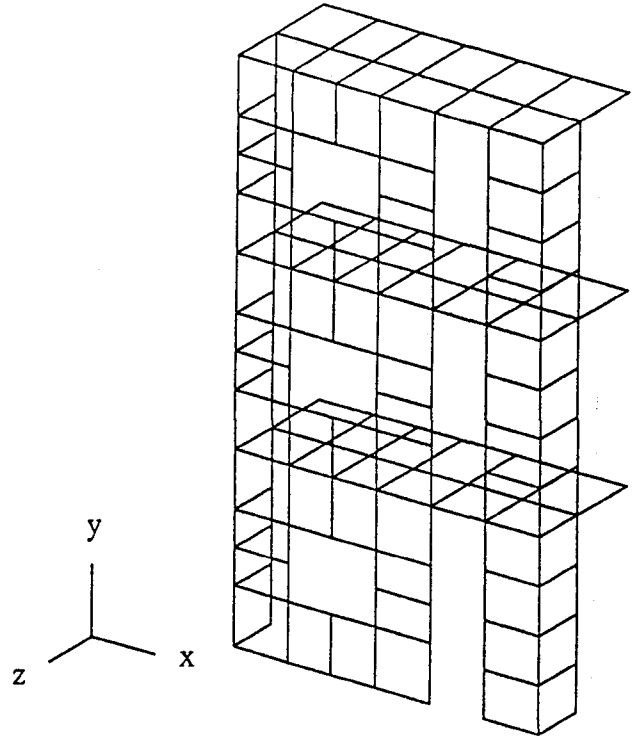

b) Structure RM3

Figure 6.3 Finite Element Meshes

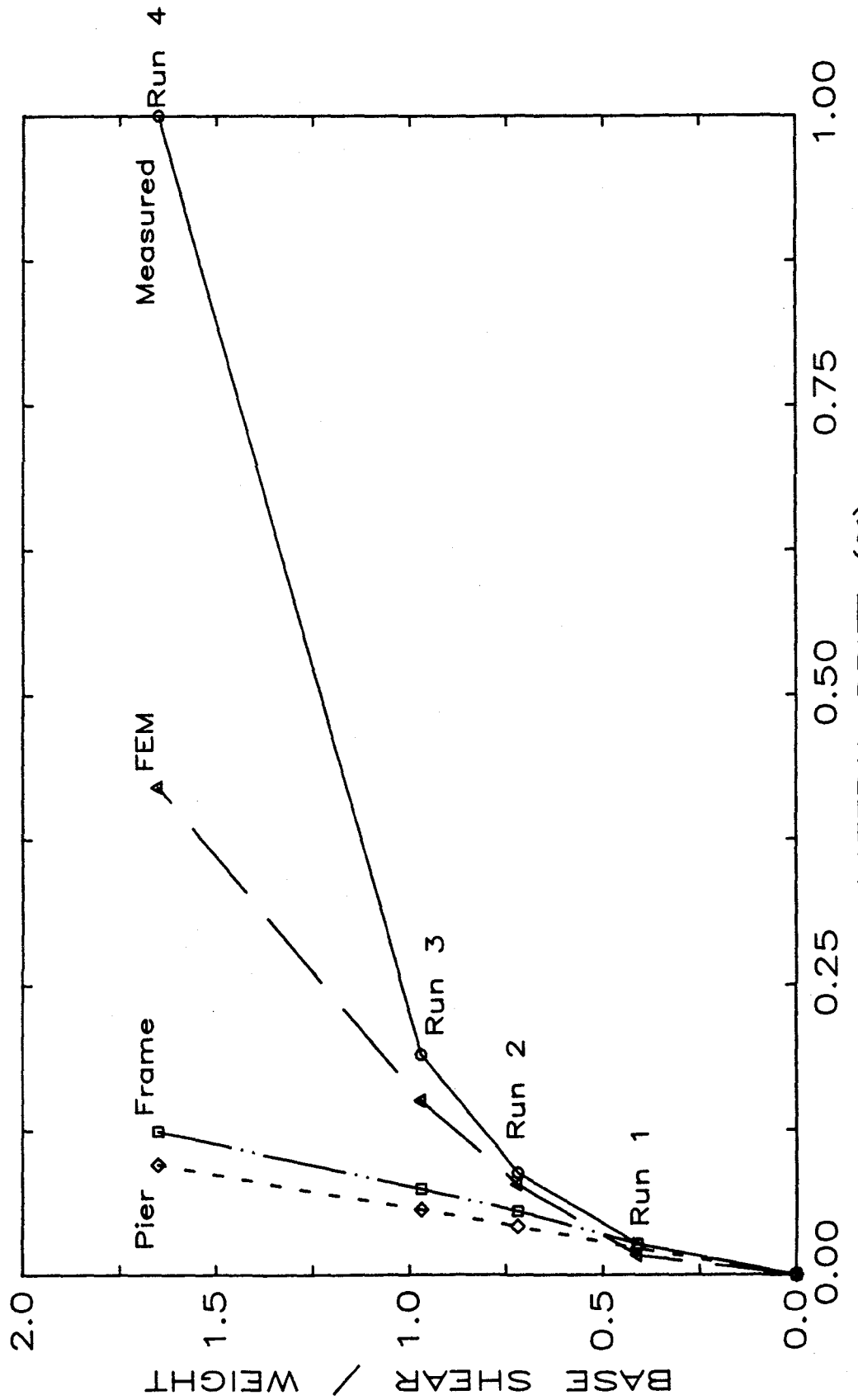

Figure 6.4 Measured and Calculated Lateral Drift (RM1)

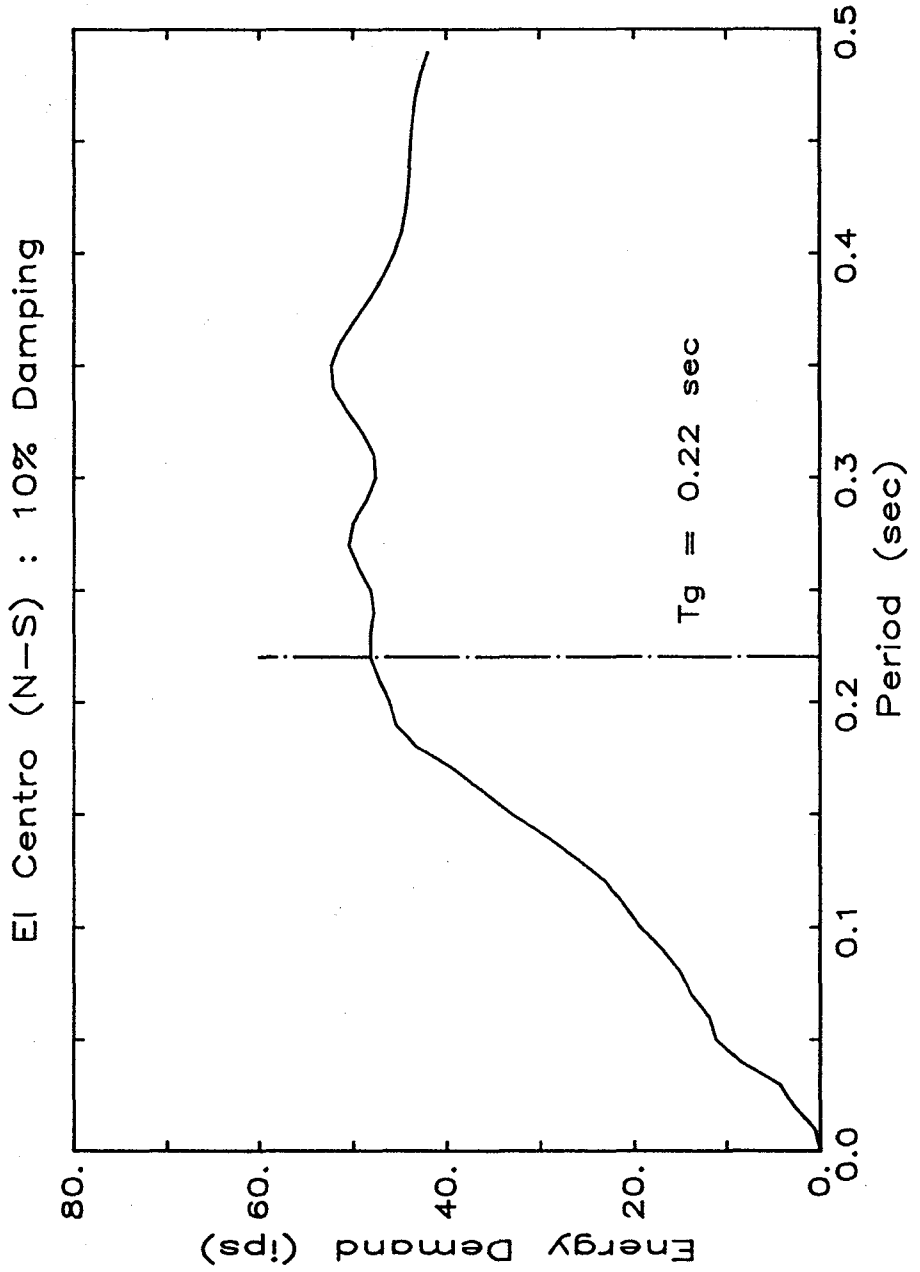

Figure 6.5 Energy Demand Response Spectrum for Test Base Motions

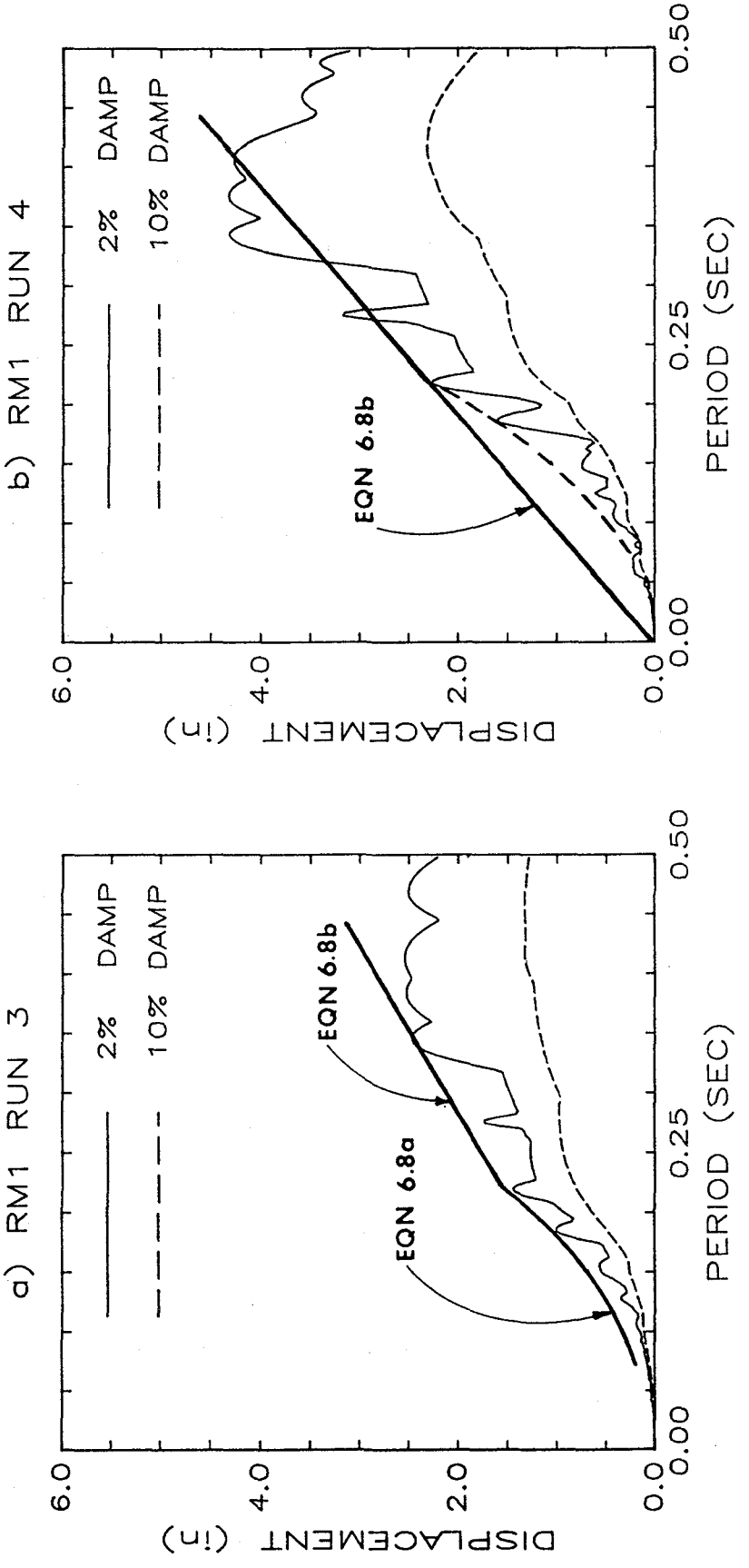

Figure 6.6 Calculated and Idealized Linear Displacement Response Spectra

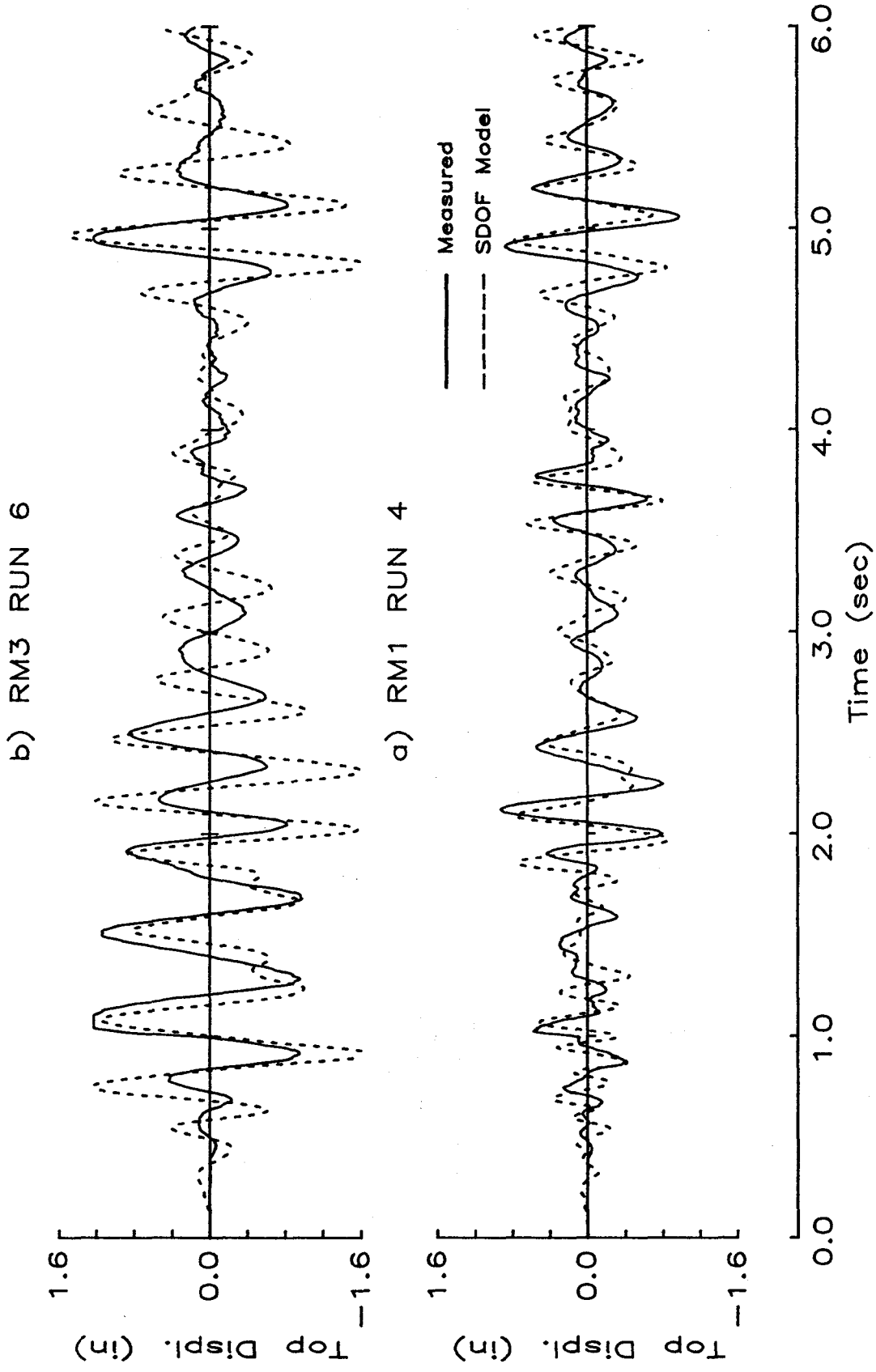

Figure 6.7 Measured and Calculated Top-Level Displacement

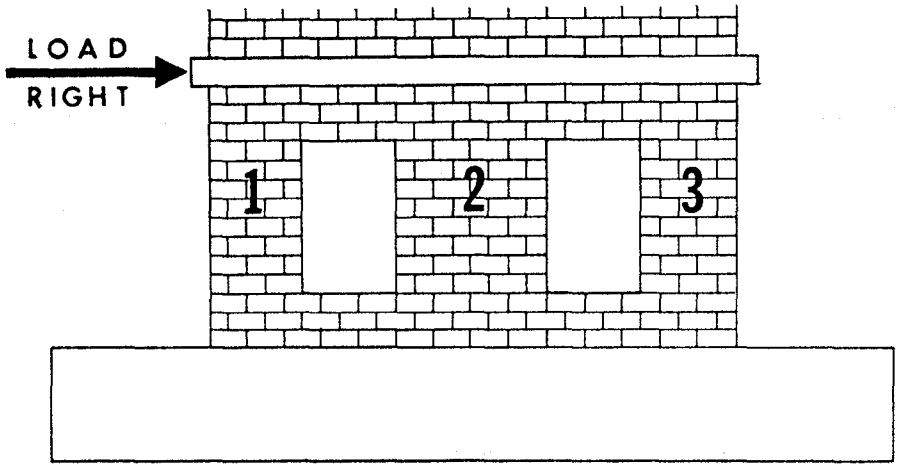

a) Structure RM1

Load Direction	Pier	Percent of Story Shear [1] Axial Load not Considered (Pier Model)	Percent of Story Shear [2] Axial Load Considered
Right	1	27	0
	2	46	51
	3	27	49
Left	1	27	49
	2	46	51
	3	27	0

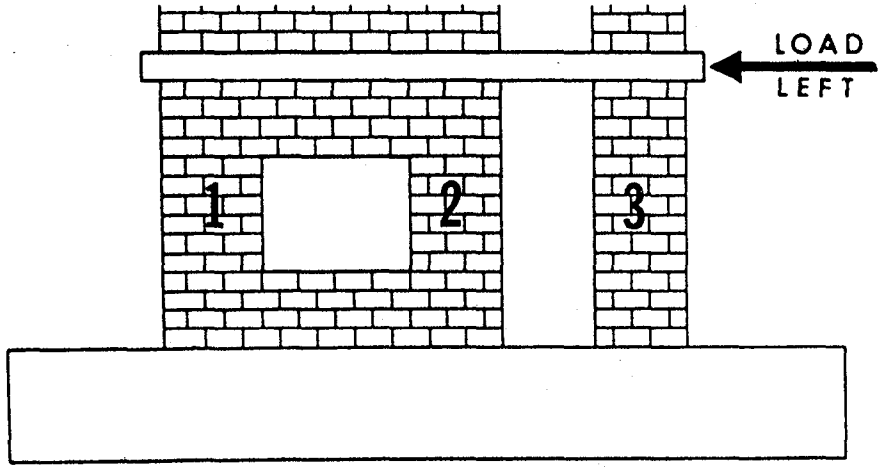

b) Structure RM3

Load Direction	Pier	Percent of Story Shear [1] Axial Load not Considered (Pier Model)	Percent of Story Shear [2] Axial Load Considered
Right	1	47	0
	2	41	56
	3	11	44
Left	1	47	65
	2	41	35
	3	11	0

Figure 7.1 Shear Distribution Predicted by Two Methods

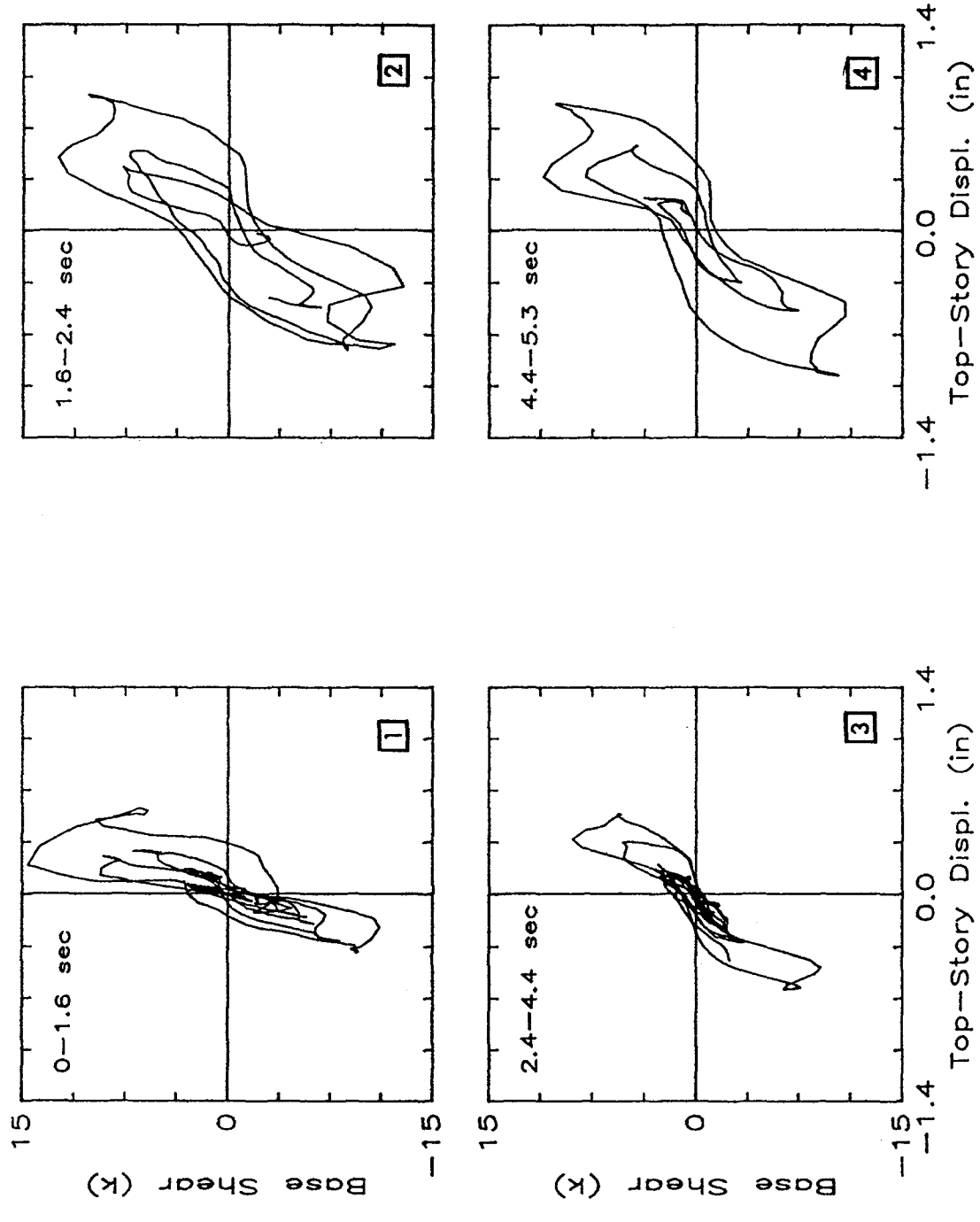

Figure 7.2 Base Shear and Top-Level Displacement (RM1 Run 4)

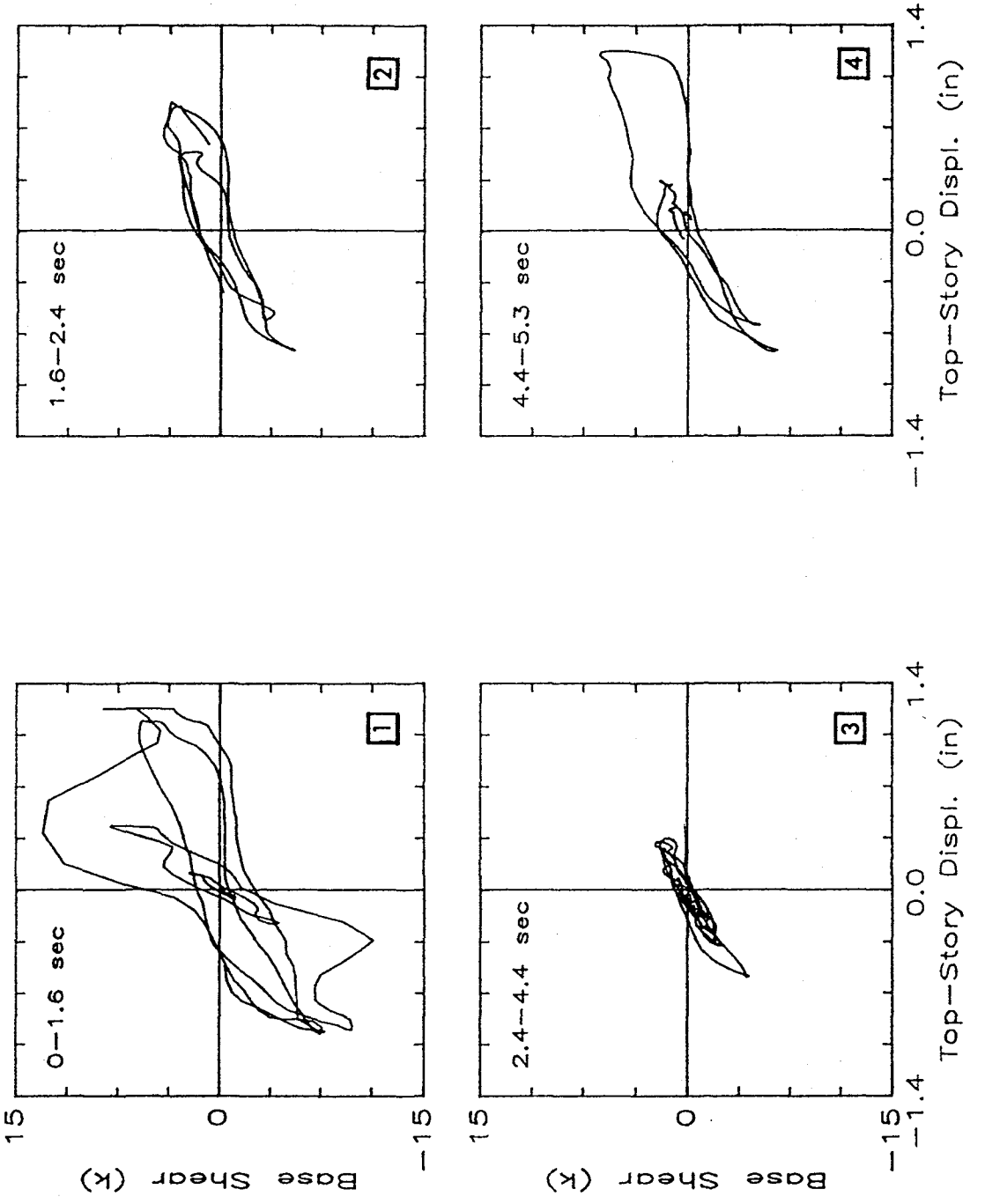

Figure 7.3 Base Shear and Top-Level Displacement (RM3 Run 6)

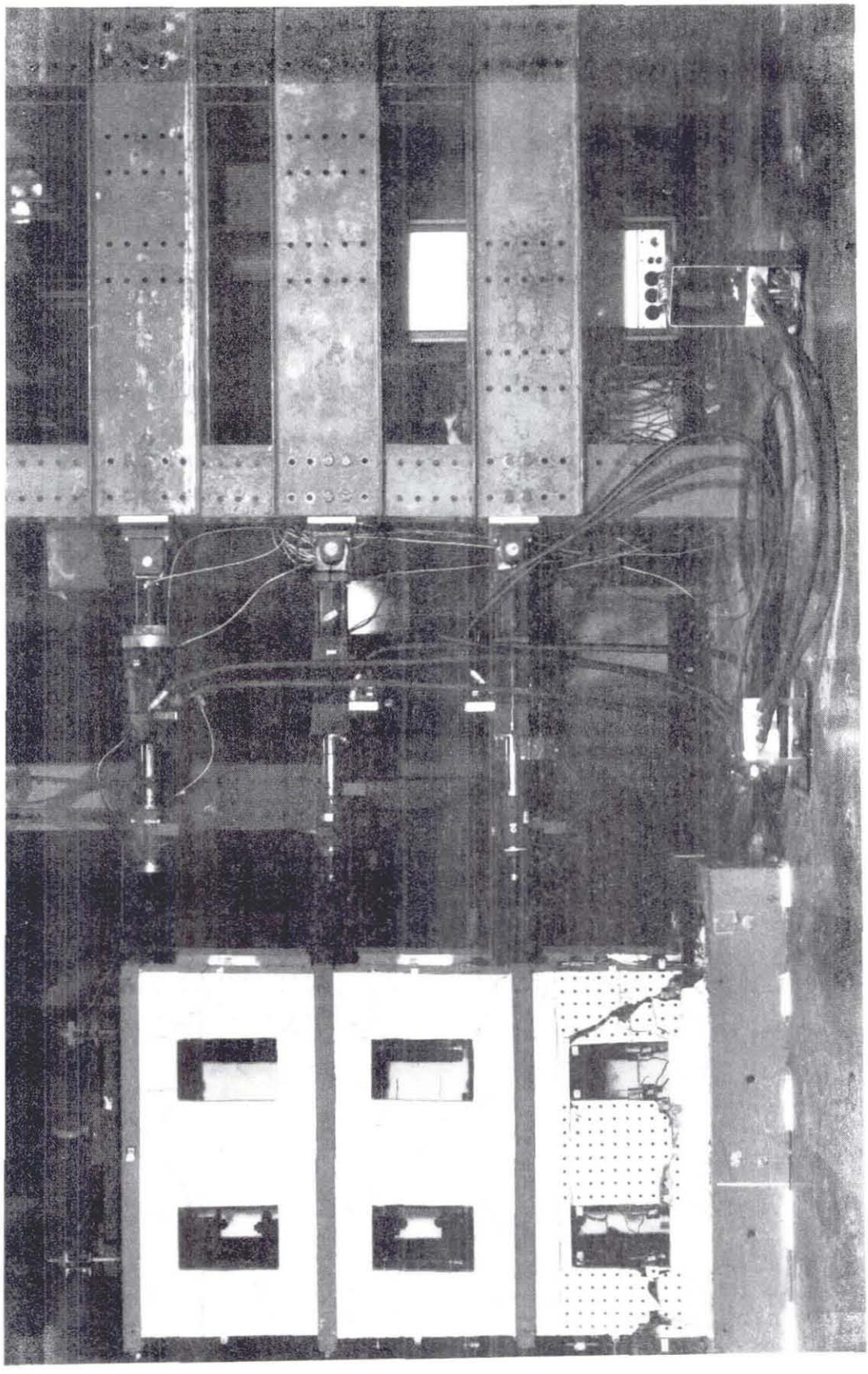

Figure 8.1 Static Test Setup

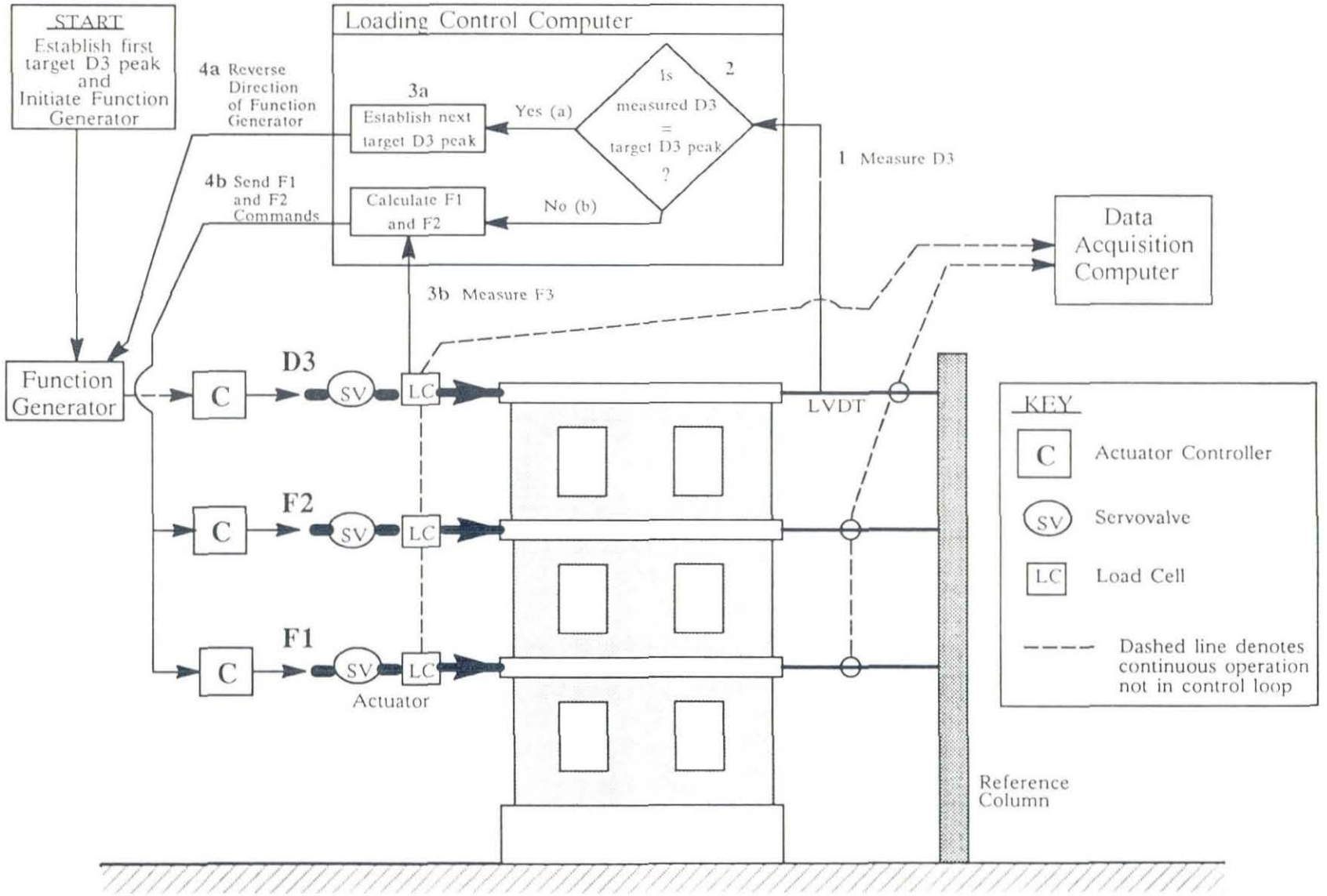

Figure 8.2 Loading Control System

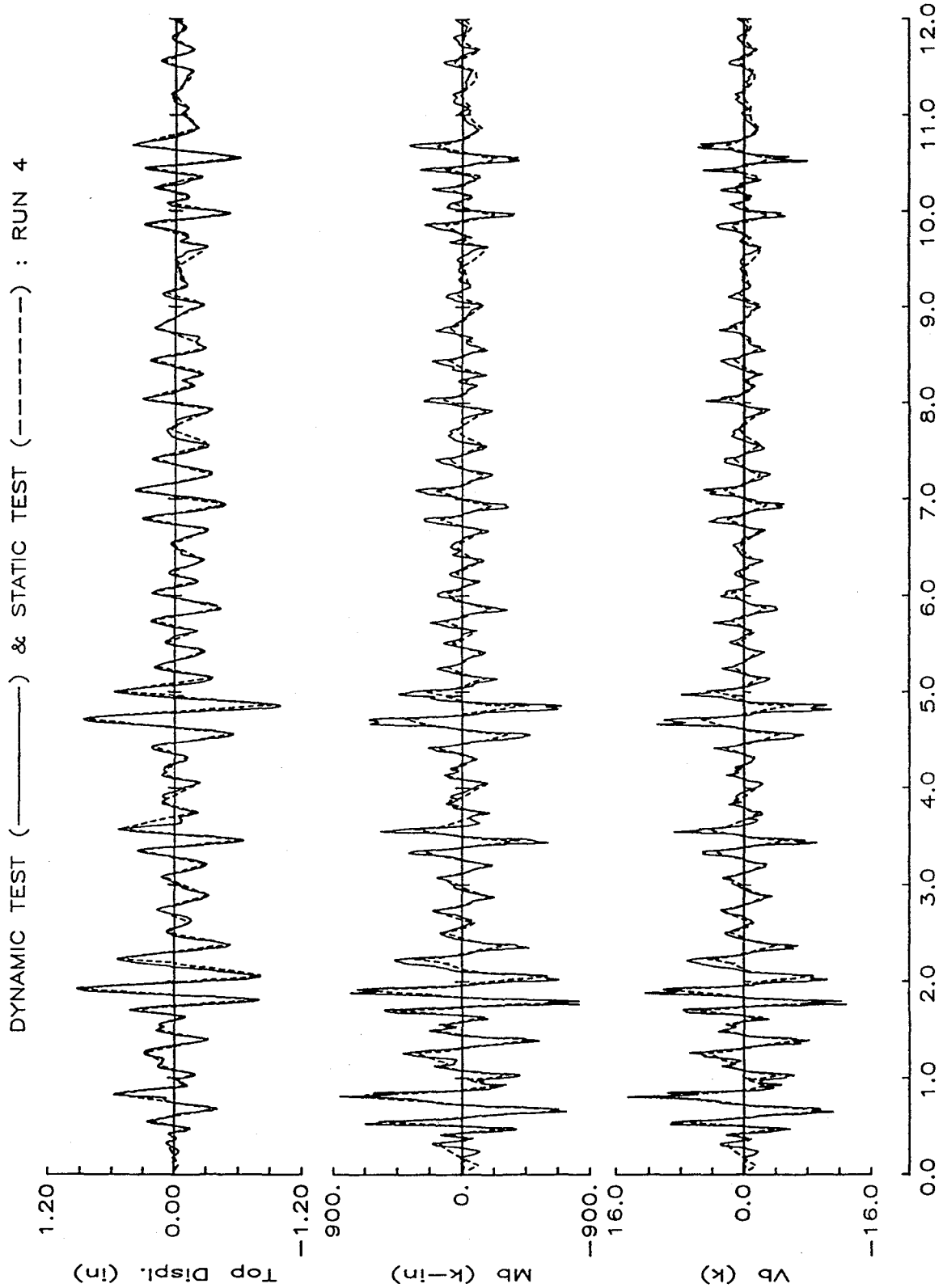

Figure 8.3 Static and Dynamic Response Histories

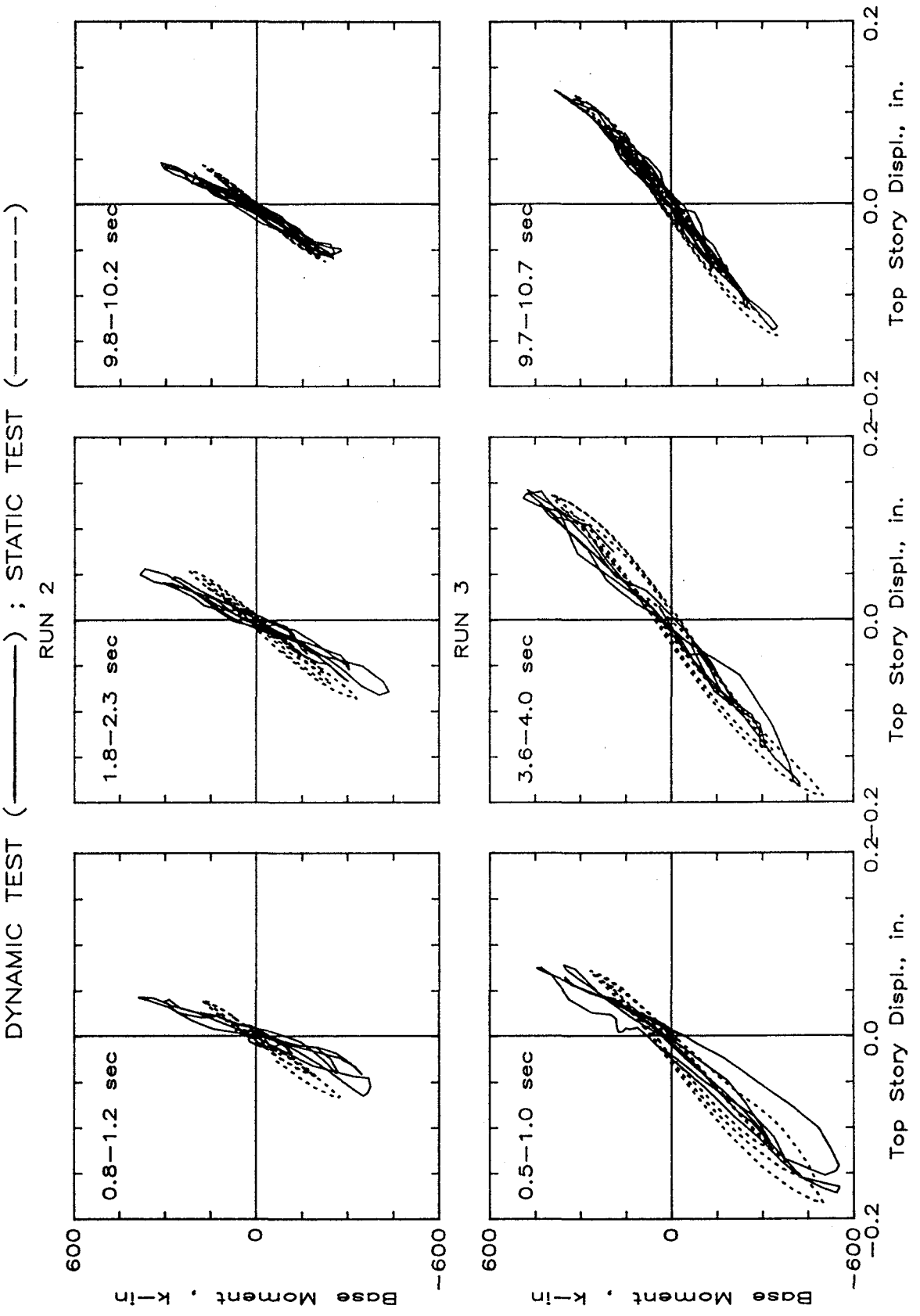

Figure 8.4 Base Moment vs. Top-Level Deflection (Runs 2 and 3)

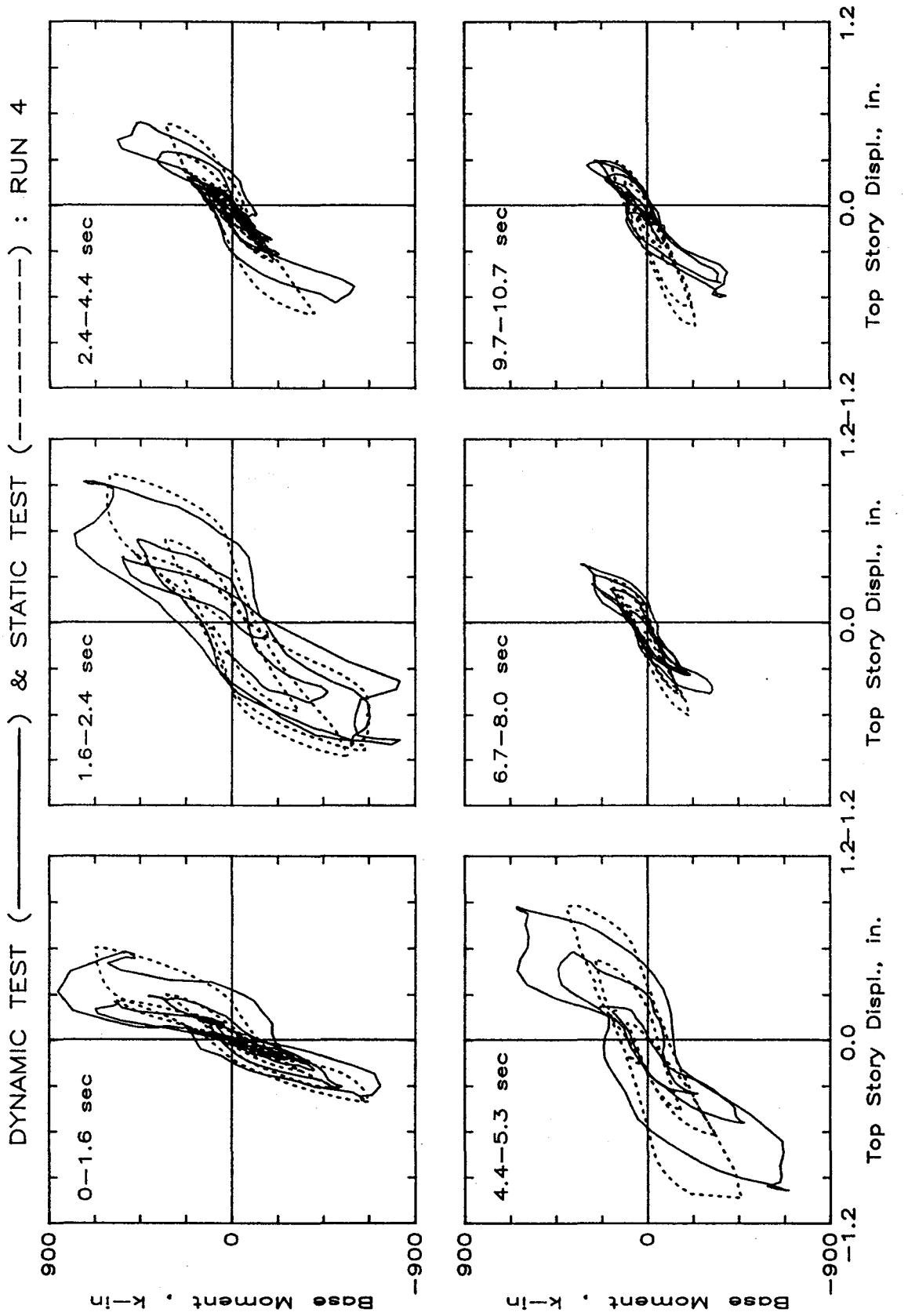

Figure 8.5 Base Moment vs. Top-Level Deflection (Run 4)

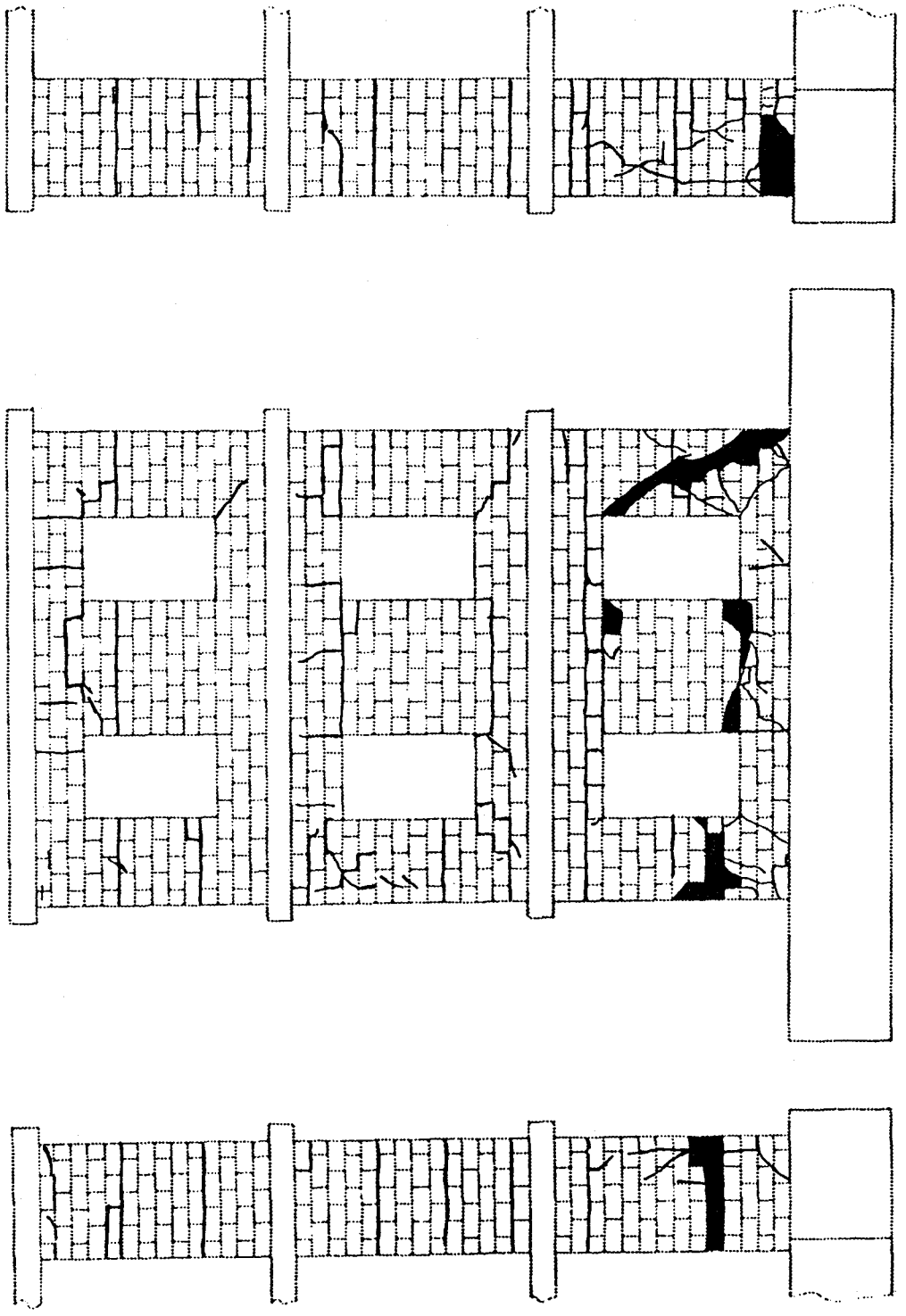

Figure 8.6 Final Crack Pattern (Static Test)

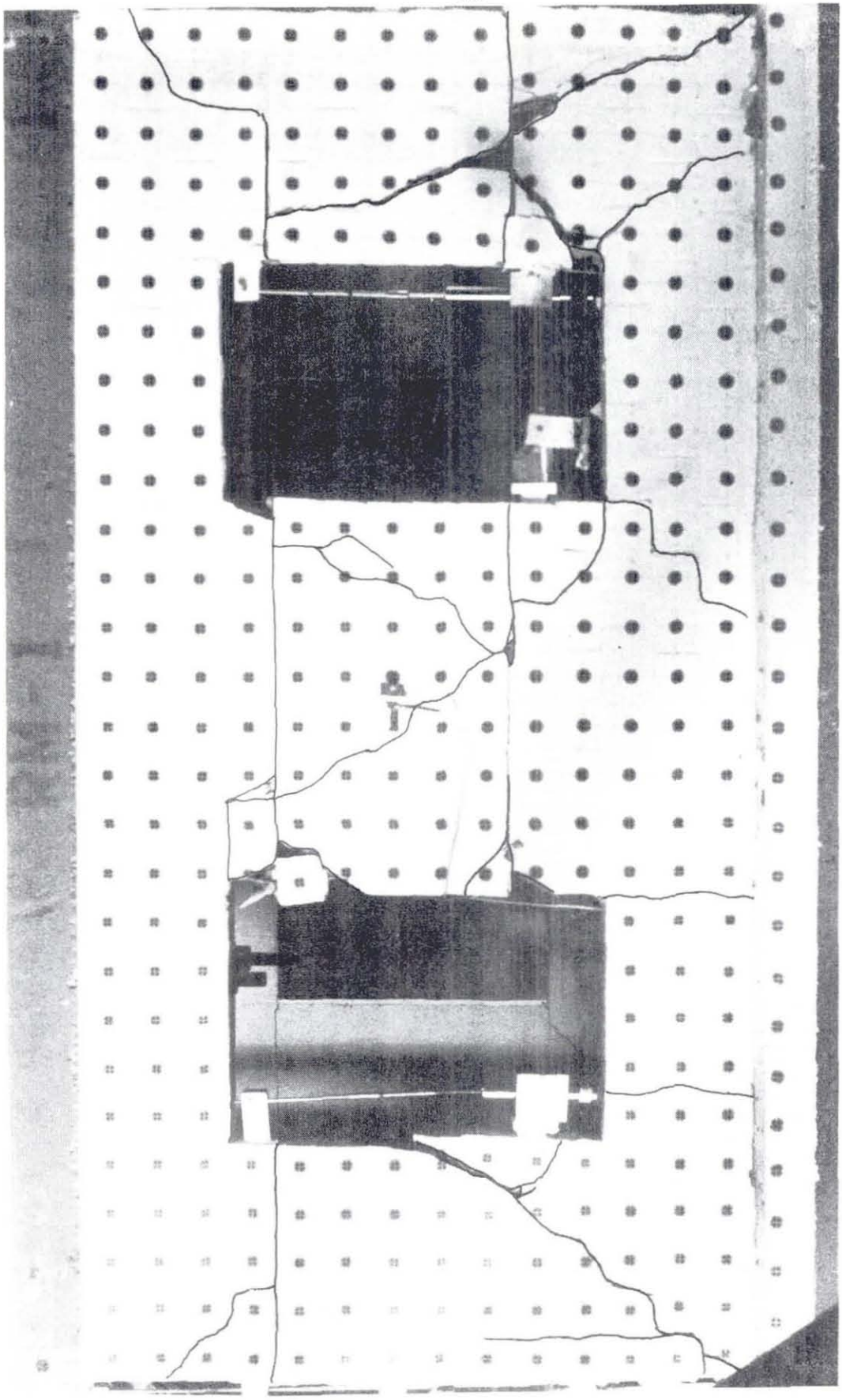

a) Dynamic Specimen (RM1)

Figure 8.7 Final Damage Pattern of Base Story

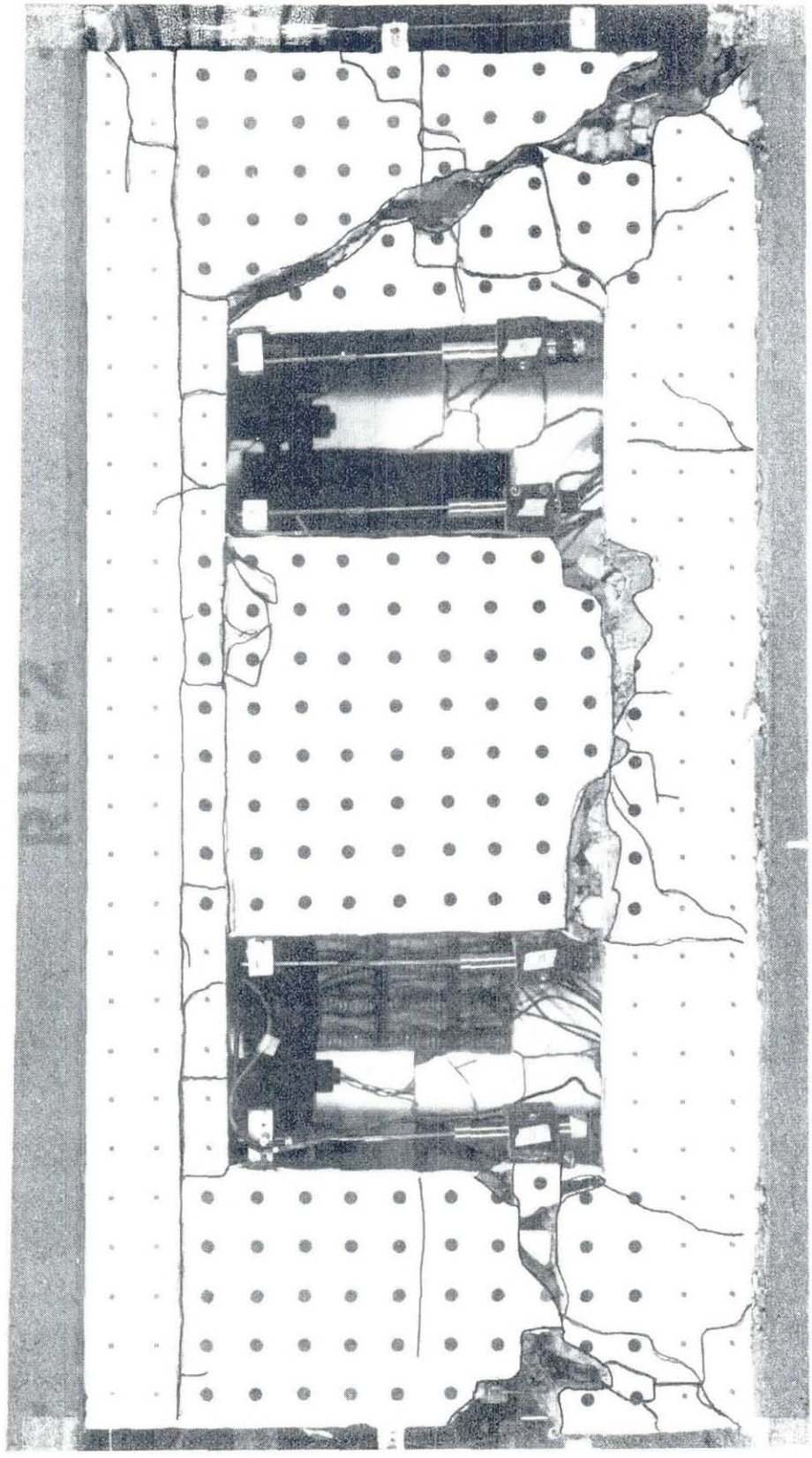

b) Static Specimen (RM2)

Figure 8.7 Final Damage Pattern of Base Story

APPENDIX A

DESCRIPTION OF TEST STRUCTURES

This appendix presents information regarding the physical characteristics of the test structures. Details of the construction materials are given in Appendix B and the test apparatus, instrumentation, and data acquisition and data reduction are described in Appendix C.

A.1 Configuration

Each of the three test specimens consisted of an identical pair of three story reinforced masonry structural walls (Figs. A.1 and A.2). Each wall had flanges, and was perforated with window and/or door openings. In all tests, the structures were oriented such that lateral forces were applied parallel to the primary plane of the walls.

Test specimens were identical in configuration with the exception of the size and location of the openings, and the width of the flanges. The walls of structures RM1 and RM2 were perforated with a symmetrical pattern of window openings, while walls of structure RM3 had an asymmetrical pattern of window and door openings. The flanges of RM1 and RM2 were 40% wider than those of RM3. Nominal dimensions of the test structures are given in Figs. A.1 and A.2.

Reinforced concrete floor slabs were cast at each floor level. Steel plates were fixed to the top and bottom of the slabs to increase inertial forces during dynamic tests and to increase vertical compressive stresses. The structures were tied to stiff base girders which were bolted to the earthquake simulator to provide a fixed-base condition.

A.2 Weight

Thick steel plate assemblages ("story masses") were added at each of the three floor levels. The story masses were placed on the top and bottom of each floor slab and bolted together through holes in the slab so that the centroid of the mass would be coincident with

the center of the slab. The configuration of the story masses was the same for all three test specimens.

For structure RM2 it was not possible to place the connection bolts through the plate assemblages due to interferences with the static test apparatus. Consequently, a harness system consisting of steel threaded rods and channel sections was used to secure the masses to the floor slabs.

The story masses and harnesses were weighed on a Toledo platform scale. A summary of the weight measurements is presented in Table A.1.

Weights of walls and floor slabs were measured so that the total specimen weight and the tributary weight acting at each floor level could be determined. For structure RM3, these weights were determined by lifting the specimen with a 20-ton overhead crane after completion of construction of each wall or floor slab. A load cell made of strain gauges was placed between the lifting hook of the crane and the pick-up point of the specimen. Differences in microstrain output were read from a Vishay digital strain indicator with the crane loaded and unloaded.

The same method was also used for structure RM1, however it was later determined that one of the strain indicator readings was in error. Consequently, wall and slab weights of RM1 were determined by a different method. Unit weights of masonry and concrete were obtained from masonry prisms and concrete cylinders cast at each stage of specimen construction. Measured dimensions of the walls and slabs were used to calculate volumes which were then multiplied by the unit weights to obtain total weights.

A summary of weight measurements is presented in Table A.2. Tributary weight at each floor level is also given as the sum of the floor slab, story mass and tributary wall weights at that level.

A.3 Construction of Specimen

Construction of the test specimens commenced in July, 1987 and all structures were completed by February, 1988. The date on which construction of each specimen was

completed is given in Table A.3. The same professional mason constructed each of the three specimens using the procedures and techniques described below.

A.3.1 Foundation

A concrete foundation grillage or "base girder" was constructed to support the test specimen and anchor the vertical wall reinforcement. The base girder was reinforced with four No. 4 reinforcing bars and No. 2-gage wire stirrups. Twelve vertical holes were blocked-out using 12-inch lengths of 1 1/2 in. diameter steel tubing. These holes permitted the base girder to be bolted to the simulator platform. Two horizontal holes, at midheight of the base girder, were also blocked-out with 16-inch lengths of tubing. Steel rods were later inserted into these holes so that the specimen could be lifted by an overhead crane. The base girder is shown in Fig. A.3.

Concrete for the base girder was mixed in the laboratory, placed by shovel, and consolidated with vibrators. After the concrete had set, the top surface was roughened to provide good bond with the first course of block. The grillage was covered with plastic and allowed to cure.

A.3.2 Reinforcement

Vertical reinforcement for the masonry walls was anchored to the base girder by providing a 90-degree hook around the bottom row of base girder reinforcement. The vertical reinforcement was No. 11-gage brite basic wire which was cleaned with a petroleum based solvent and then wiped with acetone. The location of vertical wires in each specimen was discussed in Section 2.3. Measured properties of the wire are presented in Section B.5. As discussed in Section 2.4.3, the vertical wall reinforcement was continuous from the base anchorage to the top of the structure. Consequently, a support system was required to prevent the 8 1/2 foot lengths of wire from bowing during construction. A wooden frame was built around the base girder which supported the wire at two points along its height (Fig. A.3).

Horizontal reinforcement was placed at midheight of pre-selected courses. Locations of this reinforcement were presented in Section 2.3. No. 11-gage wire was used and was cleaned with solvent and acetone. The wire was bent at wall-flange intersections so that it was continuous from wall section to flange section. Wires which terminated at an opening were anchored with a 90-degree hook into an adjacent block cavity. Since bond beam units were not available at the reduced scale, notches were cut in webs for placement of horizontal reinforcement.

A.3.3 Masonry Construction

The first course of block was laid on the base girder in the configuration shown in Fig. A.4. Each block was threaded over the top of the vertical wire, mortared and set in place by a professional mason. A story comprised fourteen courses of blocks. Excess mortar was removed from the cells of the blocks as they were placed. Grouting was done using a low-lift process after four or five courses were laid. High-lift grouting was not possible, since clean-out holes at the reduced scale would have been too small to be effective. Low-lift grouting was felt to result in better quality control with respect to placement of vertical reinforcement and grout.

A.3.4 Construction of Floor Slabs

Upon completion of a pair of walls, formwork and reinforcement for the floor slab were placed. Two No. 3 reinforcing bars were placed in each concrete slab directly above and parallel to each wall. No. 4 reinforcing bars, spaced at approximately six inches were placed perpendicular to the plane of the walls. Two sets of four PVC tubes were used to block-out vertical shafts which were necessary for the placement and fastening of the story masses. Slab formwork and reinforcement are shown in Fig. A.5. Concrete was mixed in the laboratory and placed by shovel. In order to provide a strong connection between the floor slab and the wall below, half of the cell of each block immediately below the slab was left ungrouted. This permitted the slab concrete to fill these empty half cells and create a shear key.

After placement, concrete was consolidated with vibrators and troweled to a thickness of 3 inches. The three-inch thickness was not one-quarter scale of a typical slab, since an oversized slab was required to support the weight of the story masses. The top surface of the slab was roughened at locations where the next course of block was to be laid, then covered with plastic and cured for one day. The completed first story of RM1 is shown in Fig. A.6.

A.3.5 Finishing

Following completion of construction, the external surface of the masonry was cleaned and parged with a very thin layer of a mixture of Acryl 60 (Thoro Systems Products) latex admixture and cement paste. The walls were then painted with a white latex paint to enhance the visibility of cracks.

A.4 Final Assembly of Test Specimens

A.4.1 Dynamically Tested Specimens

Test structures RM1 and RM3 were lifted at their bases and transported across the laboratory to the shaking table. Hooks of the overhead crane were attached to canvas straps which were wrapped around 1 1/2 in. diameter steel rods into horizontal sleeves in the base girder. The structures were placed on the simulator platform in a bed of hydrocal. The hydrocal ensured that the structures were level. The base girder was prestressed to the platform with twelve 1 in. diameter bolts. This prestressing, along with the hydrocal and the two steel angle end stops which were placed at each end of the base girder, prevented sliding of the structure on the platform during shaking. Fillets of hydrocal were placed along the interface between the base girder and the platform to verify that such sliding did not occur.

Story masses were placed after a test structure was secured to the platform. Steel plates were lifted by fork-lift and maneuvered into the structure through openings between the flanges. Once inside the structure a steel eye-bolt was screwed into the plates and was then

used for lifting and placement with an overhead crane. The mass on the underside of the floor slab was placed first and held in place with a harness until the mass on the top side of the slab was in place. The two story masses were bolted together with 3/4 in. diameter threaded rods through holes in the floor slab.

A.4.2 Statically Tested Specimen

After structure RM2 was tested on base isolators, the story masses were removed, and the specimen was lifted from the simulator platform to the location on the test floor where the static test was to be performed. The specimen was secured to the test floor with eight 1 in. diameter bolts which extended through shafts in the base girder and the floor. Fillets of hydrocal were placed along the base girder-to-floor interface so that any slip between the two during the test could be detected.

Once secured to the test floor story masses were set in place using the fork-lift and crane sequence described in section A.4.1. The harness system was again employed to fix the masses to the floor slabs.

Table A.1 Measured Weight of Story Masses (lbs.)

Structure	Floor Level	Weight of Top Mass	Weight of Bottom Mass	Weight of Hardware	Total Weight
RM1 & RM3	1	947	853	---	1800
	2	837	900	---	1737
	3	837	900	---	1737
RM2	1	947	853	160	1960
	2	837	900	160	1897
	3	837	900	160	1897

Table A.2 Measured Weight of Test Specimens (lbs.)

Story	Component	RM1	RM3
---	Base Girder	3790	3720
1	Wall	456	354
	Slab	739	789
	Add'l Mass	1800	1800
	Tributary Weight*	3224	3153
2	Wall	458	419
	Slab	803	773
	Add'l Mass	1737	1737
	Tributary Weight*	2994	2905
3	Wall	451	370
	Slab	760	775
	Add'l Mass	1737	1737
	Tributary Weight*	2723	2697
Weight above base girder		8941	8754
Total specimen weight		12731	12474

* Tributary weight considered to act at centerline of floor slab

Table A.3 Chronology of Experiments

Structure	Completion of Construction	Experiment
RM1	9-10-87	Dynamic Test 3-17-88
RM2	12-4-87	Base Isolation Test 7-19-87 Static Test 3-3-89 thru 3-12-89
RM3	2-3-88	Dynamic Test 6-8-88 & 6-9-88

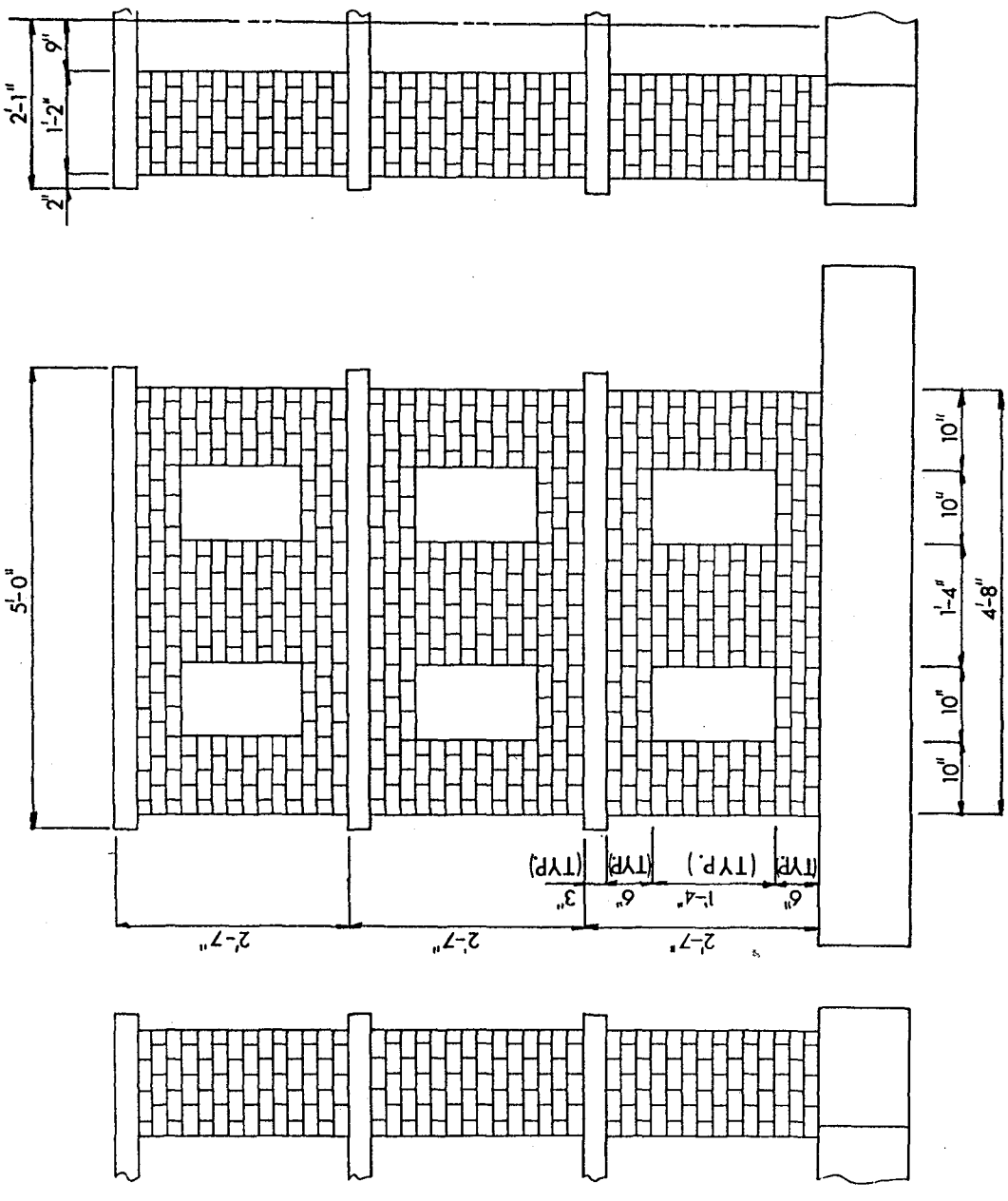

Figure A.1 Configuration of Test Specimens RM1 and RM2

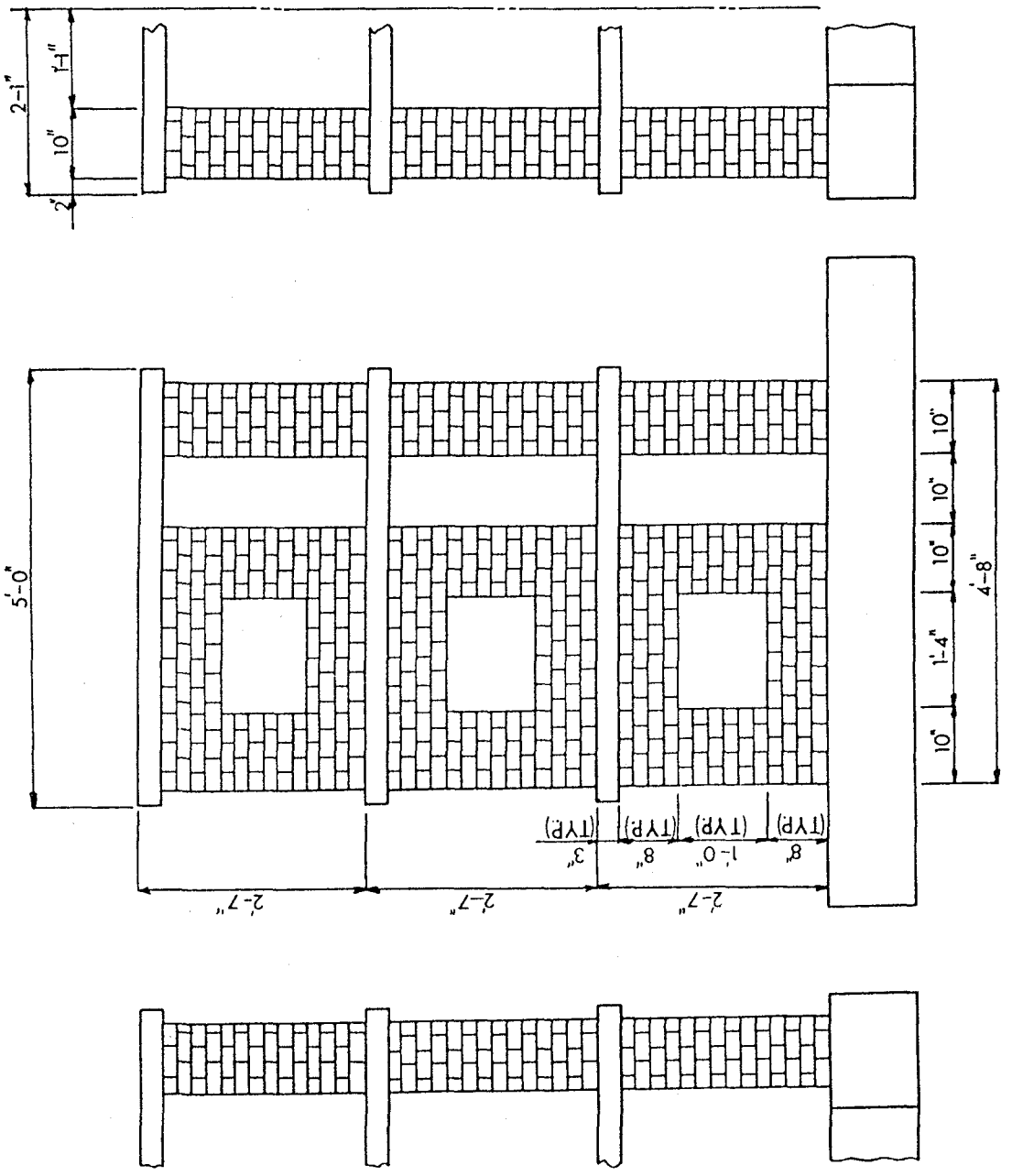

Figure A.2 Configuration of Test Specimen RM3

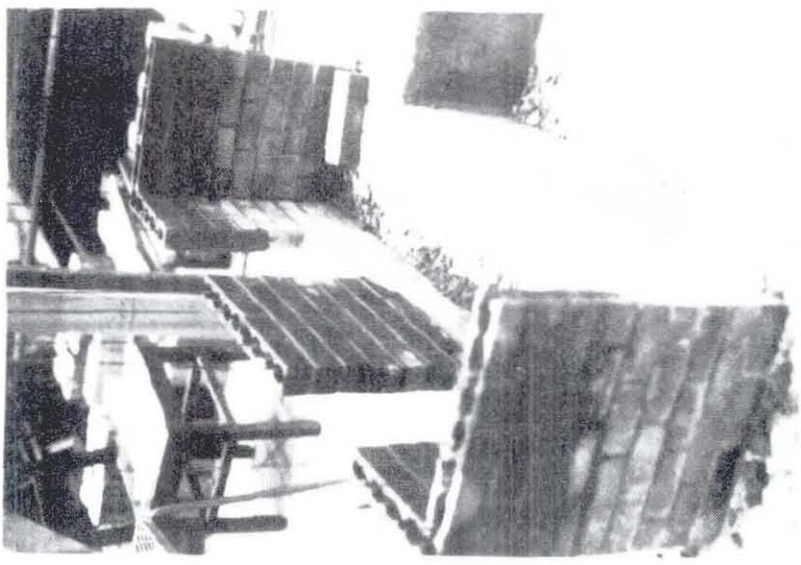

Figure A.4 Base-Story Wall of Structure RM1

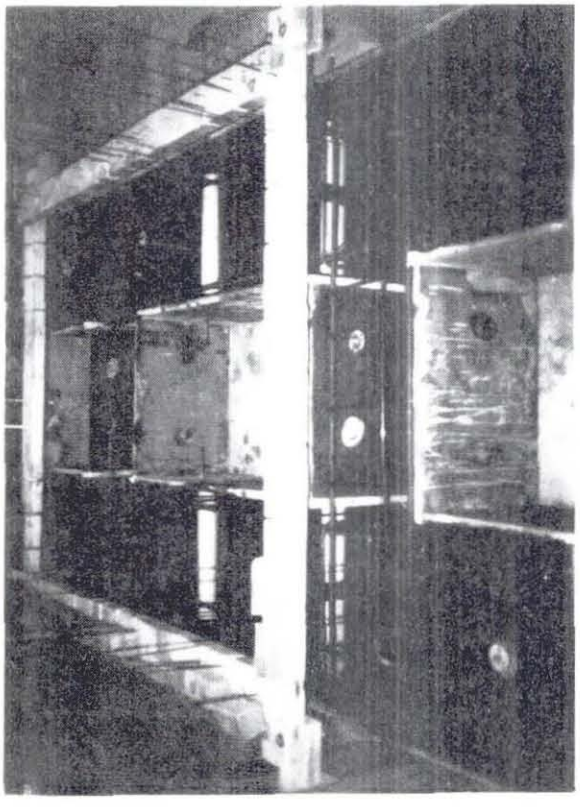

Figure A.3 Base Girder and Vertical Reinforcement Support

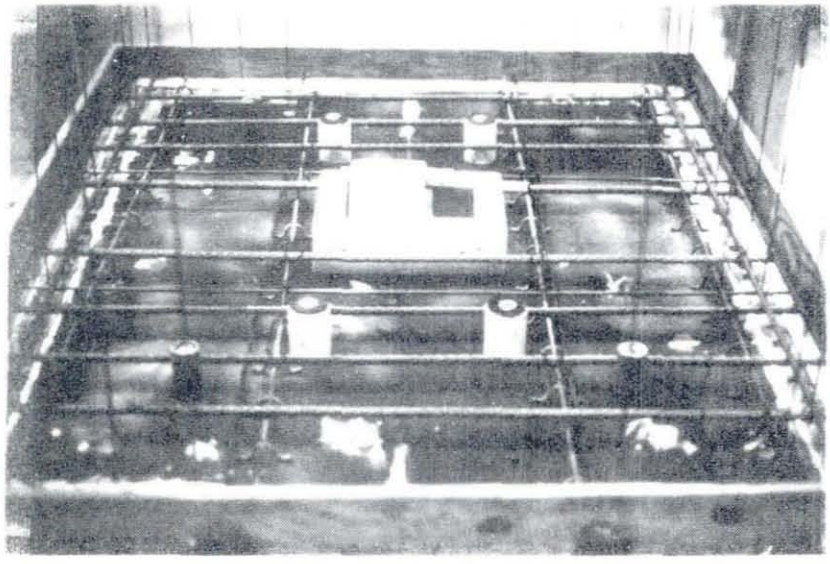

Figure A.5 Formwork and Reinforcement for Floor Slab

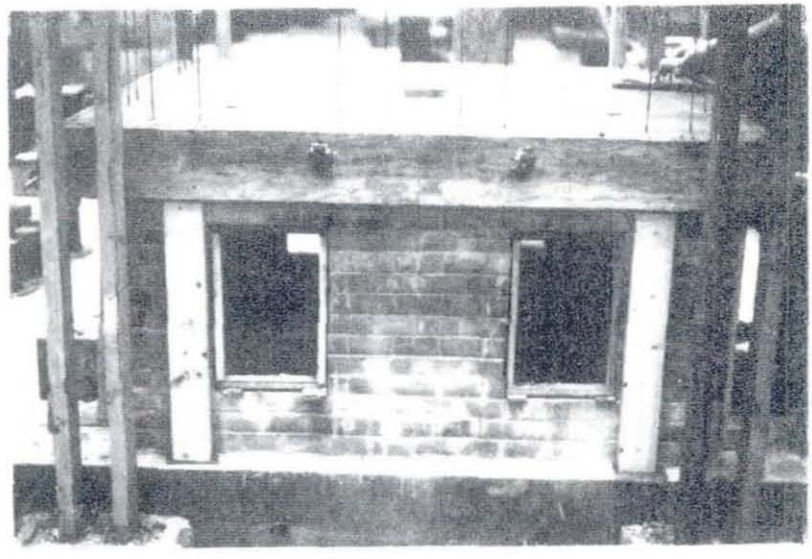

Figure A.6 Completed First-Story (RM1)

APPENDIX B

CONSTRUCTION MATERIALS

Properties of the materials used in the construction of the test structures are discuused in this appendix. Standard material tests of masonry prisms, concrete cylinders, and grout and mortar samples cast during the construction of the structures are also described.

B.1 Concrete Block

All blocks used in the construction of the specimens were hollow core concrete masonry units supplied by the Nemroc Corporation of Alpena, Michigan. The blocks were one-quarter scale of a conventional 8 inch block and had the same relative geometry as the conventional block, including the taper of the face shells. The units were nominally 1 7/8 in. in height and width and 3 7/8 in. in length. Each unit was cast in a mold manufactured by the Besser Company (Alpena, Michigan). The mix consisted of two parts (by volume) Type I-A Portland cement and one part masonry sand (sieved through a No. 16 sieve). After casting, units were moisture-cured and wrapped in newspaper to prevent breakage during shipping. Upon arrival at the University of Illinois laboratory all blocks were inspected for defects. All blocks judged to be unsuitable were discarded.

B.2 Mortar

In order to examine the properties of candidate mortars, a series of 3-unit prisms were constructed using sample blocks and both Type S and Type N mortars (ASTM C270). Although the sample blocks were of a slightly different mix design than those used in the construction of the specimens, this slight difference was not relevent to the study since the intent of the prism tests was to evaluate the effect of the mortar on the compressive strength of the masonry. Mortars were prepared in accordance with mix designs suggested by Abboud [1]. Half of the prisms were grouted (with a grout mix described in Section B.3)

and half were not grouted. Prisms were tested in uniaxial compression according to procedures described in Section B.4. Results of these tests are summarized in Table B.1. Fig. B.1 shows sample stress-strain curves for the grouted prisms. The close similarity of the curves for the two different types of mortars indicates that the stress-strain behavior of the prisms was not dependent on the mortar type because of the controlling influence of the grout.

Based on this finding, Type S mortar was chosen for use in construction of the specimens. The mortar mix was essentially the same as mixes used in full-scale construction except that only aggregates passing a No. 16 sieve were used. Ratios by weight of Type III Portland cement, sand and lime were 1.00 : 3.83 : 0.21. Water was added in an amount approximately equal to the weight of cement. Mortar was mixed in an electric mixer in approximately 6-1/2 lb. batches.

Two-inch mortar cubes were made during different stages of construction of RM1. Cubes were tested to failure in uniaxial compression according to ASTM C109-87 in a Reihle compression machine. Test-day results are presented in Table B.2.

B.3 Grout

The grout was of the same mix as used in full-scale construction (ASTM C476). Proportions by weight of Type III Portland cement, sand and lime were 1.00 : 2.13 : 0.04. To control shrinkage, Sika Intraplast-N Grout Aid was added with the water in amounts of 0.04 pounds per pound of cement. Grout was mixed in five-gallon buckets.

During grouting of each story, 1" x 1" x 1 1/2" grout prisms were made in accordance with methods prescribed in ASTM C1019-84. These were later tested in uniaxial compression. Test day strengths are given in Tables B.2 to B.4.

B.4 Masonry Prisms

During construction of each story, twelve 3-unit prisms were constructed by the mason in accordance with ASTM E447-84. The prisms were tested in uniaxial compression in an MTS 50-kip capacity servohydraulic testing machine soon after testing of a structure was completed. The rate of loading was controlled so that the vertical deflection increased at a pace of 0.015 inches/minute. Strengths are presented in Tables B.2 to B.4. Strengths are based on the maximum compressive load sustained by the prism and its measured gross cross sectional area. Axial load and deformation over the 6 in. prism height were recorded continuously with an analog x-y plotter. Deformations were measured as the vertical deflection of the loading actuator. Prism deformations were inferred from these measurements by accounting for the slight flexibility of the testing machine which was determined by recording the force-deformation characteristics of the two machine platens loaded against each other. Figs. B.2 to B.4 show stress-strain curves for each structure obtained by using a least-squares procedure to fit a parabola to the data. Strain values were shifted by the strain intercept (corresponding to zero stress) so that the curves passed through the origin of the plots.

B.5 Reinforcing Steel

All reinforcement was No. 11-gage brite basic annealed industrial quality wire. The wire was supplied in straight ten-foot lengths by Wilson Steel & Wire Company of Chicago, Illinois. Three, 5 in. coupons were cut from three randomly selected wires and tested to failure in direct tension at a nominal strain rate of 0.0008/sec to determine the stress-strain characteristics of the wire. Load and deflection were recorded on an analog x-y plotter. Measured properties are summarized in Table B.5. A representative stress-strain curve is shown in Fig. B.5.

B.6 Slab Concrete

Concrete for the floor slab consisted of Type III Portland cement, torpedo sand for fine aggregate and pea gravel for coarse aggregate in a 1.00 : 2.13 : 1.60 ratio by weight. A water/cement ratio of 0.60 was used. Concrete cylinders (4 x 8 inch) were cast from each floor slab batch and tested in compression. Strengths on the day of testing a three-story structure are given in Tables B.2 to B.4.

B.7 Preliminary Investigations of Material Properties

Prior to the selection and procurement of construction materials, preliminary experiments were performed to investigate selected mechanical properties of one-quarter scale reinforced masonry. Since the final construction materials or structural design were not known at the time of these investigations, the materials used in the experiments were similar, but not absolutely identical to, the materials used in the actual construction of the test structures. One-quarter scale concrete blocks were taken from a sample batch (with a slightly different mix than the final batch) supplied by the Nemroc Corporation. Mortar and grout mixes were similar to those used in the actual construction. No. 10-gage wire, which has a diameter 12% larger than No. 11-gage wire, was used as reinforcement.

B.7.1 Reinforcement Lap Splices

Prior to the construction of any test structure, a series of tests were carried out to determine the length of lap splice required to develop the tensile strength of the wire reinforcement. Lap splice specimens were constructed of two No. 10-gage wires (0.135 in. in diameter) lapped within 2-unit grouted prisms as shown schematically in Fig. B.6. Lap lengths of 2.0, 4.0 or 6.0 inches were used. An additional block was placed at each end of the prism and grouted. Plastic tubing was placed around the wires in these end blocks to ensure that the full tensile force would be resisted by the splice and not by tensile action of the masonry or grout. Wires were clamped at each end and pulled at a rate of 0.25

inches/minute. Applied load and displacement (as measured by the loading apparatus) were recorded on an analog x-y plotter. All samples failed by pulling apart at the splice, thus test results were not affected by the higher yield strength (88 ksi) of the No. 10 wire. Peak tensile forces achieved in the tests are plotted vs. lap lengths in Fig. B.7. A best-fit line has been drawn through the data points. The slope of the line suggests an average bond stress of 106 psi. Using this value as a basis, the lap length required to develop the yield strength of a No. 11-gage wire (diameter = 0.121 in.; fy = 47 ksi) was estimated to be 14 inches. As a result of the long lap length, no lap splices were used for vertical reinforcement.

B.7.2 Diagonal Compression Panels

Another series of preliminary experiments was performed, this time with square reinforced masonry panels constructed of the provisional materials. Three panels were built with dimensions and layout of reinforcement identical to those of the center pier of structures RM1 and RM2. In this way, results of the experiment could be used to infer characteristics of the behavior of the center pier when loaded in shear. The panels were placed in an MTS 50-kip servohydraulic testing machine and subjected to compression along a diagonal axis as shown schematically in Fig. B.8. Displacement transducers were mounted on each specimen to measure distortions parallel and transverse to the line of compressive force. These distortions were recorded along with the compressive forces (as measured by the load cell of the testing machine) on an analog x-y plotter. Measured data were reduced to plots of nominal shear stress vs. shear strain (Fig. B.9) using calculation methods prescribed in ASTM E519-81 [2]. Neglecting specimen P1 which failed prematurely due to excessive grout voids, the average strength for the given loading conditions was 240 psi. After initial cracking, cracks widened to over 2 mm without significant loss of strength. Results from these tests provided input into the design of the test structures in the manner described in Chapter 2.

Table B.1 Compressive Strength of Sample Prisms

No. of Samples	Mortar Type	Grout Type	Age (days)	f'_m (ksi)	c.o.v. (%)
3	S	none	39	1.29	11
3	N	none	30	1.20	11
3	S	N	38	1.90	12
3	N	N	27	1.93	16

Table B.2 RM1 - Standard Material Tests

Material	Location	Number & Type of Specimens	Average Compressive Strength (psi)	Coefficient of Variation (%)
Masonry Prisms	Story 1	---	---	---
	Story 2	9 3-unit prisms	1347	23
	Story 3	12 "	1116	22
	All Stories		1215	25
Mortar Cubes	Story 1	---	---	---
	Story 2	9 2-inch cubes	2950	5
	Story 3	9 "	2970	5
	All Stories		2960	5
Grout	Story 1	6 1" x 1" x 1.5"	1959	22
	Story 2	6 "	1708	30
	Story 3	6 "	1975	20
	All Stories		1875	25
Slab Concrete	Story 1	3 4-inch cyl's	5135	5
	Story 2	5 "	4061	13
	Story 3	6 "	5155	5
	All Stories		4760	14

Table B.3 RM2 - Standard Material Tests*

Material	Location	Number & Type of Specimens	Average Compressive Strength (psi)	Coefficient of Variation (%)
Masonry Prisms	Story 1	12 3-unit prisms	1279	13
	Story 2	12 "	1357	38
	Story 3	12 "	1298	29
	All Stories		1318	28
Grout	All Stories	10 1" x 1" x 1.5"	1200	24
Slab Concrete	Story 1	6 4-inch cyl's	7072	7
	Story 2	6 "	6520	8
	Story 3	6 "	5803	6
	All Stories		6460	8

*Note: Tests performed at time of static test

Table B.4 RM3 - Standard Material Tests

Material	Location	Number & Type of Specimens	Average Compressive Strength (psi)	Coefficient of Variation (%)
Masonry Prisms	Story 1	12 3-unit prisms	1185	23
	Story 2	12 "	1085	14
	Story 3	12 "	1414	16
	All Stories		1228	21
Grout	Story 1	7 1" x 1" x 1.5"	1224	16
	Story 2	6 "	1249	16
	Story 3	5 "	576	21
	All Stories		1052	33
Slab Concrete	Story 1	7 4-inch cyl's	5164	7
	Story 2	6 "	6074	11
	Story 3	6 "	5162	14
	All Stories		5451	13

Table B.5 Measured Properties of Steel Reinforcement

Wire Gage	Nominal Diam. (in)	No. of Coupons	Tensile Yield Stress (ksi)			Tensile Strength (ksi)		
			Mean	St. Dev.	c.o.v.	Mean	St. Dev.	c.o.v.
No. 11	.1205	9	47.1	1.2	2.5%	61.4	0.4	0.7%

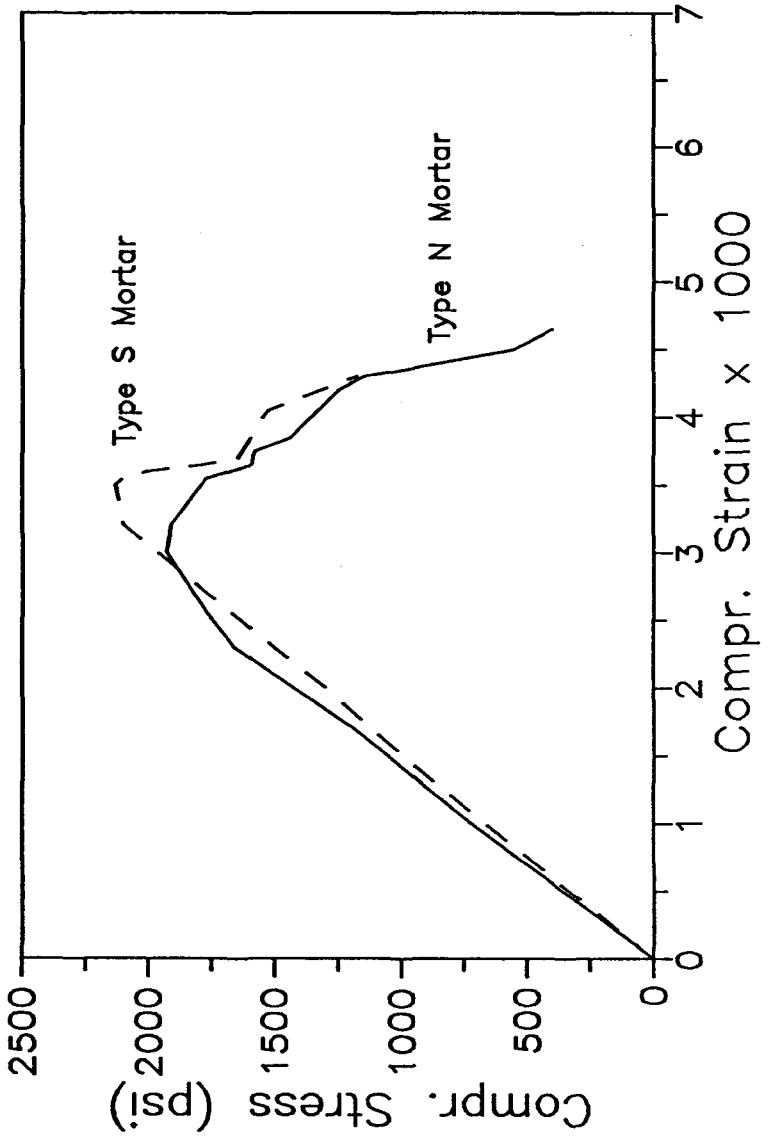

Figure B.1 Stress-Strain Relationship for Preliminary Masonry Prisms

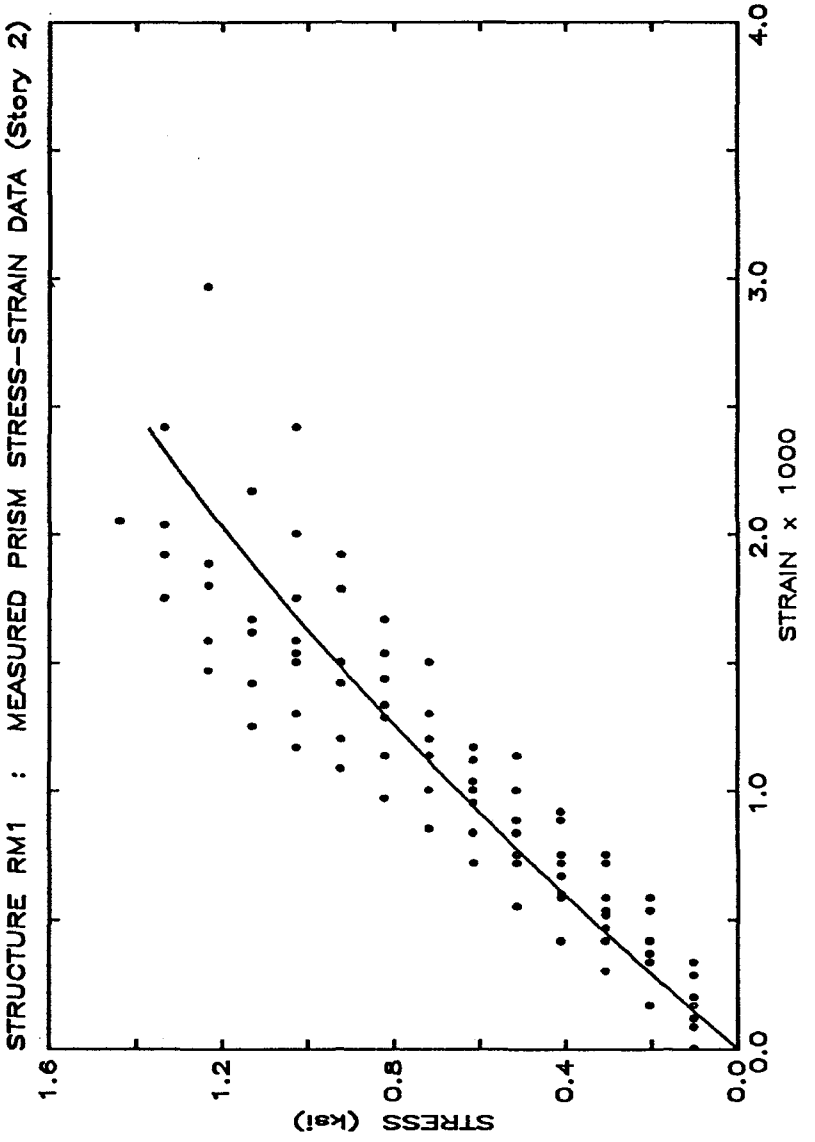

Figure B.2 Stress-Strain Relationship for RM1 Prisms

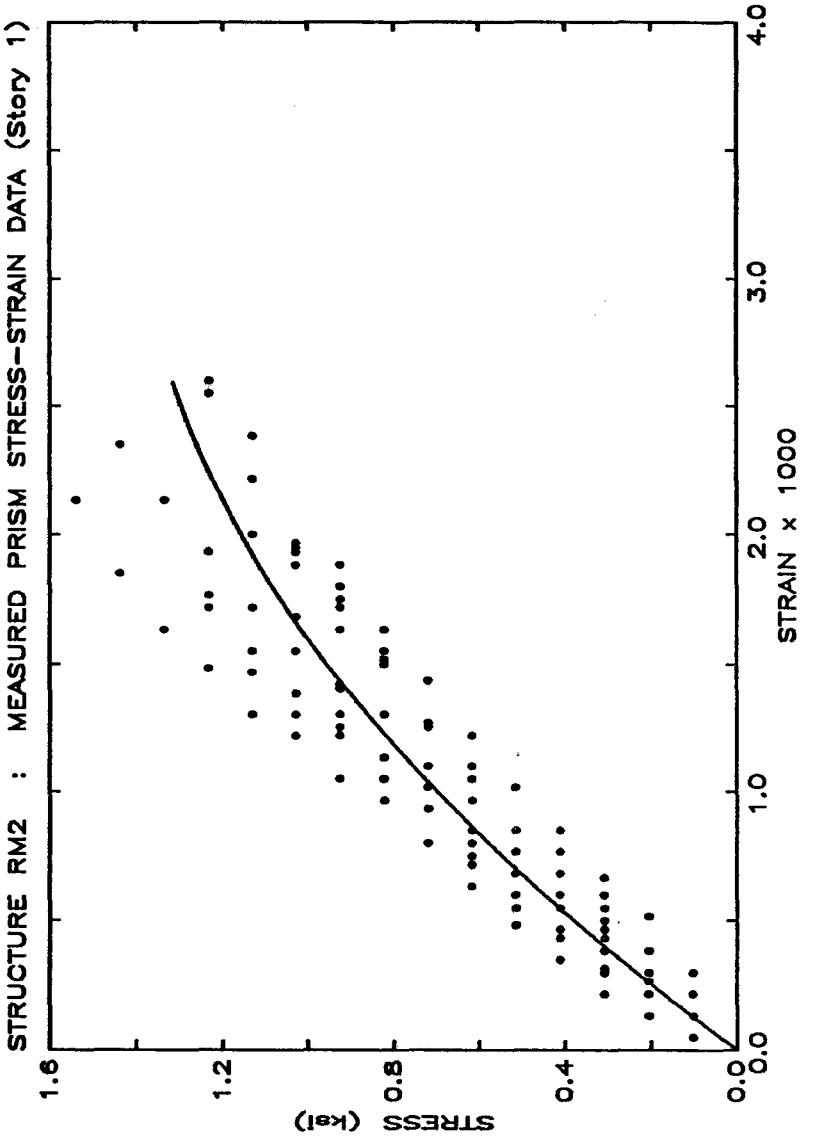

Figure B.3 Stress-Strain Relationship for RM2 Prisms

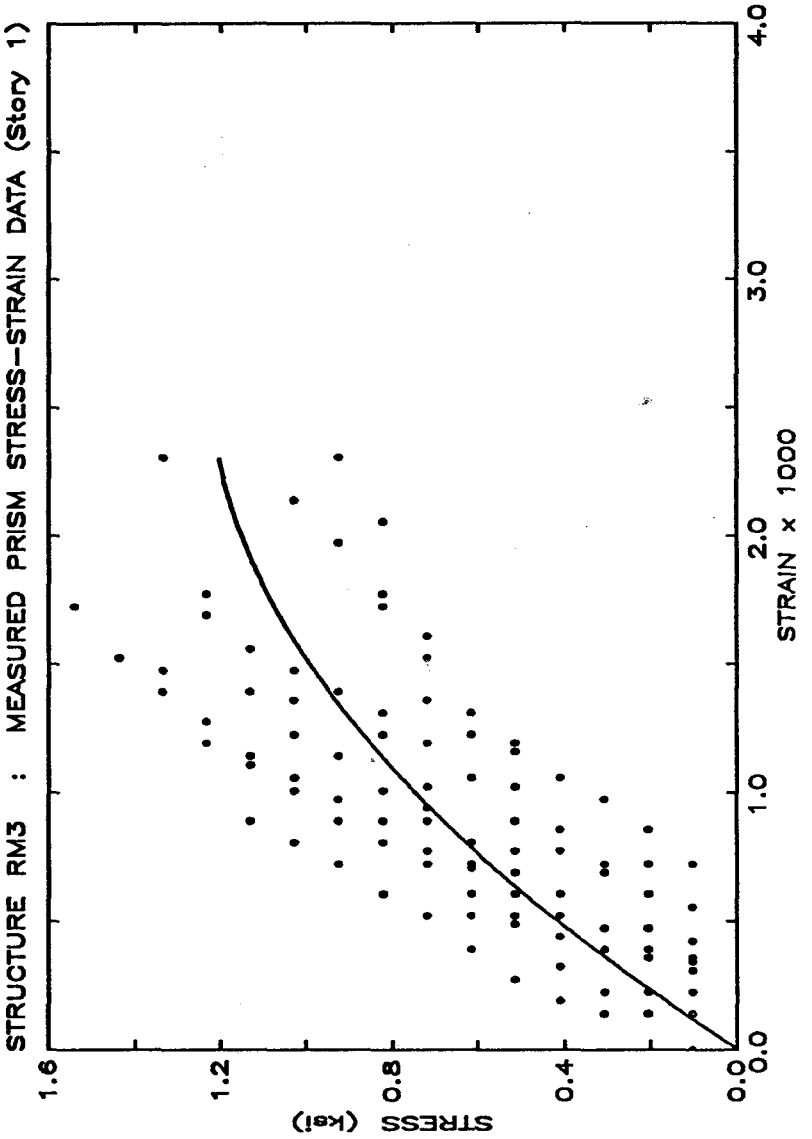

Figure B.4 Stress-Strain Relationship for RM3 Prisms

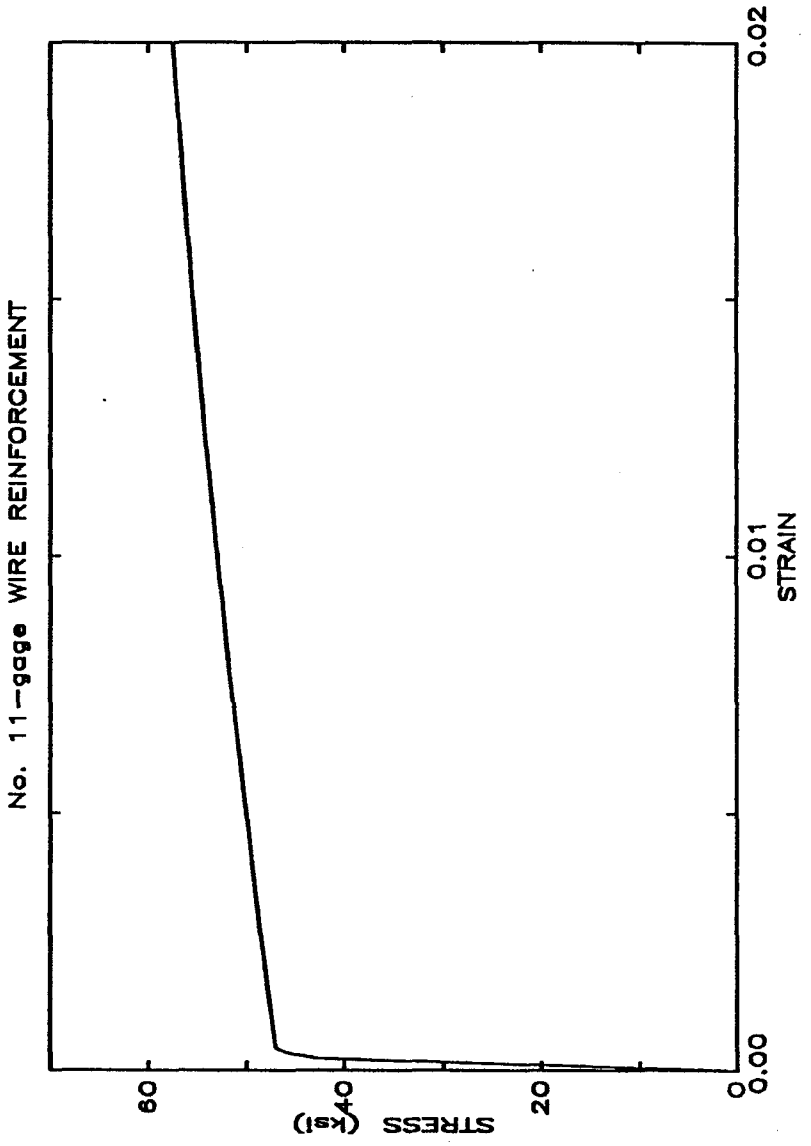

Figure B.5 Stress-Strain Relationship for Wire Reinforcement

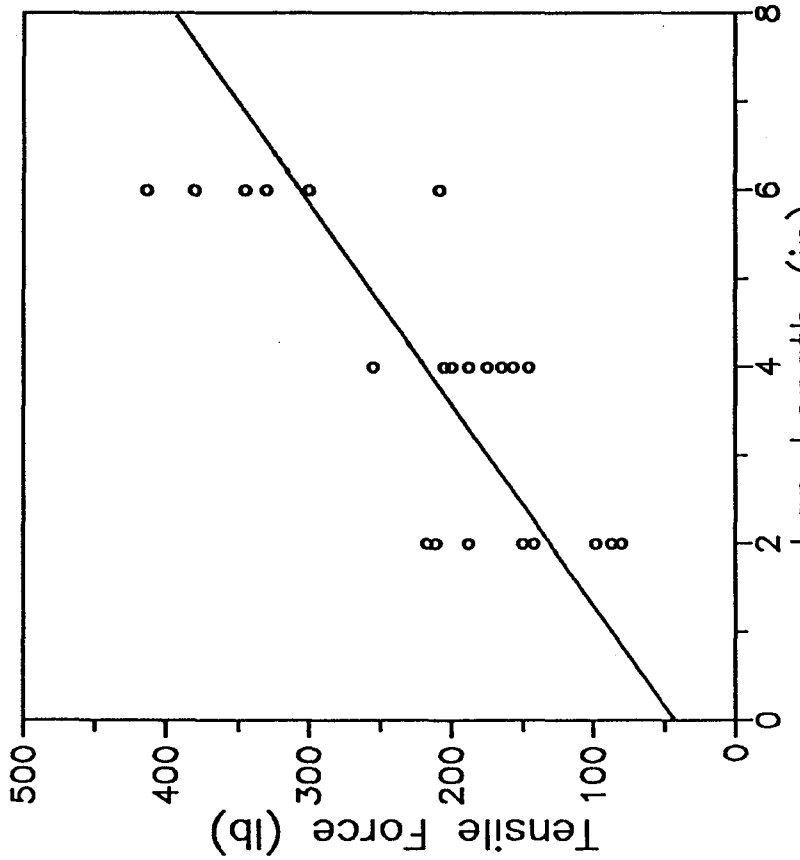

Figure B.7 Lap Length vs. Tensile Force

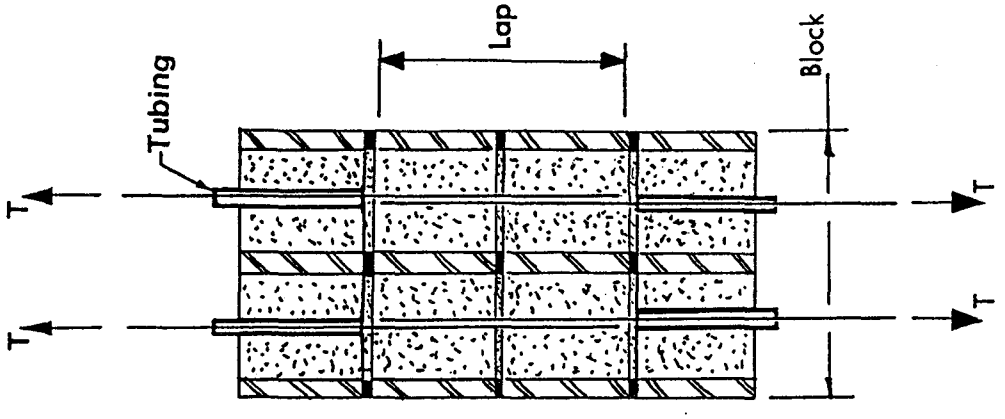

Figure B.6 Lap-Splice Specimen

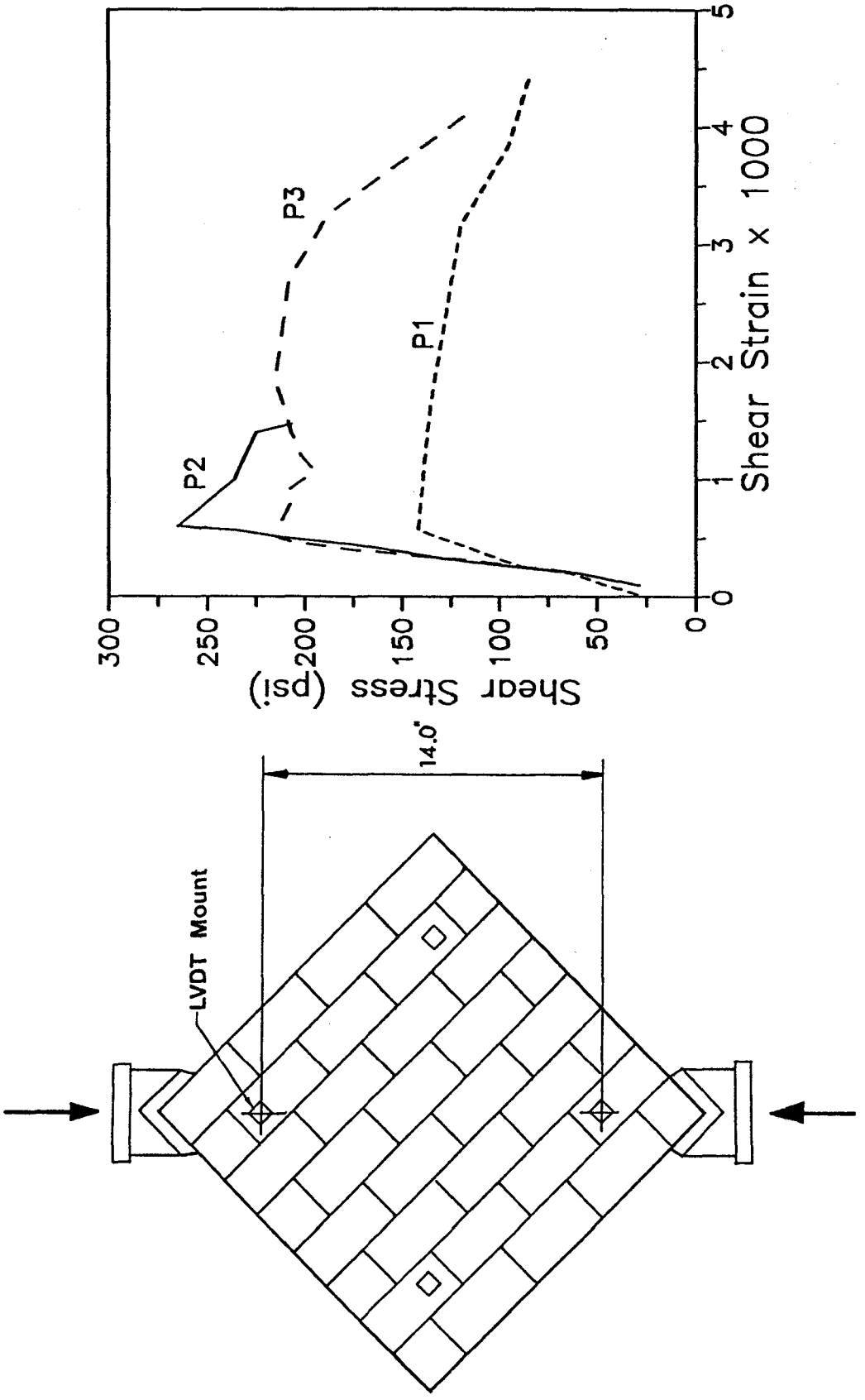

Figure B.8 Diagonal Compression Specimen

Figure B.9 Shear Stress vs. Shear Strain for Square Panel

APPENDIX C

EXPERIMENTAL EQUIPMENT

Testing procedures and equipment as well as data recording and data reduction are described in this appendix.

C.1 Experimental Equipment

C.1.1 Earthquake Simulator

All dynamic tests were conducted on the University of Illinois earthquake simulator. The simulator apparatus is comprised of a servo-control center, a hydraulic actuator system and the test platform. The actuator and platform are shown schematically in Fig. C.1. The simulator is capable of testing specimens weighing up to 12,000 lbs with a single horizontal component of base motion. More detailed information about the simulator can be found in references 3 and 4.

A 3/4 in. steel plate was bolted to the test platform before placement of a test specimen. A W21x57 column was also bolted to the west end of the platform and served as a reference column for measuring lateral deflections of the specimen relative to the base. The reference column was stiffened by a pair of 4 in. steel tubes which braced the column at two-thirds of its height.

Command signals to the hydraulic actuator were generated by an MTS 469 control system. In the present series of tests, the controller was operated in the direct displacement command mode, thus only a displacement command signal was produced by the reference generator. Feedback settings for acceleration, velocity, displacement and force controls were 4.0, 8.0, 7.0 and 4.0 respectively.

Base motions were generated from a digital record stored in virtual memory of an IBM personal computer. The digital record was converted to analog form by a Data Translation 2801 D/A A/D board with a 36 microsecond throughput. The time scale of the base motion was adjusted by specifying the time step between the drive signal data points. The

amplitude of the base motion was scaled by adjusting the span setting on the MTS 469 control panel.

C.1.2 Static Test Apparatus

The apparatus used to apply lateral loads to RM2 consisted of three servohydraulic actuators connected to a steel reaction frame as shown in Fig. C.2. The columns of the reaction frame were W12x72 sections welded to 4 in. thick base plates which were bolted to the strong floor. Pairs of steel channel sections (MC18x58) formed the cross beams at each floor level of RM2. Channels were bolted through their webs to the column flange with high strength bolts. A C-shaped steel section was fitted around the column flange and bolted to the flange along with each crossbeam to allow for attachment of the hydraulic actuators. Each actuator was bolted to the C-section with four 1/2 in. diameter bolts.

All three actuators were MTS servohydraulic models with a 25-kip force capacity and a 50-kip capacity load cell. They were connected to the test specimen at each floor level using the setup depicted in Fig. C.2.

Each hydraulic actuator functioned independently of the others and was operated by its own controller. The top actuator was operated in displacement control with an MTS 458.10B servo-controller. Actuators at the lower two levels were operated in force control with MTS 406.11 servo-controllers.

A computerized loading control system was developed to simultaneously control the activity of the three actuators. A flow chart for the computer program (operated on an IBM personal computer) was shown in Fig. 8.2. Loading of the structure was initiated by a D/A convertor-type function generator, which continuously sent displacement signals to the third-level actuator. Signals were based on a ramp function and were sent at a constant rate (on the order of 0.0012 inches per second). At the same time, the computer continuously monitored the top-level deflection of the structure relative to the strong floor. Deflections were measured with displacement transducers mounted between the top slab of the structure and a steel reference column. This transducer was used in lieu of the actuator's internal displacement transducer for absolute control because extensions or

contractions of the actuator would have also included deflection of the reference frame. However, the top-level ram was run in displacement control in accordance with signals from the internal LVDT, so that smooth and continuous operation could be attained.

A Data Translation 2801A A/D D/A board converted the analog signal to digital form, which was then compared by the program to the ensuing peak in the input record of prescribed top level deflections. When the target peak was reached a five-volt signal was sent through the D/A port to the function generator, causing it to reverse its ramp function. The actuator then displaced the structure in the opposite direction and a new target peak was read by the program from the input array.

Concurrent with the above process, the program continuously sampled the force in the third level actuator. The force was measured by a load cell and was transmitted to the program through the A/D port of the Data Translation board. Forces to be applied to the second and first level actuators were calculated as two-thirds and one-third of this force. These calculated forces were sent to the actuators through the D/A ports of two Data Translation boards. Forces were updated at intervals of less than one-tenth of a second so that a constant force profile could be maintained.

C.1.3 Free Vibration Test Setup

a) Dynamic Tests

Free vibration tests were performed prior to the first, and following each earthquake simulation so that the natural frequency of the specimen could be determined. The top of the structure was displaced laterally by a 50-lb force which was developed by hanging a weight on a pulley (Fig. C.3). A quick release mechanism was used which consisted of a collapsible link in the cable. The free vibration was monitored with accelerometers and displacement transducers at the third level. These instruments were the same as used in the dynamic tests except that outputs were amplified to improve resolution which was necessary due to the small amplitude of motion.

b) Static Test

Free vibration tests were also performed before and after the static testing of structure RM2. All three actuators were disconnected from the specimen. A wire link was then connected to the head of the third level actuator and the connection plate of the third floor slab. The structure was displaced by gradually increasing the set point on the MTS controller until the top level actuator was pulling on the structure with a force between 500 and 600 lbs. The link was cut, setting the specimen into free vibration. The motion was monitored with an accelerometer attached to the north end of the third floor slab. Data was recorded with the ASYSTANT + data acquisition program.

C.2 Instrumentation

Specimen response during each test was measured using a combination of acceleration, displacement and force (static test only) transducers. Location and orientation of instruments were similar for all tests, however some instruments were varied according to the needs of each experiment. Figs. C.4 to C.6 present the instrumention scheme for each experiment.

C.2.1 Accelerometers

Accelerometers were used to measure longitudinal, transverse and vertical accelerations during the dynamic tests. Two accelerometers were mounted at the midheight of each floor slab and the base girder to measure lateral motion in the direction of the base motion. One accelerometer was placed at the midheight of each pier to record in-plane accelerations. Transverse accelerations were measured with one accelerometer at midheight of the east and west faces of the top floor slab. Structure RM1 was instrumented with an additional accelerometer at the midheight of each flange section to detect out-of-plane motion of the flanges.

Additional acceleration measurements used in the base isolation experiment included vertical accelerations of the base girder and top slab, transverse accelerations of the base girder and acceleration of the simulator platform.

Table C.1 lists manufacturer's ratings for the accelerometers. Mechanical calibrations corresponding to accelerations of 0.0g and 1.0g were obtained by rotating the accelerometers with respect to the vertical.

C.2.2 Linear Variable Differential Transformers (LVDT's)

Displacement transducers, known as LVDT's, were used to measure relative displacements in all tests. Duplicate measurements of story displacement in the longitudinal direction of the specimen were obtained relative to a reference column by pairs of LVDT's at the midheight of each floor slab. Each pier of the south wall of the lower two stories was instrumented with a vertical LVDT on each side and one across each diagonal to detect both flexural and shear distortions. Vertical LVDT's were attached to the base girder and first story flanges of the south wall to record separation of the wall from the base girder. LVDT's were also placed between adjacent floor slabs at the east and west ends of the structure so that story rotations could be determined.

Additional LVDT's were provided for the base isolation test to detect lateral, longitudinal and vertical displacement of the structure on the isolator pads. For the static test, two LVDT's were added to the south first story wall to detect sliding along bed joints at the top of the piers.

Standard (free core) LVDT's were calibrated using brass plates machined to specified thicknesses. Gaging (captive core) LVDT's were calibrated using a depth micrometer.

C.3 Data Acquisition and Processing

C.3.1 Transducers

Analog output signals from LVDT's and accelerometers passed through conditioners and amplifiers prior to being recorded and digitized. Diagrams of the signal paths are shown in Figs. C.7 and C.8.

a) Dynamic Tests

Response data for the dynamic tests was acquired with a DEC (Digital Equipment Corporation) LSI 11/23 processor equipped with a 64 channel, analog-to-digital convertor board (Data Translation DT 2769) and a real-time clock. The board has a 20 microsecond throughput (aperture + switching time). A FORTRAN program using subroutines from a commercial software package (Data Translation CPLIB) was used to control the A/D board and clock. A sampling rate of 200 points per second was used for each channel. Raw data was scaled to engineering units and separated into files containing individual channel output.

A total of 64 channels (26 accelerometers, 36 LVDT's, 1 ram LVDT, and 1 drive signal) were recorded during RM1 tests, 57 channels (20 accelerometers, 35 LVDT's, 1 ram LVDT, and 1 drive signal) were monitored for RM3, and 40 channels (24 accelerometers, 14 LVDT's, 1 ram LVDT, and 1 drive signal) were recorded for RM2 on base isolators. Mechanical and electrical calibrations were conducted for all instruments on the day preceding the earthquake simulation. Electrical calibrations were repeated immediately before each test to assess fluctuation in channel gain between the time of calibration and test time.

b) Static Test

Data from the static test were recorded with an IBM personal computer equipped with two 16-channel analog-to-digital conversion boards (Metrabyte DASH 16). A Quick-Basic (Microsoft Corporation) program was written utilizing Metrabyte subroutines

(DASH 16) to control the A/D boards. The program employed the computer's internal clock to collect data at a frequency which could be adjusted throughout the test. Typically all channels were scanned every ten seconds. The current profile of lateral force being applied to the structure and the base moment vs. top level deflection relationship was displayed continuously on the computer screen. Digitized data were written to floppy disks and transported to a VAX 11/750 to be scaled and separated into files of individual channel output.

C.3.2 Visual Observation

All specimens were visually examined before and after each test. To detect cracks, a fluorescent liquid (Partek P1-A Fluorescent, Magnaflux Co., Chicago) was sprayed on the masonry. A fluorescent light was shone on each treated area and crack locations were then identified with colored markers and were recorded on data sheets. A hand-held video camera was used following each test run to record crack markings.

Behavior of the structures during the dynamic tests was recorded on a VHS videocassette and on 8-mm film. An 8mm video camera recorded movements of the first story during some of the test runs.

Table C.1 Manufacturer's Ratings - Accelerometers		
Manufacturer	Piezoresistive Accelerometers Endevco	Servo (Q-flex) Accelerometers Endevco
Model	2262C-25	QA116-15
Range	γ25g	γ15g
Linearity	1.0%	0.03%
Frequency Response (γ5%)	0-750 Hz	0-500 Hz
Natural Frequency	2500 Hz	1000 Hz
Fraction of Critical Damping	0.7	0.6

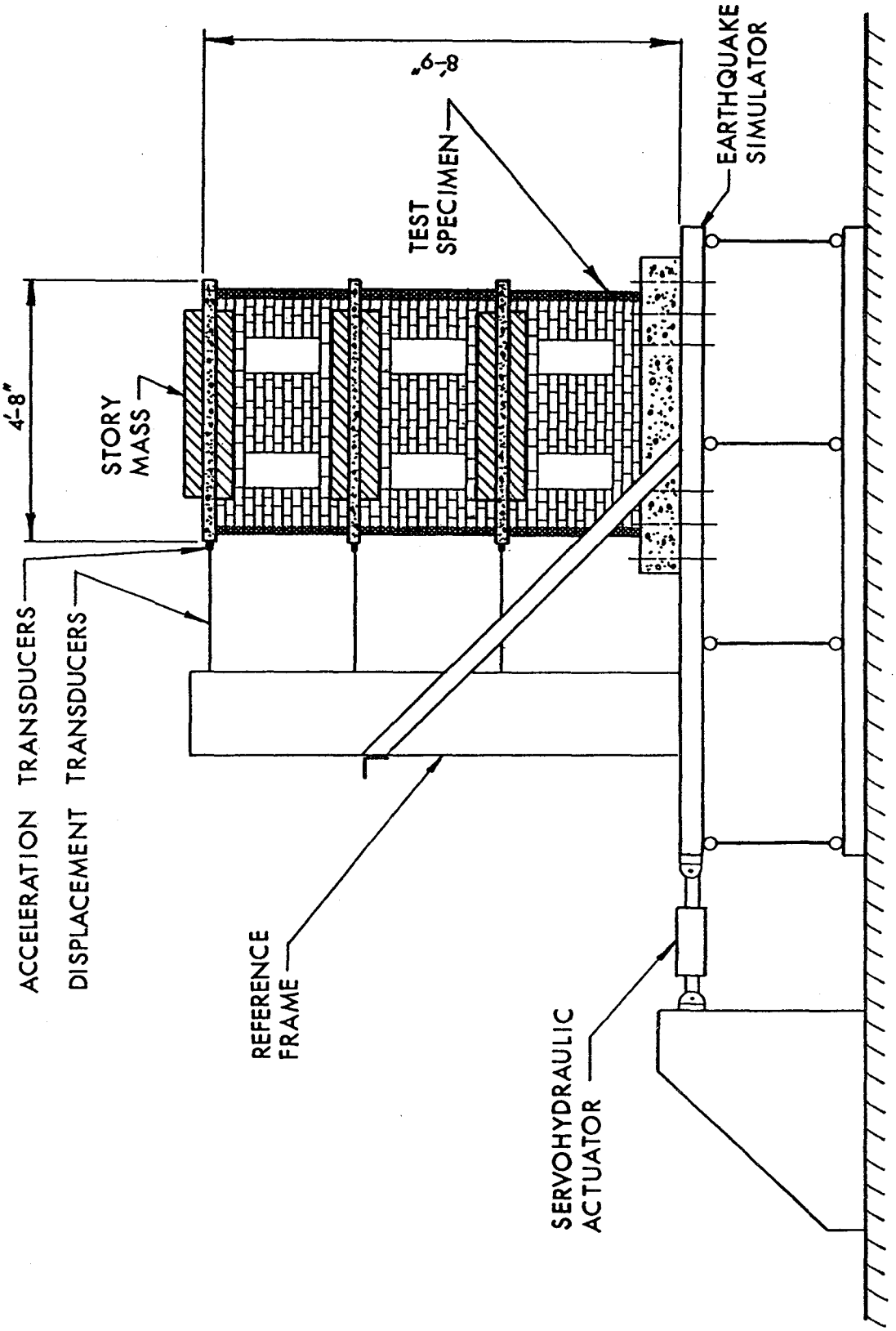

Figure C.1 Earthquake Simulator

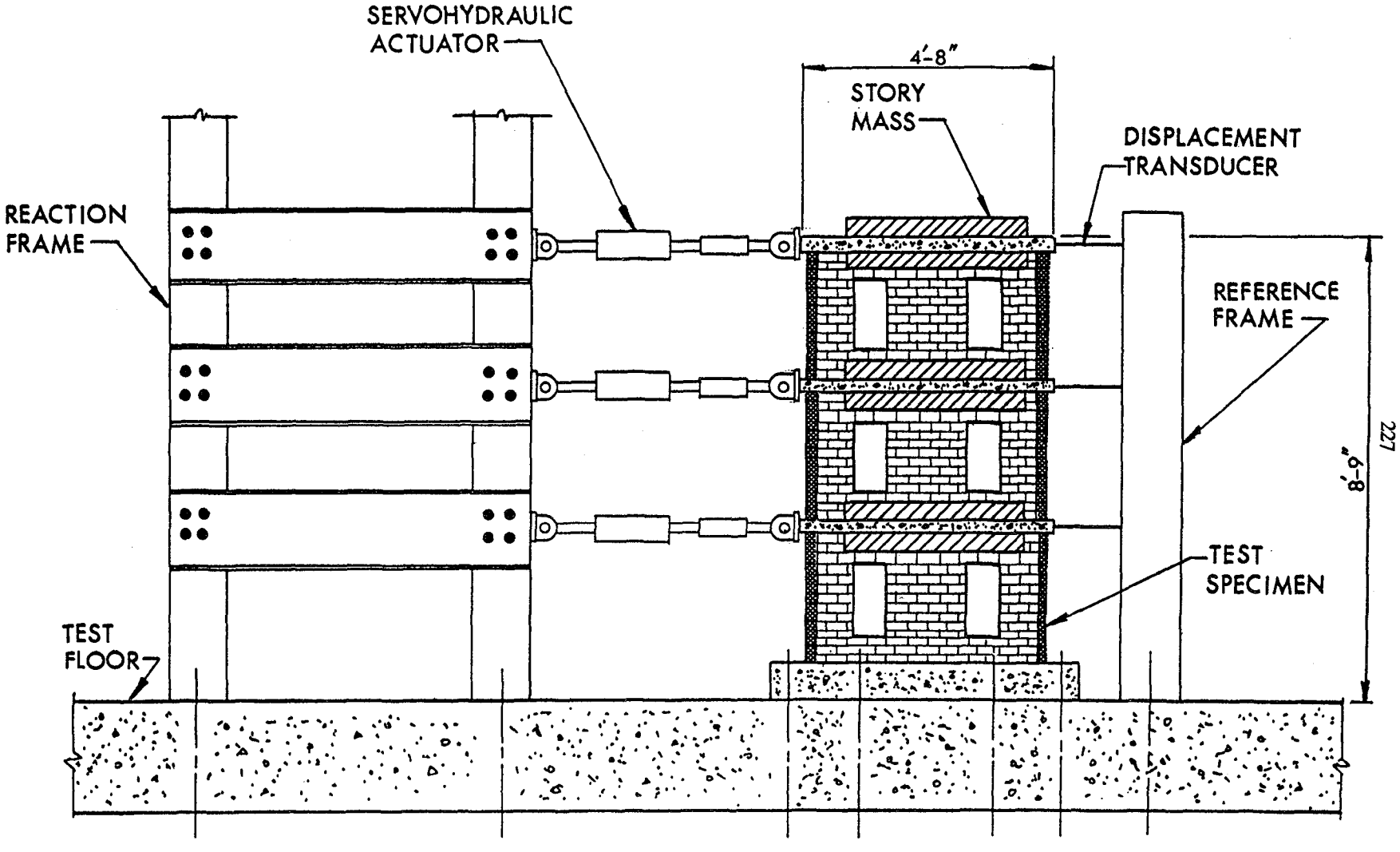

Figure C.2 Static Test Apparatus

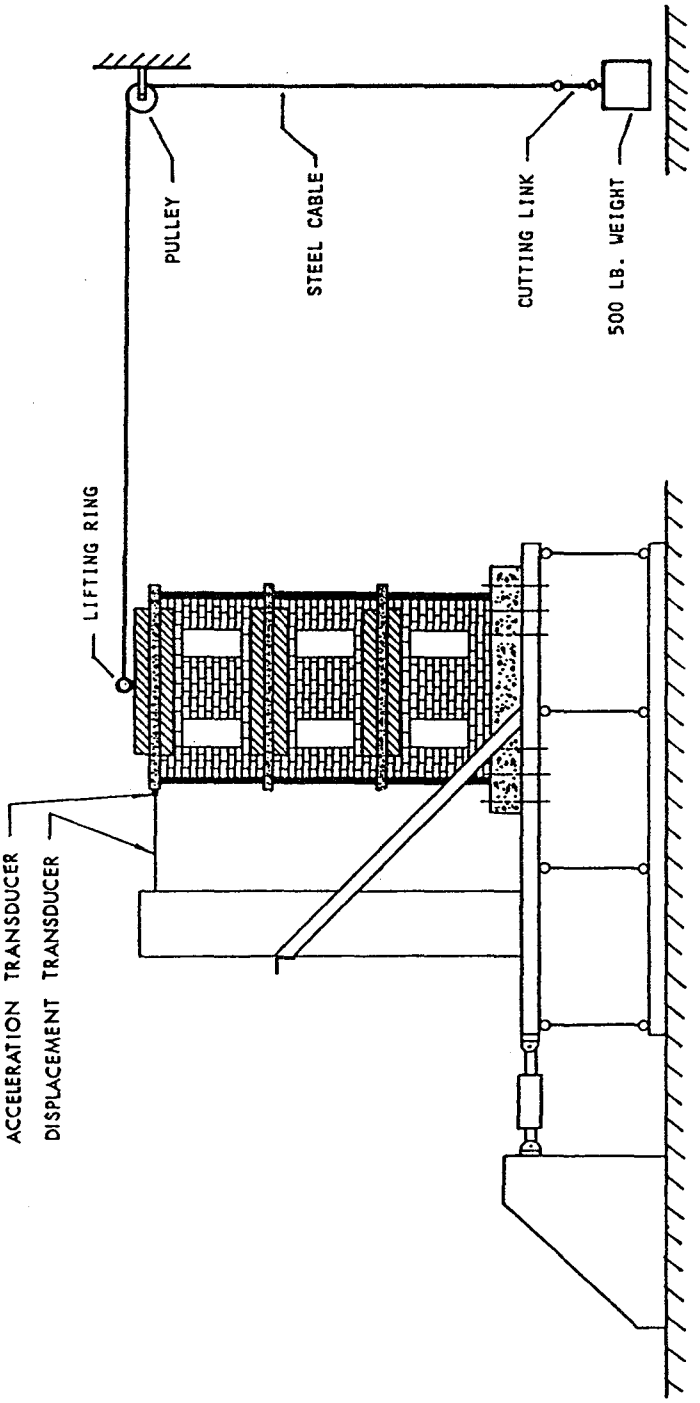

Figure C.3 Free Vibration Test

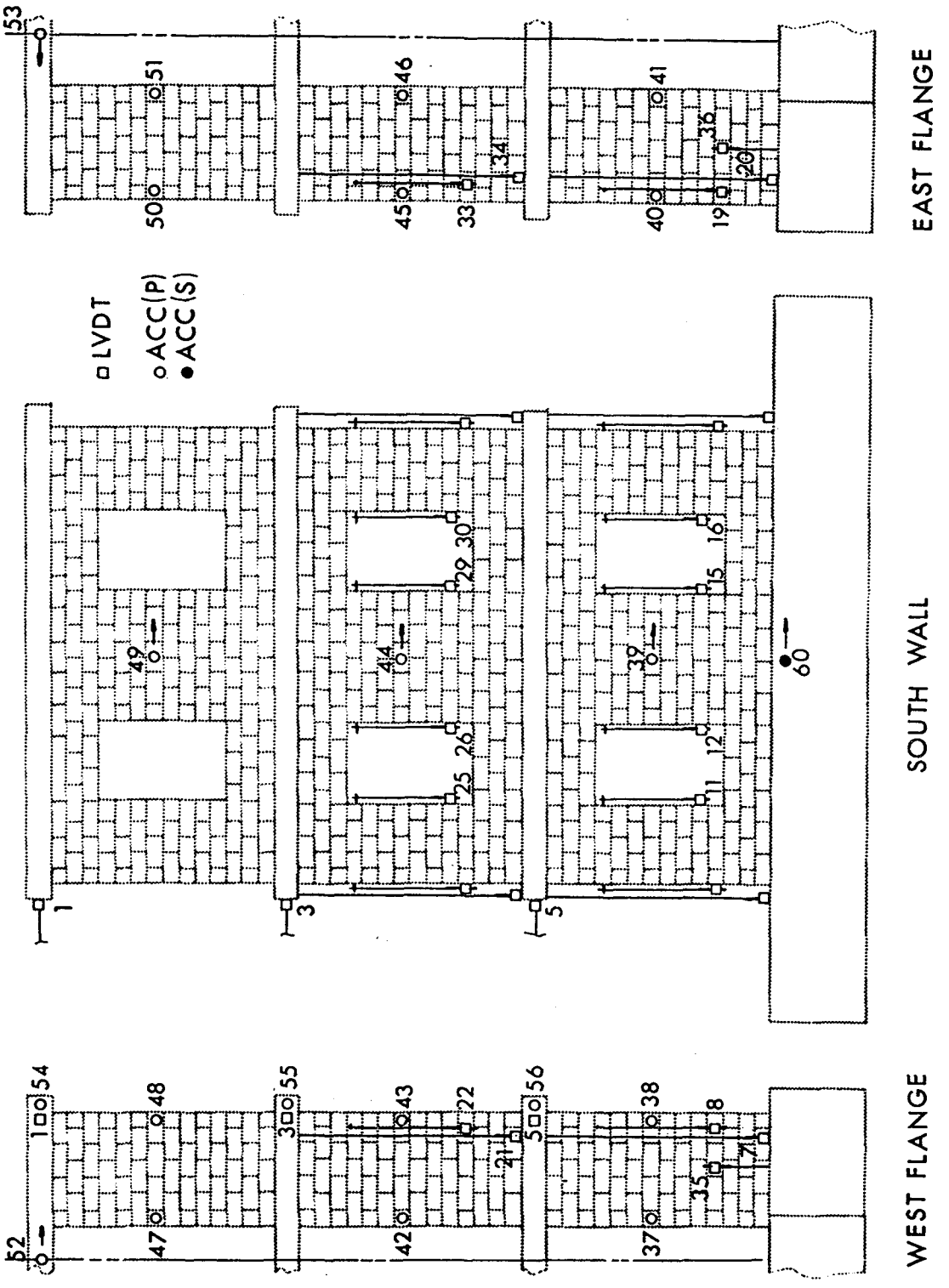

Figure C.4 Layout of Instrumentation (RM1)

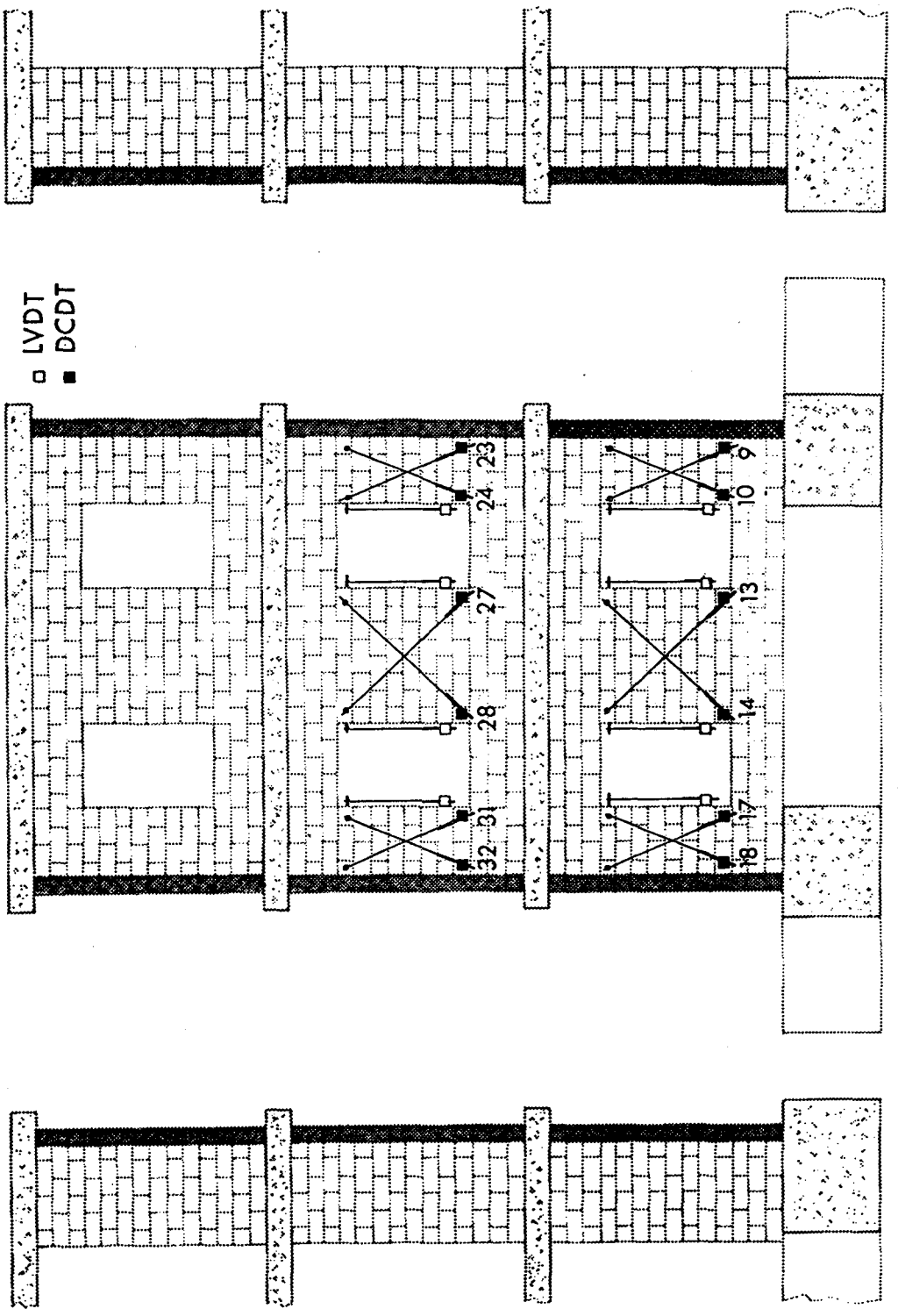

Figure C.4 (cont) Layout of Instrumentation (RM1)

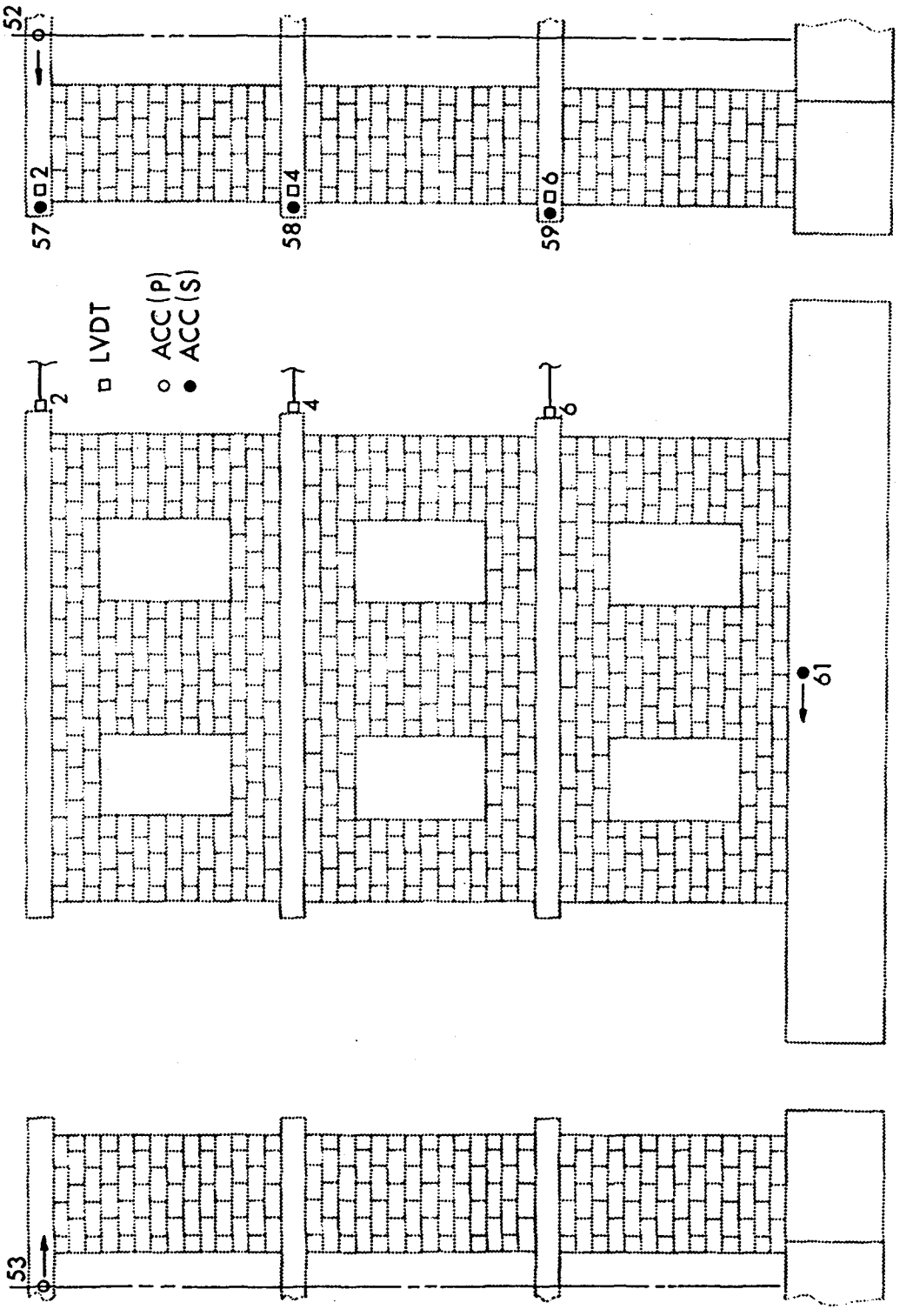

Figure C.4 (cont) Layout of Instrumentation (RM1)

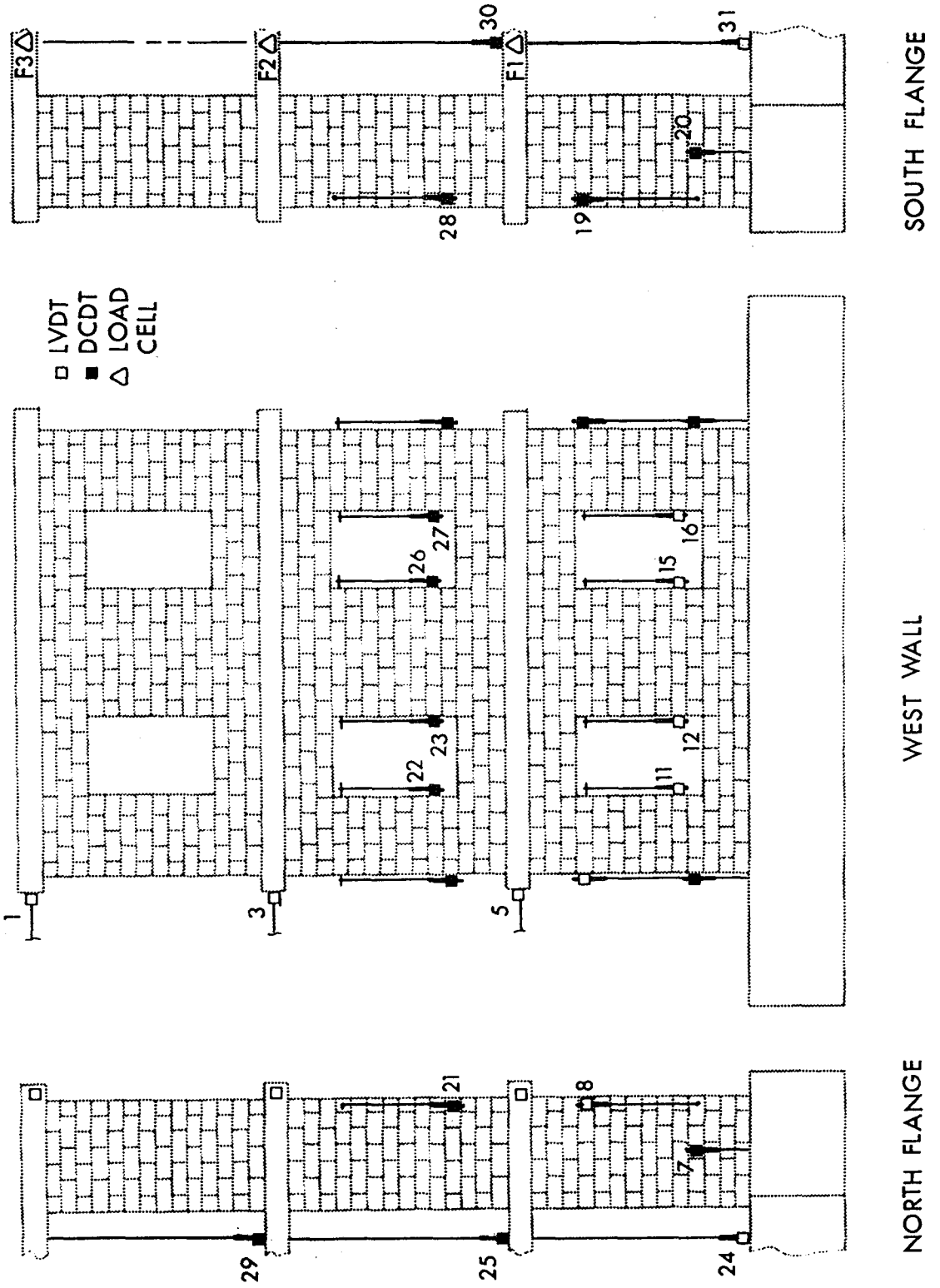

Figure C.5 Layout of Instrumentation (RM2 - Static Test)

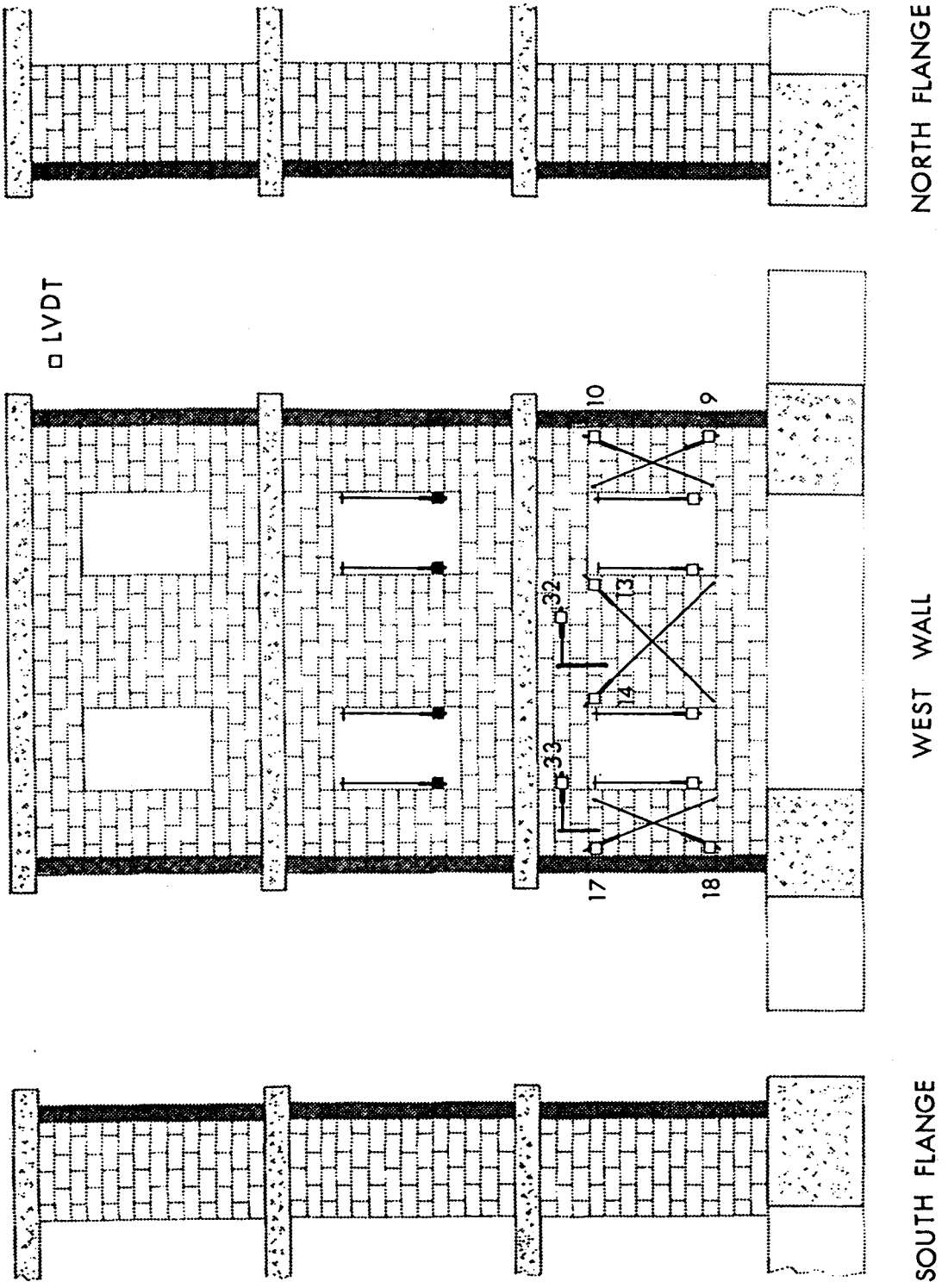

Figure C.5 (cont) Layout of Instrumentation (RM2 - Static Test)

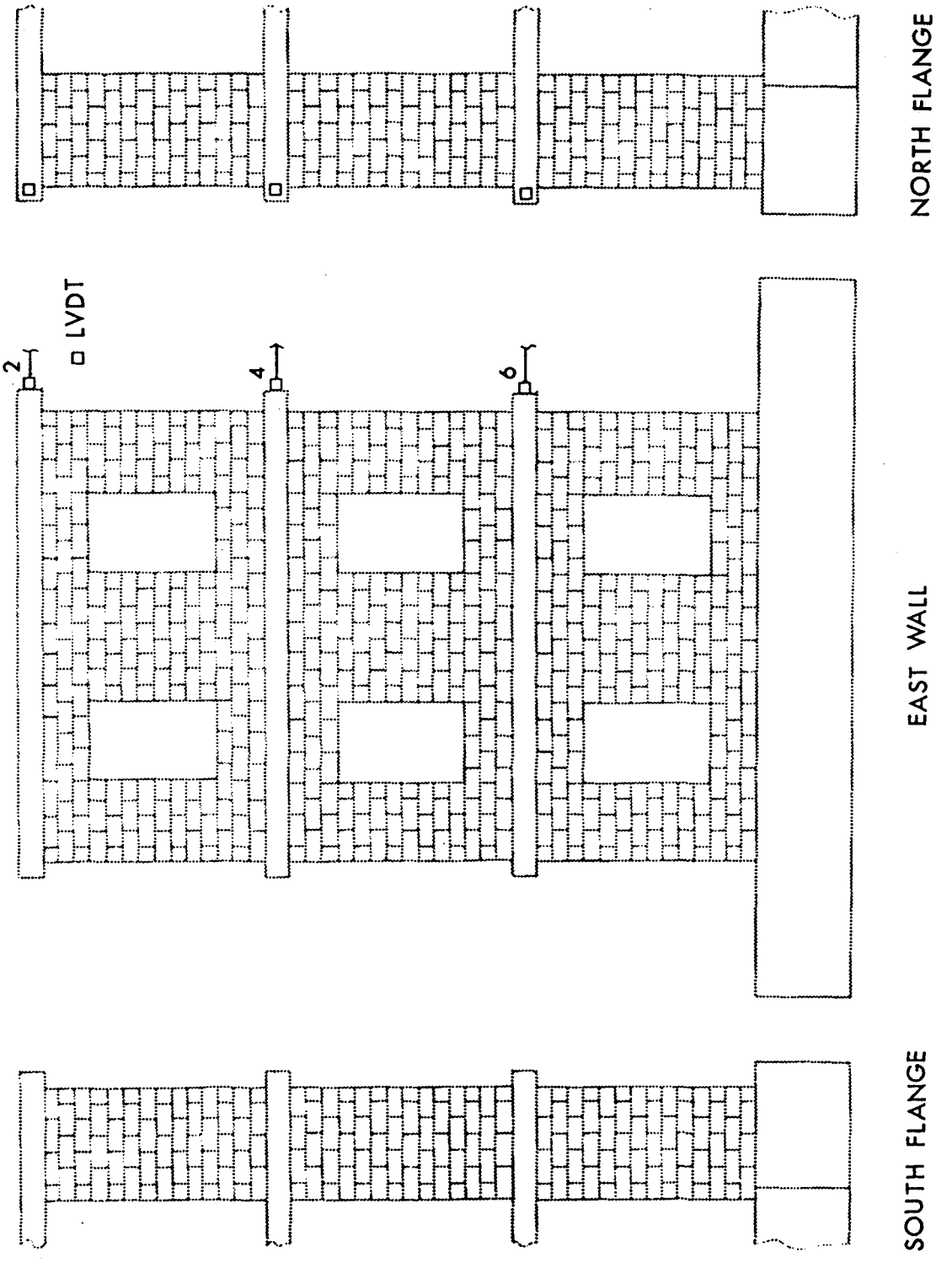

Figure C.5 (cont) Layout of Instrumentation (RM2 - Static Test)

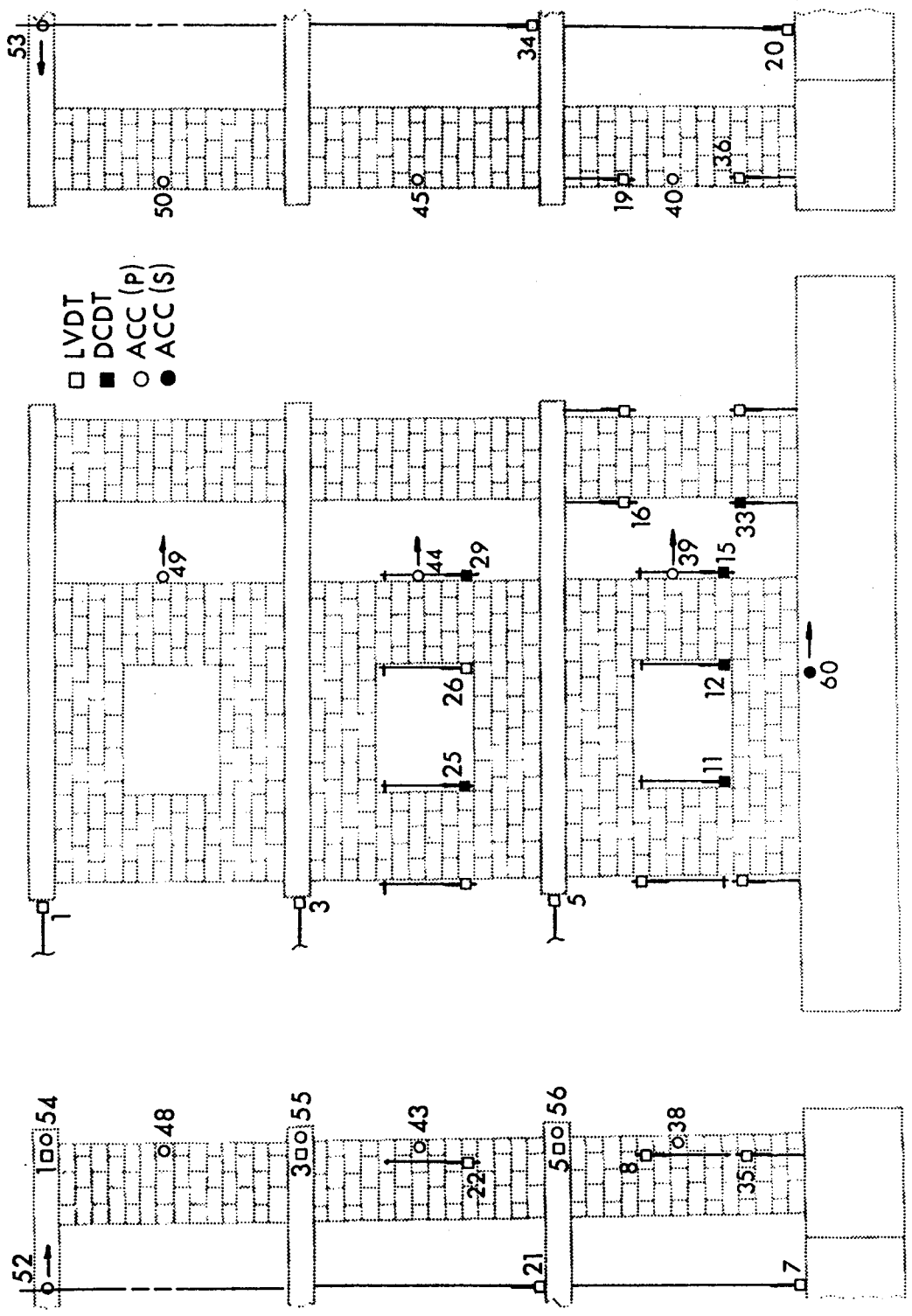

Figure C.6 Layout of Instrumentation (RM3)

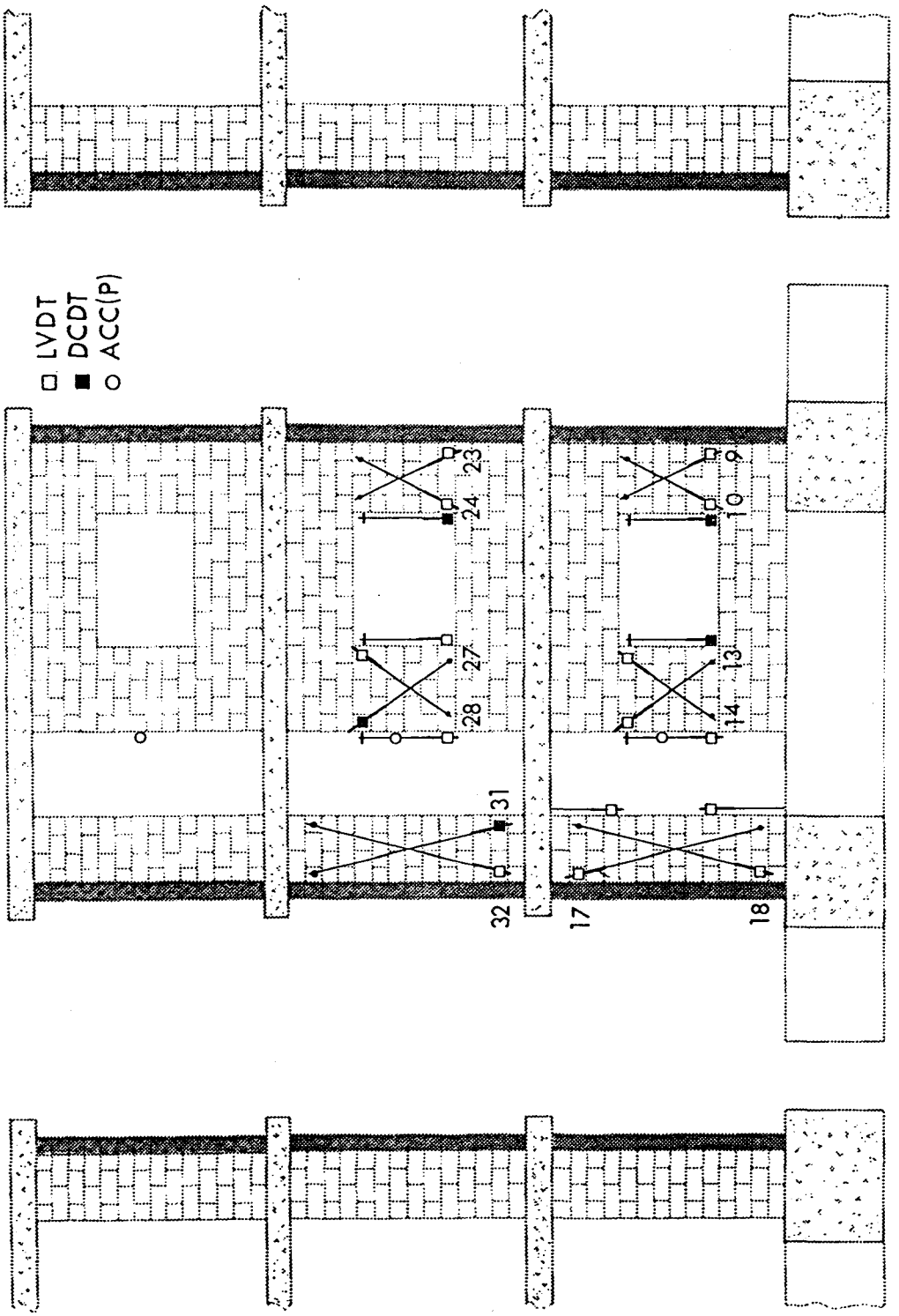

Figure C.6 (cont) Layout of Instrumentation (RM3)

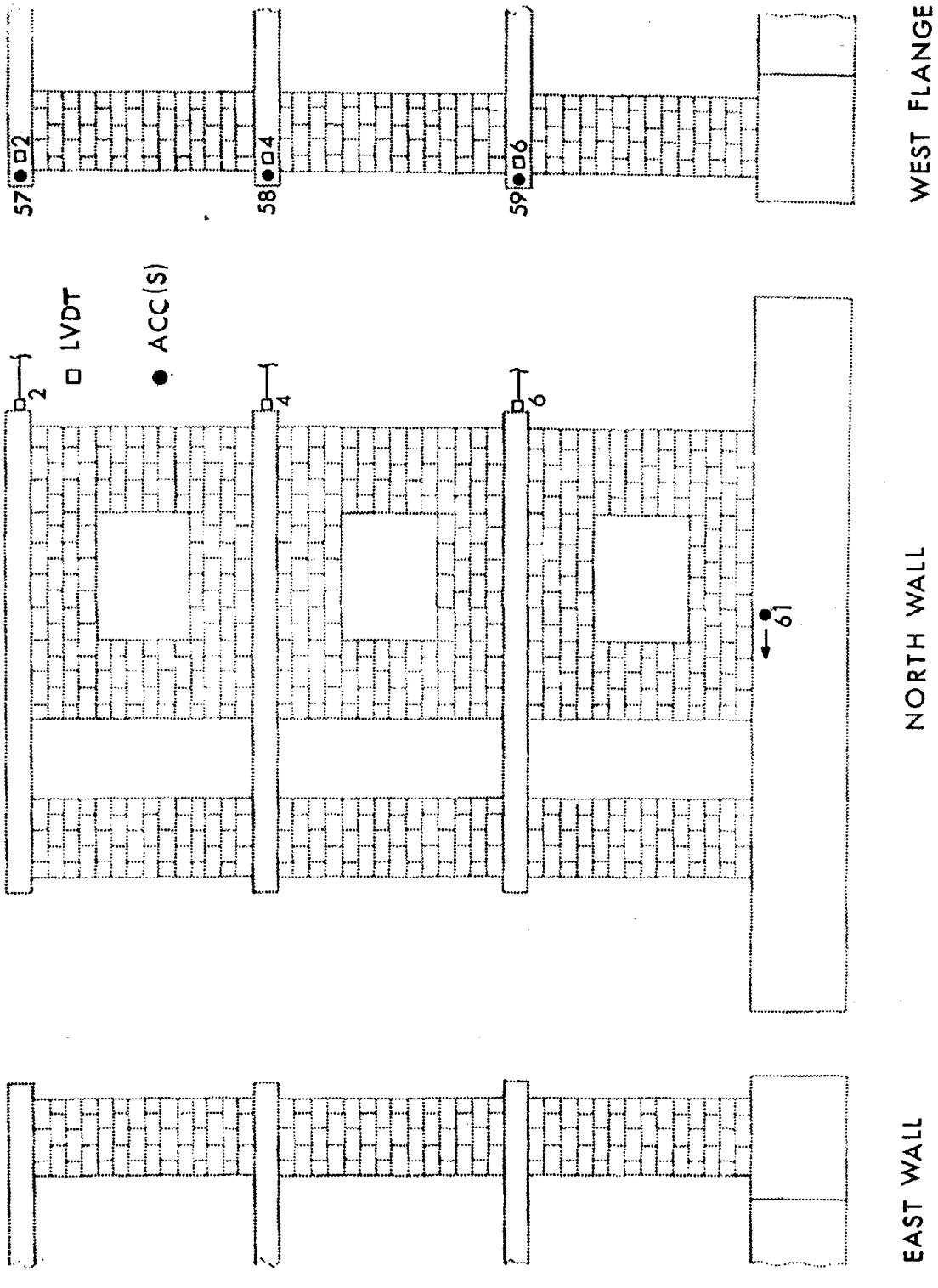

Figure C.6 (cont) Layout of Instrumentation (RM3)

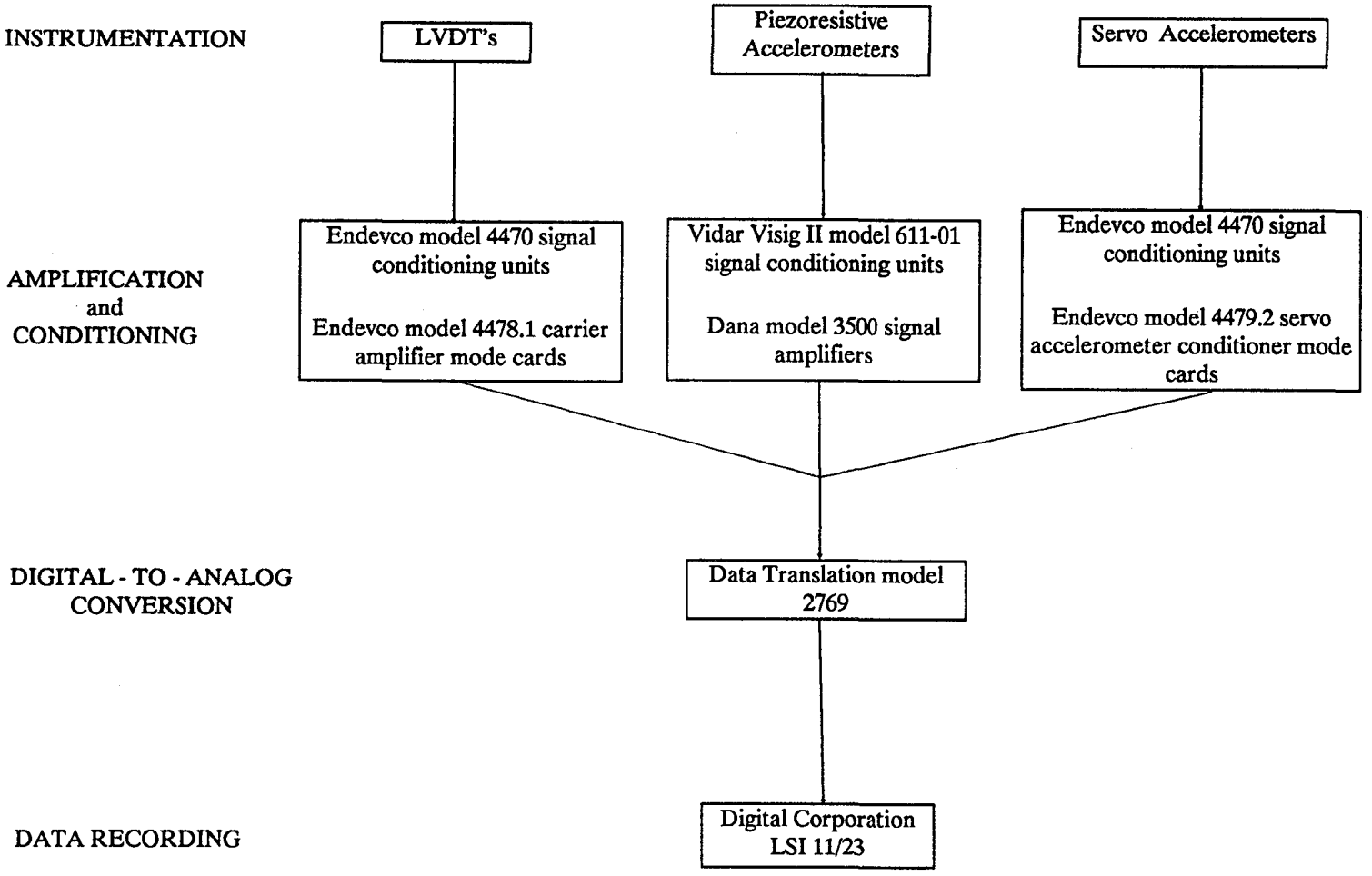

Figure C.7 Signal Path (Dynamic Tests)

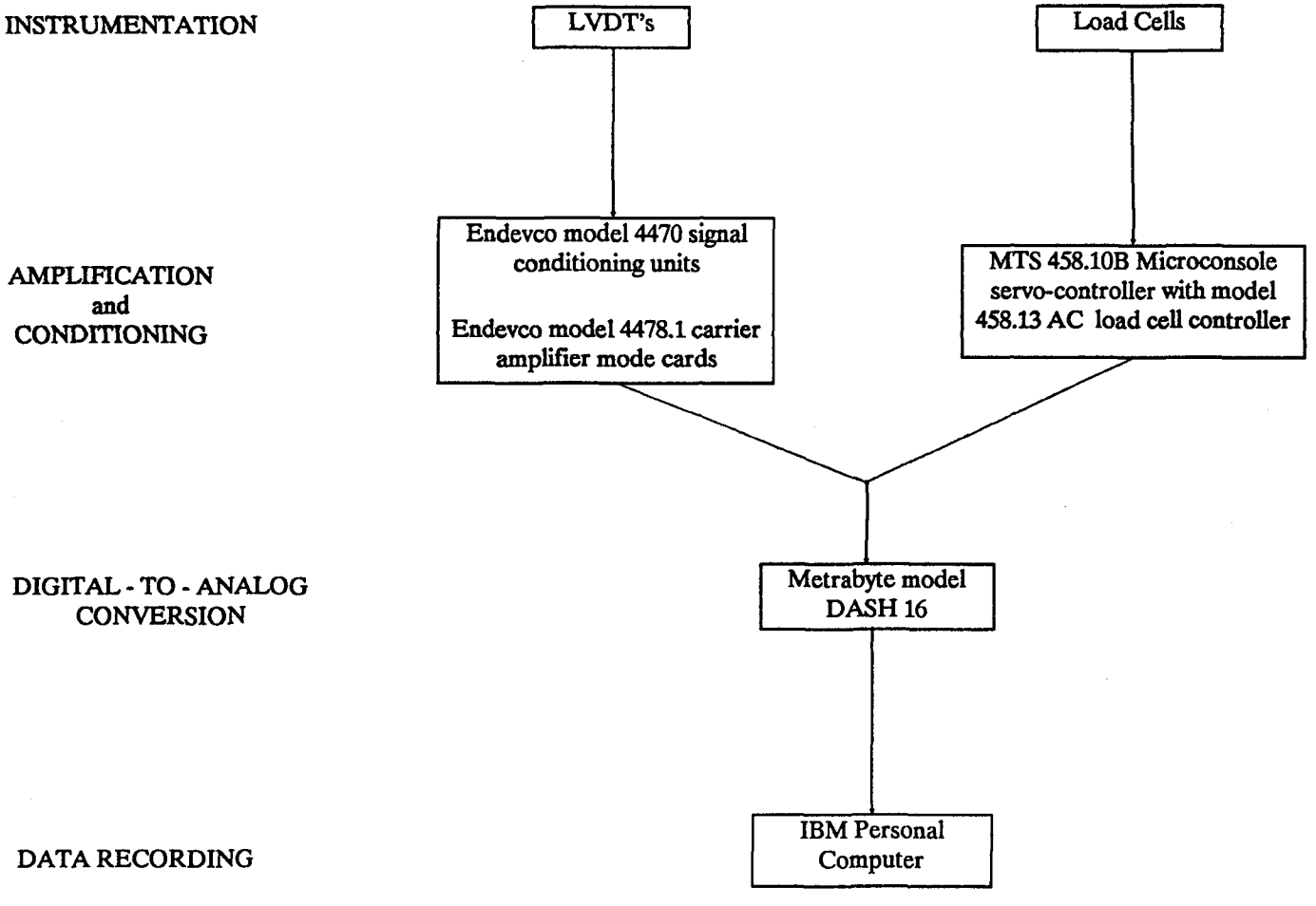

Figure C.8 Signal Path (Static Test)

APPENDIX D

CRACK PATTERNS

Cracking patterns, recorded before the first test run for each structure and following each subsequent run, are presented in this appendix.

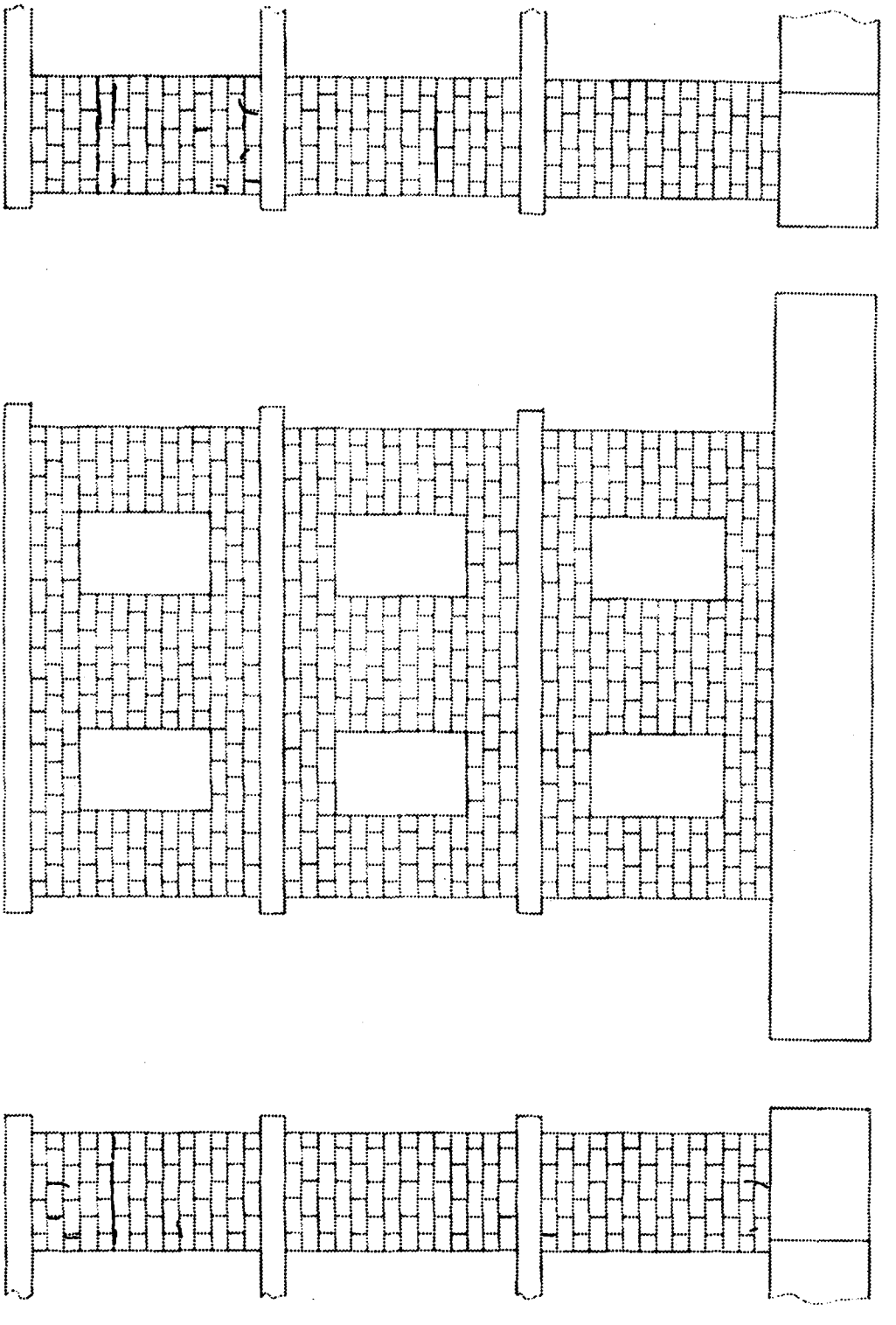

Figure D.1 RM1 Crack Patterns

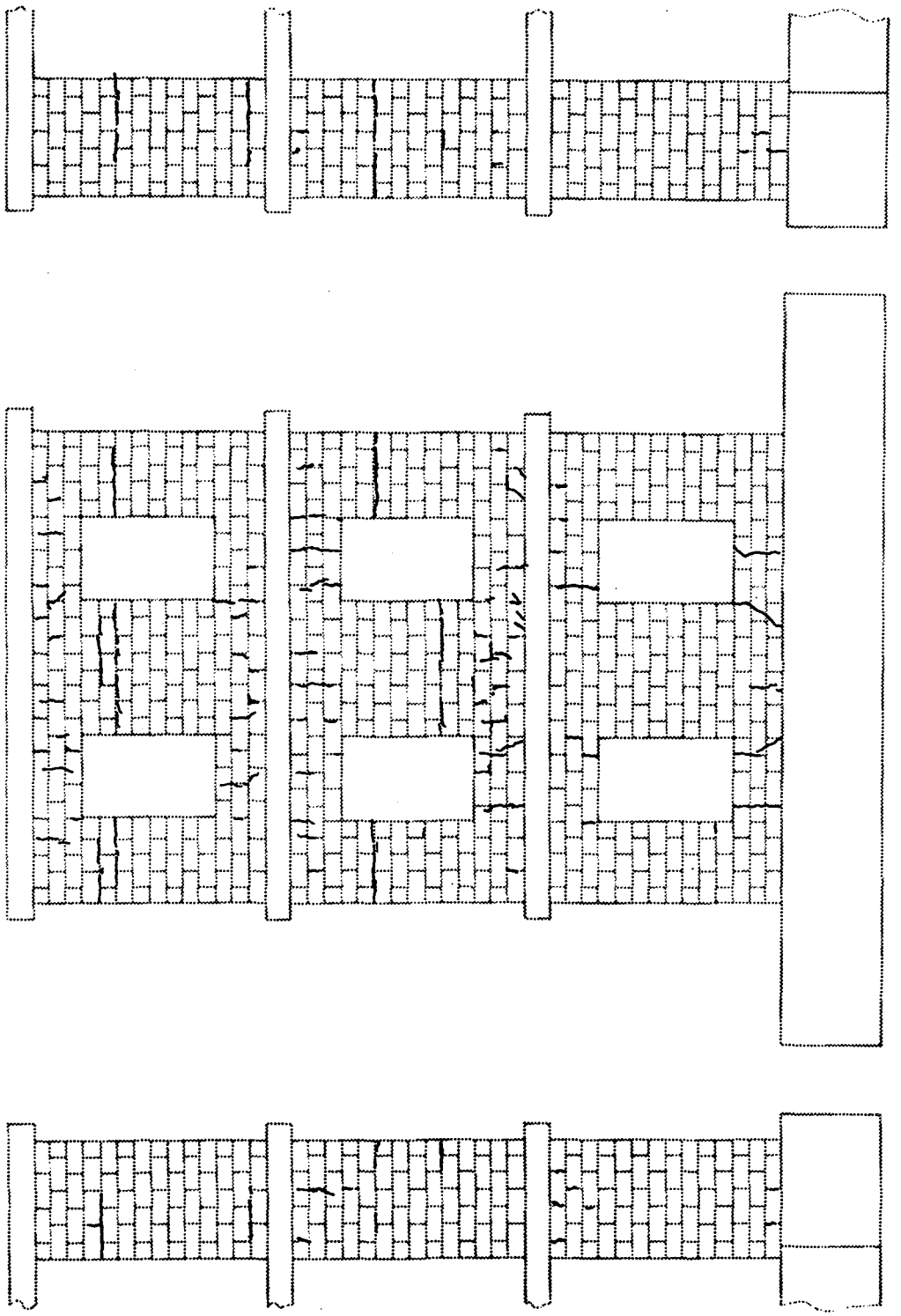

Figure D.1 (cont) RM1 Crack Patterns

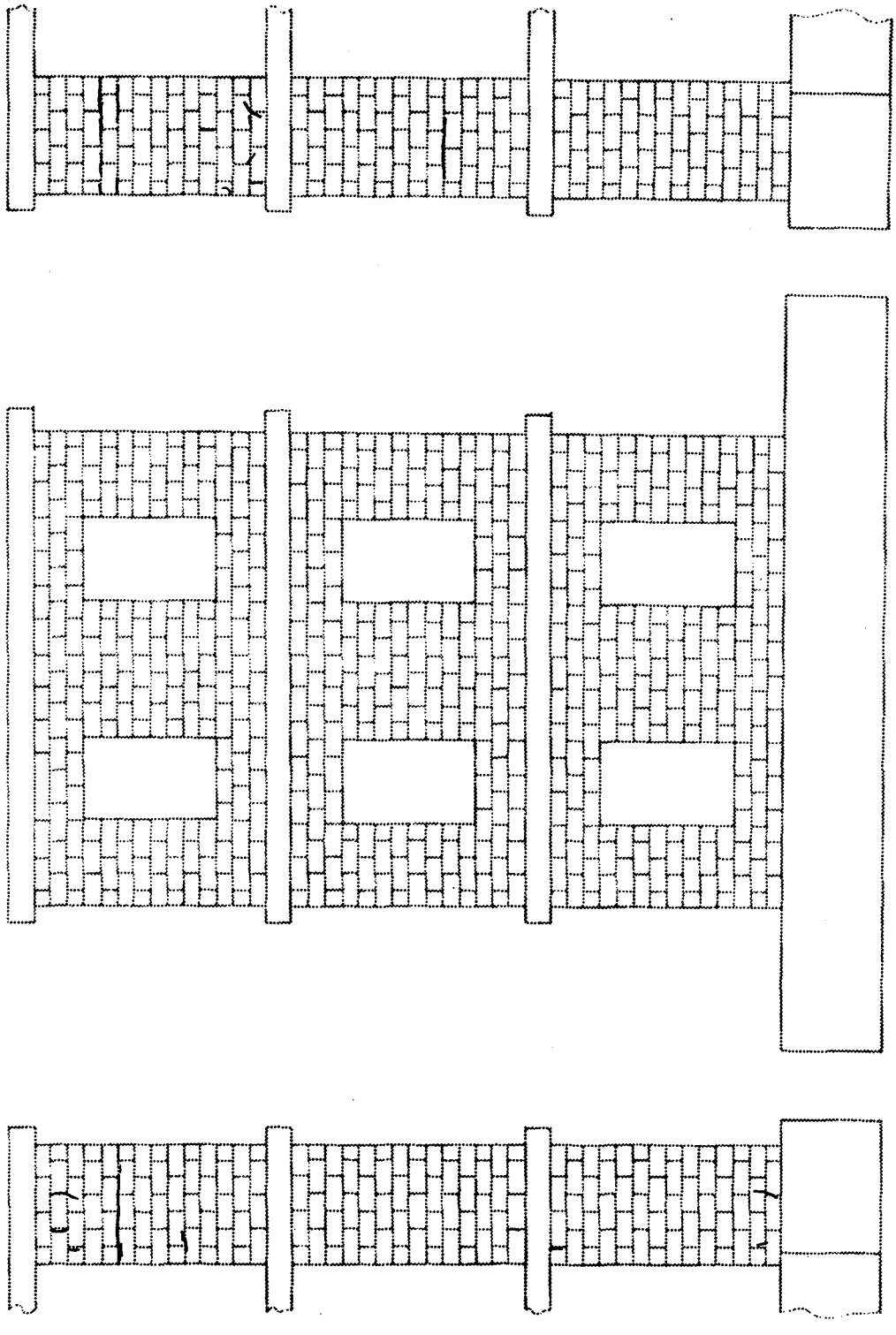

Figure D.1 (cont) RM1 Crack Patterns

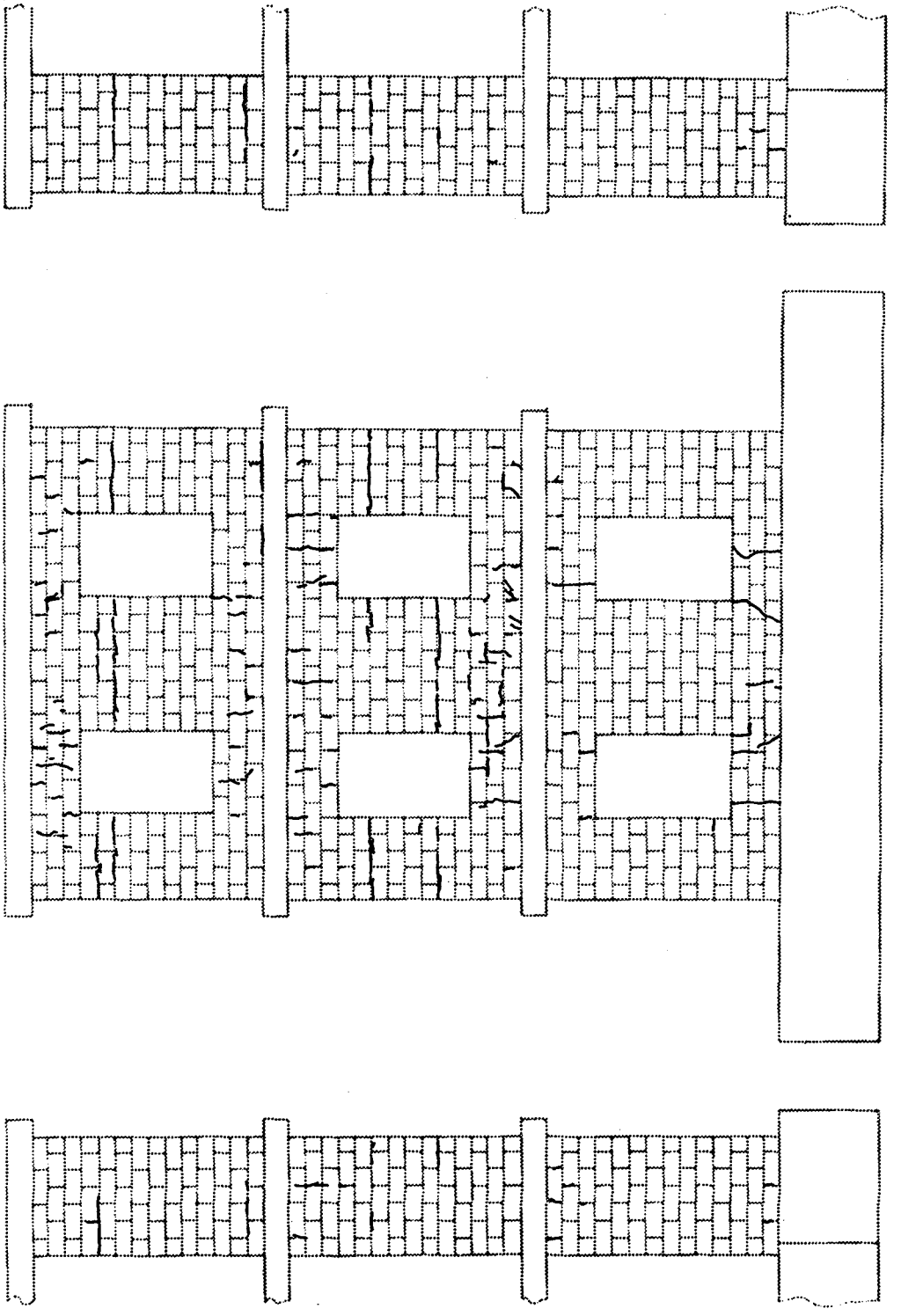

Figure D.1 (cont) RM1 Crack Patterns

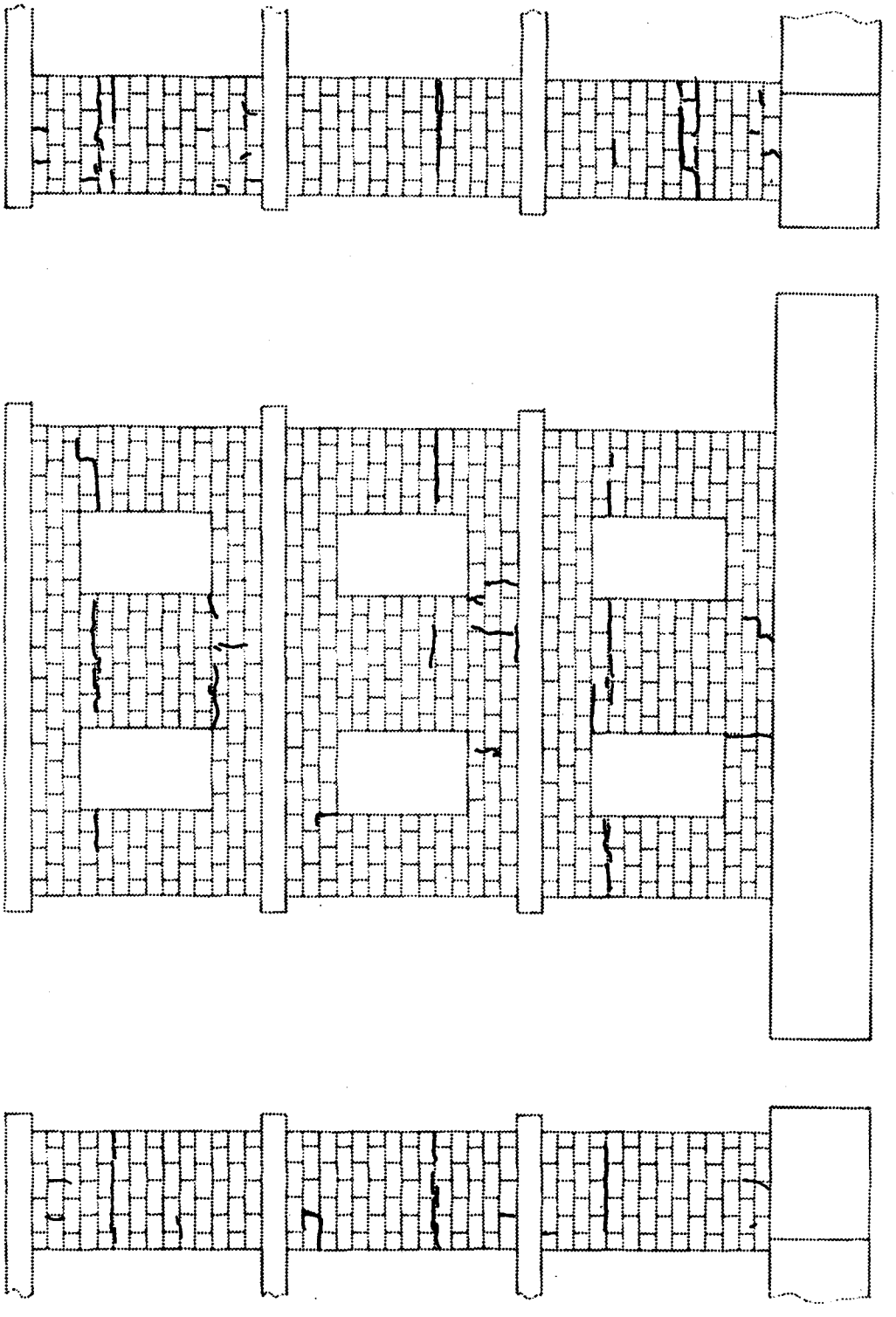

Figure D.1 (cont) RM1 Crack Patterns

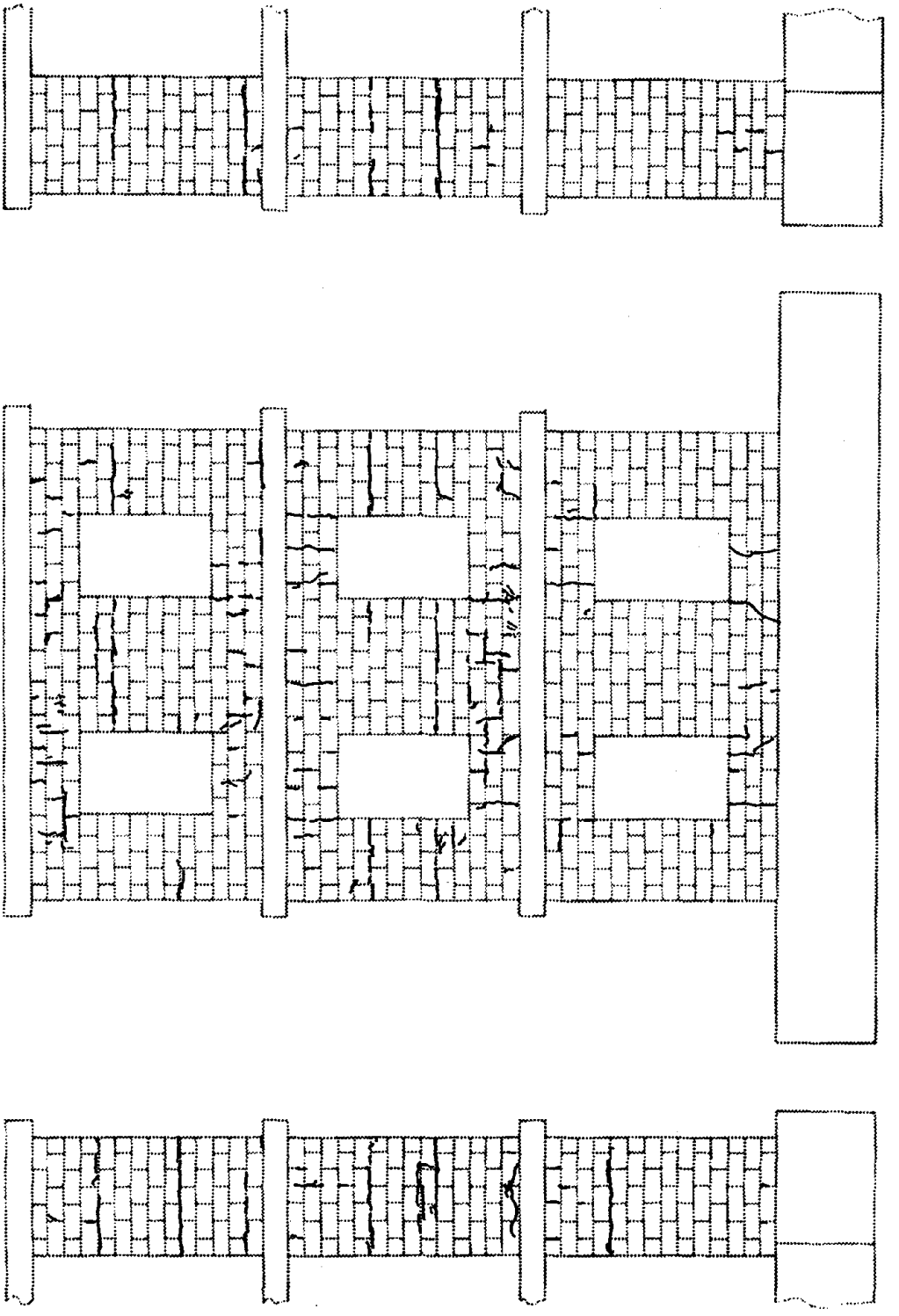

Figure D.1 (cont) RM1 Crack Patterns

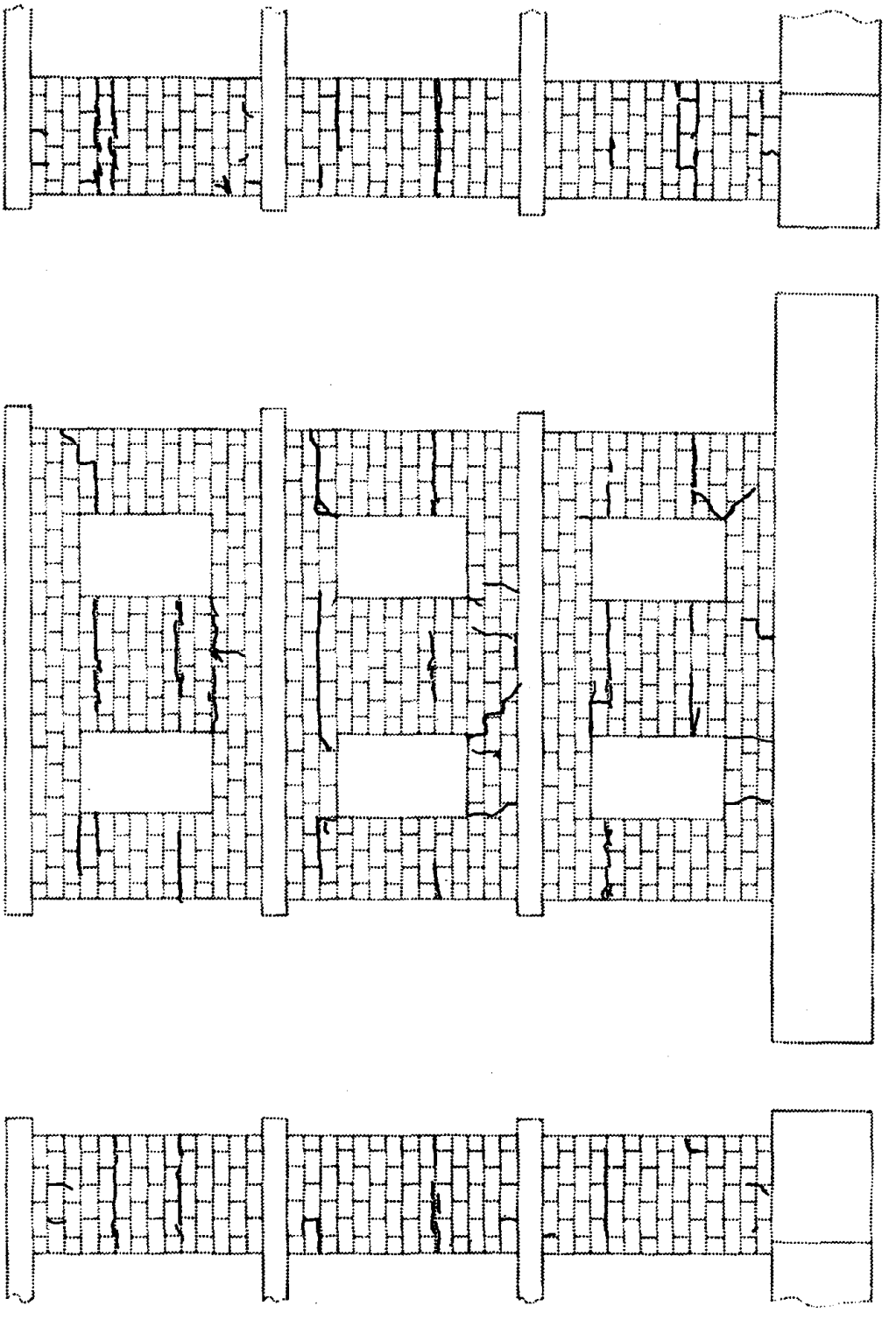

Figure D.1 (cont) RM1 Crack Patterns

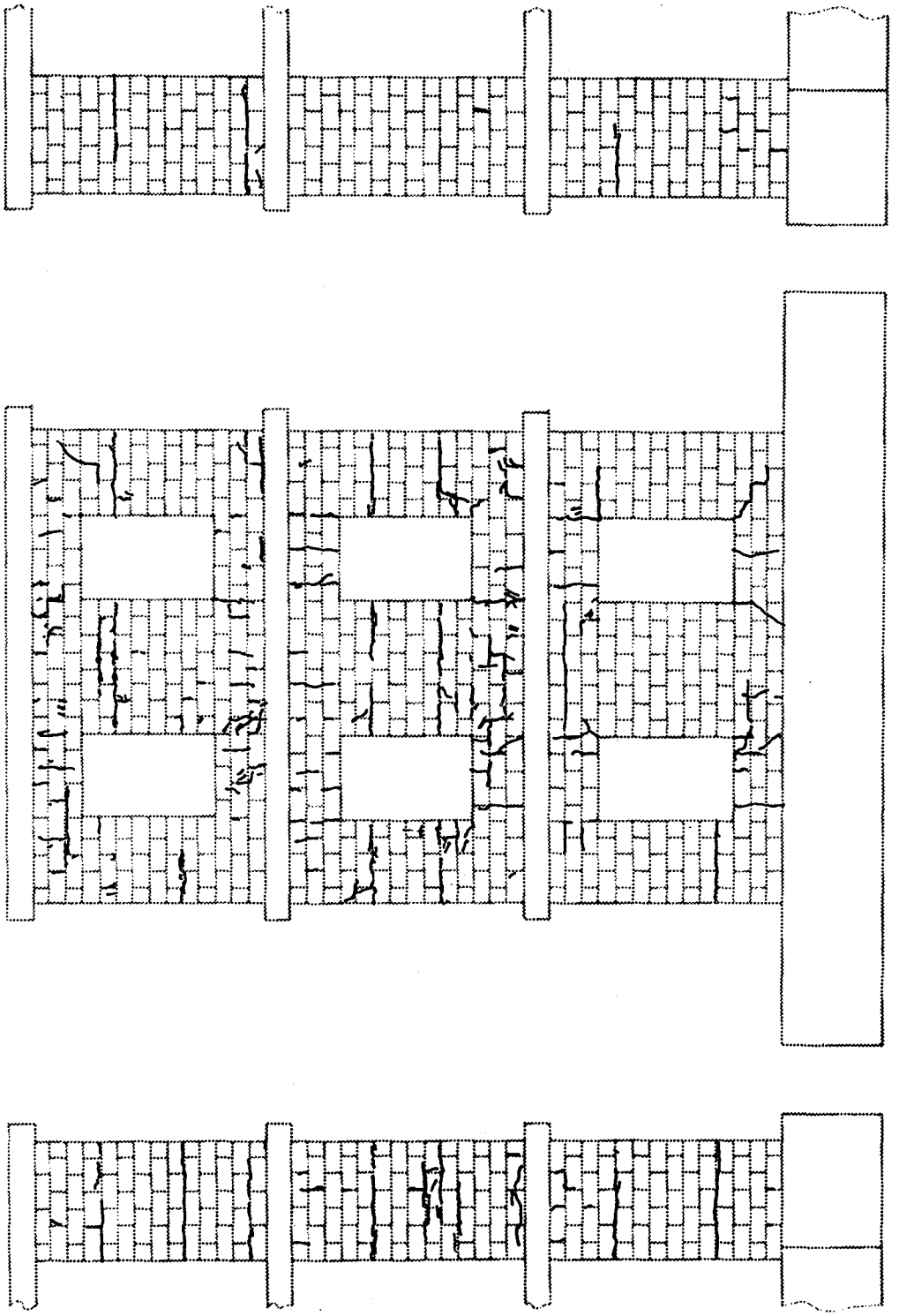

Figure D.1 (cont) RM1 Crack Patterns

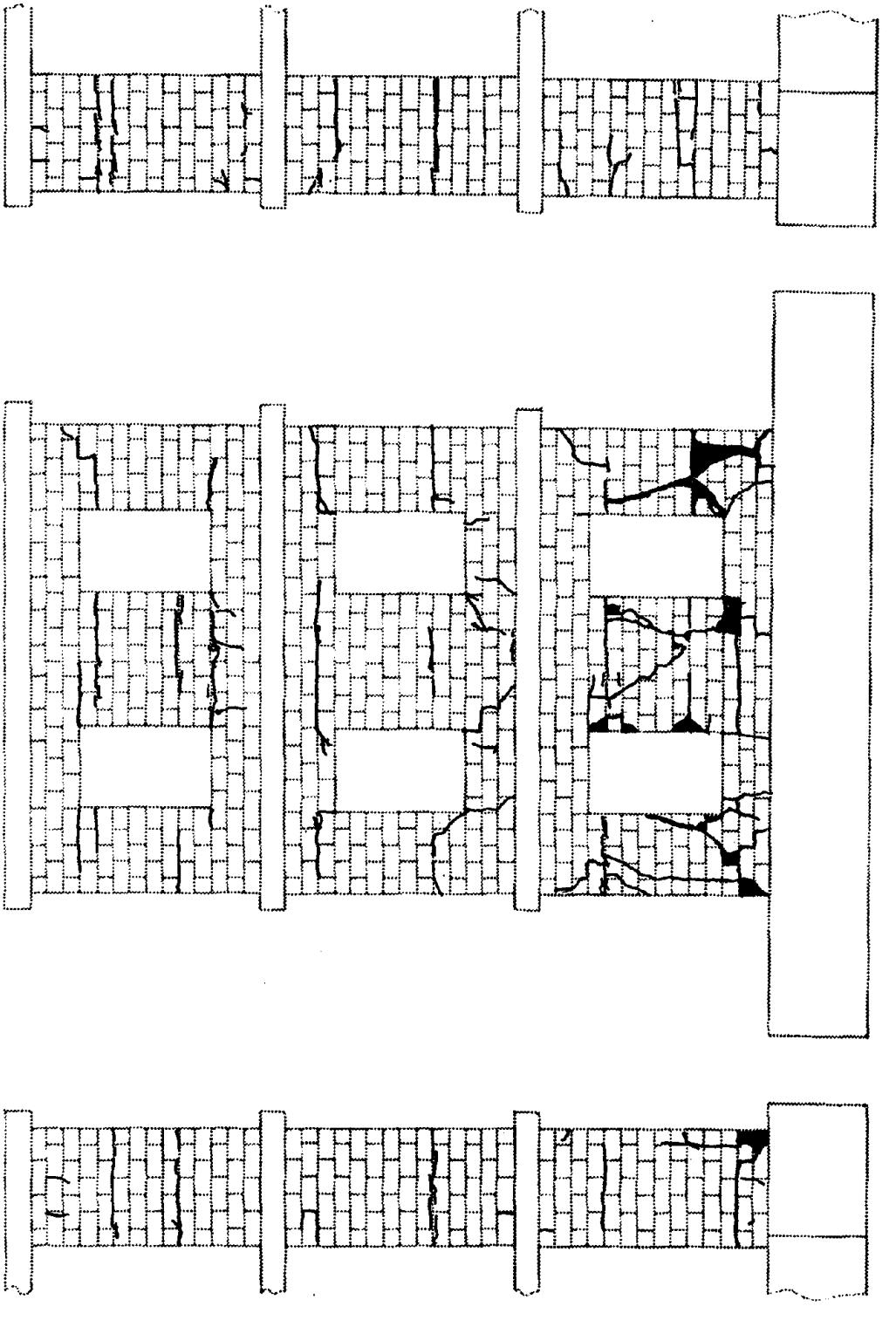

Figure D.1 (cont) RM1 Crack Patterns

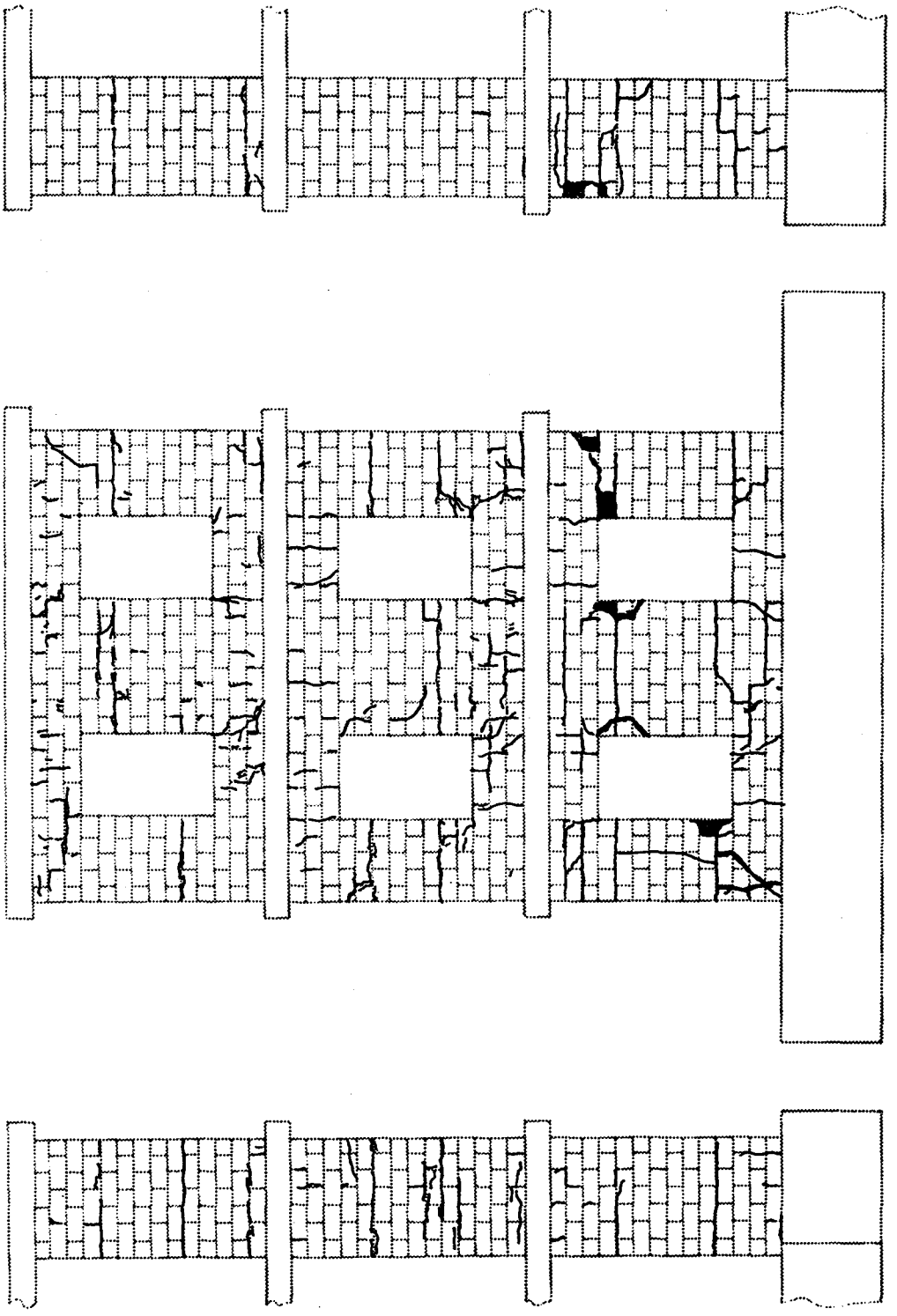

Figure D.1 (cont) RM1 Crack Patterns

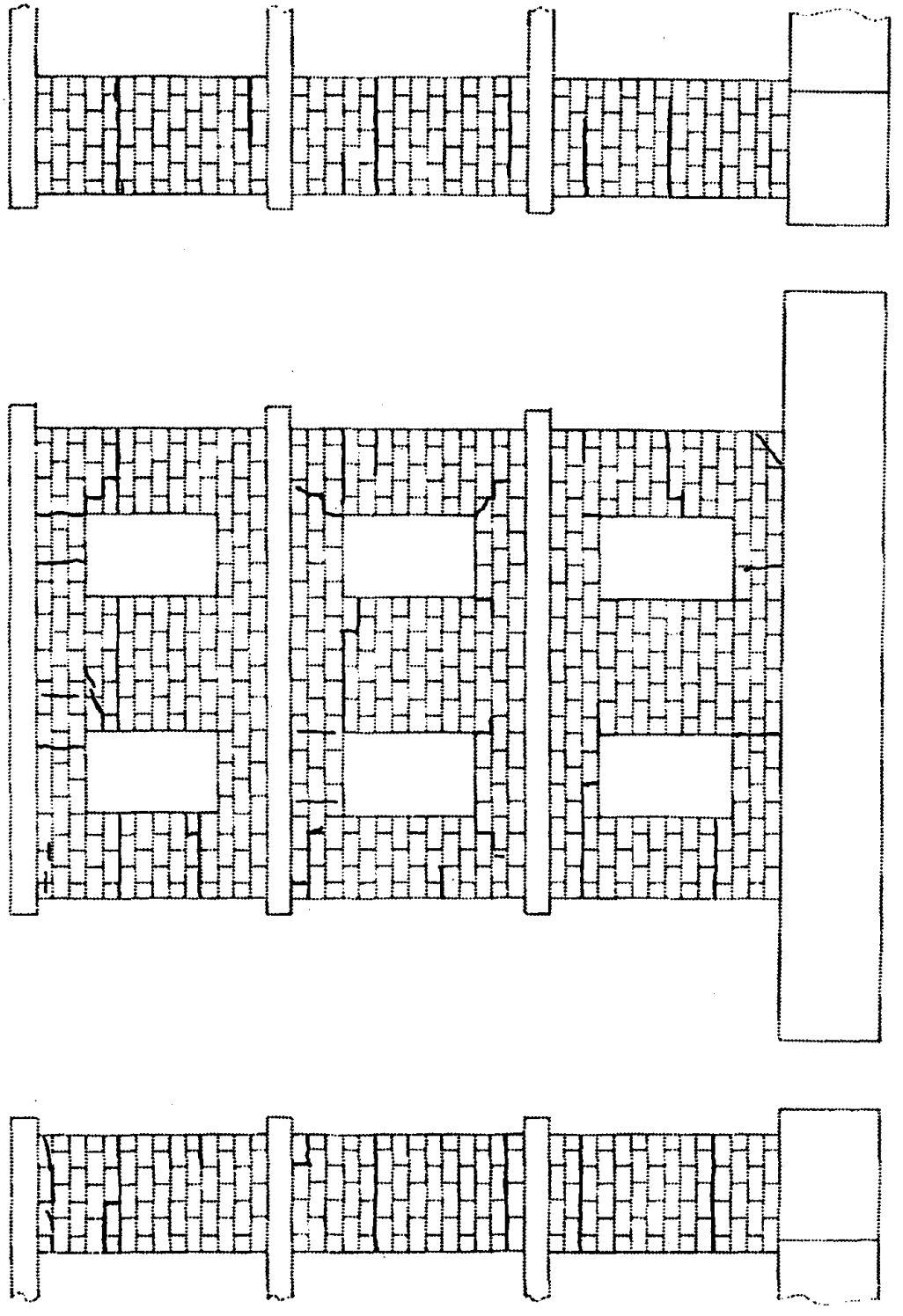

Figure D.2 RM2 Crack Patterns

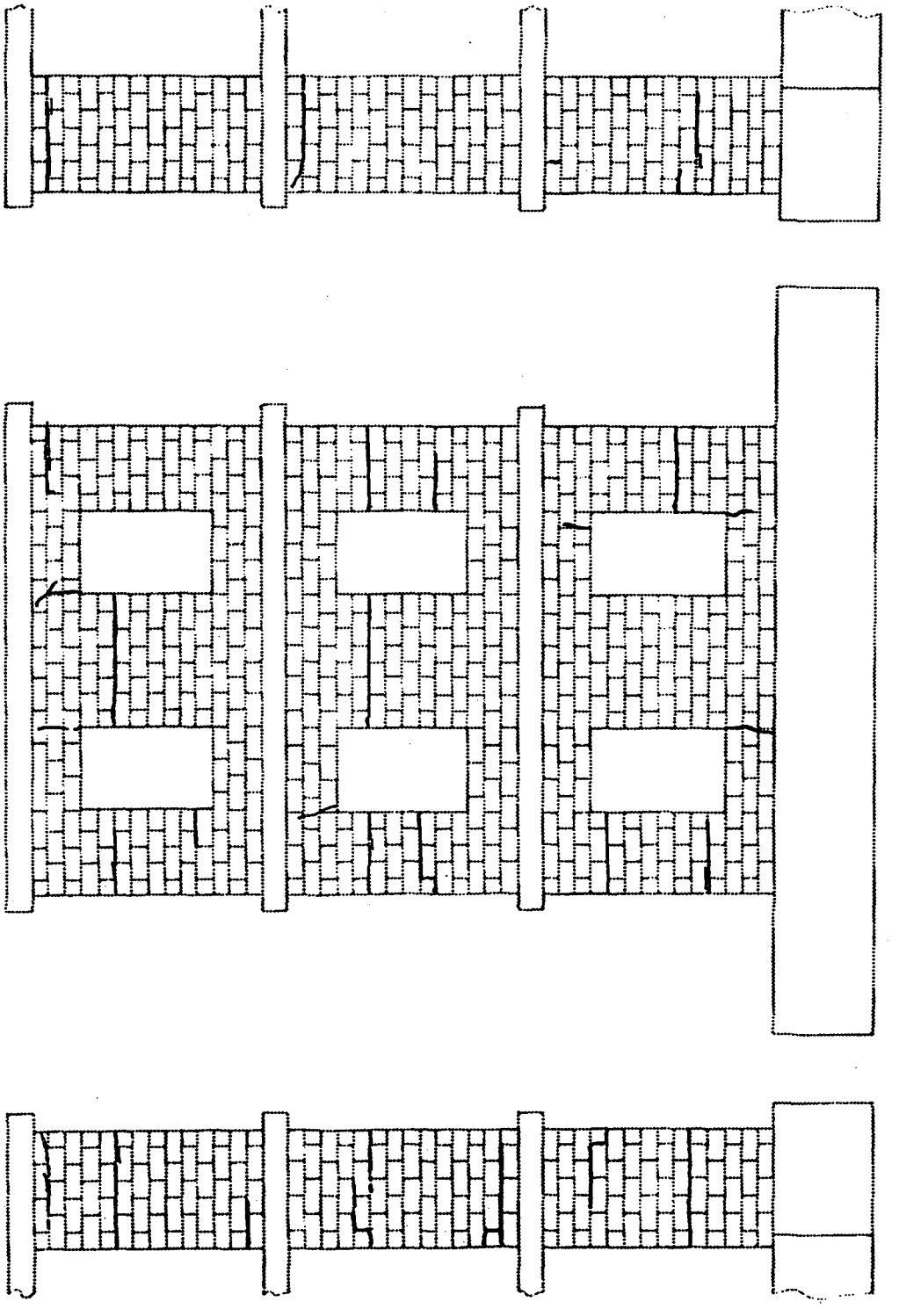

Figure D.2 (cont) RM2 Crack Patterns

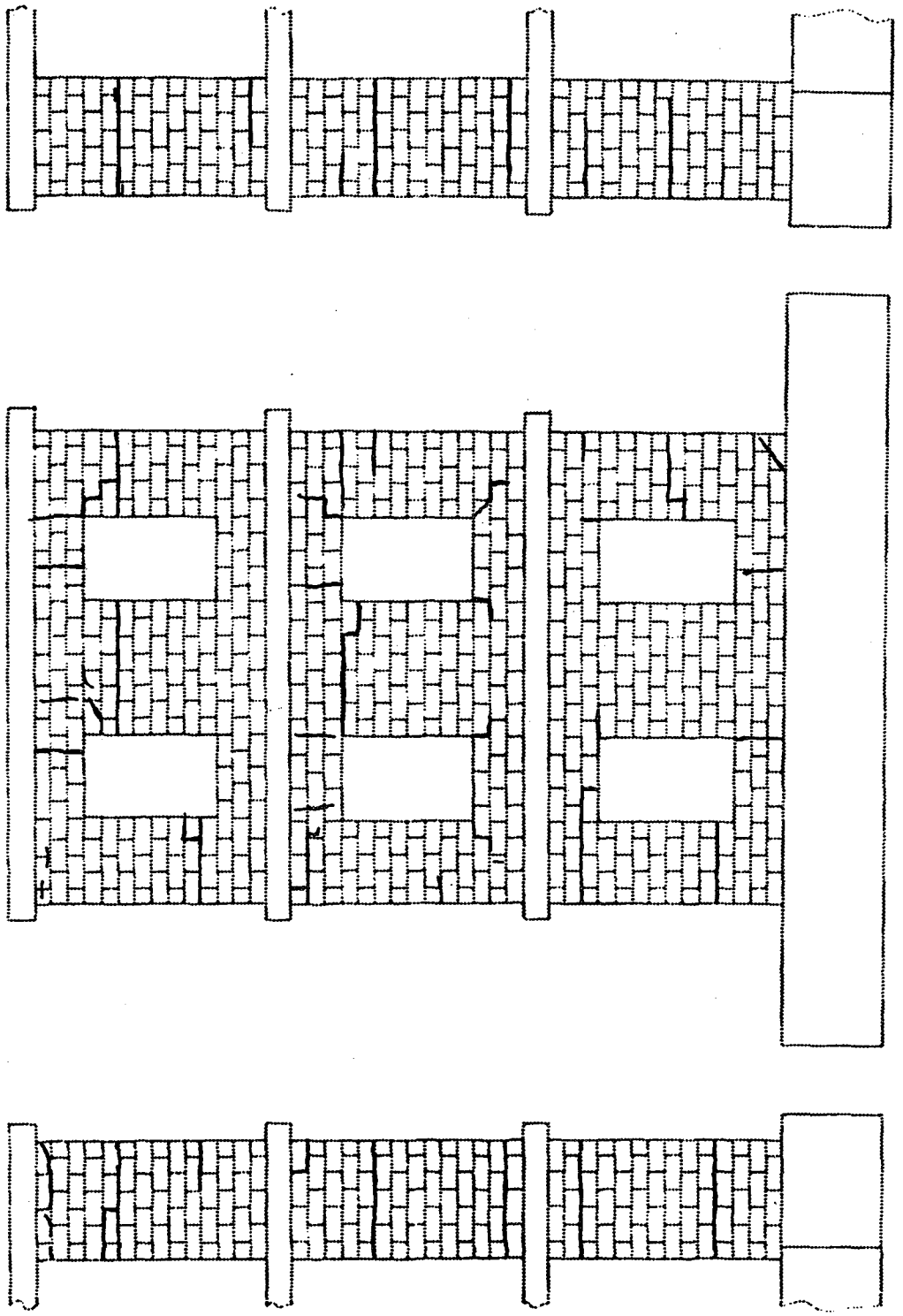

Figure D.2 (cont) RM2 Crack Patterns

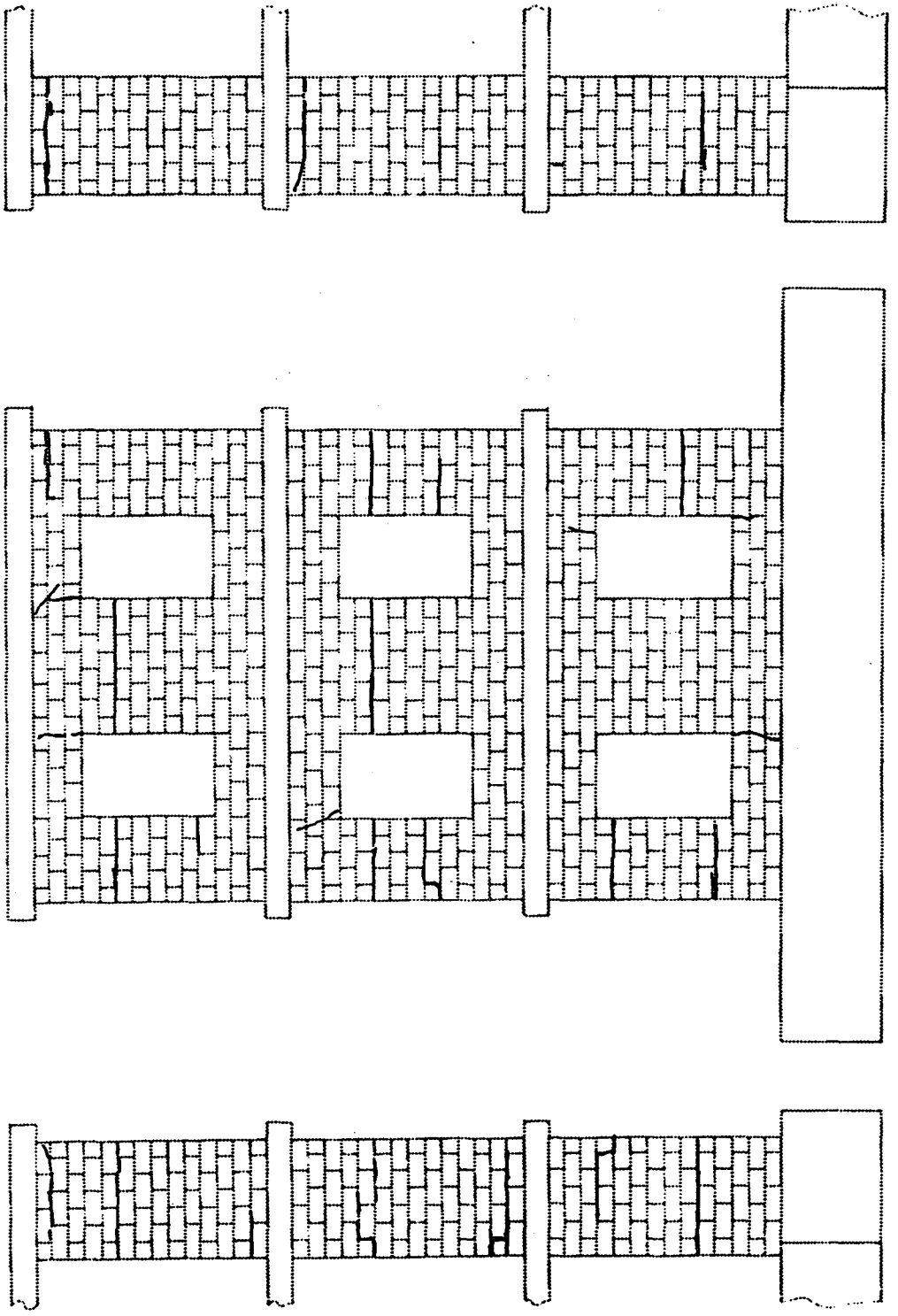

Figure D.2 (cont) RM2 Crack Patterns

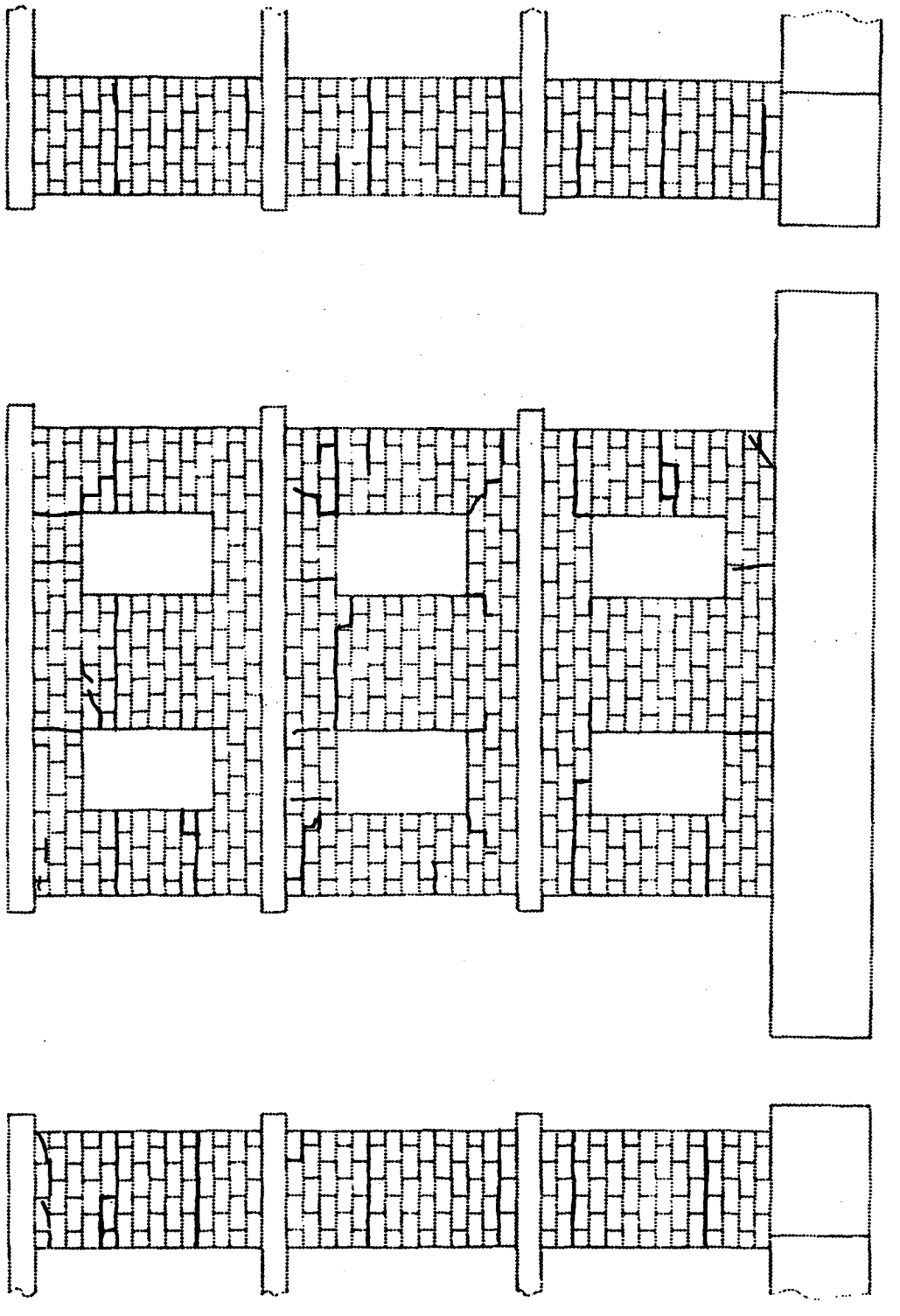

Figure D.2 (cont) RM2 Crack Patterns

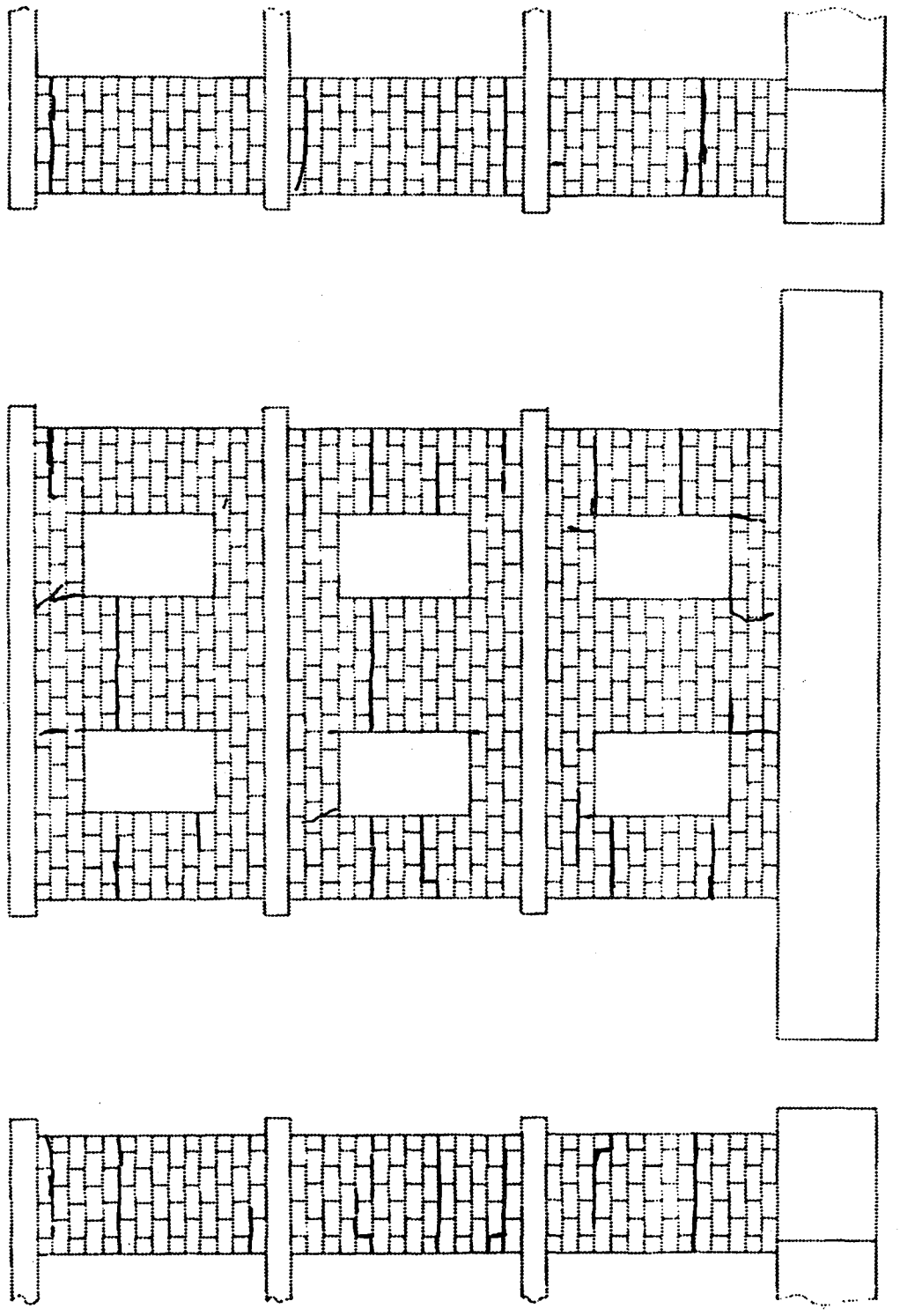

Figure D.2 (cont) RM2 Crack Patterns

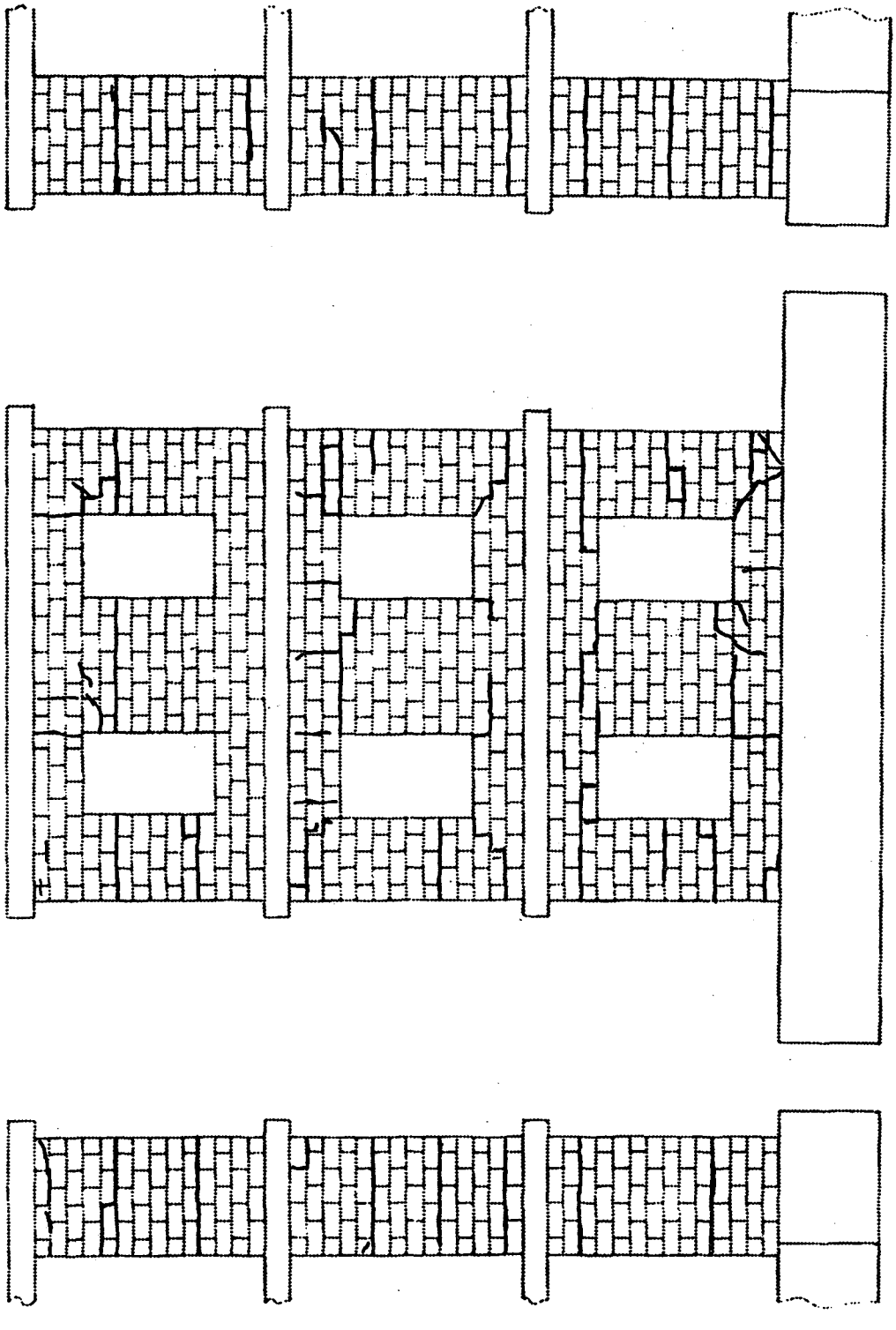

Figure D.2 (cont) RM2 Crack Patterns

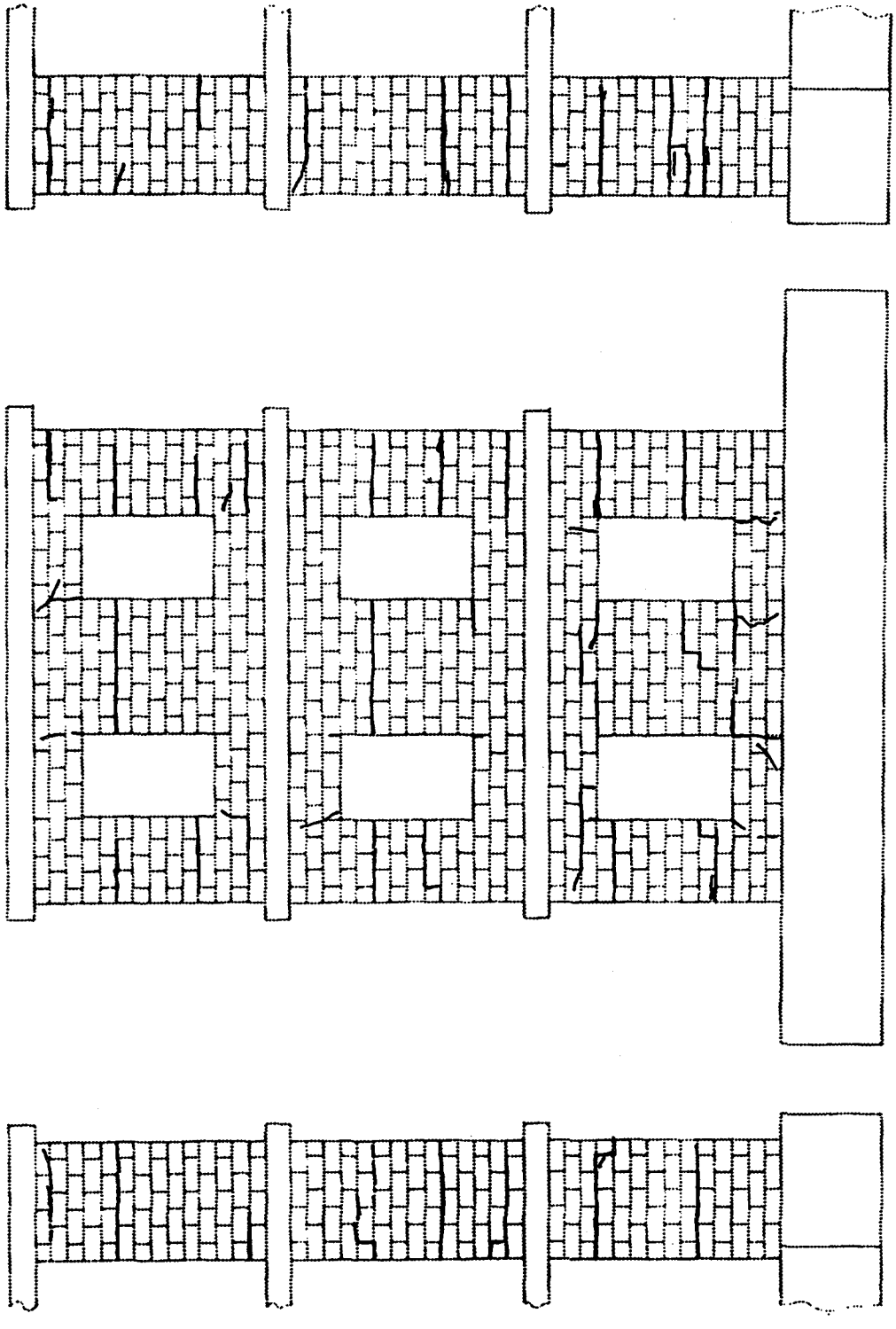

Figure D.2 (cont) RM2 Crack Patterns

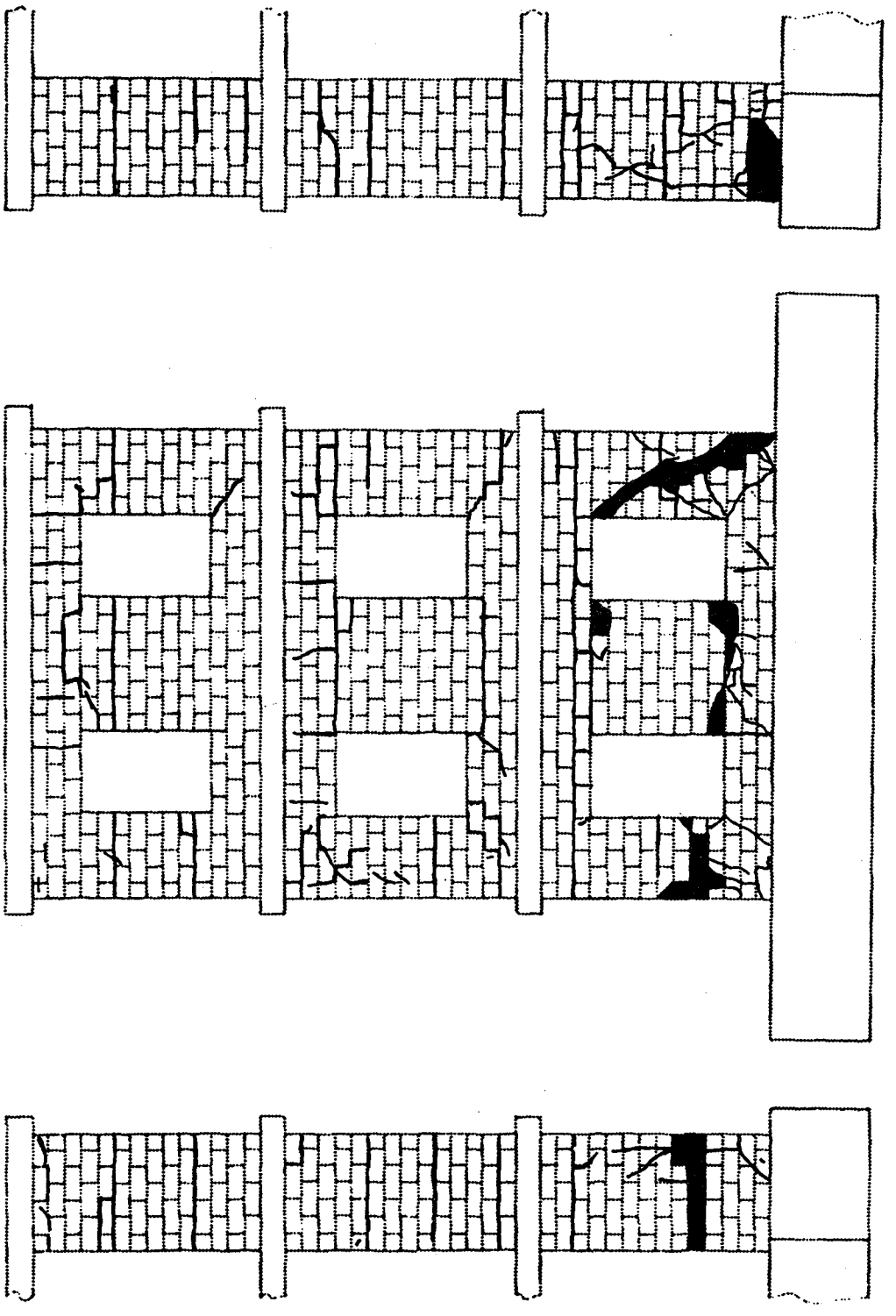

Figure D.2 (cont) RM2 Crack Patterns

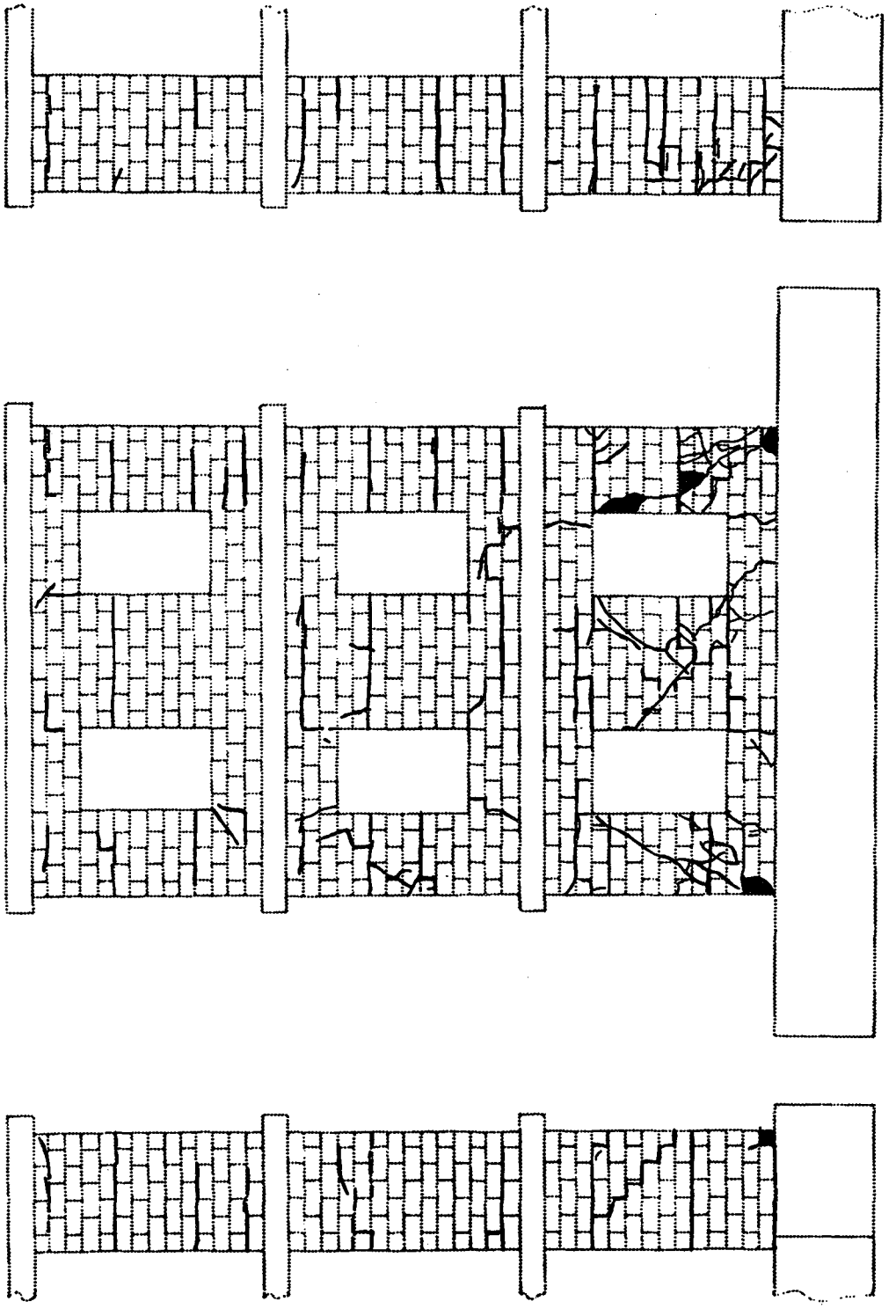

Figure D.2 (cont) RM2 Crack Patterns

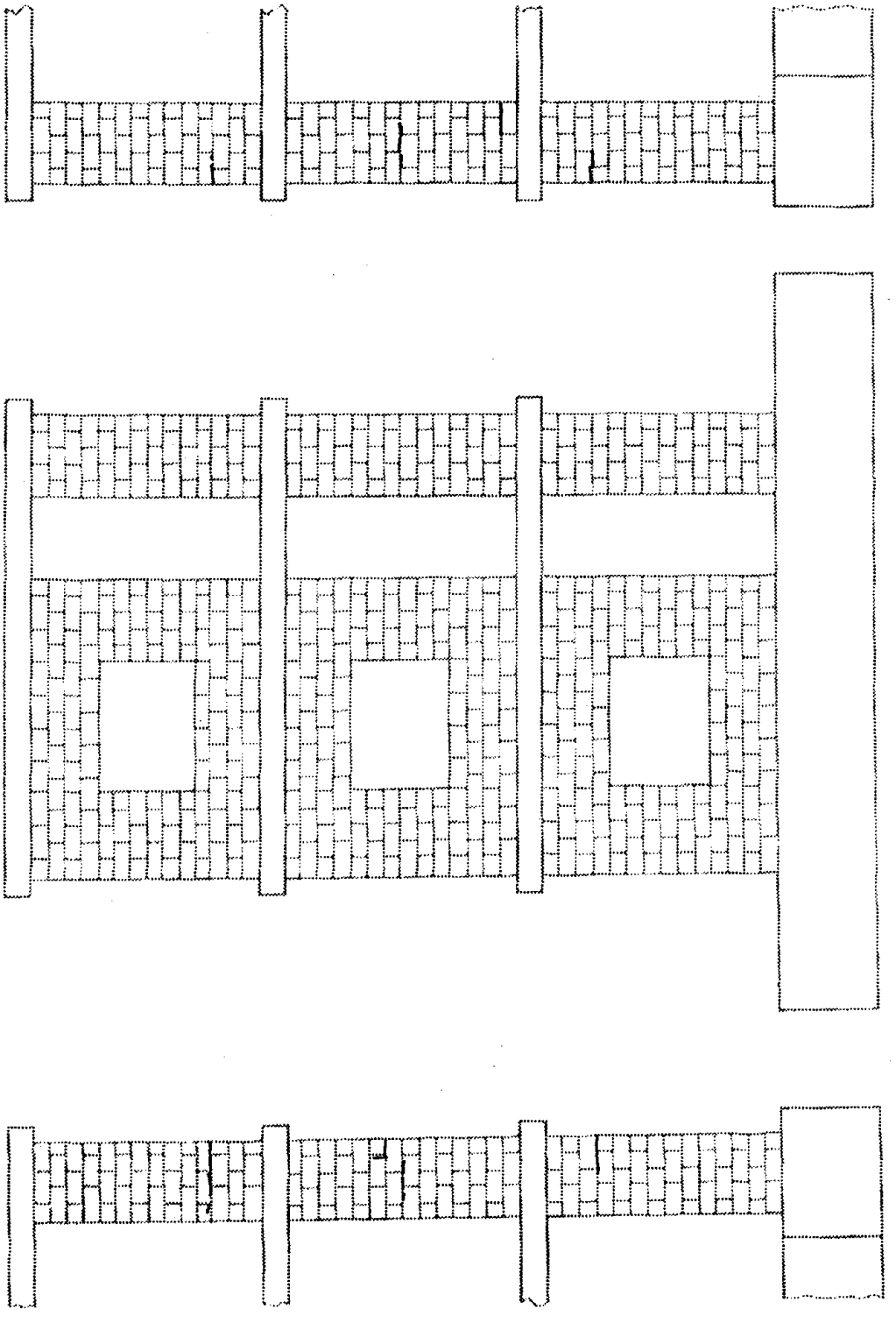

Figure D.3 RM3 Crack Patterns

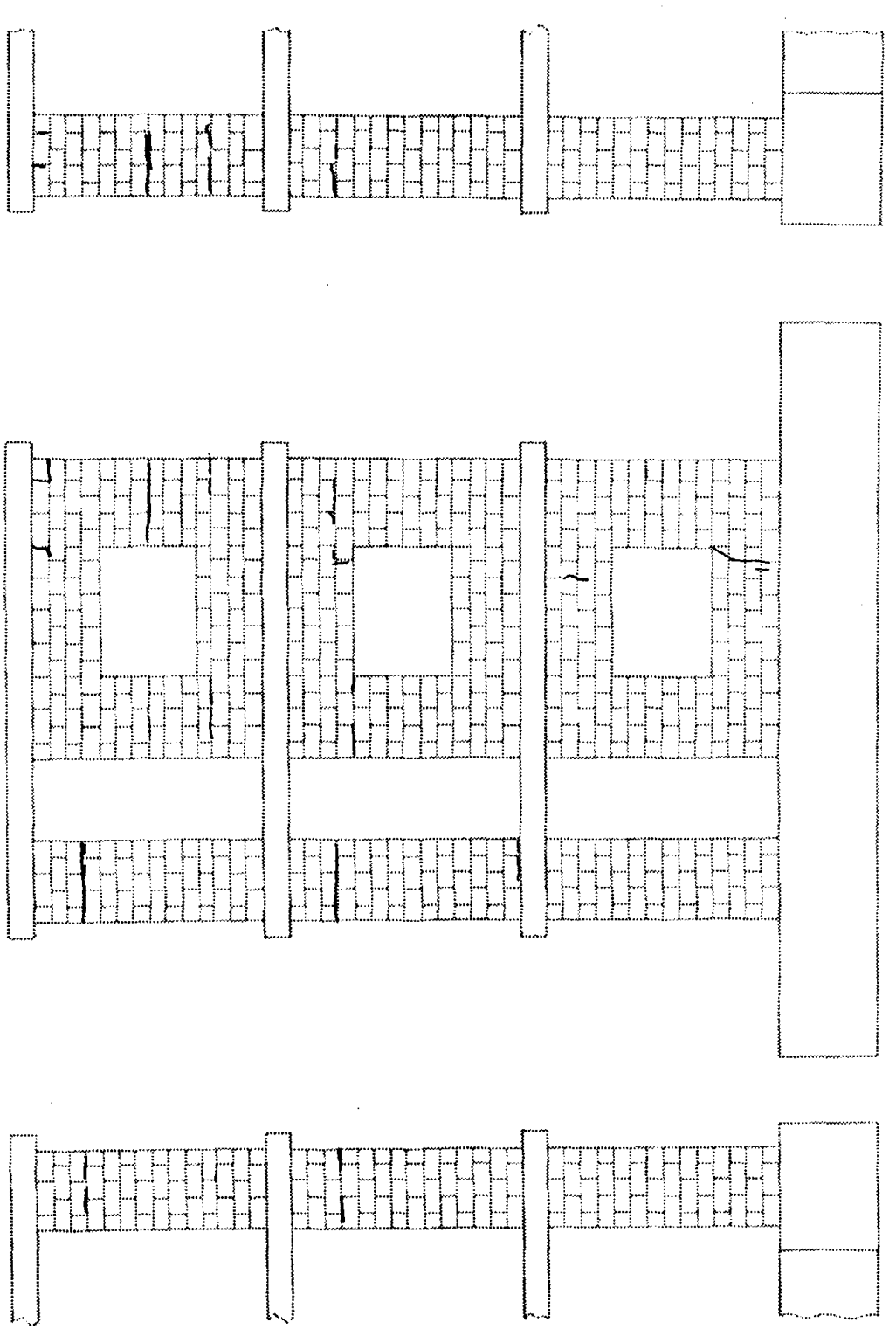

Figure D.3 (cont) RM3 Crack Patterns

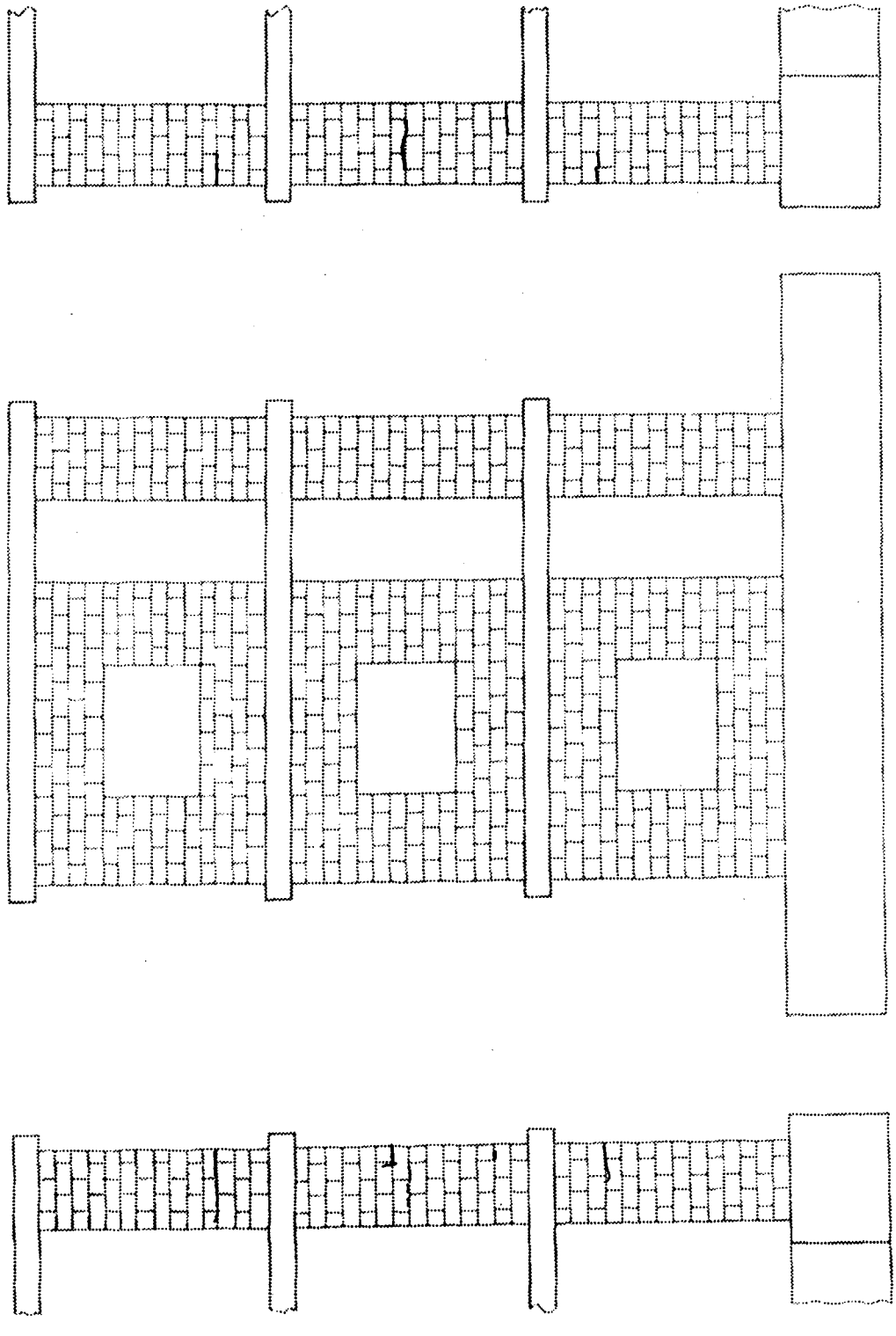

Figure D.3 (cont) RM3 Crack Patterns

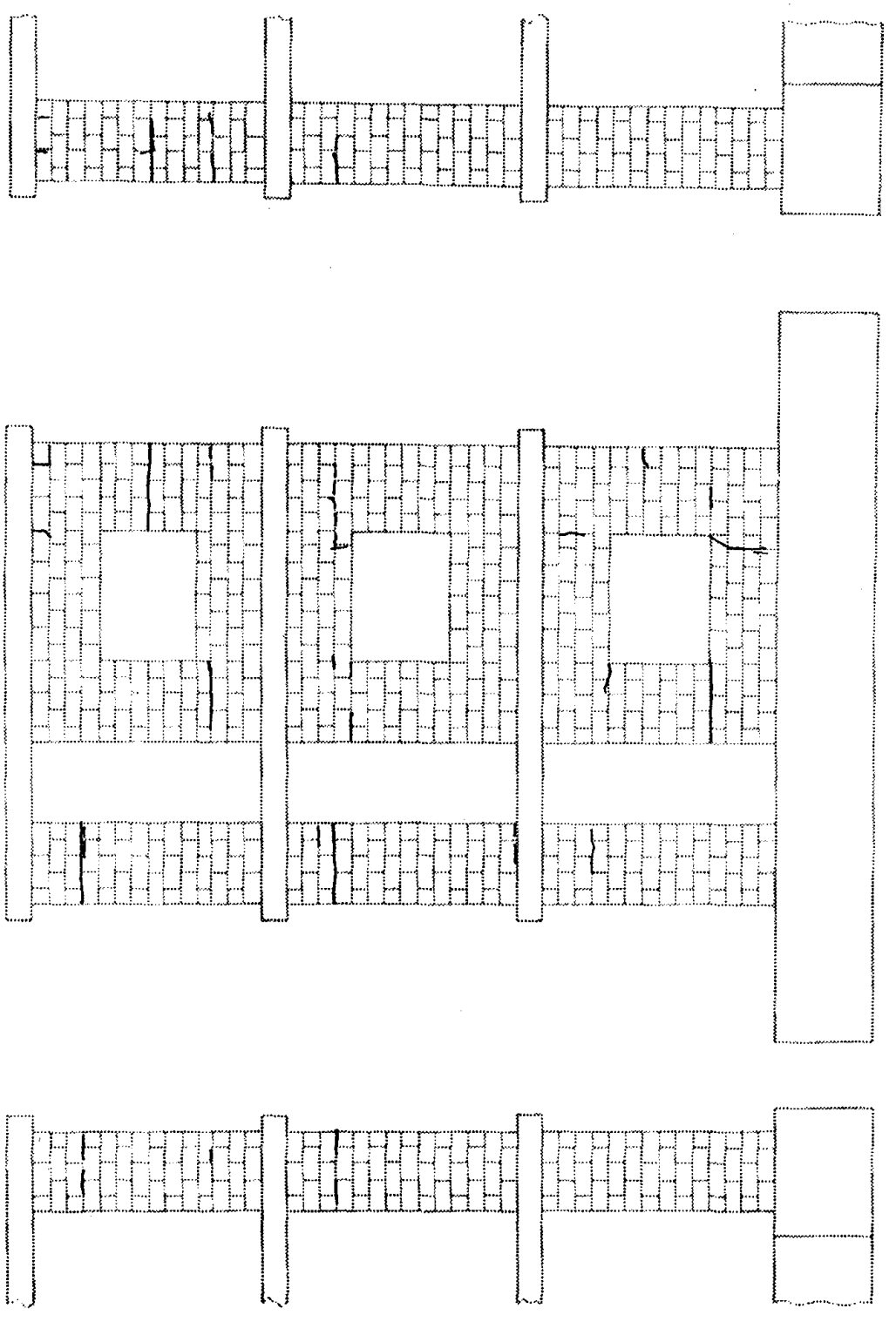

Figure D.3 (cont) RM3 Crack Patterns

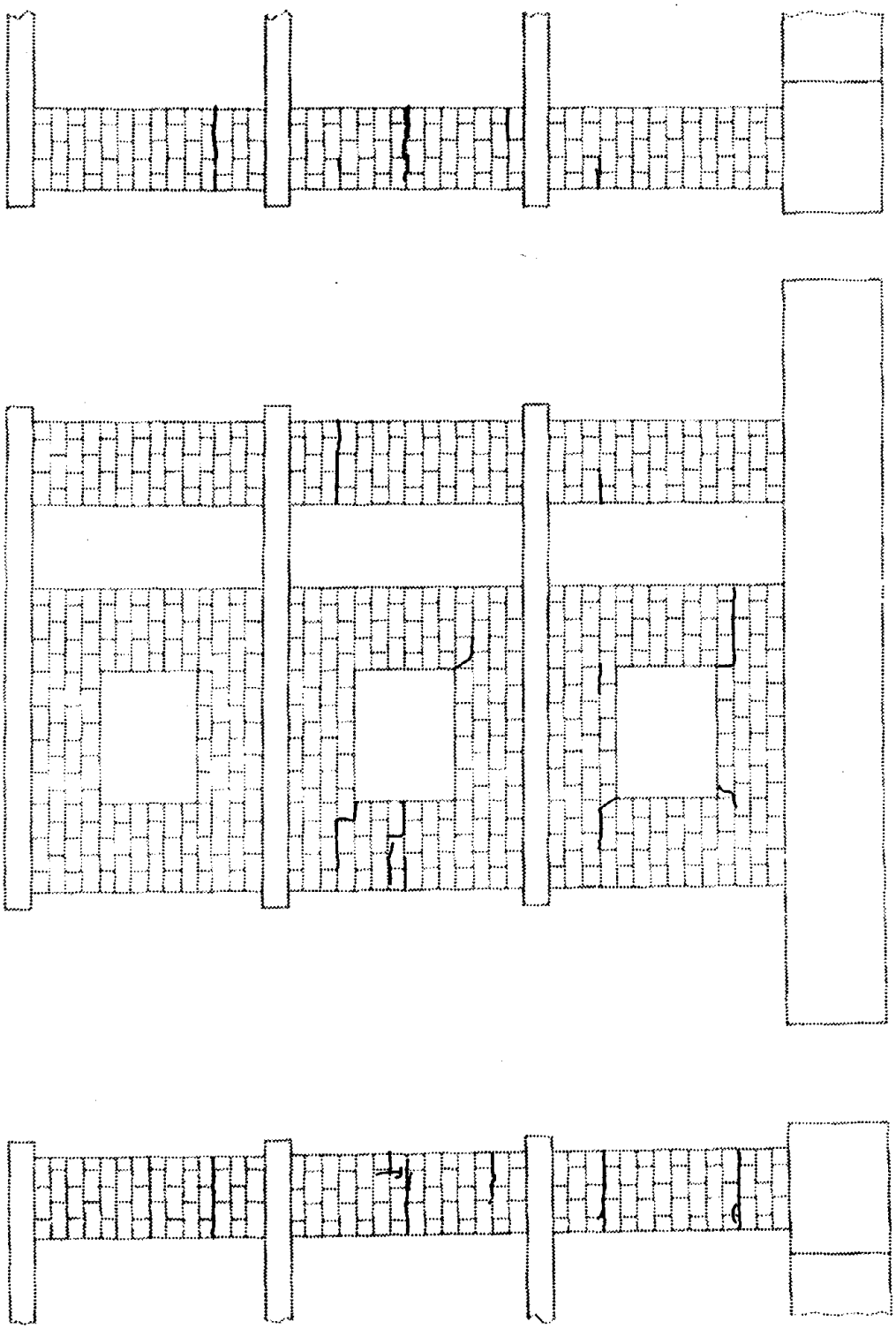

Figure D.3 (cont) RM3 Crack Patterns

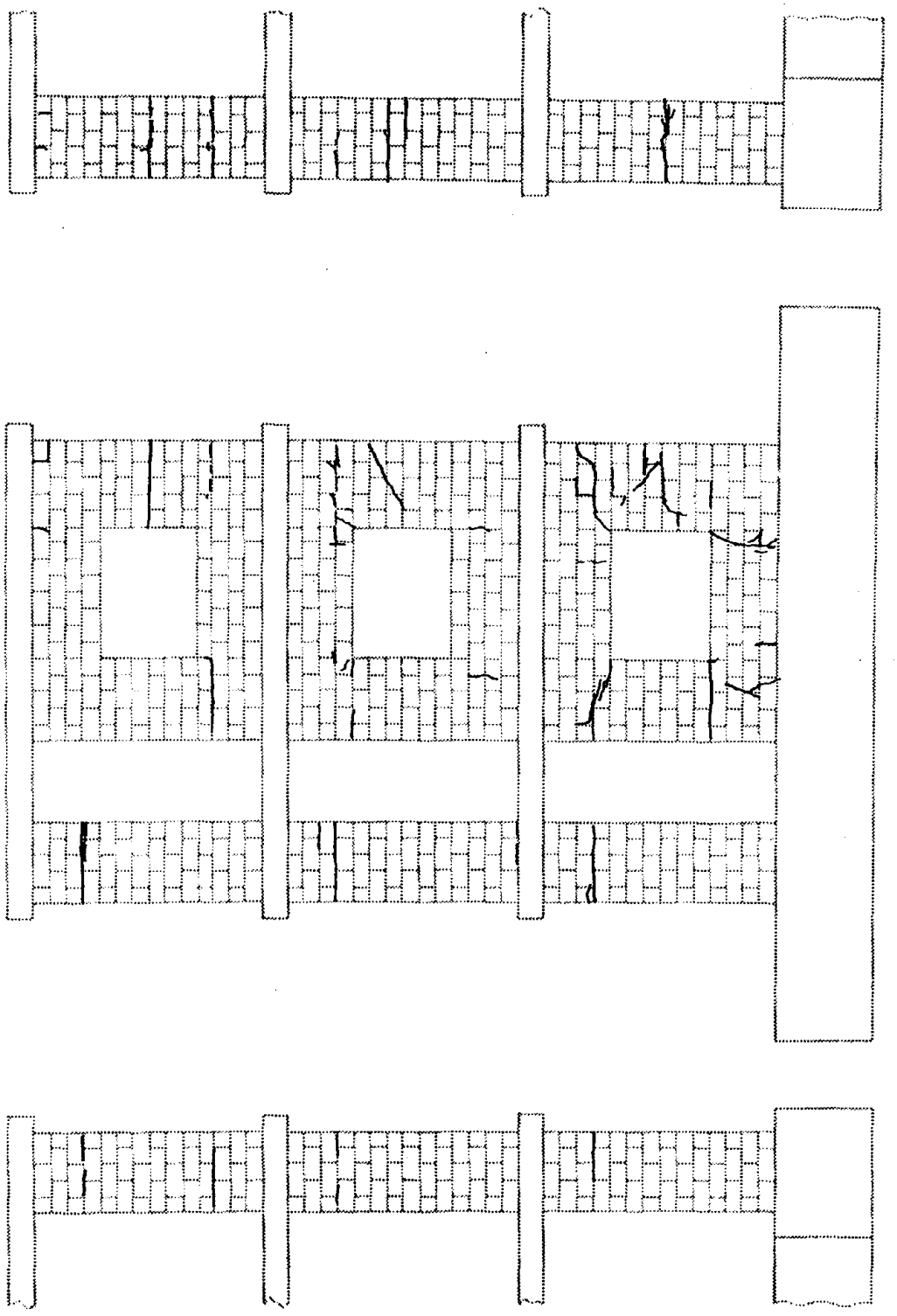

Figure D.3 (cont) RM3 Crack Patterns

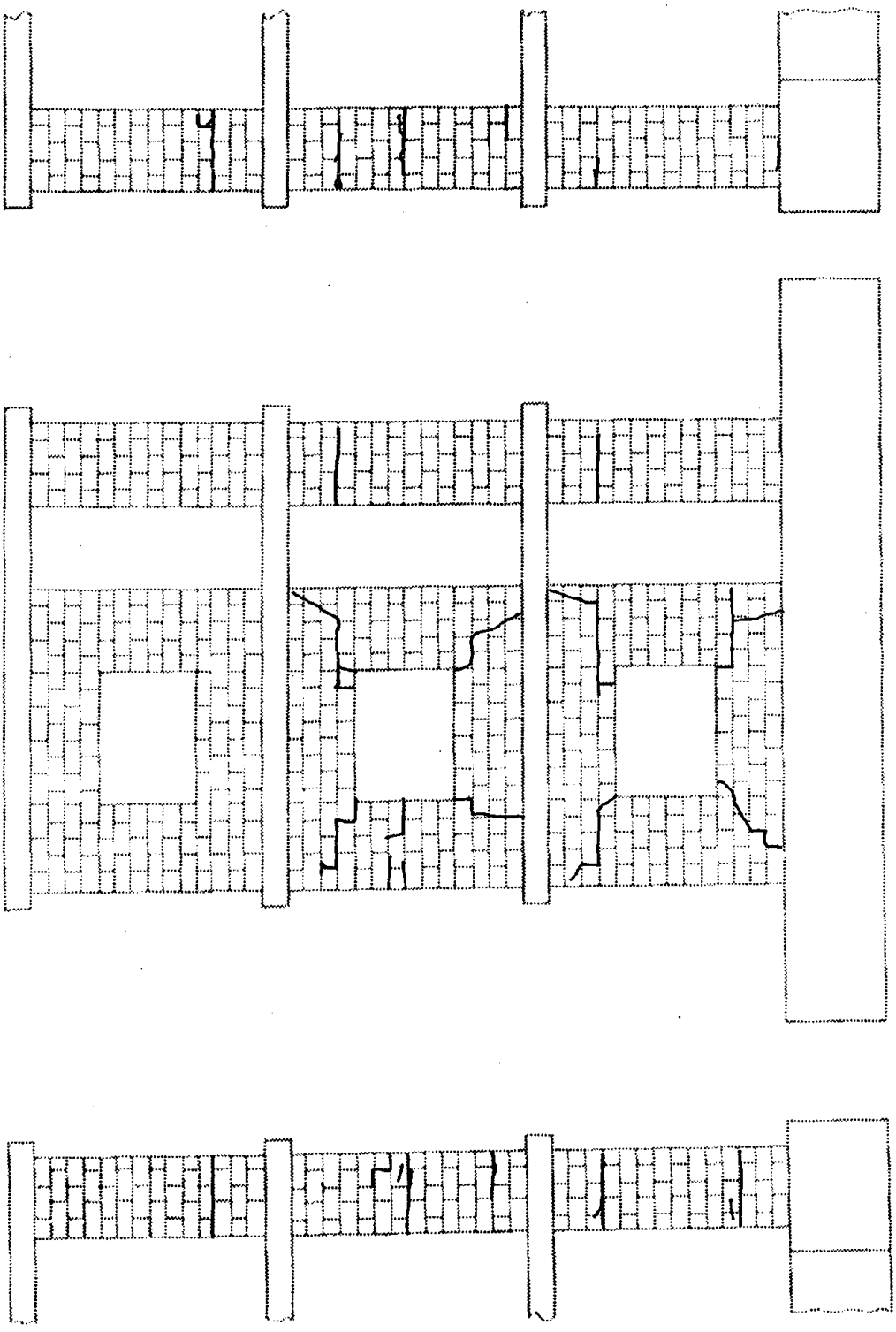

Figure D.3 (cont) RM3 Crack Patterns

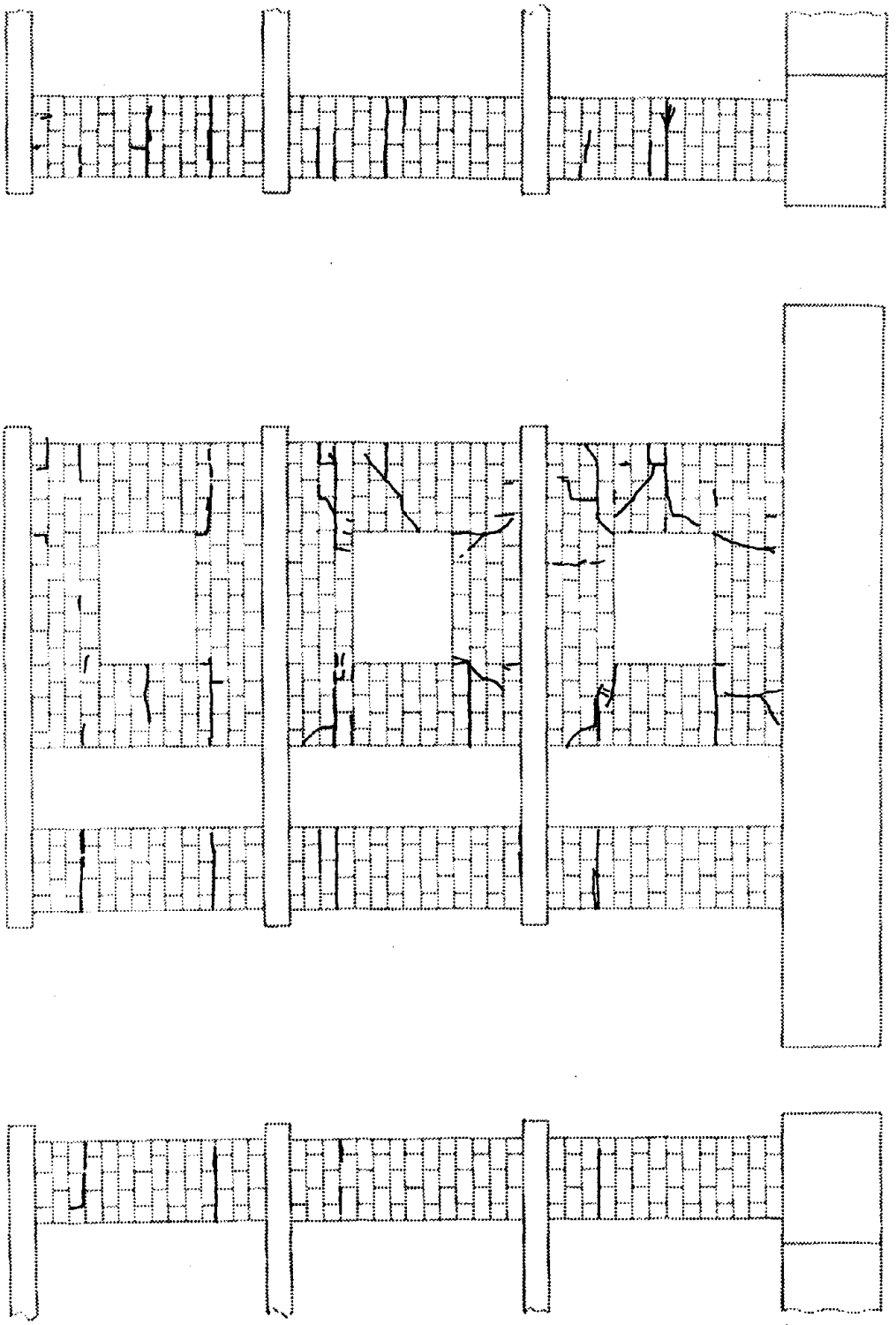

Figure D.3 (cont) RM3 Crack Patterns

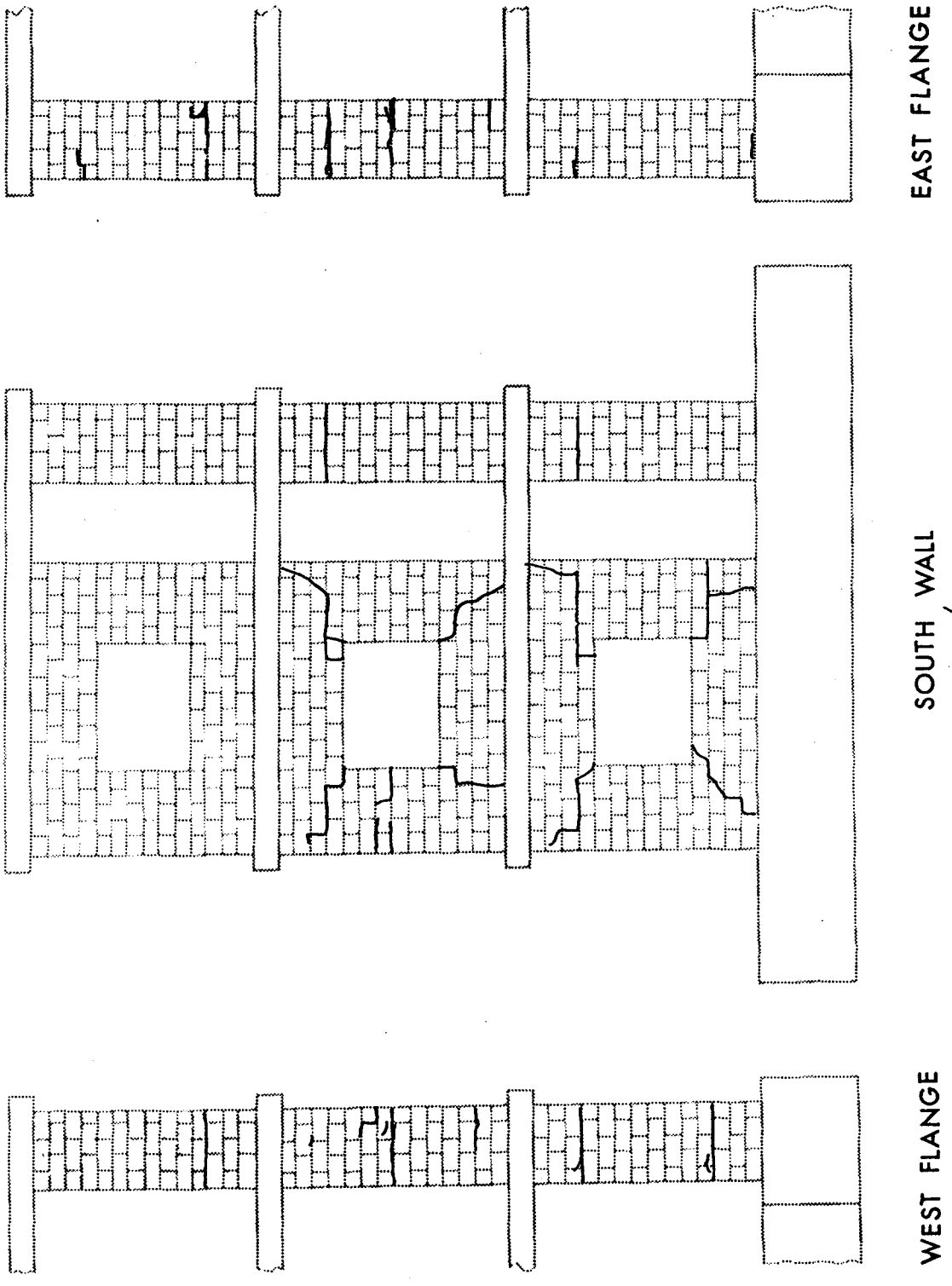

Figure D.3 (cont) RM3 Crack Patterns

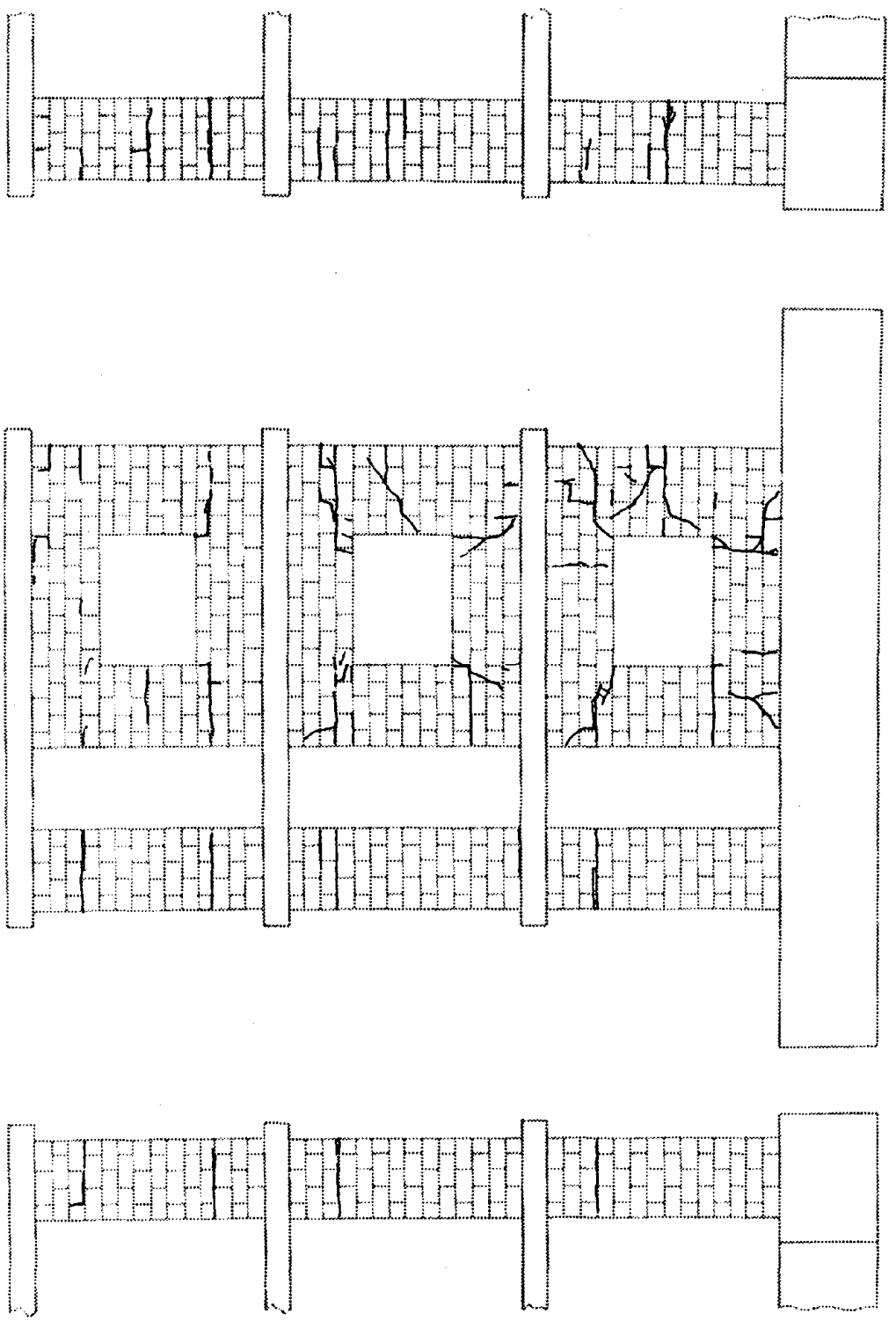

Figure D.3 (cont) RM3 Crack Patterns

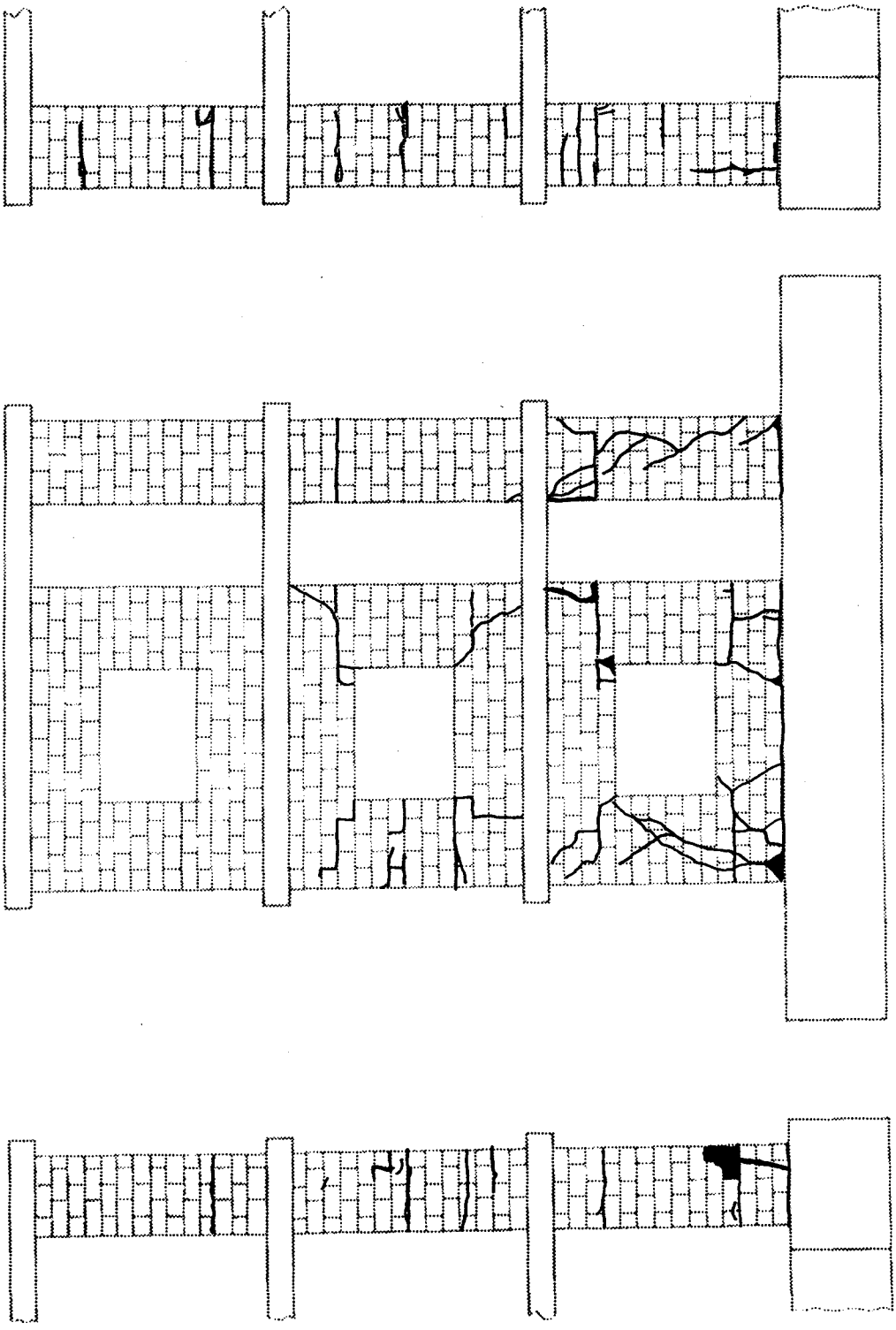

Figure D.3 (cont) RM3 Crack Patterns

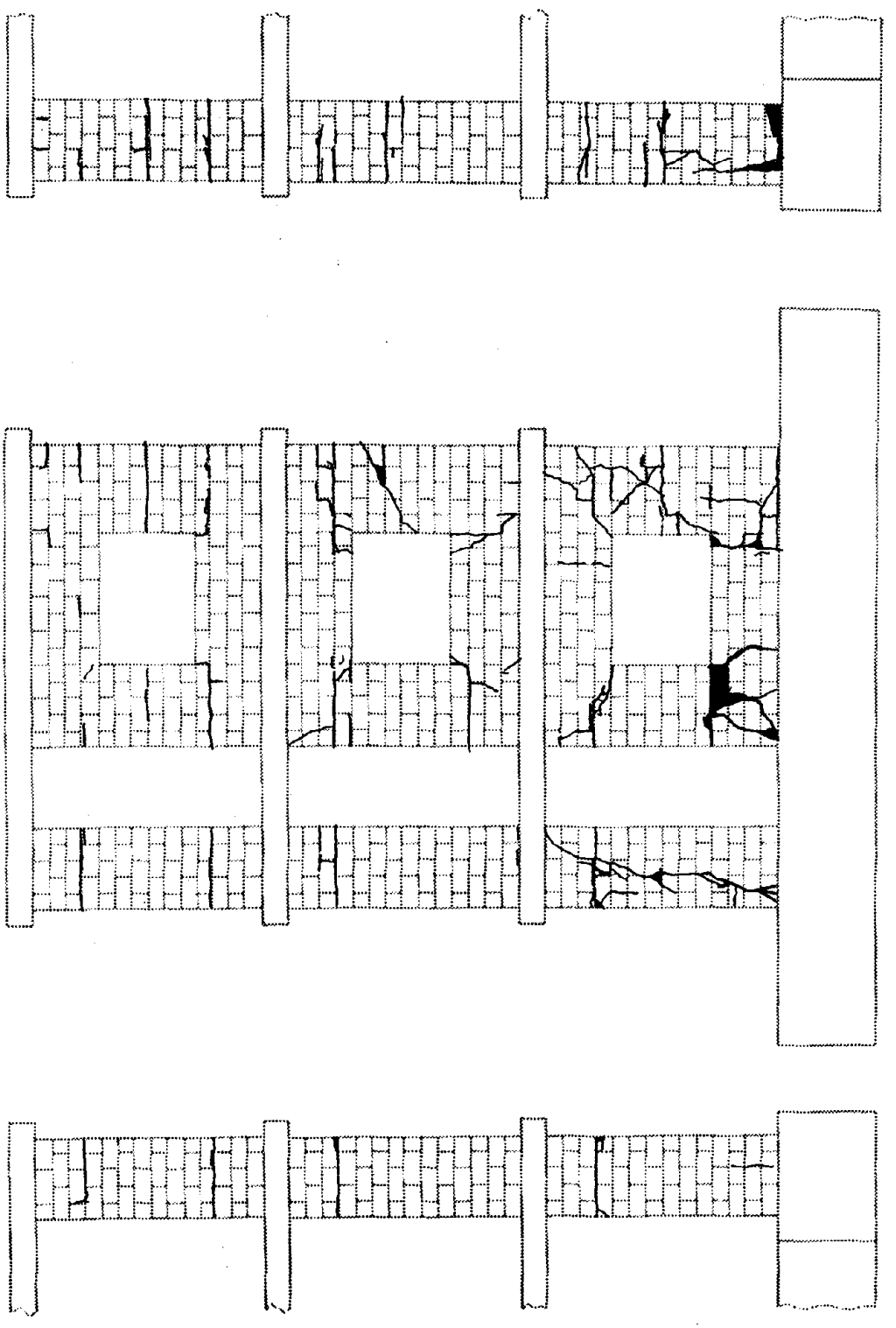

Figure D.3 (cont) RM3 Crack Patterns

APPENDIX E

MEASURED RESPONSE

This appendix presents the response measured during each dynamic test of structure RM1 and structure RM3. Recorded response includes histories of lateral acceleration and lateral displacement at each floor level as well as histories of base shear and base moment which were obtained from the measured accelerations.

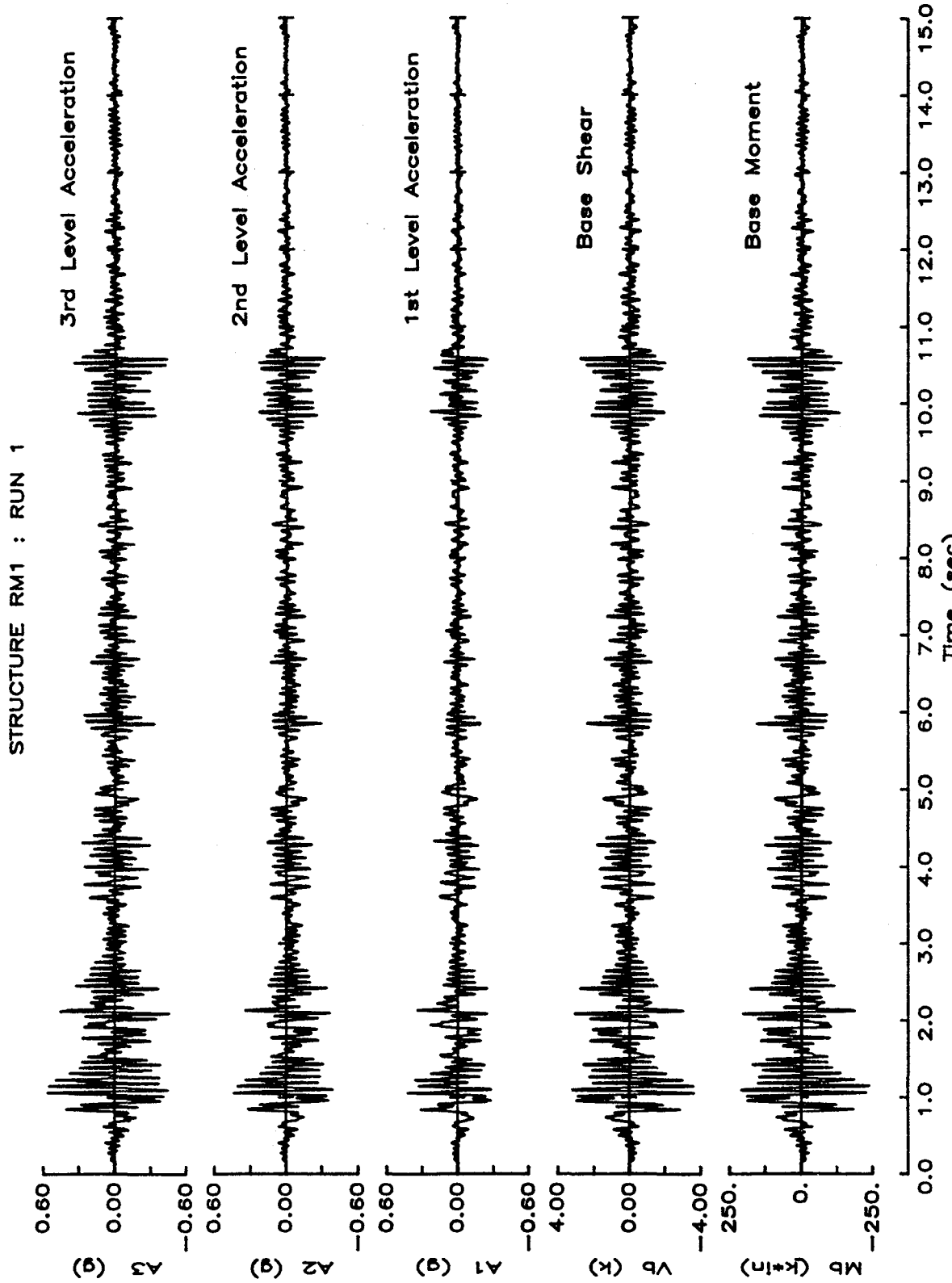

Figure E.1 RM1 Acceleration, Base Shear, Base Moment Response

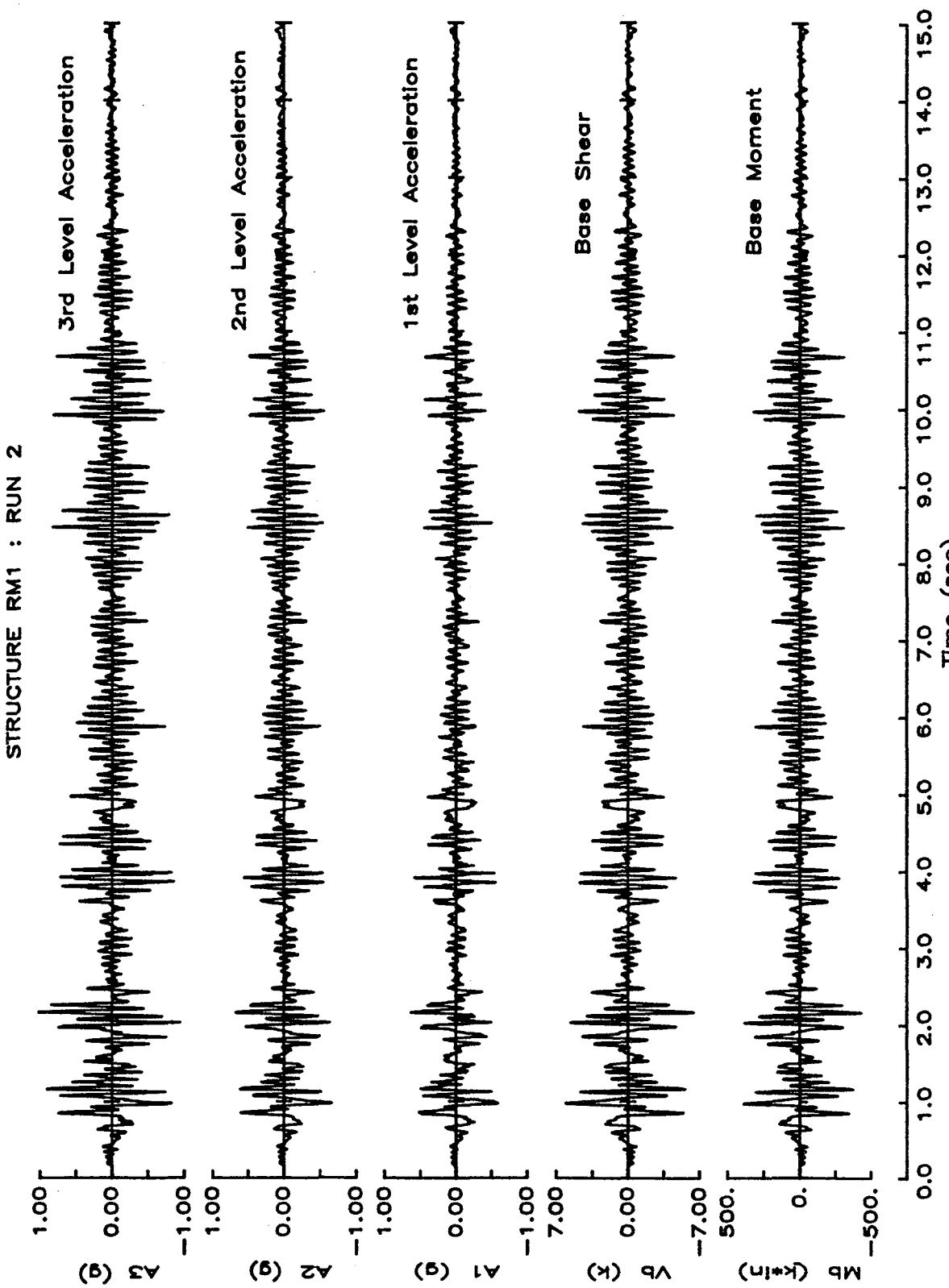

Figure E.1 (cont) RM1 Acceleration, Base Shear, Base Moment Response

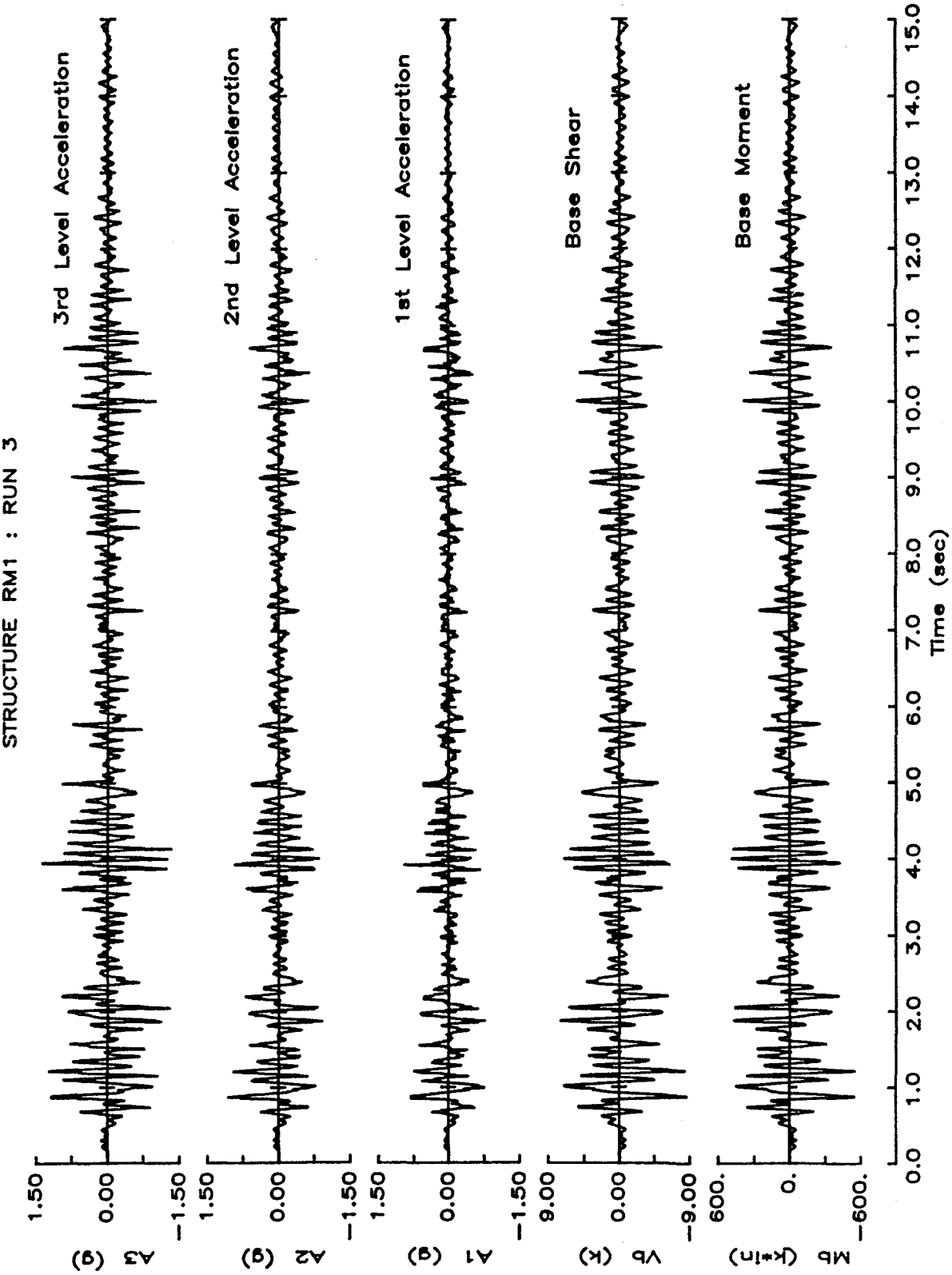

Figure E.1 (cont) RM1 Acceleration, Base Shear, Base Moment Response

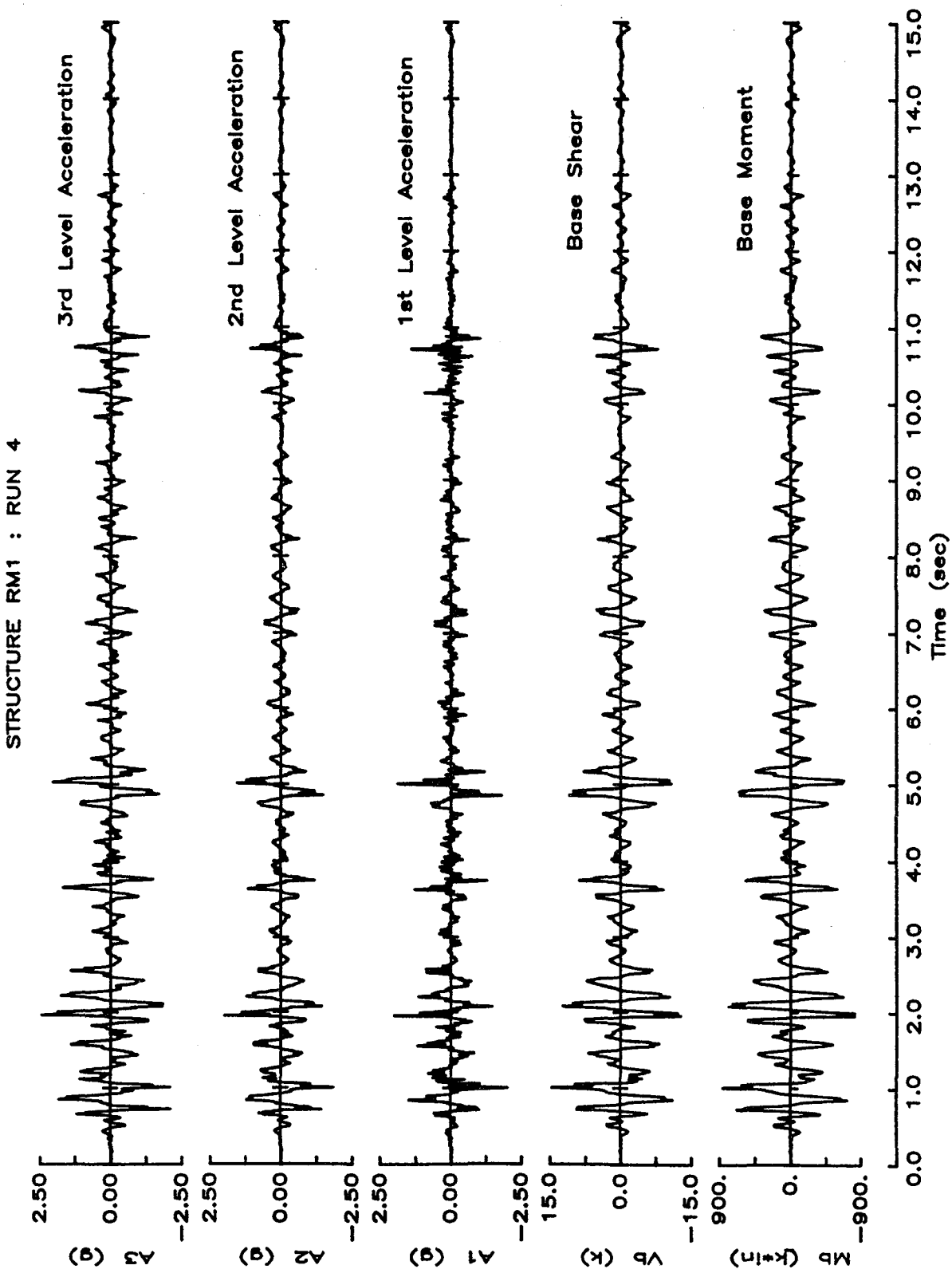

Figure E.1 (cont) RM1 Acceleration, Base Shear, Base Moment Response

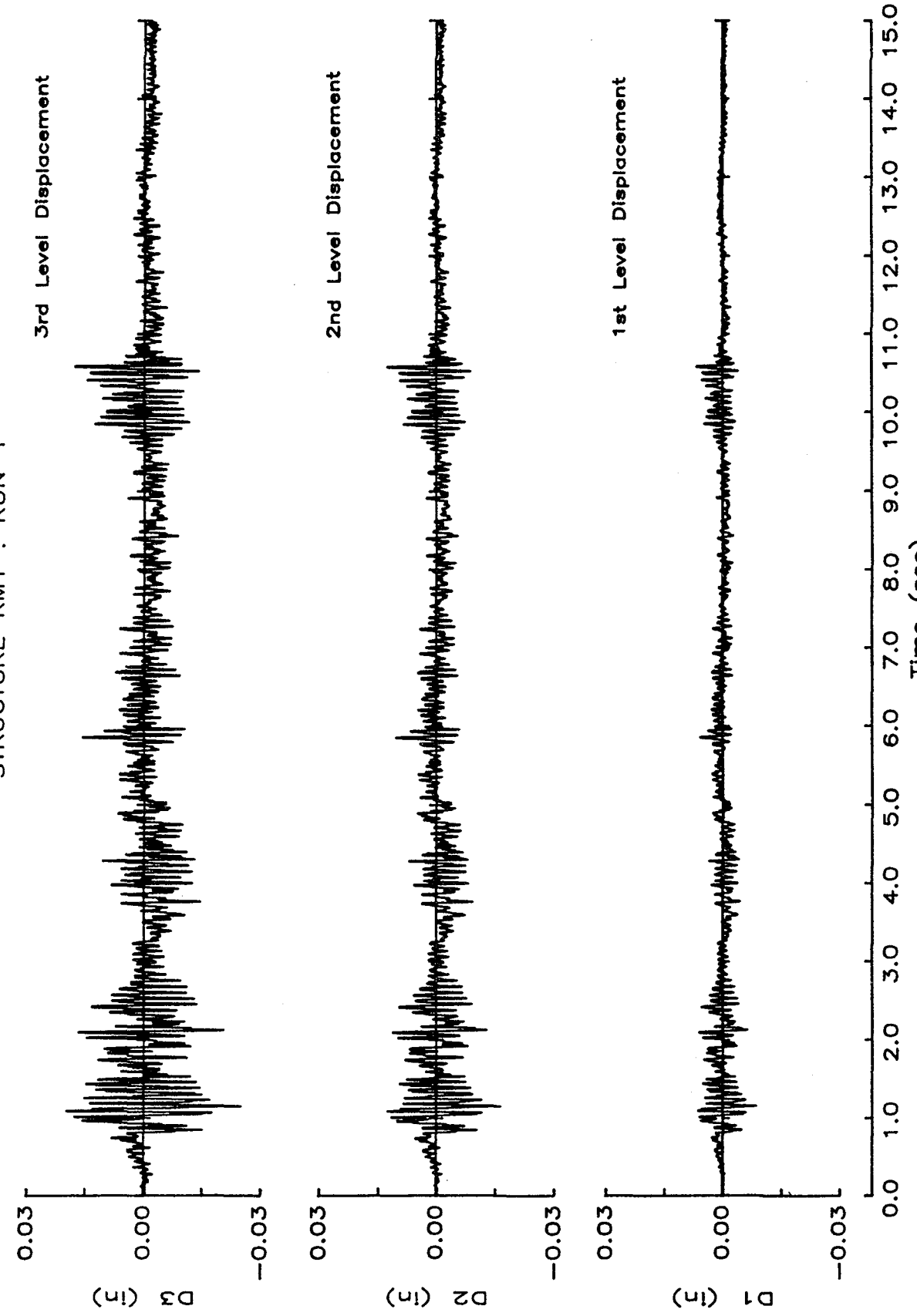

Figure E.2 RM1 Displacement Response

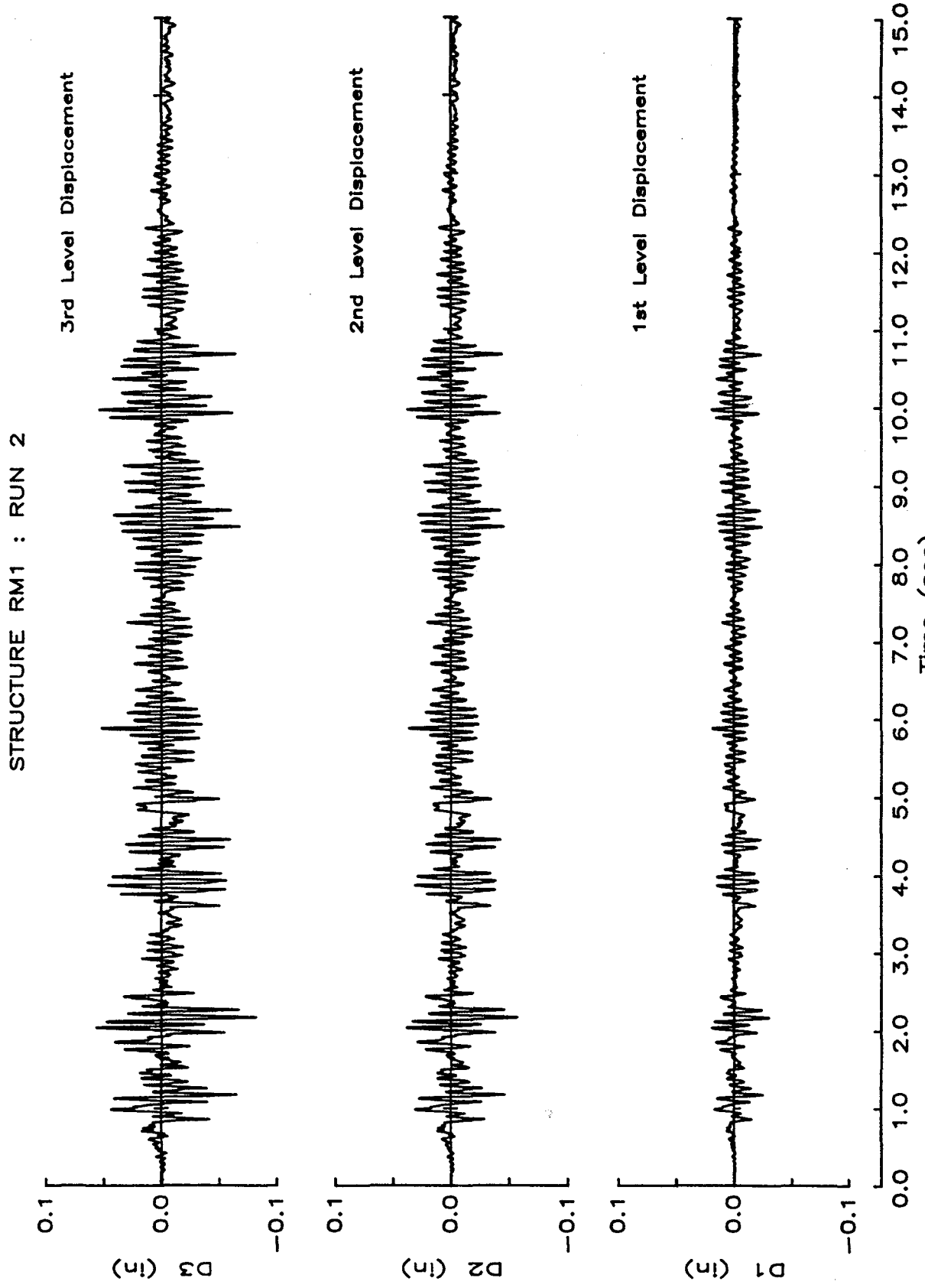

Figure E.2 (cont) RM1 Displacement Response

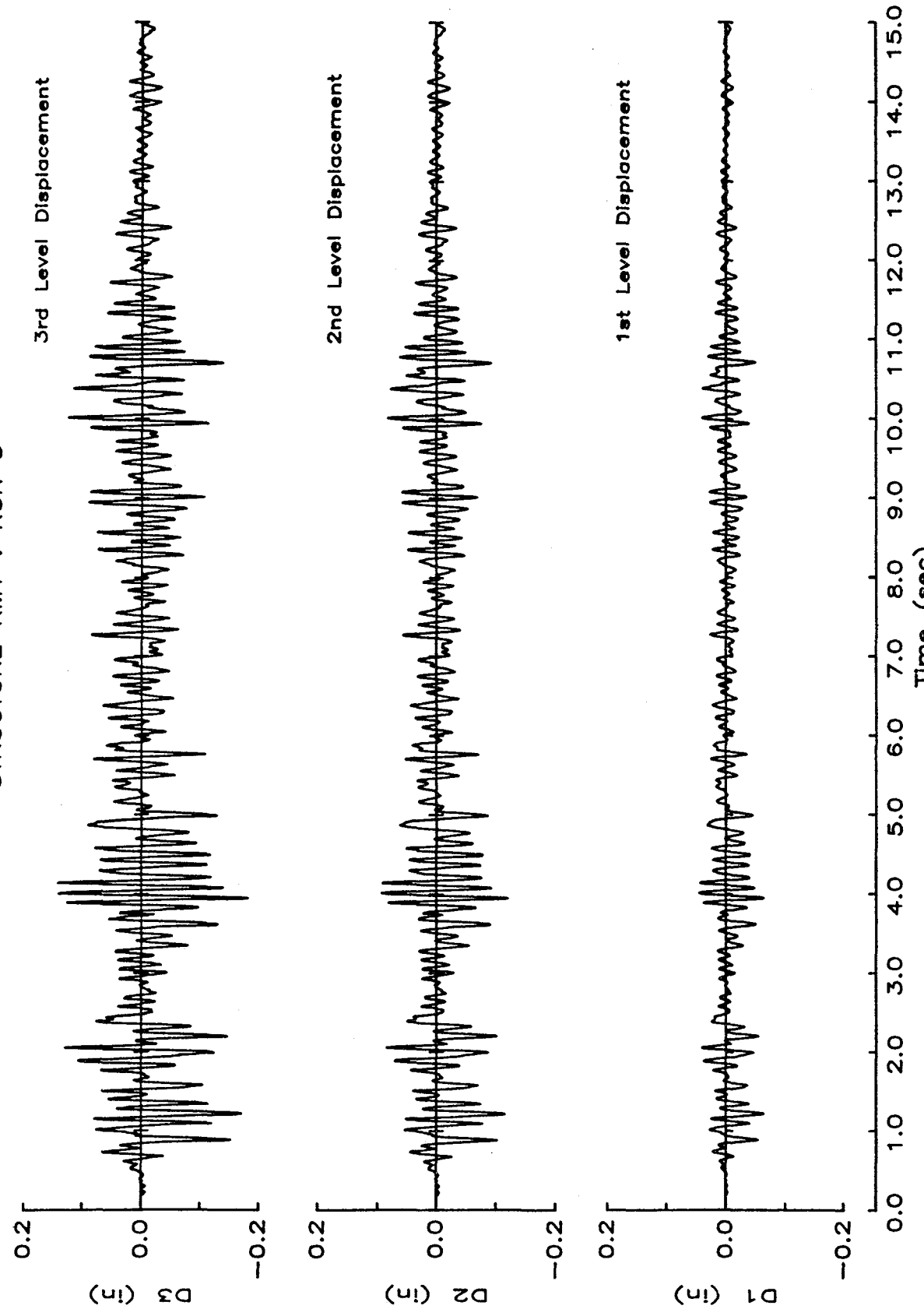

Figure E.2 (cont) RM1 Displacement Response

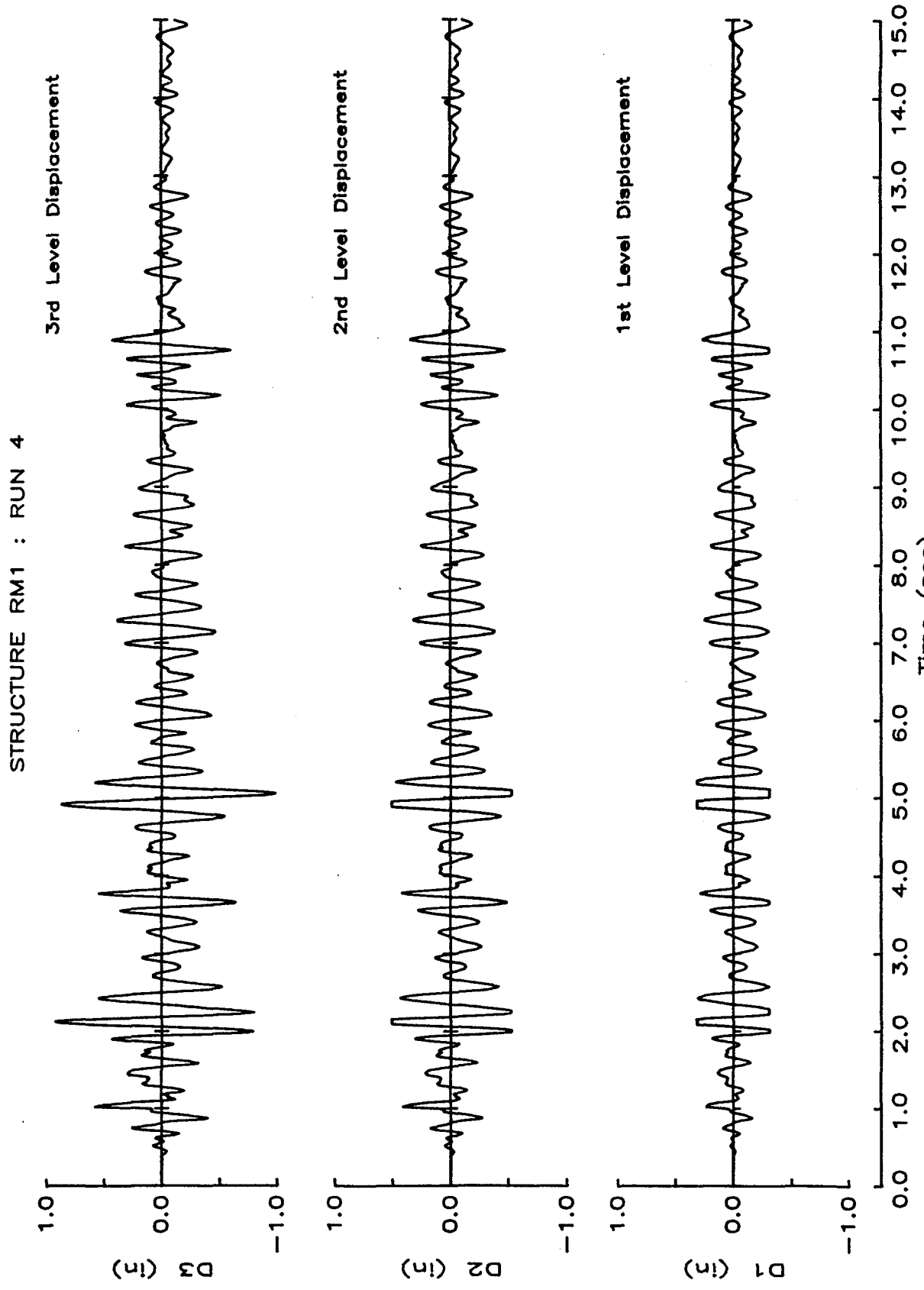

Figure E.2 (cont) RM1 Displacement Response

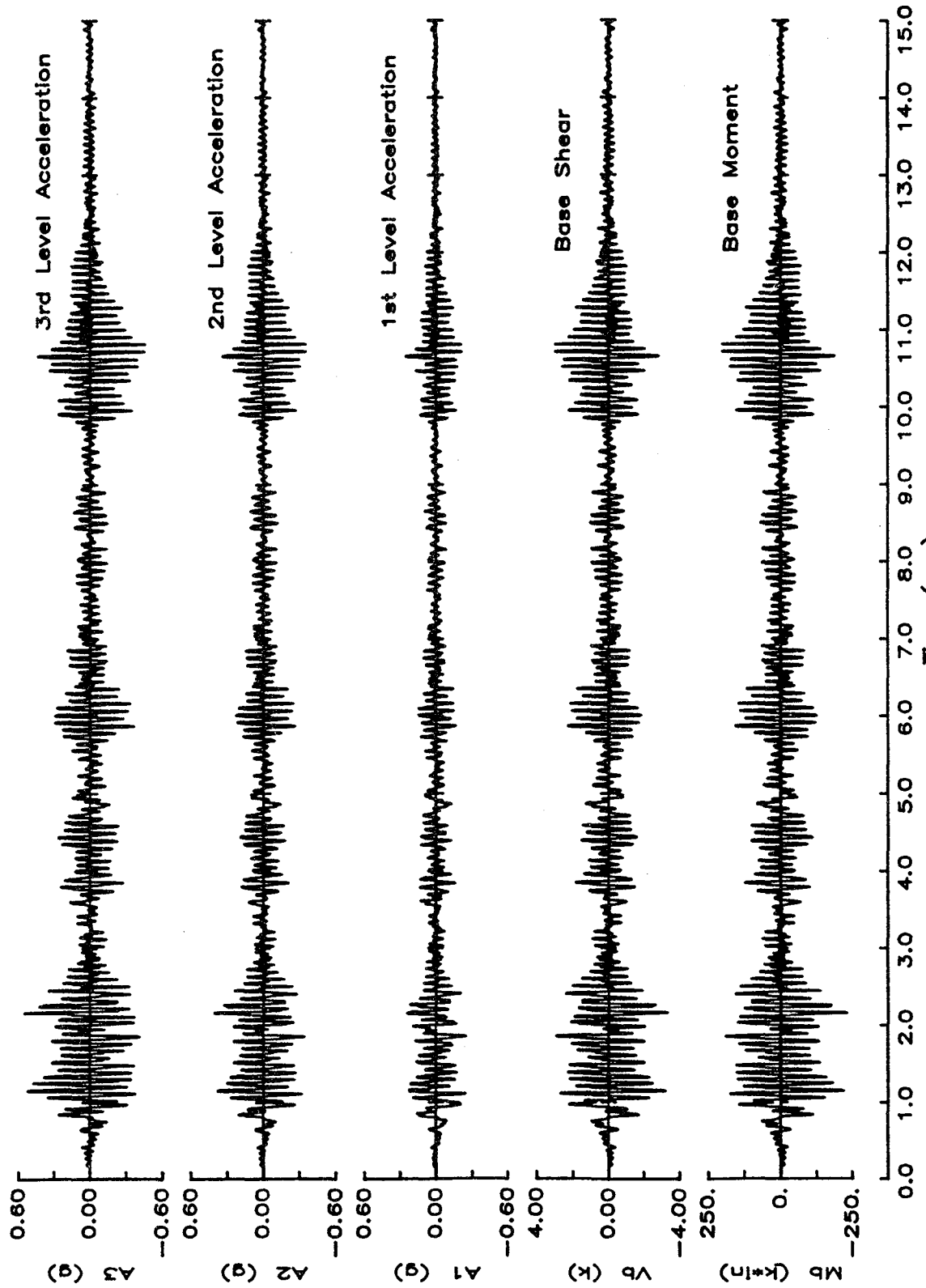

Figure E.3 RM3 Acceleration, Base Shear, Base Moment Response

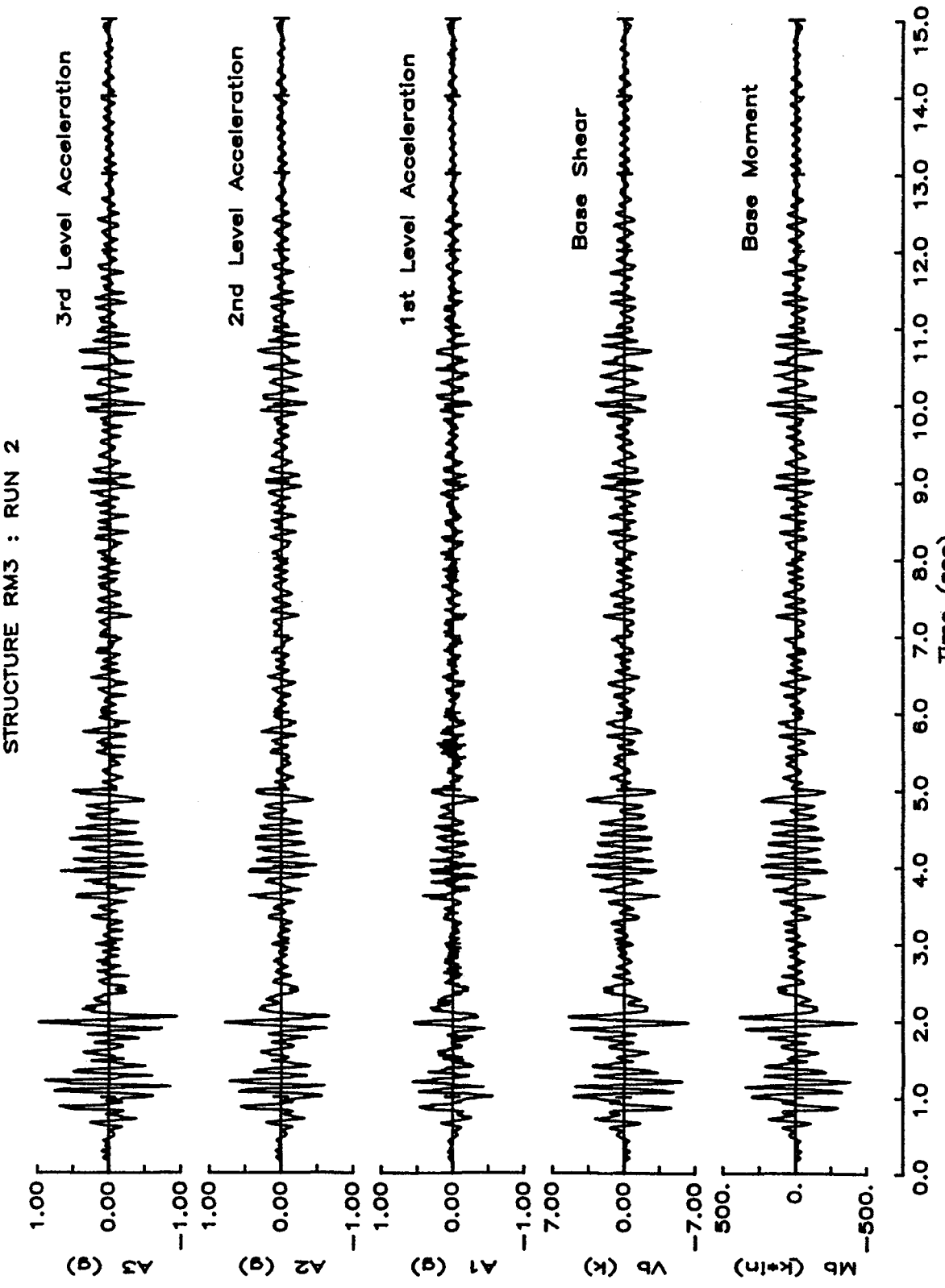

Figure E.3 (cont) RM3 Acceleration, Base Shear, Base Moment Response

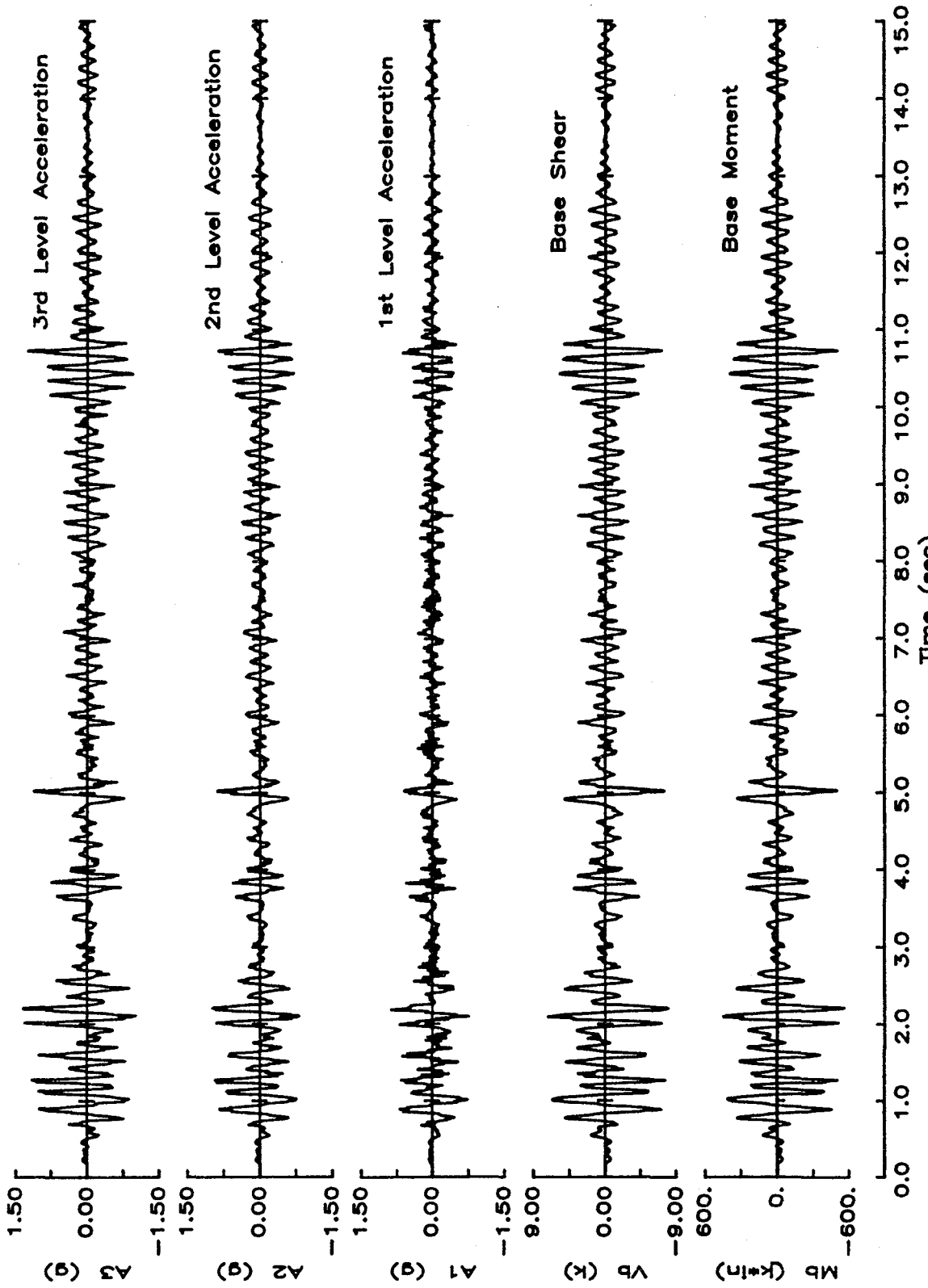

Figure E.3 (cont) RM3 Acceleration, Base Shear, Base Moment Response

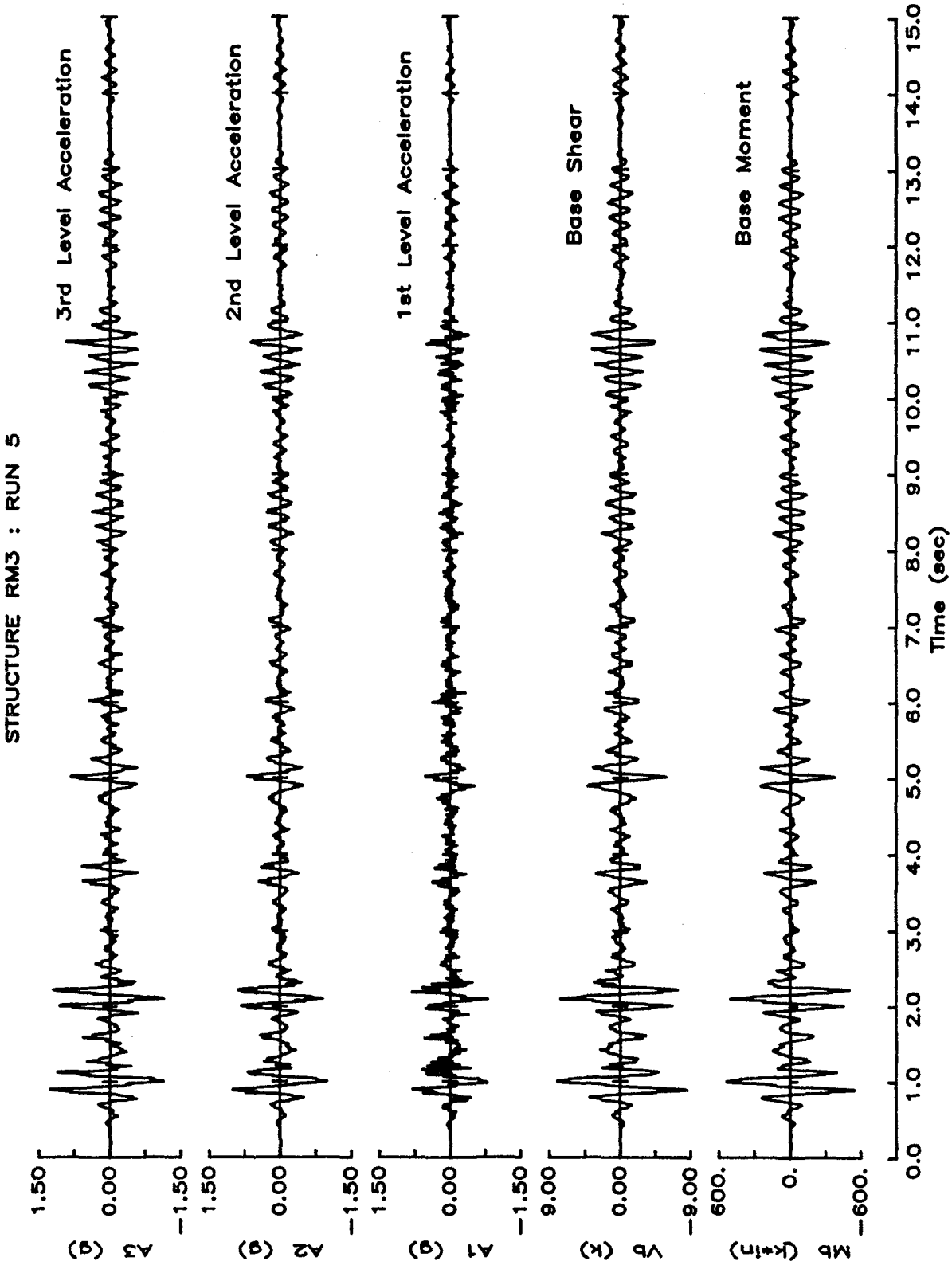

Figure E.3 (cont) RM3 Acceleration, Base Shear, Base Moment Response

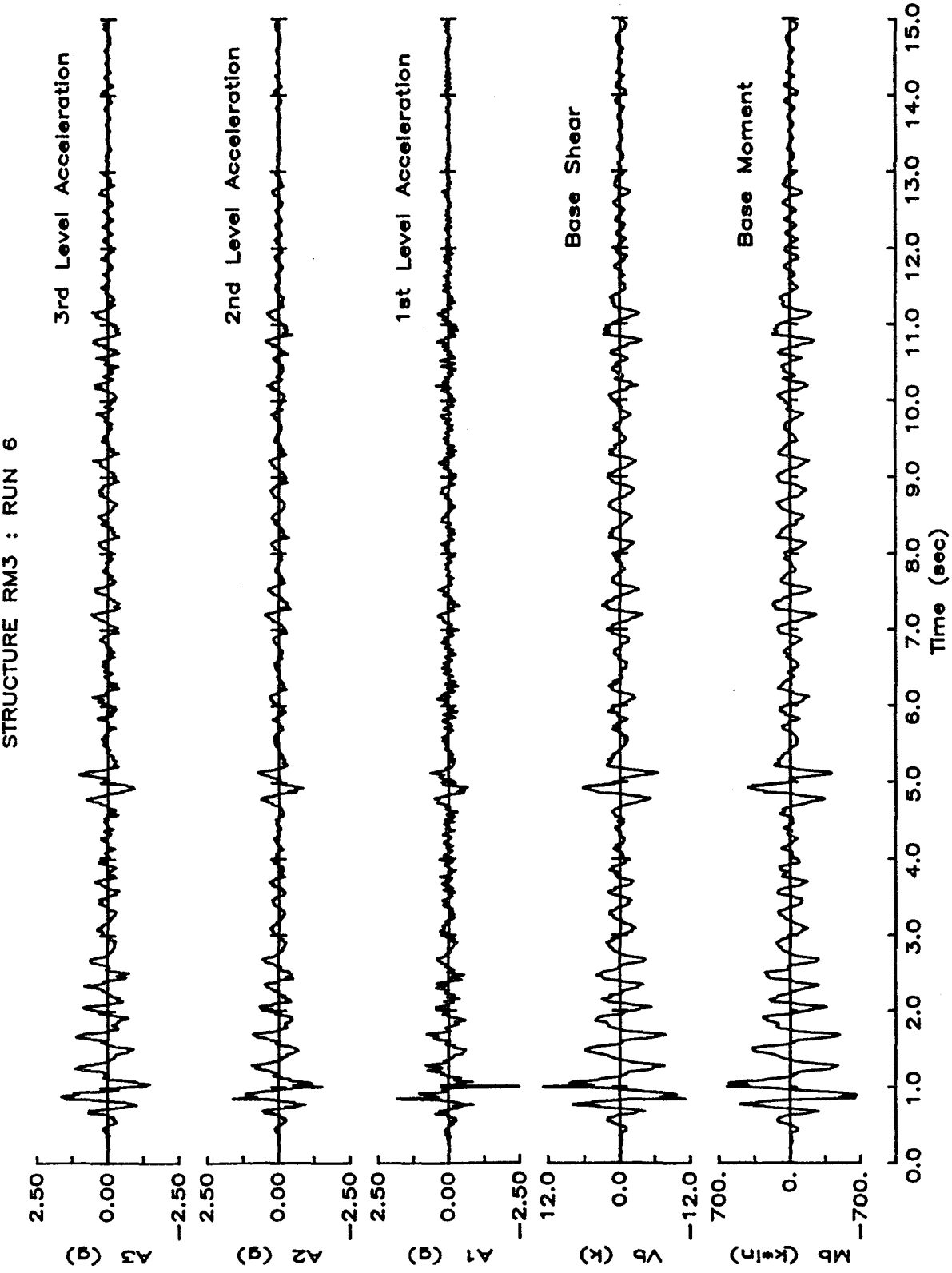

Figure E.3 (cont) RM3 Acceleration, Base Shear, Base Moment Response

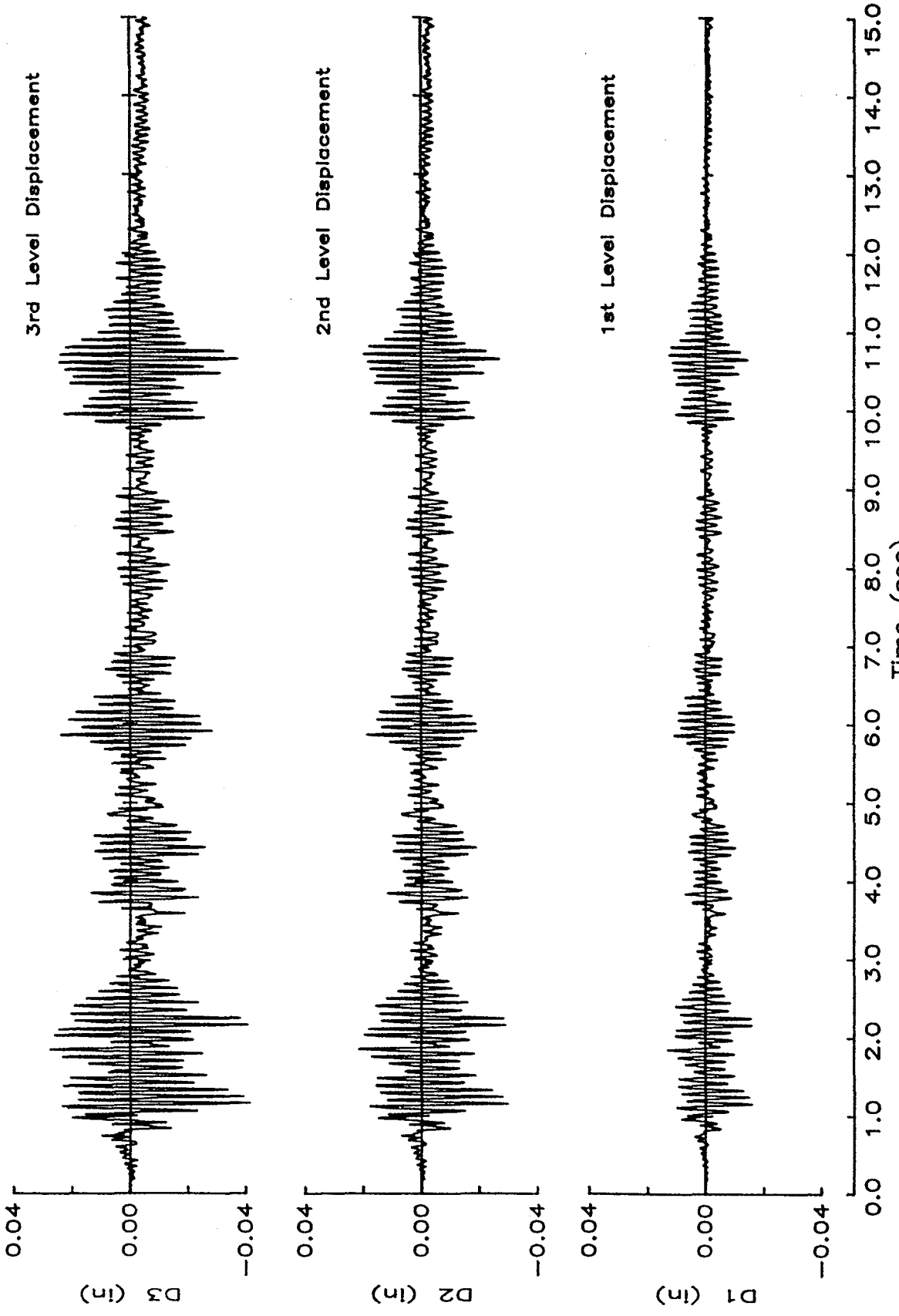

Figure E.4 RM3 Displacement Response

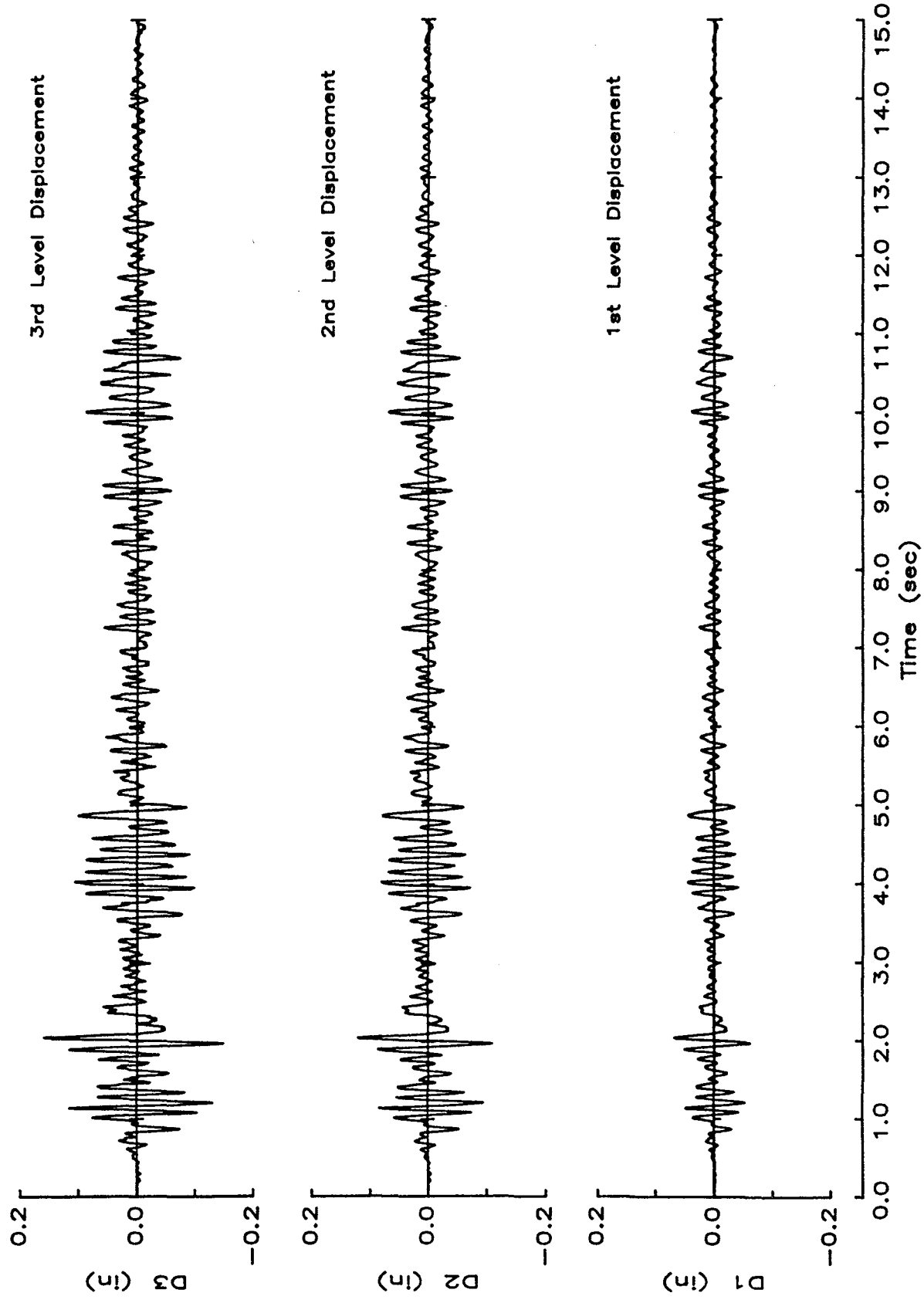

Figure E.4 (cont) RM3 Displacement Response

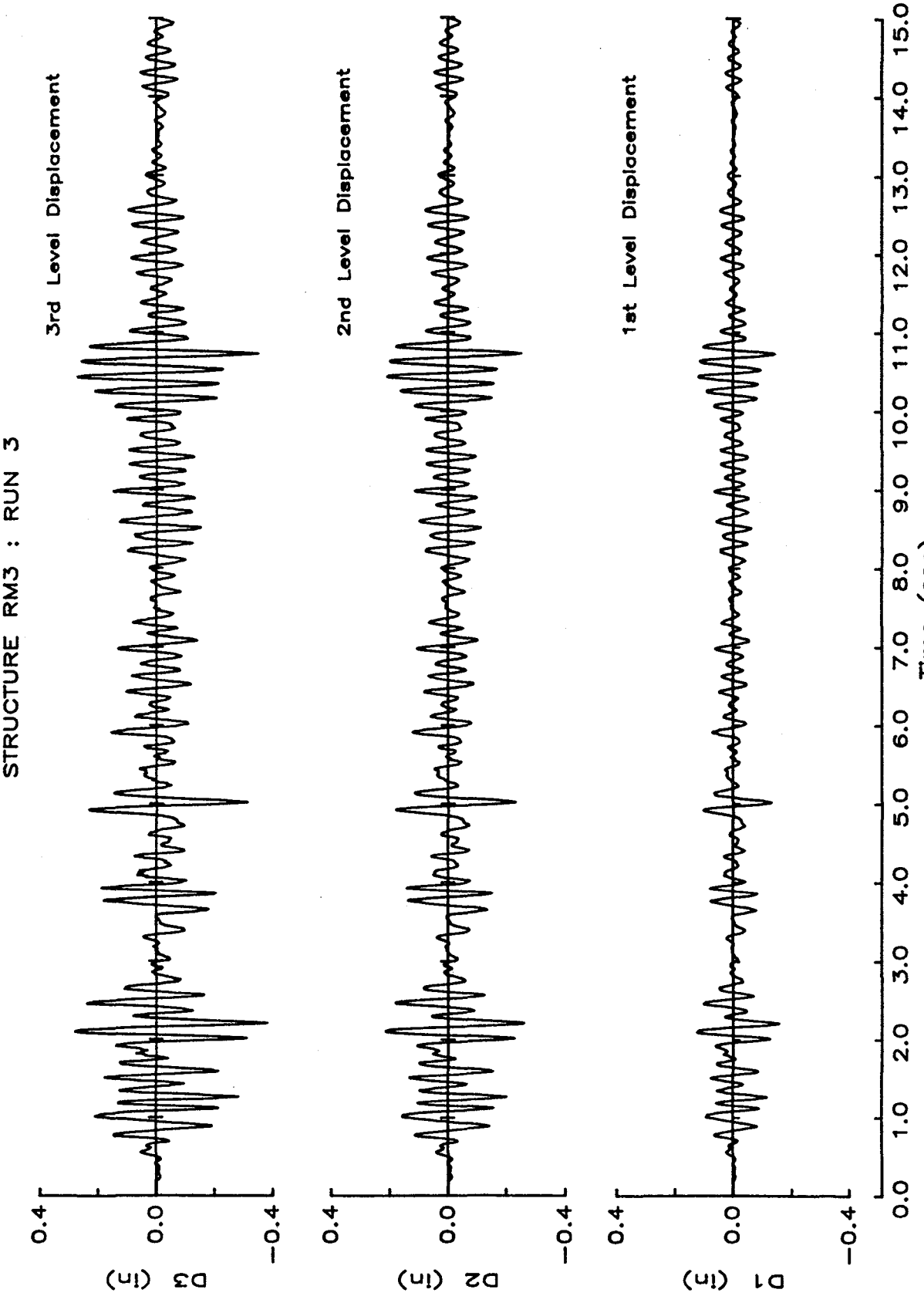

Figure E.4 (cont) RM3 Displacement Response

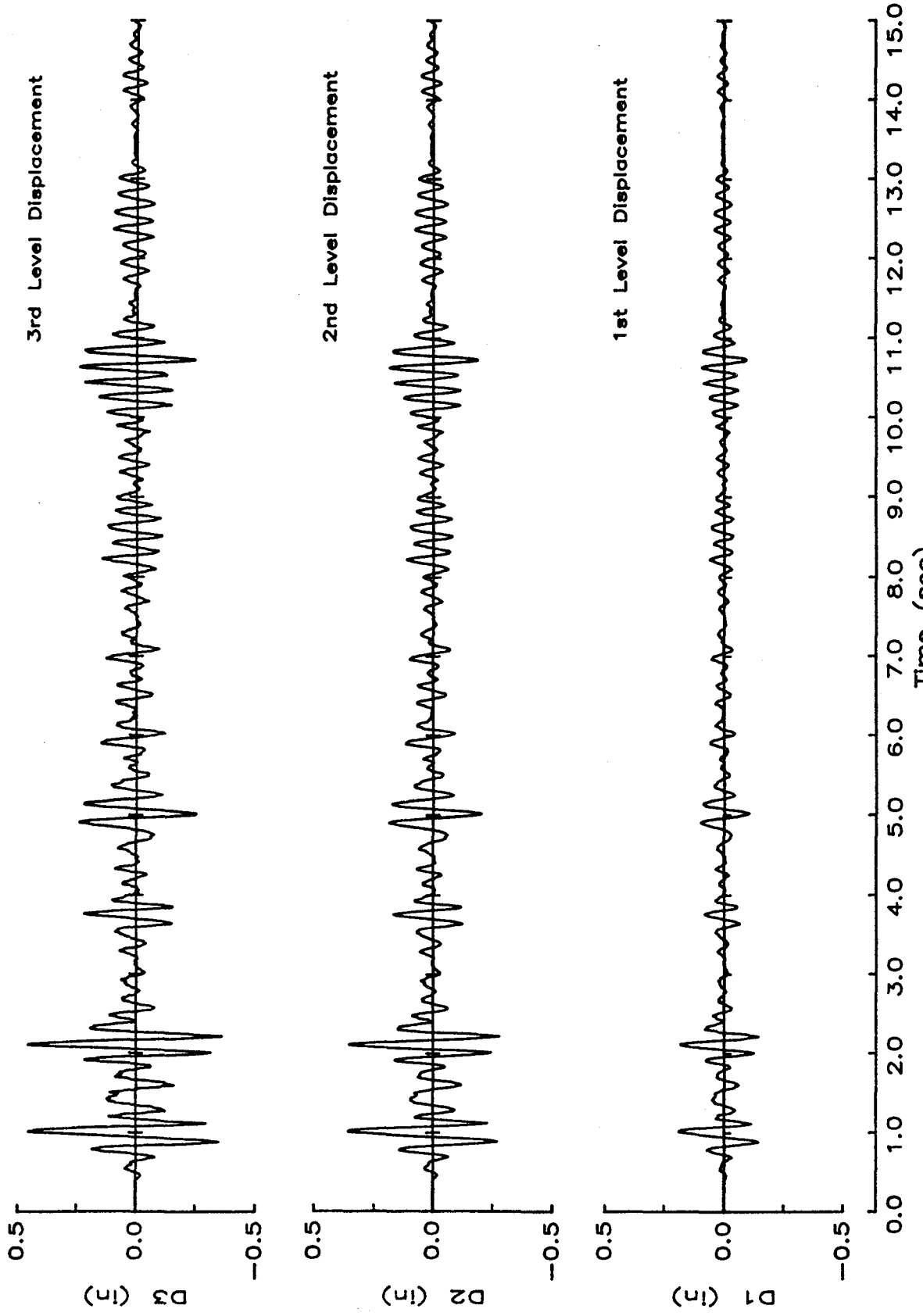

Figure E.4 (cont) RM3 Displacement Response

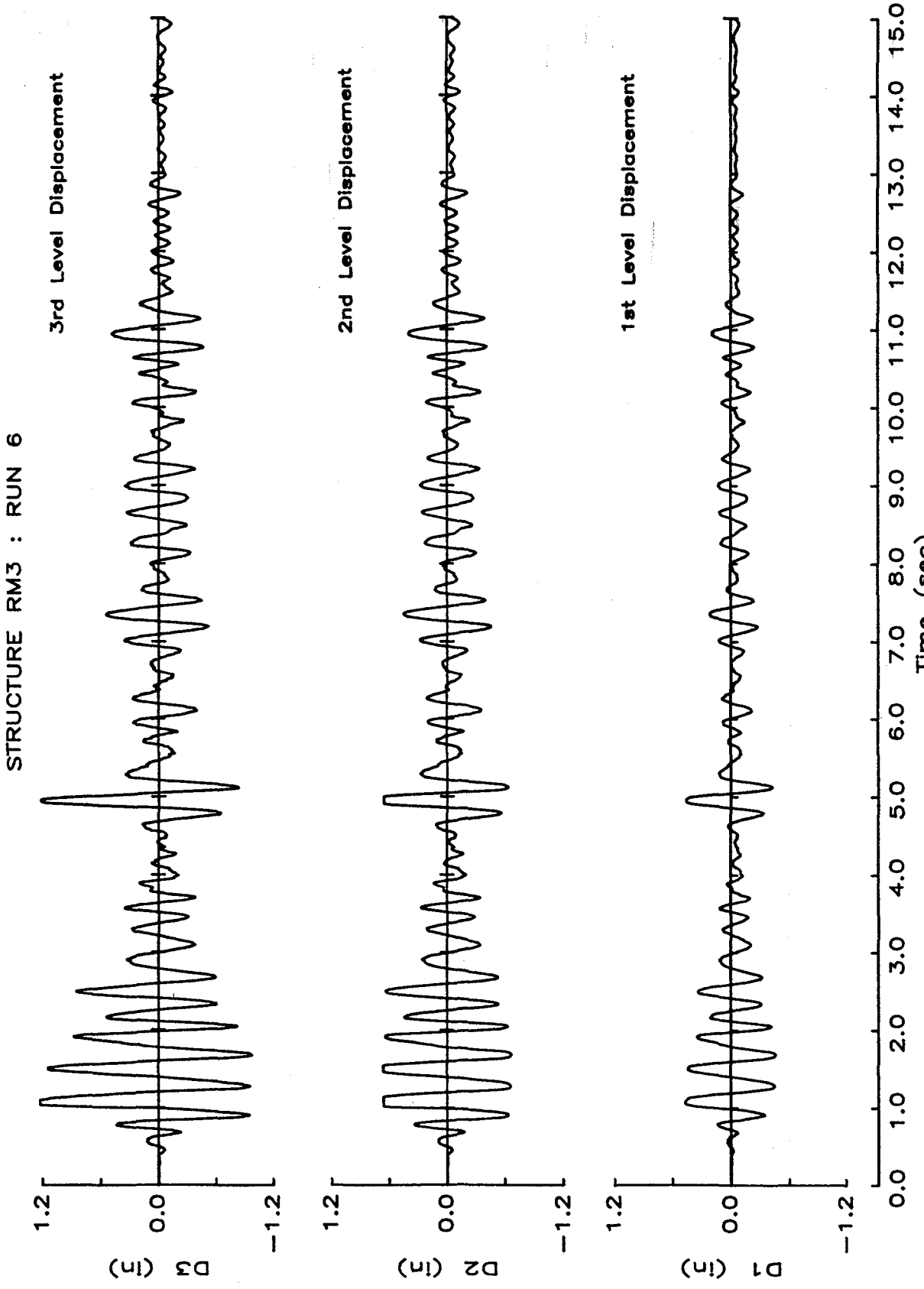

Figure E.4 (cont) RM3 Displacement Response

REFERENCES

1. Abboud, B. E., "The Use of Small Scale Direct Models for Concrete Block Masonry Assemblages and Slender Reinforced Walls Under Out-of-Plane Loads," Ph.D. Thesis, Department of Civil Engineering, Drexel University, June 1987.

2. Abrams, D. P., "Lateral Resistance of a Two-Story Block Building," Advances in Analysis of Structural Masonry, ASCE, 1986 Structures Congress, New Orleans, pp. 41-57.

3. Abrams, D. P., "Computation of Dynamic Response for Concrete and Masonry Structures Using a Microcomputer," Computer Applications in Concrete Technology, SP 98-8, American Concrete Institute, 1987, pp. 159-181.

4. American Society of Testing Materials, Designation E 519-81, Annual Book of ASTM Standards, Vol. 04.07, 1981.

5. Amrhein, J. A., Reinforced Masonry Engineering Handbook, Masonry Institute of America, 4th Edition, Los Angeles, CA, 1983.

6. Bazan, E., M. Padialla, and R. Meli, "Seguridad Ante Sismos de Casas de Adobe," Report of the Institute of Engineering, National University of Mexico, Mexico City, 1979.

7. Benedetti, D. and A. Castoldi, "Dynamic and Static Experimental Analysis of Stone Masonry Buildings," Proceedings, Seventh European Conference on Earthquake Engineering, Athens, 1982.

8. Blondet, D. M. and L. Esparza, "Analysis of Shaking Table-Structure Interaction Effecting During Seismic Simulation Tests," Earthquake Engineering and Structural Dynamics, Vol. 16, No. 4, May 1988, pp. 473-490.

9. Blondet, M., R. L. Mayes, T. E. Kelly, R. Villablanca, and R. Klingner, "Observed Behavior of Chilean Masonry Buildings; Implications on U.S. Design Codes," Proceedings, Fifth North American Masonry Conference, Vol. I, Urbana, IL, June 1990, pp. 13-29.

10. Bonacci, J., "Experiments to Study Seismic Drift of Reinforced Concrete Structures," Ph.D. Dissertation submitted to the Graduate College of the University of Illinois, Urbana, IL, 1989.

11. California Institute of Technology, Earthquake Engineering Research Laboratory, "Strong Motion Earthquake Accelerograms, Digitized and Plotted Data," EERL Report No. 71-50, Pasadena, CA, 1971.

12. Dickey, W. L. and R. R. Schneider, Reinforced Masonry Design, Prentice-Hall, Inc. Englewood Cliffs, NJ, 1987, 682pp.

13. Eberhard, M., "Experiments and Analyses to Study the Seismic Response of Reinforced Concrete Frame-Wall Structures with Yielding Columns," Civil Engineering Studies, Structural Research Series No. 548, University of Illinois, Urbana, IL, September 1989.

14. Englekirk, R. E. and G. C. Hart, Earthquake Design of Concrete Masonry Buildings, Vol. 2, Prentice-Hall, Inc., Englewood Cliffs, NJ, 1984, 268pp.

15. Ewing, R. D., J. C. Kariotis, R. E. Englekirk, and G. C. Hart, "Analytical Modeling for Reinforced Masonry Buildings and Components - TCCMAR Category 2 Program," Proceedings, Fourth North American Masonry Conference, UCLA, CA, August 1987.

16. Gulkan, P. and M. A. Sozen, "Inelastic Response of Reinforced Concrete Structures to Earthquake Motions," ACI Journal, Vol. 71, No. 12, December 1974, pp. 604-610.

17. Gulkan, P., R. L. Mayes, and R. W. Clough, "Shaking Table Study of Single-Story Masonry Houses, Volumes 1, 2 and 3," Report No. EERC 79-23, 24 and 25, University of California at Berkeley, 1979.

18. Harris, H. G., B. Labrouski, and S. G. Lafis, "Material Characterization for Direct Modeling of Reinforced Block Masonry Structures," Proceedings, Fifth North American Masonry Conference, Vol. II, pp. 639-650.

19. Housner, G. W., "Behavior of Structures During Earthquakes," Journal of the Engineering Mechanics Division, ASCE, Vol. 85, No. EM4, October 1959, pp. 109-130.

20. International Conference of Building Officials, Uniform Building Code, 1985 Edition, Whittier, CA, 1985.

21. International Conference of Building Officials, Uniform Building Code, 1988 Edition, Whittier, CA, 1988.

22. Kariotis, J. C., Md. A. Rahman, and A. M. El-Mustapha, "Investigation of Current Seismic Design Provisions for Masonry Shear Walls," Proceedings, Fifth Meeting of the U.S.-Japan Joint Technical Coordinating Committees on Masonry Research, Category D, Paper No. 5, Tsukuba, Japan, 1989.

23. Kariotis, J. C., A. M. El-Mustapha, and R. D. Ewing, "Influence of Nonlinear Models on Dynamic Displacements," Proceedings, Structures Congress '89, Structural Design, Analysis and Testing, ASCE, New York, NY, 1989, pp. 999-1008.

24. Leiva, G., M. Merryman, and R. Klingner, "Design Philosophies for Two-Story Concrete Masonry Walls with Door and Window Openings, Proceedings, Fifth North American Masonry Conference, Vol. I, pp. 287-295.

25. Lopez, L., R. Dodds, D. Rehak, and R. Schmidt, "POLO-FINITE, A Structural Mechanics System for Linear and Nonlinear, Static and Dynamic Analysis," Civil Engineering Systems Laboratory, University of Illinois at Urbana-Champaign, Urbana, IL, 1987.

26. Maison, B. F. and C. F. Neuss, "SUPER-ETABS: An Enhanced Version of the ETABS Program," Report of the National Science Foundation, J. G. Boukamp, Inc., January 1983.

27. Newmark, N. M., "A Method of Computational for Structural Dynamics," Journal of the Engineering Mechanics Division, ASCE, Vol. 85, No. EM3, July 1959, pp. 69-86.

28. Noland, J. L., "A Review of the U. S. Coordinated Program for Masonry Building Research," Proceedings, Fourth North American Masonry Conference, UCLA, CA, August 1987, pp. 38-2 to 38-17.

29. Paulson, T. J., D. P. Abrams, and R. L. Mayes, "Base Isolation of Masonry Building Structures," Submitted to Journal of Structural Engineering, ASCE, for review, October 1990.

30. Rinawi, A. M., R. W. Clough, and J. M. Blondet, "Pitching and Interaction Effects in EERC Seismic Simulator," Proceedings, Ninth World Conference in Earthquake Engineering, Tokyo-Kyoto, Japan, August 1988, pp. IV-5 to IV-10.

31. Shimazaki, K. and M. A. Sozen, "Seismic Drift of Reinforced Concrete Structures," Research Reports, Hazama-Gumi, Tokyo, 1984, pp. 145-166.

32. Sozen, M. A., S. Otani, and N. N. Nielsen, "The University of Illinois Earthquake Simulator," Proceedings, Fourth World Conference on Earthquake Engineering, Santiago, Chile, Vol. III, Session B5, January 1969, pp. 139-150.

33. Sozen, M. A. and S. Otani, "Performance of the University of Illinois Earthquake Simulator in Reproducing Scaled Earthquake Motions," Proceedings, U.S.-Japan Seminar on Earthquake Engineering with Emphasis on the Safety of School Buildings, Sandai, September 1970, pp. 278-302.

34. Sozen, M. A., "A Frame of Reference," Ralph B. Peck Symposium, University of Illinois, Urbana, IL, April 1987.

35. Tena-Colunga, A. and D. P. Abrams, "Estimating Response of Masonry Structures with Linear Finite Elements," Proceedings, Fifth North American Masonry Conference, Vol. I, Urbana, IL, June 1990, pp. 213-224.

36. Tomazevic, M., "Experimental and Analytical Study of Dynamic Behavior of Masonry Buildings Subjected to Earthquake Loading," Institute for Testing and Research in Materials and Structures, Report No. ZRMK/IKPI-84/06, Ljubljana, Yugoslavia, 1984.

37. Wakabayashi, M., T. Fujiwara, T. Nakamura, M. Tomazevic, and Y. Orito, "Experimental Study of the Seismic Resistance of Brick Masonry Walls," Proceedings, Sixth Japan Earthquake Engineering Symposium, Tokyo, 1982.

38. Wu, M., "Shaking Table Test of Block Masonry Building Strengthened with Concrete Columns," Proceedings, US/PRC Workshop on Seismic Design of Masonry Structures, State Seismological Bureau, Institute of Engineering Mechanics, Harbin, China, May 1986.

39. Xu, S., "Study on Earthquake Performance of Hollow Block Masonry Buildings," Proceedings, US/PRC Workshop on Seismic Design of Masonry Structures, State Seismological Bureau, Institute of Engineering Mechanics, Harbin, China, May 1986.

40. Yokel, F. Y. and S. G. Fattal, "Failure Hypothesis for Masonry Shear Walls," Journal of the Structural Division, ASCE, March 1976, pp. 515-532.

41. Zhu, B. and L. Xilin, "Earthquake Simulation on an Unreinforced Masonry Building," Closed Loop Magazine, MTS Corp., Minneapolis, MN, Winter 1985.

42. Zhu, B., "Aseismic Tests of Brick Structures," Proceedings, US/PRC Workshop on Seismic Design of Masonry Structures, State Seismological Bureau, Institute of Engineering Mechanics, Harbin, China, May 1986.